

**Time-Dependent Deformation of a Nonlinear
Viscoelastic Rubber-toughened Fiber
Composite with Growing Damage**

by
Robert Thomas Bocchieri, B.S., M.S.

Dissertation
Presented to the Faculty of the Graduate School of The University of Texas at
Austin

Supported by Funding From:
Minerals Management Service
Under the MMS/OTRC Cooperative Research Agreement
1435-01-99-CA-31003
Task Order 16176
MMS Project Number 365

May 2001

OTRC Library Number: 05/01B113

“The views and conclusions contained in this document are those of the authors and should not be interpreted as representing the opinions or policies of the U.S. Government. Mention of trade names or commercial products does not constitute their endorsement by the U. S. Government”.



For more information contact:

Offshore Technology Research Center

Texas A&M University
1200 Mariner Drive
College Station, Texas 77845-3400
(979) 845-6000

or

Offshore Technology Research Center

The University of Texas at Austin
1 University Station C3700
Austin, Texas 78712-0318
(512) 471-6989

A National Science Foundation Graduated Engineering Research Center

Copyright

by

Robert Thomas Bocchieri

2001

**Time-Dependent Deformation of a Nonlinear
Viscoelastic Rubber-toughened Fiber
Composite with Growing Damage**

by

Robert Thomas Bocchieri, B.S., M.S.

Dissertation

Presented to the Faculty of the Graduate School of

The University of Texas at Austin

in Partial Fulfillment

of the Requirements

for the Degree of

Doctor of Philosophy

The University of Texas at Austin

May 2001

**Time-Dependent Deformation of a Nonlinear
Viscoelastic Rubber-toughened Fiber
Composite with Growing Damage**

**Approved by
Dissertation Committee:**

To Ally

Acknowledgments

I would like to first thank my advisor, Dr. Richard Schapery, whose guidance and patient instruction is deeply appreciated. I also want to thank my Dissertation Committee for many helpful discussions and for reviewing this work.

Next I'd like to extend my gratitude to all those who have offered their time and help over the years, especially Dr. Melanie Violette for all the time we have spent in the lab together, Dr. Timothy P. Crain for his crash course in Genetic Algorithms and to Prof. Isao Kimpara and everyone in Giso-ken at The University of Tokyo for being gracious hosts during my stay.

I would also like to thank Ally Rosa for all of her love and support. Ally, you have been a great friend.

Finally, the financial support of the Offshore Technology Research Center and the National Science Foundation is gratefully recognized.

ROBERT THOMAS BOCCHIERI

The University of Texas at Austin

May 2001

Time-Dependent Deformation of a Nonlinear Viscoelastic Rubber-toughened Fiber Composite with Growing Damage

Publication No. _____

Robert Thomas Bocchieri, Ph.D.
The University of Texas at Austin, 2001

Supervisor: R. A. Schapery

One important factor in the durability of polymeric composites is their loss in stiffness over time due to many softening mechanisms, including nonlinear viscoelasticity, viscoplasticity and damage. Damage here refers to all ply-level microstructural changes such as matrix cracking, fiber-matrix debonding and shear yielding. This dissertation uses the theory previously established by Schapery (1999) to develop experimental and data analysis methods for isolating these softening effects.

Schapery's constitutive theory is first tailored for a continuous fiber composite and evaluated for creep/recovery loading where nonlinear viscoelasticity, viscoplasticity and damage growth have a significant effect on strain. *Numerical methods*, implementing a Genetic Algorithm, are developed

to fit material parameters in the recovery equations. This method successfully fits simulated recovery data with hereditary damage effects, but was not implemented on real data due to the unusually complex recovery behavior of the material studied.

A method of *Acoustic emission* monitoring and waveform analysis is developed as a means for tracking two of the primary damage mechanisms in these materials, matrix-cracking and fiber/matrix debond. With direct monitoring, the extent of damage in the material does not need to be inferred from its effect on the stress-strain response. Unidirectional 30° , 45° and 90° coupons of a rubber-toughened carbon/epoxy are monitored in this way for various loading histories. A method of comparing waveforms from different samples is also suggested. An interpretation of the AE data is proposed based on an initial population of existing flaws. Then a cumulative distribution function (CDF) of microcracking is defined and used to study effects of stress history. After developing an idealized model of the material consisting of two viscoelastic phases, a single loading parameter, which is theoretically independent of loading history and derived from viscoelastic fracture mechanics, is found to collapse data from all samples and loading histories, thus supporting the theory.

Finally a *Damage Effect Study* is proposed which identifies the material parameters affected by damage, thereby separating the damage and stress effects on softening. This method is based on vertical shifting of recovery data at different damage states, much like vertical shifting for the effect of stress. Two significant simplifications are found for the material studied; damage does not affect the time scale of the viscoelastic strain and enters through only one parameter in the transverse strain. Viscoelastic shear strain requires two parameters, however. Also, the elastic component of the modulus

is found to increase with increased damage. Results from material testing at fixed damage states indicate a 2-phase viscoelastic constitutive model may be needed to characterize this particular rubber-toughened composite material.

Contents

Acknowledgments	v
Abstract	vi
List of Tables	xiii
List of Figures	xiv
Chapter 1 Introduction	1
1.1 Background	2
1.2 Objective	11
1.3 Summary	13
Chapter 2 Nonlinear Viscoelastic/Viscoplastic Constitutive Theory	17
2.1 Constitutive Theory	17
2.2 Creep/Recovery with Damage Growth	22
2.3 Damage Effect Study	25
2.3.1 Analysis of Conditioned Material	25
2.3.2 Evaluating the Effect of Damage	28

Chapter 3	Numerical Curve Fitting Methods	31
3.1	Genetic Algorithm / Levenberg-Marguart Numerical Routine .	31
3.2	Formulations of Recovery Strain for use in the GA/LM Method	35
3.3	Experiments for Conducting Numerical Fitting	38
Chapter 4	Analysis of Distributed Microcracking	39
4.1	Viscoelastic Crack Growth - Theoretical Background	39
4.1.1	Crack Growth Criteria - J_v Integral	41
4.1.2	Unstable Crack Growth for a Power-law Material . . .	42
4.1.3	Effect of 2-Phase Material on the J_v Integral	43
4.2	Analysis of Crack Growth	48
4.2.1	Analysis and Simplification of the 2-Phase Material . .	48
4.2.2	Analysis of Distributed Cracking	54
Chapter 5	Experimental Setup	58
5.1	Material and Processing Information	58
5.2	Load Frames and Strain Measurement	59
5.3	Acoustic Emission Equipment and Setup	60
5.3.1	AE Testing of Off-Axis Specimens	62
Chapter 6	Acoustic Emission Testing	69
6.1	Microstructural Damage and AE Detection	69
6.2	Anticipated Waveforms	75
6.3	Waveform Filtering	77
6.3.1	Digital Filtering	77
6.3.2	Filtering by location	77

Chapter 7 Acoustic Emission Results and Analysis	80
7.1 Waveform Analysis	80
7.1.1 Waveforms detected at location sensors	81
7.1.2 Extensional and Flexural Waveforms	99
7.2 Cumulative Events versus Load Level	105
7.3 Waveform Energy	107
7.4 Location of Large Events	113
7.5 Ramp/Hold Testing	117
7.6 Interpretation of AE Results	120
7.7 Change in Material Acoustical Properties	124
7.8 Calculation of the CDF of Microcracking	132
7.9 Final Comments on AE Experiments and Analysis	140
Chapter 8 Characterization of Viscoelastic Functions	141
8.1 Linear Viscoelastic Properties	141
8.1.1 Effect of Damage on Linear Viscoelastic Response	146
8.2 Cyclic Effect on Creep and Recovery	147
8.2.1 Cyclic Response of 90° Samples	148
8.2.2 Cyclic Response of 30° Off-axis Samples	153
8.3 Results from the Damage Effect Study	157
8.3.1 Damage Effect in 90° Samples	157
8.3.2 Damage Effect in 45° Samples	161
8.3.3 Damage Effect in 30° Samples	167
8.4 Conditioned Material Behavior	172
8.4.1 90° testing	173
8.4.2 30° off-axis testing	173
8.5 Discussion on Viscoelastic Behavior	178

Chapter 9 Conclusion	182
Appendix A Genetic Algorithm Code	189
References	218
Vita	225

List of Tables

5.1	Typical hardware and software settings for the two acoustic emission sensors used.	61
7.1	Hardware settings on AE-CAL to produce waveforms for the wavespeed/damping study.	125
7.2	Effective transverse properties of the LVE phase used to calculate the loading parameter L for 90° samples.	136
8.1	Creep cycling and the effect on g_1^{lc} in 90° samples.	147
8.2	Creep cycling and the effect on g_1^{lc} in 30° off-axis samples. . .	147
8.3	Damage states used in the damage effect study on 90° samples.	157
8.4	Damage states used in the damage effect study on 45° samples.	162
8.5	Damage states used in the damage effect study on 30° samples.	167

List of Figures

2.1	Unidirectional ply with arbitrary fiber angle.	19
2.2	Generic loading history for conducting a damage effect study. .	26
3.1	GA Flow Chart.	34
4.1	Cross section of a crack in nonlinear viscoelastic material showing contour C_1 (- - -) used in the line integral.	41
4.2	Cross section of a crack in nonlinear viscoelastic material at the fiber/matrix interface.	47
4.3	Cross-sectional diagram of a fiber composite.	49
4.4	Idealized mechanical analog of the material driving the crack growth.	51
4.5	Generalized Voigt unit.	52
5.1	Creep testing frame with plexiglass tank.	59
5.2	Hardware and software used for acoustic emission and stress-strain data acquisition.	64
5.3	Unidirectional coupon with placement of strain gages, acoustic emission sensors and dampers shown.	64

5.4	Face to face calibration of a Digital Wave Corp. B1025 broad-band sensor.	65
5.5	Face to face calibration of a Digital Wave Corp. B225 broad-band sensor.	65
5.6	Stress distribution in a 30° off-axis sample.	66
5.7	Wave Direction.	66
5.8	Relative arrival times in a 45° off-axis sample.	67
5.9	Lead break positions on an off-axis sample.	67
5.10	Relative arrival times for events occurring at the bottom edge, center, and top edge of a 30° off-axis sample.	68
6.1	Glowing debonds in a sample prior to loading.	70
6.2	Crack in the bottom of a void which has grown to neighboring debonds while under load.	71
6.3	Coalesced debonds while under load.	71
6.4	Cumulative events detected in a 90° unidirectional sample during loading/unloading and reloading cycles.	73
6.5	Cumulative events detected in a 30° off-axis sample during loading/unloading and reloading cycles.	74
6.6	Wavespeed as a function of angle relative to the fiber direction for AS4C/E719LT.	76
6.7	Background noise detected by the B1025 and B225 sensors in the laboratory working environment.	79
6.8	Histogram of cracking in the free length of a 90° sample. . . .	79
7.1	Typical large event detected from a 90° sample where cracking occurred close to sensor 1. B1025 sensors were used (1V=47db).	

7.2	Typical large event detected from a 90° sample where cracking occurred close to the center of the free length. B1025 sensors were used (1V=47db).	83
7.3	Typical small event detected from a 90° sample where cracking occurred close to the center of the free length between sensors. B1025 sensors were used (1V=47db).	84
7.4	Windowed waveform (TCOT=15μs) of the event shown in Figure 7.1	84
7.5	Windowed waveform (TCOT=15μs) of the event shown in Figure 7.2	85
7.6	Windowed waveform (TCOT=15μs) of the event shown in Figure 7.3	85
7.7	Frequency distribution of the event shown in Figure 7.4	86
7.8	Frequency distribution of the event shown in Figure 7.5	86
7.9	Frequency distribution of the event shown in Figure 7.6	88
7.10	Typical large event detected from a 90° sample where cracking occurred close to the center of the free length. B225 sensors were used (1V=50db).	88
7.11	Windowed waveform (TCOT=15μs) of the event shown in Figure 7.10	89
7.12	Frequency distribution of the event shown in Figure 7.11	89
7.13	Typical large event detected from a 90° sample where cracking occurred close to sensor 2. B225 sensors were used (1V=50db).	90
7.14	Windowed waveform (TCOT=15μs) of the event shown in Figure 7.13	90
7.15	Frequency distribution of the event shown in Figure 7.14	91

7.16	Typical small event detected from a 90° sample. B225 sensors were used (1V=50db).	91
7.17	Windowed waveform (TCOT=15μs) of the event shown in Figure 7.16	92
7.18	Frequency distribution of the event shown in Figure 7.17	92
7.19	Typical large event detected from a 30° sample. B225 sensors were used (1V=50db).	93
7.20	Windowed waveform (TCOT=25μs) of the event shown in Figure 7.19.	93
7.21	Frequency distribution of the event shown in Figure 7.20	94
7.22	Typical moderate event detected from a 30° sample. B225 sensors were used (1V=50db).	94
7.23	Windowed waveform (TCOT=25μs) of the event shown in Figure 7.22.	95
7.24	Frequency distribution of the event shown in Figure 7.23	95
7.25	Typical large event detected from a 45° sample. B225 sensors were used (1V=50db).	96
7.26	Windowed waveform (TCOT=25μs) of the event shown in Figure 7.25.	97
7.27	Frequency distribution of the event shown in Figure 7.26	97
7.28	Typical moderate event detected from a 45° sample. B225 sensors were used (1V=50db).	98
7.29	Windowed waveform (TCOT=25μs) of the event shown in Figure 7.28.	98
7.30	Frequency distribution of the event shown in Figure 7.29	99

7.31	Four sensor setup. Two B225 sensors (1 & 4) are used for location. The B1025 sensors (2 & 3) are used to evaluate waveforms. Units in cm.	100
7.32	(a) Waveforms detected directly beneath sensors 2 and 3 in a 90° sample. (b) Extensional and (c) flexural components of the waveform in (a). (c) FFT of the extensional and flexural components. (1V=47 dB)	101
7.33	(a) Waveforms detected directly beneath sensors 2 and 3 in a 90° sample. (b) Extensional and (c) flexural components of the waveform in (a). (c) FFT of the extensional and flexural components. (1V=47 dB)	102
7.34	(a) Waveforms detected directly beneath sensors 2 and 3 in a 30° off-axis sample. (b) Extensional and (c) flexural components of the waveform in (a). (c) FFT of the extensional and flexural components. (1V=47 dB)	103
7.35	(a) Waveforms detected directly beneath sensors 2 and 3 in a 30° off-axis sample. (b) Extensional and (c) flexural components of the waveform in (a). (c) FFT of the extensional and flexural components. (1V=47 dB)	104
7.36	Cumulative AE events detected in 90° samples versus axial stress for three loading rates.	105
7.37	Cumulative AE events versus stress detected in 45° off-axis samples versus axial stress for two loading rates.	106
7.38	Cumulative AE events versus detected in 30° off-axis samples versus axial stress for two loading rates.	106
7.39	Cumulative AE events detected in 30° off-axis samples with B1025 sensors.	107

7.40	Average event energy detected in 90° unidirectional samples for three loading histories.	109
7.41	Average event energy detected in 45° off-axis samples at 0.92 MPa/min.	111
7.42	Average event energy detected in 30° off-axis samples for two loading rates.	112
7.43	Average event energy detected in two 45° off-axis samples from 30 MPa to failure for two loading rates.	112
7.44	Average event energy detected in 30° off-axis samples from 90 MPa to failure	113
7.45	Location histogram of microcracking in the free length of a 30° off-axis sample.	114
7.46	Location histogram of microcracking in the free length of a 45° off-axis sample.	114
7.47	Location histogram of microcracking in the free length of a 30° off-axis sample.	115
7.48	Location histogram of microcracking in the free length of a 45° off-axis sample.	116
7.49	Loading history and strain response from ramp/hold testing. .	118
7.50	Cumulative AE events versus time detected during ramp/hold testing of a 90° sample.	119
7.51	Cumulative AE events versus stress detected during ramp/hold testing of a 90° sample.	119
7.52	Average event energy during the ramp and hold periods of testing.	121
7.53	Extensional and flexural waveforms at 150kHz detected by sensors 2&3 and produced by sensor 4 in a 90° sample.	126

7.54	Extensional and flexural waveforms at 300kHz detected by sensors 2&3 and produced by sensor 4 in a 90° sample.	127
7.55	Extensional and flexural waveforms at 150kHz detected by sensors 2&3 and produced by sensor 4 in a 30° sample.	128
7.56	Extensional and flexural waveforms at 300kHz detected by sensors 2&3 and produced by sensor 4 in a 30° sample.	129
7.57	Maximum amplitude of the pulsed waves in a 90° sample at 150 and 300kHz versus axial stress.	130
7.58	Maximum amplitude of the pulsed waves in a 30° sample at 150 and 300kHz versus axial stress.	131
7.59	Loading histories used in AE testing of 90° samples.	133
7.60	PMF of AE events detected from 90° samples loaded with different histories when using axial stress as the distribution parameter.	134
7.61	CDF of AE events detected from 90° samples loaded with different histories when using axial stress as the distribution parameter.	134
7.62	CDF of AE events detected from 90° samples using axial stress as the distribution parameter	135
7.63	CDF of AE events detected from off-axis samples loaded with different rates when axial stress is used as the distribution parameter.	135
7.64	CDF of AE events detected from all 90° samples with L as the distribution parameter.	136
7.65	CDF of AE events detected from off-axis and 90° samples loaded with different rates with L as the distribution parameter.	139

7.66	CDF of AE events detected from off-axis and 90° samples loaded with different rates with L as the distribution parameter.	139
8.1	Linear viscoelastic creep of a 90° unidirectional sample.	142
8.2	Linear viscoelastic recovery of a 90° unidirectional sample. . .	144
8.3	Linear viscoelastic recovery of the shear compliance in a 30° off-axis sample.	144
8.4	Linear viscoelastic recovery of the transverse compliance in a 30° off-axis sample.	145
8.5	Linear viscoelastic recovery of the shear compliance in a 45° off-axis sample.	145
8.6	Linear viscoelastic recovery of the transverse compliance in a 45° off-axis sample.	146
8.7	Cyclic transverse creep compliance at 41 MPa in a 90° sample.	149
8.8	Cyclic transverse recovery compliance at 41 MPa in a 90° sample.	149
8.9	Cyclic transverse creep compliance at 55 MPa in a 90° sample.	151
8.10	Cyclic transverse recovery compliance at 55 MPa in a 90° sample.	151
8.11	Cyclic transverse recovery compliance at 55 MPa in a 90° sample.	152
8.12	Cyclic (a) shear and (b) transverse creep compliance at 69 MPa in a 30° off-axis sample.	154
8.13	Cyclic (a) shear and (b) transverse recovery compliance at 69 MPa in a 30° off-axis sample.	155
8.14	Cyclic shear recovery compliance at 69 MPa in a 30° off-axis sample.	156
8.15	Stress strain response of 90° samples with the stresses used in the damage effect study.	158

8.16	Transverse creep compliance of a 90° sample at 31 MPa for three damage states.	158
8.17	Transverse creep compliance of a 90° sample at 41 MPa for three damage states.	159
8.18	Transverse recovery compliance of a 90° sample at 31 MPa for three damage states.	159
8.19	Transverse recovery compliance of a 90° sample at 41 MPa for three damage states.	160
8.20	Transverse recovery compliance of a 90° sample at 31 and 41 MPa. Higher damage states have been vertically shifted to the lowest state tested.	160
8.21	Transverse compliance damage effect ratios from a 90° sample.	161
8.22	Stress strain response of 45° samples with the stresses used in the damage effect study.	162
8.23	Shear creep compliance of a 45° off-axis sample at 38 MPa and 62 MPa for three damage states.	163
8.24	Shear recovery compliance at 38 and 62 MPa of a 45° off-axis sample. Higher damage states have been vertically shifted to the lowest state tested.	164
8.25	Shear compliance damage effect ratios from a 45° sample.	164
8.26	Transverse creep compliance of a 45° off-axis sample at 38 MPa and 62 MPa for three damage states.	165
8.27	Transverse recovery compliance at 38 and 62 MPa of at 45° off-axis sample. Higher damage states have been vertically shifted to the lowest state tested.	166
8.28	Transverse compliance damage effect ratios from a 45° sample.	166

8.29	Stress strain response of 30° samples with the stresses used in the damage effect study.	167
8.30	Shear creep compliance of a 30° off-axis sample at 38 MPa and 59 MPa for three damage states.	168
8.31	Shear recovery compliance at 38 and 59 MPa of at 30° off-axis sample.	169
8.32	Shear compliance damage effect ratios from a 30° sample. . .	169
8.33	Transverse creep compliance of a 30° off-axis sample at 38 MPa and 59 MPa for three damage states.	170
8.34	Transverse recovery compliance at 38 and 59 MPa of a 30° off-axis sample. Higher damage states have been vertically shifted to the lowest state tested.	171
8.35	Transverse compliance damage effect ratios from a 30° sample.	171
8.36	Transverse creep compliance of a 90° sample at various stress levels.	174
8.37	Transverse recovery compliance of a 90° sample from creep at various stress levels.	174
8.38	Shear creep compliance of a 30° sample from creep at various stress levels.	175
8.39	Transverse creep compliance of a 30° sample from creep at various stress levels.	175
8.40	Shear recovery compliance of a 30° off-axis sample from creep at various stress levels.	176
8.41	Transverse compliance of a 30° off-axis sample from creep at various stress levels.	177

Chapter 1

Introduction

One important factor in the durability of polymeric composites is their loss in stiffness over time. At the fiber and ply-level, this softening is primarily due to viscoelasticity and viscoplasticity of the polymer matrix and time-dependent damage growth. Damage here refers to all microstructural changes such as matrix cracking, fiber/matrix debonding and shear yielding. A good understanding of this softening behavior and its causes is needed to make reliable predictions of more serious larger-scale damage, such as transverse cracking, which may lead to fiber breakage, delamination and finally catastrophic failure. Indeed, these other damage mechanisms, prior to catastrophic failure, may themselves be ‘design-driving’ failure modes depending on the application.

1.1 Background

Modeling of the Inelastic Behavior of Composites

Experimentally observed damage growth in laminated composites comprised of unidirectional plies with one or more fiber orientations indicates the following general sequence of events occur during loading (Nairn and Hu, 1994). Optical microscopy of the edge of a carbon/epoxy laminate in tension, in a ply whose fibers are not parallel to the loading direction, show the initial form of damage, microcracking, initiates at fiber debonds. Fiber debonds eventually coalesce as load is increased to form a macrocrack which causes ply-failure. In glass/epoxy where their transparency makes investigation of the material interior possible, stress whitening is seen in some glass/epoxy laminates prior to any ply failure. As observed from optical microscopy, this effect is from fiber/matrix debond which also eventually coalesces into ply-failure or a so-called transverse crack (a crack running the entire width and thickness of a group of plies in the same direction). Significant transverse cracking typically initiates delamination at the crack tips [e.g. (Bader et al., 1979), (Highsmith and Reifsnider, 1982)]. Both delamination and transverse cracking can cause premature fiber-failure, that is below that estimated by a simple strength calculation or netting analysis. It has been found in some cases that transverse cracking, for example, is a time or rate-dependent phenomenon [e.g. (Moore and Dillard, 1990)] indicating the time-dependence of the material needs to be understood to make damage growth predictions. An excellent review on damage mechanics of composite materials is given in Talreja (1994). Regardless of which failure mode drives a design, to make accurate predictions of these more serious forms of damage, good knowledge of ply-level stresses is needed. Herein, this aspect of the durability issue is addressed; namely, how

ply-level properties of a rubber-toughened carbon/epoxy vary with time due to nonlinear viscoelasticity and small microstructural damage.

Past progress in assessing the time-dependent properties of viscoelastic/viscoplastic materials with growing damage fall essentially into three categories. The first approach is to lump damage and other nonlinear time-dependent effects into single functions of stress and time. A second approach is to mechanically condition the material until the damage growth and increase in viscoplastic strain are negligible over the time frame of testing and characterize this conditioned behavior. A final method is to make certain simplifying assumptions about the material behavior at the outset and derive the effect of damage solely from stress-strain information. All of these methods have been successful in their particular experimental studies. However, all are limited to either certain materials, which display simplified behavior, or to specific loading conditions. More robust methods are needed to assess material behavior without these simplifications.

Many publications on time-dependent, nonlinear behavior in composites use incremental or deformation plasticity theory to develop ply-level constitutive equations [e.g. (Hashin and Rosen, 1974), (Sun and Chung, 1993)(Budiansky and Fleck, 1993)]. These equations reflect the combined effect of transverse and shearing stresses on the softening of a given ply. In some instances, a Ramberg-Osgood nonlinear power law representation is used. Zhu and Sun (2000) expanded these models to include unloading with the use of an overstress function in the plasticity model. Good predictions of loading and unloading are made for various fiber angle off-axis specimens for multiple strain rates. For monotone increasing loading, a quasi-elastic type constitutive equation, with stress nonlinearity in the form of a Ramberg-Osgood power law, and rate effects reflected by a power-law in time, have been

found sufficient to characterize two rubber-toughened carbon/epoxy systems (Mignery and Schapery, 1991) (Bocchieri and Schapery, 2000). These methods are limited as they assume all softening effects are one in the same and do not address the specific nature of each mechanism. Some mechanisms are reversible, such as nonlinear elasticity and nonlinear viscoelasticity, while others are permanent, viscoplastic strain and microstructural damage. *Reliable long-term predictions necessitate the isolation of each softening effect.*

Much of damage mechanics uses continuum theories which implement damage variables to relate the size, shape and orientation and density of damage, or cracks, with the global response [e.g. (Kamimura, 1985), (Talreja, 1985a)]. Behavior can be complicated due to the directional nature of this effect where an initially isotropic material can become anisotropic due to the damage. One simplifying feature of these theories, however, is that all permanent softening is due to the growth of this damage. The damage state is directly tied to the amount of observed softening. When the softening effects of damage are coupled with viscoelasticity and/or viscoplasticity, softening occurs due to the inherent viscoelastic behavior of the undamaged material, the growth of damage, and time-dependent opening or sliding of the crack faces that have formed. Just determining which softening mechanism is responsible for the observed behavior becomes more complicated. Indeed, the damage itself may now grow over time without increasing the load.

One approach has been to precondition the material, that is repeatedly load the material to a given stress level until the growth of damage becomes negligible over the time frame of loading. It has been observed that the most significant amounts of damage are accumulated in the first few loading cycles up to a given load. Lou and Schapery (1971), in studying a glass/epoxy composite, found that mechanical preconditioning was necessary before a mean-

ingful viscoelastic characterization could be accomplished. After 10 cycles at a given load, a good characterization of creep/recovery response was made for different fiber angle coupons using a nonlinear viscoelastic model without growing damage (Schapery, 1969). Beckwith (1974), (Beckwith, 1980) also saw this large cycle to cycle effect in another glass/epoxy.

Others have added a viscoplastic strain component to the model proposed by Schapery (1969) to improve predictions of cycle to cycle behavior in composites. Tuttle et al. (1995) added a viscoplastic strain suggested by Zapas and Crissman (1984) to characterize the first cycle behavior of a graphite/bismaleimide composite. Their predictions of a different laminate than those used in the characterization, a $(90, \pm 45, 90)$ laminate, for a sequence of 10 creep/recovery cycles (at the same stress) was very good. Post inspection of the sample showed no damage to the laminate, however. Guedes and Marques (1998) performed a similar characterization on T300/5208 again based on first cycle behavior. However, predictions of long-term cyclic creep/recovery are not very good. Qin et al. (1998), again applying the same model as Guedes and Marques, to another carbon/epoxy composite, but finding the material parameters in Schapery's model with a neuro-fuzzy network from first cycle behavior, made cyclic predictions. The addition of viscoplastic strain aids in keeping in step with the accumulated strain, but quickly failed to capture the shape of each cycle of creep and recovery. Tamuzs and Aniskevich (1998) performed creep tests on 45° , 70° and 90° off-axis samples of glass-fiber reinforced polyester with 25% of the layers with chopped strand mat. By analysis of the creep portion of cyclic loadings, they found that only the instantaneous portion of the constitutive equation varied from cycle to cycle and with stress where the time-dependent, viscoelastic portion stayed the same.

Schapery (1987)(Schapery, 1990b) developed a theory for elastic media with growing damage based on irreversible thermodynamics where internal state variables were used to describe the effect of microstructural changes. Schapery (1989) and Schapery and Sicking (1995) applied the model to a carbon/epoxy where nonlinearity was due to nonlinear elasticity and the effect of damage. In the latter study, two internal state variables were used for damage, one accounting for changes in the microstructure (scale smaller than the layer thickness) and the second to represent the effect of thermo-mechanically induced transverse cracking. These effects were assumed to enter the constitutive equations as separate factors. Inelastic behavior of a graphite/epoxy was successfully characterized by this method.

Schapery (1990a)(Schapery, 1990b) extended this model to include linear viscoelastic effects with rate-dependent damage growth. Park and Schapery (1997) and Ha and Schapery (1997) applied this to a particle filled elastomer. Using a rate-type equation to describe the growth of damage in the microstructure, they successfully characterized the stress and dilatation response with different levels of strain, strain rate, confining pressure and temperature. Although no unloading was performed, the model also successfully predicted the stress and dilatation of dual strain rate experiments. The same theory was successfully applied to the uniaxial response of asphalt concrete for various strain rates (Park et al., 1996).

Abdel-Tawab and Weitsman (1998) proposed a thermodynamically based model for viscoelastic materials with continuum damage behavior. A uniaxial model was derived from this theory for a swirl-mat glass fiber composite using linear viscoelasticity and a damage variable that enters through an effective stress to affect the elastic and viscoelastic strain components in the same way. This model was contained in the model proposed by Park

and Schapery (1997). Damage was assumed to grow as a power-law in time and stress. This model is then successfully fit to creep data at various stress levels. However, no predictions of other loading histories are given to check the various assumptions made in the model.

Pyrz (1990) attempted to characterize the uniaxial response of a woven glass fabric polyimide composite with a linear viscoelastic and damage growth model. All nonlinearity was assumed to enter through a single damage parameter. He defined this damage parameter as the length density of cracks. This length density was measured at certain strain levels throughout the test by taking microphotographs of a representative volume of material. Simultaneously, acoustic emissions were monitored with two sensors. It was found that the damage parameter and the cumulative hits versus strain had the same general shape. However, predictions of saw-tooth stress-strain behavior were poor and only captured the behavior qualitatively.

Zhang (1995) found no cyclic effects in characterizing a polyester resin. In fact, only two of the nonlinear parameters in Schapery's uniaxial constitutive model were needed. Lai and Bakker (1995) needed only to add a viscoplastic strain to the Schapery model to describe the cyclic behavior of High Density Polyethylene.

Apparently, as one would expect, varying degrees of complexity need to be incorporated into constitutive equations depending on the material, stress level and stress history. In general, the coupling of damage growth with other nonlinear factors needs to be addressed.

As will be discussed in Chapter 2, when a material contains all the complexity mentioned; i.e. nonlinear viscoelasticity, viscoplasticity and damage; there is no apparent way to isolate the effect of damage and its growth from the other softening effects based solely on stress-strain information. If

the state of damage could be monitored directly, it would not need to be inferred through whatever assumptions have been made to derive the constitutive equations. Tracking the density of transverse cracking (large scale cracking typically of an entire ply), for example, has been shown to be a good damage parameter for predicting softening in cross-ply laminates under tensile loading. An excellent review of this subject is given by Nairn and Hu (1994). Density of such macro-cracking has been measured by various means, including x-radiography, polar backscatter scans, edge-replication and acoustic emission monitoring. When deriving ply-level behavior, however, the type of damage is not this type of large more-easily seen cracking, but widely distributed microcracking or fiber/matrix debonding. Any form of visual inspection to count microcracks is simply an intractable situation. A real-time, efficient method for tracking this type of damage is needed. Monitoring their acoustic emissions may be the only practical method. Use of this technique is one of the major subjects of this research.

Acoustic Emission Testing of Fiber Composites

A large number of acoustic emission studies involve attempts to differentiate different forms of damage occurring concurrently in a laminate [e.g. (Gustafson and Selden, 1985), (Roy and Gaucher, 1988), (Wevers et al., 1991), (Zimcik et al., 1988)]. For example, in any but a unidirectional material, fiber breaking, microcracking, fiber/matrix debond, transverse cracking (or ply-failure), and delamination all can happen in a test. Each mechanism has its own effect on the degradation of the material and each, in principle, could have a particular acoustic (ultrasonic) signature. In cross-ply laminates, partial cracking, as opposed to entire ply failure, can further complicate anal-

ysis of AE data. As the focus of this study is on ply-level behavior, we are primarily interested in AE testing performed on unidirectional laminates, that is with all fibers at the same angle relative to loading.

A relatively small amount of acoustic emission testing has been published on unidirectional polymeric composites. Even with testing in the fiber direction multiple damage mechanisms can occur. These studies cover several methods to discern matrix-cracking, debonding and fiber breakage and fiber pull-out from one another with little success.

De Groot and Janssen (1995) ran tensile experiments on 0° , 90° and 10° off-axis carbon/epoxy samples and on the pure matrix resin. They report evidence of matrix cracking, debonding, fiber-pullout and breaking. Some conclusions were drawn on the frequency content of each mechanism, but these results are not clear because only one broadband sensor was used. Events from the grips were therefore not filtered from the data and the difference in attenuation with frequency was not considered as the distance of the acoustic source to the sensor was not known.

Chen and Baer (1992) studied unidirectional glass fiber reinforced polyphenylene. Although two sensors were used, testing was only done in 4-point bending with the bending axis in the fiber direction. Komai et al. (1991) investigated a unidirectional carbon/epoxy again with loading in the 0° direction. They used techniques such as amplitude distribution and C/D ratio (C/D ratio = AE ring-down-count/AE event duration at a single frequency) to differentiate failure mechanisms. Valentin (1985) attempted to differentiate fiber breakage, matrix cracking and decohesion in carbon/epoxy and carbon/psp materials by amplitude. He fit a power-law distribution function to amplitude histograms at different stress levels. Difficulty in differentiating the matrix cracking and decohesion is reported. Wevers et al.

(1985) observed matrix cracking and debond along with fiber fracture in fatigue loading of a DFR epoxy composite. To track each failure mode, he used signal energy. However, only two resonant sensors were used so only energy at a given frequency was considered.

Laroche and Bunsell (1998) performed a fiber fracture detection study using a 200 kHz resonant sensor. They report only detecting fiber fracture as the same exponential increase in AE counts is seen with load on cured 0° material and the prepreg prior to cure. The assumption is that no matrix cracking occurs in the prepreg. They correlated the AE hits with a Weibull distribution of fiber bundle strength.

Rotem and Baruch (1974) studied time-dependent fiber fracture of E-glass fibers in a viscoelastic epoxy matrix. They used a single narrow band transducer (100 to 300kHz) to detect acoustic signals, so the location of events are unknown. Despite not knowing the location of the detected events, the use of band-pass filtering to eliminate events coming from the gripping regions, yielded some interesting results. They show that the total AE count is proportional to the theoretical relative number of fiber fractures based on a shear lag analysis in a viscoelastic material.

It appears that there is no clearly defined method for discriminating the different damage mechanisms even for unidirectional material. Fortunately, however, we are only concerned in this dissertation with damage occurring in the matrix and not fiber-breaking. We may therefore study cracking by loading at off-axis angles so that the fibers do not see significant load, eliminating fiber breaking and pullout as pertinent damage modes, leaving fiber/matrix debonding and microcracking near the fibers as the dominant damage modes. One published study was found that directly addresses this issue.

Okoroafor and Hill (1996) performed an acoustic emission study on a special specimen with bundles of fibers centered in a dog-bone sample of different resin material where the fibers are oriented perpendicular to the axis of loading. The specific focus of the experiment was to demonstrate the utility of acoustic emission monitoring to evaluate the effect of different sizings on fiber/matrix adhesion. They presume that this test geometry results in interfacial failure as the predominant failure mechanism. For various fiber materials and matrices they created an especially poor bond by coating the fibers with silicone oil. Results from these samples are compared to uncoated fibers and fibers that had been sized. Total acoustic emission events clearly increase as fiber/matrix adhesion is degraded. Strain at the onset of AE also decreases.

1.2 Objective

Review of the literature shows that varying degrees of complexity need to be incorporated in constitutive models, depending on the composite system studied. In some studies only the addition of viscoplastic strain was needed to make good predictions of material behavior. In others, damage only appears to affect the elastic strain. For certain materials only linear viscoelasticity, where all nonlinearity came from damage, was needed.

When approaching a new material, one frequently generates stress-strain data from constant load-rate or strain-rate tests, cyclic load/unload tests and ramp to failure experiments. A proposed constitutive model is applied which captures the effects seen for some limited amount of data. Complexity is built in as necessary to explain results from all of the experiments. Finally, some ‘validation’ experiments are run where the loading history, or

perhaps in the case of composites, a different laminate is tested to justify the constitutive model used.

In terms of durability, material behavior over long times or many fatigue cycles is needed. Certain material behavior, such as viscoelasticity, may seem negligible over typical time-frames used for tests in the laboratory if standard rate-type loadings are used. However, in ten or fifteen years neglected strains may become significant. The time-dependent microcracking detected in 90° material, discussed in Chapter 7, is a good example of where rate-loadings do not give any indication of time-dependent effects.

Here we take the opposite approach and leave as much material complexity in place as possible so that testing methodologies will have the widest applicability. Experiments are used that emphasize the time-effect, although the change in creep strains measured over the short time-frame of testing is small. These methods are evaluated using a composite which displays all of the mentioned complexities.

This work uses the theory previously established by Schapery (1999) to develop experimental and data analysis methods for isolating the softening effects of nonlinear elasticity, nonlinear viscoelasticity, viscoplasticity and damage. Damage enters through internal state variables. If all these mechanisms are significant, the author is not aware of any existing method to extract both the damage evolution and to differentiate its effect on the material parameters from that of stress based solely on stress-strain information. A direct measure of microcracking is needed to help separate these effects. A major focus, therefore, was to develop relatively short-term experimental and data analysis methods for determining which material complexities have a significant effect on material behavior. The major difficulty is separating the intrinsic effect of stress from that of damage on the nonlinear viscoelas-

tic (NLVE) behavior. This problem was addressed with three concurrent approaches:

1. Develop experiments and *numerical data analysis methods* to fit strain data which are affected by hereditary damage effects.
2. Conduct a *Damage Effect Study* to identify which nonlinear material parameters are affected by damage.
3. Develop a *real-time nondestructive method to monitor damage growth*.

The focus of the first effort was to assess the *effect* of damage on each material parameter, in particular the parameter which causes hereditary damage effects. The material displays a fading memory of the loading path with which it arrived at a given damage state. Testing methodology and methods of data analysis were devised without removing any material complexity. The Damage Effect Study was designed to determine which material parameters are affected by damage. This information can then be used to simplify the analysis. Acoustic emission monitoring was used in the third effort to track how damage evolves with different loading histories and load combinations. With this knowledge, the state of damage in the material will be known for any loading and can be used to tie together the first two efforts.

1.3 Summary

In Chapter 2 a constitutive theory derived by Schapery (1999) and based on nonequilibrium thermodynamics, rate-process theory and viscoelastic fracture mechanics is introduced. This theory accounts for effects of nonlinear viscoelasticity, viscoplasticity, growing damage and aging. The constitutive

equations are then tailored in this dissertation for a continuous fiber composite based on past observed behavior in these materials so that a single hereditary integral describes viscoelastic effects. They are subsequently evaluated for a creep/recovery loading when damage and viscoplastic strain may grow while under load. Based on these equations, an experimental procedure called the Damage Effect Study is outlined. A method of analyzing data for various fixed states of damage at identical stress levels is suggested to isolate the effect of damage from that of stress on the elastic and viscoelastic strains. This method implements vertical shifting of recovery data collected at different damage states similar to the way data is shifted for the effect of stress. An underlying assumption is that damage does not accelerate the viscoelastic strains in the way stress or temperature can for some materials.

With all the material complexity in the material model, creep with growing damage contains many parameters evolving concurrently. It is doubtful any numerical scheme would be successful in fitting the assumed functional forms for all these parameters. Recovery, however, is more manageable. Assuming a functional form for only one damage-dependent parameter, the recovery strain is evaluated in Chapter 3. A hereditary effect of damage results. Several formulations of the recovery strain for numerical evaluation are given. A numerical method using a Genetic Algorithm in conjunction with the calculus based Levenberg-Marguart scheme is developed to fit the recovery equation. This method is then used to fit simulated data containing hereditary effects of damage growth.

The distributed microcracking in a unidirectional ply is addressed in Chapter 4. First, the theoretical basis for crack growth in nonlinear viscoelastic media as proposed by Schapery (1984)(Schapery, 1986) is introduced. Based on results of the acoustic emission testing it was found necessary to

consider crack growth with two phases of viscoelastic material, a nonlinear phase in the vicinity of the crack tip and a surrounding linear one. Due to the complexity of this behavior, an idealized model is suggested and a method of data analysis outlined. The derived criterion for crack growth is extended to distributed cracking by assuming a distribution of initial flaws which grow dynamically upon failure and stop upon reaching some crack inhibitor. The distribution of flaws is captured with a combined loading parameter of all the factors affecting fracture and formulated to be proportional to a functional of the stresses acting on the NLVE phase of the material. Use of the *Cumulative Distribution Function* (CDF) of this combined parameter is introduced as a damage variable.

In Chapter 6 the fracture modes of unidirectional material when tensile loaded off-axis to the fibers are reviewed. Although a one-to-one correspondence between an observed fracture event and its detected acoustic wave is not possible at this time due to the very small scale of cracking, several steps were taken to assure that only fracture mechanisms serving to soften the material are considered. Methods of discriminating these events from the large numbers detected from the gripping regions of a coupon are discussed. In particular, a novel method of testing off-axis samples is introduced. Testing was performed using a relatively new method of acoustic emission testing, called Modal AE Testing, where waveforms are acquired digitally and waveform analysis can be performed based on principles of elastic wave propagation. To the author's knowledge, this new method of AE testing has not been used previously to study microcracking in polymeric composites.

Chapter 7 covers the acoustic emissions detected in 90° and off-axis unidirectional samples using various loading histories so that the time or rate dependence of cracking can be studied. First, waveforms measured from two

broadband sensors on each sample type are reviewed. A new method, suggested by Dr. Michael Gorman of Digital Wave Corporation, for separating the detected plate waves into their extensional and flexural modes is also discussed. This method, along with two locating sensors, is used to examine fracture events directly below the sensors used for separating plate modes. In this way, differences in attenuation with direction and distance are eliminated and comparison of events from different fiber angles can be made. Next, a histogram of event energy versus load level is used to study the effect of stress level on arrested crack length. This study also indicates whether the ‘detectability’ of a given flaw when it fails dynamically changes during the test, thereby affected the perceived distribution. Changes in material acoustical properties as the material is loaded are also considered. Finally, data collected from 90° , 45° and 30° off-axis samples loaded with various histories are used to find a single CDF of the microcracking.

Viscoelastic behavior of the carbon/epoxy AS4C/E719LT with and without growing damage is reviewed in Chapter 8. Linear viscoelastic behavior, cyclic creep and recovery with growing damage and conditioned material behavior at multiple stress levels is presented. Results from the Damage Effect Study are also given for 90° , 30° and 45° off-axis samples for two stress levels and multiple conditioned damage states.

Chapter 2

Nonlinear Viscoelastic/Viscoplastic Constitutive Theory

2.1 Constitutive Theory

A constitutive theory presented by Schapery (1999), and based on nonequilibrium thermodynamics, rate-process theory and viscoelastic fracture mechanics, is used to model material behavior. This theory accounts for effects of nonlinear viscoelasticity, viscoplasticity, growing damage and aging. Total strain is

$$\epsilon_i = -\frac{\partial G_e}{\partial \sigma_i} + \Delta\epsilon_i + \epsilon_i^{vp} \quad (2.1)$$

where the $-\frac{\partial G_e}{\partial \sigma_i}$ are elastic strains, $\Delta\epsilon_i$ are viscoelastic strains and ϵ_i^{vp} are viscoplastic strains. Viscoelastic strains, excluding thermal expansion terms, are given by

$$\Delta\epsilon_i = \frac{\partial \hat{\sigma}_j}{\partial \sigma_i} (I_j^{(1)} + I_j^{(3)}) \quad (2.2)$$

where

$$I_j^{(1)} = \int_0^\psi \Delta S_{jk}(\psi - \psi') \frac{d}{d\psi'} \left(\frac{\hat{\sigma}_k}{a_2} \right) d\psi' \quad (2.3)$$

$$I_j^{(3)} = \int_0^\psi \Delta \tilde{S}_{jk}(\psi - \psi') \frac{d}{d\psi'} \left(\frac{\tilde{\sigma}_k}{a_2} \right) d\psi'. \quad (2.4)$$

where terms reflecting stress-free straining (e.g. due to temperature) have been removed for the present study. The quantity ψ is reduced time,

$$\psi = \int_0^t \frac{a_2}{a_1} dt' \quad (2.5)$$

where a_1 and a_2 are scalar valued functions of stress, σ , temperature and damage, \mathbf{S} , among other variables. The quantity \mathbf{S} is a set of internal state variables representing all high-energy microstructural changes such as microcracking and shear banding. The ΔS_{ij} and $\Delta \tilde{S}_{ij}$ are linear viscoelastic or master creep compliances,

$$S_{jk}(\psi) = \sum_r S_{jk}^r (1 - e^{-\psi/\tau_r}), \quad (2.6)$$

$$\tilde{S}_{jk}(\psi) = \sum_{r'} \tilde{S}_{jk}^{r'} (1 - e^{-\psi/\tau_{r'}}) \quad (2.7)$$

where τ_r are relaxation times. The set of quantities $\hat{\sigma}_{\mathbf{k}} = \hat{\sigma}_{\mathbf{k}}(\sigma, \mathbf{S})$, and

$$\tilde{\sigma}_k \equiv P_{ki} \hat{\sigma}_i \quad (2.8)$$

where $P_{ij} = P_{ij}(\sigma, \mathbf{S})$ is a set of damage effect coefficients.

Tailoring this theory for ply-level behavior of a continuous fiber composite, we will use single index notation common to lamination theory, shown in Figure 2.1, where 1 is the fiber direction,

$$\left\{ \begin{array}{c} \epsilon_1 \\ \epsilon_2 \\ \epsilon_6 \end{array} \right\} = \left\{ \begin{array}{c} \epsilon_{11} \\ \epsilon_{22} \\ \gamma_{12} \end{array} \right\}. \quad (2.9)$$

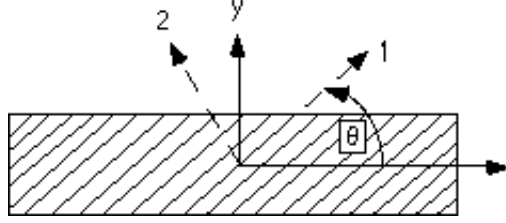


Figure 2.1: Unidirectional ply with arbitrary fiber angle.

Given that the fibers carry most of the load in the fiber direction, negligible time dependence is seen in the 1-direction $\Rightarrow I_1^{(j)} = 0$. The viscoelastic strains of interest are the transverse and shear strains,

$$\Delta\epsilon_2 = \frac{\partial\hat{\sigma}_2}{\partial\sigma_2}(I_2^{(1)} + I_2^{(3)}) + \frac{\partial\hat{\sigma}_6}{\partial\sigma_2}(I_6^{(1)} + I_6^{(3)}) \quad (2.10)$$

$$\Delta\epsilon_6 = \frac{\partial\hat{\sigma}_2}{\partial\sigma_6}(I_2^{(1)} + I_2^{(3)}) + \frac{\partial\hat{\sigma}_6}{\partial\sigma_6}(I_6^{(1)} + I_6^{(3)}). \quad (2.11)$$

This representation would require four convolution integrals be used to model the material.

As discussed in Chapter 1, many researchers have found that a single integral representation is adequate to characterize a variety of NLVE materials without growing damage. That is, upon conditioning the material with multiple loadings to a given stress, subsequent loadings are repeatable and can be characterized with the single integral representation originally proposed by Schapery (1969), sometimes with the addition of plastic strain. It was based on this evidence that the following simplifications were made and the subsequent testing schemes devised.

First, assume that the damage effect coefficients, P_{ij} , are negligible. Consequently, $\tilde{\sigma} = \mathbf{0}$ and $I_2^{(3)} = I_6^{(3)} = 0$. Also, assume $\partial\hat{\sigma}_2/\partial\sigma_6 = \partial\hat{\sigma}_6/\partial\sigma_2 =$

0. Transverse and shear strains may then be written as

$$\Delta\epsilon_2 = -\frac{\partial G_e}{\partial\sigma_2} + \frac{\partial\hat{\sigma}_2}{\partial\sigma_2} \left(\int_0^\psi \Delta S_{22}(\psi - \psi') \frac{d}{d\tau} \left(\frac{\hat{\sigma}_2}{a_2} \right) d\tau \right) + \epsilon_2^{vp} \quad (2.12)$$

$$\Delta\epsilon_6 = -\frac{\partial G_e}{\partial\sigma_6} + \frac{\partial\hat{\sigma}_6}{\partial\sigma_6} \left(\int_0^\psi \Delta S_{66}(\psi - \psi') \frac{d}{d\tau} \left(\frac{\hat{\sigma}_6}{a_2} \right) d\tau \right) + \epsilon_6^{vp} \quad (2.13)$$

This notation is now similar to the one-dimensional constitutive equation proposed by (Schapery, 1969) without growing damage, but with a viscoplastic term added

$$\epsilon = g_0 D_0 \sigma + g_1 \int_0^\psi \Delta D(\psi - \psi') \frac{d(g_2 \sigma)}{d\tau} d\tau + \epsilon^{vp}. \quad (2.14)$$

where,

$$\psi = \int_0^t \frac{dt'}{a_\sigma} \quad (2.15)$$

and

$$\psi' = \int_0^\tau \frac{dt'}{a_\sigma} \quad (2.16)$$

are reduced times. Relating the nonlinear parameters,

$$\begin{aligned} g_0 D_0 &= -\frac{dG_e}{d\sigma} \\ g_1 &= \frac{d\hat{\sigma}}{d\sigma} \\ g_2 \sigma &= \frac{\hat{\sigma}}{a_2} \\ a_\sigma &= \frac{a_2}{a_1}. \end{aligned} \quad (2.17)$$

This notation is much easier to use when working with real data where separate linear viscoelastic creep compliances and nonlinear parameters g_0 , g_1 , g_2 and a_σ are found for the transverse and shear strains. However, now all of the nonlinear parameters may also be functions of damage, S . Without growing damage, they may be evaluated through creep/recovery testing as originally proposed by Schapery (1969). With damage evolution, data analysis becomes more difficult.

Upon loading a material with sufficient stress to cause damage, and if all material complexity is present, none of the nonlinear parameters will be constant. Even under the most simple loading possible, creep, all four material parameters may evolve along with the possibility of viscoplastic strain. ‘Creep’ occurs due to the inherent viscoelasticity, $\Delta D(\psi)$, the evolution of material parameters g_0 , g_1 , g_2 , and a_σ due to damage, and viscoplastic strain. Even the elastic component of the strain may contribute to creep as g_0 may increase due to damage growth. The primary difficulty is in separating the effect of stress from that of damage while keeping track of the state of damage in the material. By making simplifying assumptions it is possible to isolate these separate effects.

Without making further simplifying assumptions about the constitutive behavior than those leading to Equations 2.14 to 2.17, the author is not aware of any existing method to extract both the damage evolution and to differentiate its effect on the material parameters from that of stress based solely on stress-strain information. This is the major focus of this work and was addressed with three concurrent approaches:

1. Develop experiments and *numerical data analysis methods* to fit strain data which are affected by hereditary damage effects.
2. Conduct a *Damage Effect Study* to isolate which nonlinear material parameters are affected by damage.
3. Develop a *real-time nondestructive method to monitor damage growth*.

In order to isolate the effect of damage on material softening from that of stress, there are two separate issues. First, how does each material parameter depend on damage? Second, how does damage evolve with loading

history? Each of the three major efforts is needed to answer one or both of these questions. Each was done concurrently due to the time involved in conducting the testing for each approach.

The objective of the first effort was to mathematically describe the *effect* of damage on each material parameter, in particular the parameter which causes hereditary damage effects. Testing methodology and methods of data analysis were devised without removing any material complexity. The Damage Effect Study was designed to determine which material parameters are affected by damage. This information can then be used to simplify the analysis. Acoustic emission monitoring was used in the third effort to track how damage evolves with different loading histories and load combinations. With this knowledge, the state of damage in the material will be known for any loading and can be used to tie together the first two efforts.

2.2 Creep/Recovery with Damage Growth

Creep/recovery testing; a step loading to a given stress for time a time, t_i , followed by a step unloading to no stress; was used to determine the effect of damage on material response. This type of loading affords certain advantages for assessing the nonlinear parameters, as is also the case without growing damage. We shall start by evaluating Equation 2.14 for creep/recovery loading when the material has never been loaded previously and when significant damage is done to the material. To emphasize the functional dependence of the nonlinear parameters on both stress and damage, notation such as $g_2(\sigma, S)$ will be used. Also, the damage state expressed by the one scalar, $S(\sigma, t)$, will vary with both stress and time.

If the material is loaded for a time, t_i , at stress, σ_0 , the creep strain is,

$$\begin{aligned} \epsilon_c = & g_0[\sigma_0, S(\sigma_0, t)]D_0\sigma_0 + \\ & g_1[\sigma_0, S(\sigma_0, t)] \int_0^t \Delta D(\psi - \psi') \frac{d}{d\tau} (g_2[\sigma_0, S(\sigma_0, t)]) d\tau + \epsilon_{vp}[\sigma_0, t, S(\sigma_0, t)]. \end{aligned} \quad (2.18)$$

To isolate the effect of each parameter, one would need to assume explicit mathematical forms for each and use some nonlinear numerical scheme to fit the resulting equation to the creep data. Abdel-Tawab and Weitsman (1998), for example, assumed all nonlinearity was in the g_2 and it behaved as a power-law in time while under constant stress to fit creep data from a swirl-mat composite. Without such an assumption, the complexity of this equation makes it doubtful that any numerical scheme would be successful. However, for recovery the situation is more tractable. There is no elastic strain and plastic strain is a constant for the given creep load and time. Recovery strain is

$$\epsilon_r = g_1[0, S(\sigma_0, t_i)] \int_0^{t_i} \Delta D(\psi - \psi') \frac{d[g_2(\sigma_0, S)\sigma_0]}{d\tau} d\tau + \epsilon_{vp}[\sigma_0, t_i, S(\sigma_0, t_i)]. \quad (2.19)$$

Both g_1 and ϵ_{vp} are constants. The integral

$$I_1 = \int_0^{t_i} \Delta D(\psi - \psi') \frac{dg_2\sigma_0}{d\tau} d\tau \quad (2.20)$$

has to be evaluated and functional forms for g_2 and a_σ need to be assumed. For simplicity, a_σ shall be assumed independent of damage. This assumption will be justified later from the material data. The linear viscoelastic creep compliance, ΔD , is known from low stress testing and is commonly described with a power-law in time or a prony-series. At constant stress, g_2 will only vary with time as the damage parameter evolves. If we assume g_2 can be described with a second power-law in time, functional forms can be found for either power-law or prony-series representations for ΔD .

In general, for a step-loading

$$g_2\sigma_0 = \sigma_0 G(\sigma_0, \tau)[H(t) - H(t - t_i)] \quad (2.21)$$

where $G(\sigma, t)$ is some function reflecting the time-dependent damage effect on g_2 for a given stress and $H(t)$ is the heaviside unit step function. Then

$$\frac{d\sigma_0 g_2}{d\tau} = \sigma_0[\delta(\tau) - \delta(\tau - t_i)]G + \sigma_0[H(\tau) - H(\tau - t_i)]\frac{dG}{d\tau}. \quad (2.22)$$

Substituting into I_1 ,

$$I_1 = \sigma_0 [\Delta D(\psi)G(0) - \Delta D(\psi - \psi'(t_i))G(t_i) + I_s] \quad (2.23)$$

where

$$\begin{aligned} \psi &= \frac{t_i}{a_\sigma} + t - t_i \\ \psi - \psi'(t_i) &= (t - t_i). \end{aligned} \quad (2.24)$$

and

$$I_2 = \int_0^{t_i} \Delta D(\psi - \psi')\frac{\partial G}{\partial \tau} d\tau. \quad (2.25)$$

The integral I_2 reflects a hereditary damage effect on the recovery strain. We will therefore call it the *damage history integral*. Combining Equations 2.19, 2.20, 2.23 and 2.25,

$$\epsilon_r = g_1(t_i)\sigma_0[g_2(0)\Delta D(\psi) - g_2(t_i)\Delta D(\psi - \psi'(t_i)) + I_2] + \epsilon_{vp}(t_i) \quad (2.26)$$

where the notation

$$\begin{aligned} g_1(t_i) &= f_1[0, S(\sigma_0, t_i)] \\ g_2(0) &= g_2(\sigma_0, S(\sigma_0, 0)) \\ g_2(t_i) &= g_2(\sigma_0, S(\sigma_0, t_i)) \\ \epsilon_{vp}(t_i) &= \epsilon_{vp}[\sigma_0, t_i, S(\sigma_0, t_i)] \end{aligned} \quad (2.27)$$

has been used.

2.3 Damage Effect Study

The damage effect study was designed to take advantage of the data analysis method developed by Schapery (1969) for evaluating NLVE material parameters without growing damage. By conditioning the material at various stress levels and evaluating the conditioned response at the identical stress for each damaged state, one can quickly tell which material parameters are affected by damage. A single specimen should be used so that specimen variability is not an issue.

Figure 2.2 shows a generic loading history for conducting a Damage Effect Study. Three damage states are shown, designated by state S_i , having been conditioned at stress σ_i . For this material, it was found that 9 cycles was sufficient for conditioning as the response became repeatable indicating no further damage or viscoplastic strain over the time of each cycle. Each conditioning cycle was for the same time as the subsequent cycles. Duplicate ‘conditioned’ cycles were performed at each stress, for each damaged state to obtain an average response. In this generic example, the NLVE parameters can be compared at three damage states for stress σ_1 and at two damage states at σ_2 . Sufficient time for recovery should be left between conditioning and subsequent cycles so that the rate of change in strain does not affect the subsequent cycle (waiting for complete recovery is not always practical).

2.3.1 Analysis of Conditioned Material

Returning to the form of the recovery strain with damage growth, Equation 2.26, if the material is cycled each time for time t_i at stress σ (dropping the notation σ_0 for simplicity), the additional viscoplastic strain and the growth of damage becomes negligible over the time t_i . When this is

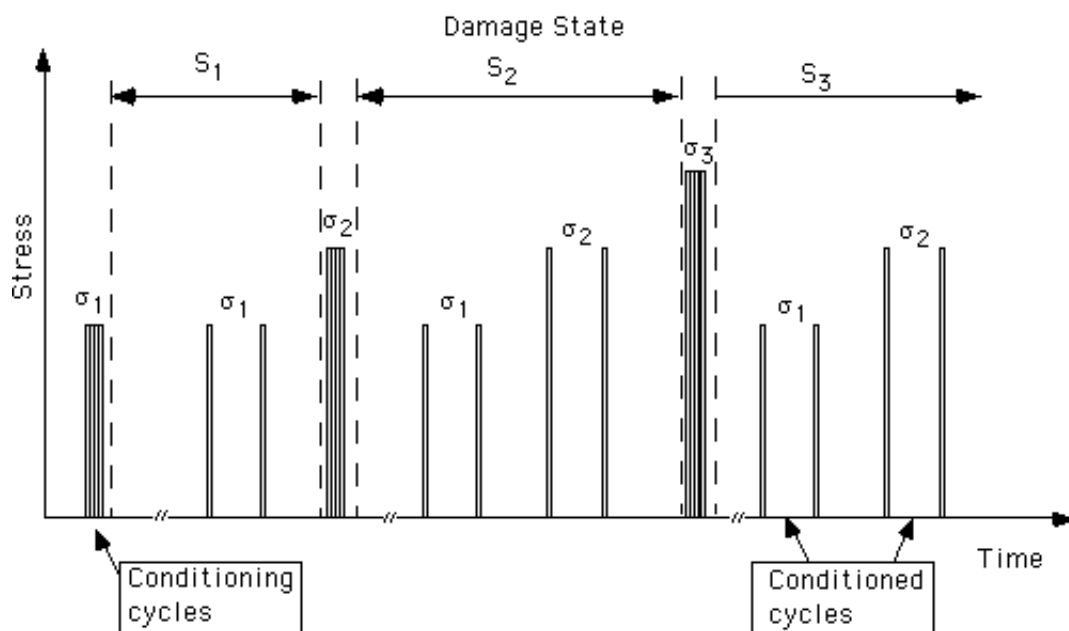


Figure 2.2: Generic loading history for conducting a damage effect study. Three damage states are shown, designated by S_i corresponding to conditioning at σ_i .

the case we will call it ‘conditioned’ and having constant damage, S^c . In the conditioned state,

$$\begin{aligned} I_2 &= 0 \\ \epsilon_{vp} &= \epsilon_{vp}^c \\ g_2(0) &= g_2(t_i) = g_2^c \\ g_1(t_i) &= g_1^{lc} \end{aligned} \tag{2.28}$$

where the superscript ‘c’ has been used to designate a ‘conditioned’ value. Substituting in 2.26,

$$\epsilon_r = g_1^{lc} g_2^c \sigma [\Delta D(\psi) - \Delta D(\psi - \psi'(t_i))] + \epsilon_{vp}^c \tag{2.29}$$

which is similar to the form from Schapery (1969)

$$\epsilon_r = g_2 \sigma [\Delta D(\psi) - \Delta D(\psi - \psi'(t_i))] \tag{2.30}$$

except here g_1^{lc} may not equal unity due to the effect of damage.

After conditioning the material, the *creep* strain from Equation 2.18 is

$$\epsilon_c = g_0^c D_0 \sigma + g_1^c g_2^c \Delta D \left(\frac{t}{a_\sigma} \right) \sigma + \epsilon_{vp}^c. \tag{2.31}$$

which is identical to that for a material without damage except g_0^c, g_1^c, g_2^c can take different values for different damage states at the same stress. Here

$$\begin{aligned} g_1^c &= g_1^c(\sigma, S^c) \\ g_0^c &= g_0^c(\sigma, S^c). \end{aligned} \tag{2.32}$$

Specializing the creep and recovery strains for a power-law ΔD , and using the normalized time

$$\lambda = \frac{t - t_i}{t_i} \tag{2.33}$$

then Equations 2.31 and 2.29 become

$$\epsilon_c = g_0^c D_0 \sigma + g_1^c g_2^c D_1 \sigma \left(\frac{t}{a_\sigma} \right)^n + \epsilon_{vp}^c \tag{2.34}$$

$$\epsilon_r = g_1^{lc} g_2^c D_1 \left(\frac{t_i}{a_\sigma} \right)^n \sigma [(1 - a_\sigma \lambda)^n - (a_\sigma \lambda)^n] + \epsilon_{vp}^c. \quad (2.35)$$

Removing the strain at the beginning of each cycle and normalizing the recovery strain for any length creep, the creep and recovery compliances for a conditioned loading are

$$\frac{\epsilon_c - \epsilon_{vp}^c}{\sigma} = g_0^c D_0 + \frac{g_1^c g_2^c}{a_\sigma^n} D_1 t^n \quad (2.36)$$

$$\frac{(\epsilon_r - \epsilon_{vp}^c)}{\sigma t_i^n} = \frac{g_1^{lc} g_2^c}{a_\sigma^n} D_1 [(1 - a_\sigma \lambda)^n - (a_\sigma \lambda)^n]. \quad (2.37)$$

2.3.2 Evaluating the Effect of Damage

Damage Effect on Creep

Analysis of creep at different damage states is performed just as for the linear viscoelastic response where data are plotted versus t^n ; n is known from low stress testing. The slope gives $\frac{g_1^c g_2^c D_1}{a_\sigma^n}$ and the intercept $g_0^c D_0$. It has been assumed that a_σ is independent of damage. Comparing creep curves at the same stress, the ratio of the slopes for damage states S_a and S_b is

$$R_c = \frac{g_1^c(S_b) g_2^c(S_b)}{g_1^c(S_a) g_2^c(S_a)}. \quad (2.38)$$

The ratio of the intercepts is,

$$R_e = \frac{g_0^c(S_b)}{g_0^c(S_a)}. \quad (2.39)$$

Damage Effect on Recovery

The effect of damage on recovery can be evaluated by plotting the recovery data on a log-log scale similar to evaluating the effect of stress. From Equation 2.37,

$$\log \left(\frac{\epsilon_r - \epsilon_{vp}^c}{\sigma t_i^n} \right) = \log(g_1^{lc} g_2^c) + \log \left(\frac{D_1}{a_\sigma^n} \right) + \log[(1 - a_\sigma \lambda)^n - (a_\sigma \lambda)^n]. \quad (2.40)$$

If, indeed, the effect of damage is only in $g_1^{lc}g_2^c$, data at different damage states can be vertically shifted to coincide. The ratio of this shift is

$$R_r = \frac{g_1^{lc}(S_b)g_2^c(S_b)}{g_1^{lc}(S_a)g_2^c(S_a)}. \quad (2.41)$$

The effect of damage on g_1^{lc} can be found from low stress testing. That is, the LVE recovery can be re-evaluated at each damage state. At low stress ($g_2^c = a_\sigma = 1$), Equation 2.37 becomes

$$\frac{(\epsilon_r - \epsilon_{vp}^c)}{\sigma t_i^n} = g_1^{lc} D_1 [(1 - \lambda)^n - \lambda^n]. \quad (2.42)$$

Any change in the LVE recovery is due to g_1^{lc} . In principle, one could add low stress cycles at each damage state shown in Figure 2.2 to determine g_1^{lc} at each state. However, as shown in Section 8.1.1, it was found that the small change in this parameter parameter was approximately the same for all stresses considered and can therefore be neglected in evaluating the higher stress response. Therefore we set it to unity,

$$R_r = \frac{g_2^c(S_b)}{g_2^c(S_a)} \quad (2.43)$$

reflects only the effect of damage on g_2^c .

Comparison of the Damage Effect on Creep and Recovery

Evaluating R_c , R_e , R_r at different damage levels can immediately yield meaningful conclusions:

1. If the effect of damage is only the vertical shift of Equation 2.40 $\Rightarrow a_\sigma$ is independent of damage.

With a_σ independent of damage:

1. If $R_r = R_c \Rightarrow g_1^c$ is independent of damage.

2. If $R_e = 1 \Rightarrow g_0^c$ is independent of damage. The elastic response is not affected.

Even if changes in g_1^{lc} with damage state are not negligible, R_r can be adjusted for this change and the first comparison still made.

Chapter 3

Numerical Curve Fitting Methods

3.1 Genetic Algorithm / Levenberg-Marguart Numerical Routine

The complexity of the equations describing recovery of a nonlinear viscoelastic/viscoplastic material with hereditary effects from damage growth necessitate the use of powerful numerical methods to find all the material parameters in the constitutive model. A numerical method using a Genetic Algorithm in conjunction with the calculus-based Levenberg-Marguart (LM) method was developed for this purpose.

Standard calculus-based numerical methods require an initial guess of the parameters in an equation

$$y = f(x, \mathbf{a}) \tag{3.1}$$

to be fit to data, where \mathbf{a} are the set of parameters and x the free variable.

They then use the partial derivatives of this equation with respect to each parameter to drive the solution to an optimum, best solution. The least-squares difference between calculated values of a function and data are used to drive the method to the best answer. The Levenberg-Marguart method works well and has become the standard of nonlinear least-squares routines (Press and Flannery, 1986). The shortcoming of such methods is that the final solution can depend on the initially guessed values if there are multiple minimum. Genetic Algorithm (GA) routines were devised to find the best solution in these situations.

Numerical methods which implement GAs are based upon analogy to the theory of evolution and the survival-of-the-fittest paradigm. This is a rapidly growing and broad field of optimization so only a brief synopsis of the method will be outlined here. The reader is referred to (Goldberg, 1989) and (Crain, 1999) for a more detailed coverage.

Sets of initial parameters are randomly generated through their binary equivalents and grouped into arrays called *chromosomes* (the parameter genotype). The entire set of genotypes is called a *population*. This population is a set of L initial guesses for the parameters. These chromosomes are then translated to their real valued format (the parameter phenotype). Each phenotype is then evaluated in terms of its *performance*, where performance is defined as the inverse of the mean square error. Performance of the i^{th} chromosome, C_i , will be designated $F_i(C_i)$. The performance is then scaled to a fitness, f_i , where the fitness is a normalization of the individual performance of each chromosome

$$f_i = \frac{F_i}{\sum_{k=1}^L F_k} \quad (3.2)$$

where L is the population size. This fitness now acts as as discrete probability

mass function for reproduction, which is the likelihood that the chromosome will be crossed with others so parts of its binary sequence will be passed to the next generation. A random *selection* operator chooses two ‘parents’ to cross based on their fitness. A second operator, called *crossover*, determines how the binary information will be exchanged between parents, that is where in the array of zeros and ones to flip-flop the binary code between parents. Finally, the resulting new chromosome is *mutated* by randomly switching a 1 to a 0 and vice versa, with a small probability of mutation. This process of *selection*, *crossover* and *mutation* is repeated $L - 1$ times to create a new population. Each time, the chromosome with best fitness from the previous population is kept in the current one. A finite number of populations are evaluated. A flow-chart of the GA method is shown in Figure 3.1.

The GA technique also has limitations. Of significance here is convergence ambiguity. Convergence ambiguity results from shallow minima surfaces resulting in a cluster of local solutions which dilute the performance of the best solution. The GA method has been modified in this study to avoid this problem. It has been combined with that of the calculus-based LM method. In this way, each phenotype in a population is driven to the local minimum, which is the *best* solution for that initial phenotype. Fitnesses of these best solutions are used in the *selection* and *crossover* procedure. Effectively, each initial guess for a solution is driven to the local best answer by the LM method and the performance of these solutions are compared.

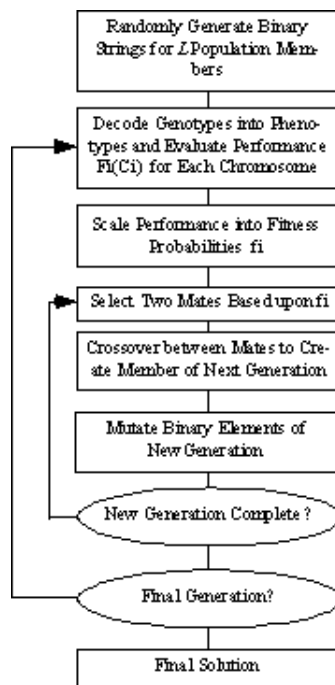


Figure 3.1: GA Flow Chart. Borrowed with permission from Crain (1999) with minor changes.

3.2 Formulations of Recovery Strain for use in the GA/LM Method

In Chapter 2 the equation for recovery strain with hereditary damage effects was derived, Equation 2.26. Now it will be evaluated with an explicit functional form for the G function. Indeed, the major advantage of this method is that the functional form for only one nonlinear parameter needs to be assumed. We assume a power-law creep compliance,

$$\Delta D(t) = D_1 t^n \quad (3.3)$$

and a generalized power-law for G while under load,

$$G(\sigma, t) = G_0 + G_1 t^m \quad (3.4)$$

where G_0 and G_1 are functions of stress. The damage history integral is now,

$$I_2 = D_1 \sigma G_1 m \int_0^{t_i} (\psi - \psi')^n \tau^{(m-1)} d\tau \quad (3.5)$$

where

$$\psi - \psi' = \frac{t_i - \tau}{a_\sigma} + t - t_i. \quad (3.6)$$

Evaluating I_2 ,

$$I_2 = D_1 \sigma G_1 t_i^m \left(t - t_i + \frac{t_i}{a_\sigma} \right)^n F_{21} \left[m, -n; 1 + m; \frac{t_i}{t_i + a_\sigma(t - t_i)} \right] \quad (3.7)$$

where

$$F_{21}[a, b; c; z] = 1 + \sum_{k=1}^{\infty} \frac{a(-b)_k}{a+k} \frac{z^k}{k!} \quad (3.8)$$

is the hypergeometric function. By again using the normalized time defined in Equation 2.33, recovery strain may be written as

$$\begin{aligned} \frac{\epsilon_r - \epsilon_{vp}(t_i)}{\sigma D_1 \left(\frac{t_i}{a_\sigma} \right)^n} &= g_1(t_i) \{ G_0 [(1 + \lambda a_\sigma)^n - (\lambda a_\sigma)^n] \\ &+ G_1 t_i^m [F_{21} \left(m, -n, 1 + m, \frac{1}{1 + \lambda a_\sigma} \right) (1 + \lambda a_\sigma)^n - (\lambda a_\sigma)^n] \}. \end{aligned} \quad (3.9)$$

There are five free parameters to fit to the data; $g_1(t_i)G_0$, $g_1(t_i)G_1$, $\epsilon_{vp}(t_i)$, a_σ and m . A sample code for this method is given in Appendix A. Data were then simulated with some arbitrary functions for G and the other parameters. Implementing the GA/LM method on this simulated data, the correct solution is eventually found. However, it requires a slow task of narrowing the range over which each parameter may vary based on previous runs. Due to the slowness of this procedure, some alternative formulations were devised that make use of multiple sets of data.

A formulation to use on two data sets of different length creep

The first formulation making use of two data sets was based on the observation that the recovery strain can be normalized for different length creep times when tested at the same stress. Rearranging Equation 3.9,

$$\left\{ \frac{\epsilon_r - \epsilon_{vp}(t_i)}{\sigma D_1 \left(\frac{t_i}{a_\sigma}\right)^n g_1(t_i)} - G_0[(1 + \lambda a_\sigma)^n - (\lambda a_\sigma)^n] \right\} \frac{1}{t_i^m} = G_1[F_{21} \left(m, -n, 1 + m, \frac{1}{1 + \lambda a_\sigma}\right) (1 + \lambda a_\sigma)^n - (\lambda a_\sigma)^n]. \quad (3.10)$$

Note that the RHS of the equation is independent of creep time, t_i . Recovery strain normalized for the time under load will be called

$$\epsilon_{rn}^i = \left\{ \frac{\epsilon_r - \epsilon_{vp}(t_i)}{\sigma D_1 \left(\frac{t_i}{a_\sigma}\right)^n g_1(t_i)} - G_0[(1 + \lambda a_\sigma)^n - (\lambda a_\sigma)^n] \right\} \frac{1}{t_i^m} \quad (3.11)$$

where the superscript i refers to creep data for time t_i . Using data from two different length creep cycles, we define

$$y = \epsilon_{rn}^1 - \epsilon_{rn}^2 = 0 \quad (3.12)$$

as the function to minimize, where $t_1 \neq t_2$. Although more parameters need to be found ($g_1(t_1)$, $g_1(t_2)$, $\epsilon_{vp}(t_1)$, $\epsilon_{vp}(t_2)$, a_σ , G_0 and m) the v/p strains

are converged upon quickly and computational time for each population is decreased as the hypergeometric function, F_{21} , does not need to be calculated.

Looking ahead to real data however, this method requires the use of different specimens loaded for different creep times. Specimen variation may very well mask differences due to different amounts of damage.

A formulation to use on two data sets from the same sample

An alternative approach using only a single specimen is to only fit the difference between first cycle behavior and the conditioned response. A qualitative discussion of the differences seen in real data are given in Chapter 8. For notational simplicity, we shall return to the form of the recovery equation without having assumed functional forms for G . In fact, this formulation will work for any functions for which I_2 can be analytically evaluated. Subtracting Equations 2.19 and 2.35,

$$\begin{aligned} \frac{(\epsilon_r^1 - \epsilon_r^c) - (\epsilon_{vp}^1 - \epsilon_{vp}^c)}{\sigma} &= (g_1^1(t_i)g_2^1(0) - g_1^{lc}g_2^c)\Delta D(\psi) - \\ &(g_1^1(t_i)g_2^1(t_i) - g_1^{lc}g_2^c)\Delta D(\psi - \psi'(t_i)) + g_1^1(t_i)I_2 \end{aligned} \quad (3.13)$$

The superscript ‘1’ has been used to designate data from the first cycle and not for creep time t_1 as used in the previous section. Values of $g_1^{lc}g_2^c$ and ϵ_{vp}^c are known from fitting the conditioned data. One major advantage of this formulation is that a_σ is also known (or at least closely known) from fitting the conditioned response. In practice, this numerical method is very sensitive to values of a_σ . Better fits are made when it is left as a free parameter. Now a very small window of values over which the GA method guesses solutions can be used. Consequently, convergence occurs much more quickly.

3.3 Experiments for Conducting Numerical Fitting

While the various formulations of recovery strain were being developed and coded, an experimental program was initiated concurrently due to the time involved in conducting each task. Multiple samples of off-axis 30° and 90° material were loaded at three separate stress levels for creep times of 100s, 1000s, and 10000s. A separate sample is of course needed for each stress-creep time combination. Many of these samples were then cycled 9 more times to get the conditioned response.

Upon fitting the recovery strain, a functional form for g_2 is found. Also from these fits, $g_1(t_i)$ and $\epsilon_{vp}(t_i)$ will be known. The different length creep cycles at different stress levels provide discrete data points for these functions. They can be constructed in a piecewise fashion by plotting data at identical stress levels versus time and identical times versus stress.

Unfortunately, these data were not used with the above methods. After sufficient data was collected and the conditioned response examined, it became clear a more complicated constitutive model was needed for this particular material. The equations for conditioned material behavior were not adequate to fit the data, as will be discussed in Chapter 8. Consequently, hereditary damage effects could not be distinguished. Hopefully, the GA/LM method developed will be useful in analyzing data from the wide class of materials whose conditioned response have been characterized by the equations used in this study.

Chapter 4

Analysis of Distributed Microcracking

4.1 Viscoelastic Crack Growth - Theoretical Background

The theoretical basis for predicting crack initiation and growth in *linear* viscoelastic media has been established by Schapery (1975a)(Schapery, 1975b). Work on fracture in polymers preceding this theory is summarized by Knauss (1973). Few restrictions are placed on the failing material at the crack tip and it may be nonlinear, rate-dependent and discontinuous.

This work was extended by Schapery to include a class of nonlinear viscoelastic materials where a J-like integral is used as a fracture characterizing parameter [(Schapery, 1984), (Schapery, 1986)]. This J-integral is based on the introduction of a path-independent J-integral by Rice (1968) for fracture of materials exhibiting time-dependent and nonlinear behavior. In order to use such a parameter, path independence of J must be established. If the

stress-strain behavior of the continuum material can be characterized by a work potential, Φ , this will be the case. That is

$$\sigma_{ij} = \frac{\partial \Phi}{\partial \epsilon_{ij}} \quad (4.1)$$

where $\Phi = \Phi(\epsilon_{ij}, x_k, t)$ and $i, j, k = 1, 2, 3$. By making certain assumptions about the material constitutive behavior, Schapery found that significant generalizations could be made to the crack growth theory by replacing strains by ‘pseudo strain’, ϵ_{ij}^R , so that stress

$$\sigma_{ij} = \frac{\partial \Phi}{\partial \epsilon_{ij}^R} \quad (4.2)$$

where $\Phi = \Phi(\epsilon_{ij}^R, x_k, t)$ is referred to as the ‘pseudo strain energy density’.

Deformation behavior is assumed to be characterized by a nonlinear viscoelastic constitutive equation,

$$\epsilon_{ij} = E_R \int_0^t D(t - \tau, t) \frac{\partial \epsilon_{ij}^e}{\partial \tau} d\tau \quad (4.3)$$

where

$$\epsilon_{ij}^e = \epsilon_{ij}^e(\sigma_{kl}, x_m, t) \quad (4.4)$$

is a second order tensor material function. The E_R is a free constant called a ‘reference modulus’ and D is a creep compliance. By expressing stress in terms of strain and changing the notation of ϵ_{ij}^e to ϵ_{ij}^R , Equation 4.3 rewritten as

$$\sigma_{ij} = \sigma_{ij}(\epsilon_{kl}^R, x_m, t). \quad (4.5)$$

The pseudo strain

$$\epsilon_{ij}^R \equiv E_R^{-1} \int_0^t E(t - \tau, t) \frac{\partial \epsilon_{ij}^e}{\partial \tau} d\tau \quad (4.6)$$

where E is a relaxation modulus.

4.1.1 Crack Growth Criteria - J_v Integral

In an analogy with the J-integral for nonlinear elastic behavior, Schapery (1984) introduces

$$J_v = \int_{C_1} \left(\Phi dx_2 - T_i \frac{\partial u_i^R}{\partial x_1} ds \right) \quad (4.7)$$

where C_1 is the contour shown in Figure 4.1 starting at point 1 and ending at point 2. The T_i are tractions and u_i^R are displacements in a reference elastic body with stresses σ_{ij}^R and strains ϵ_{ij}^R .

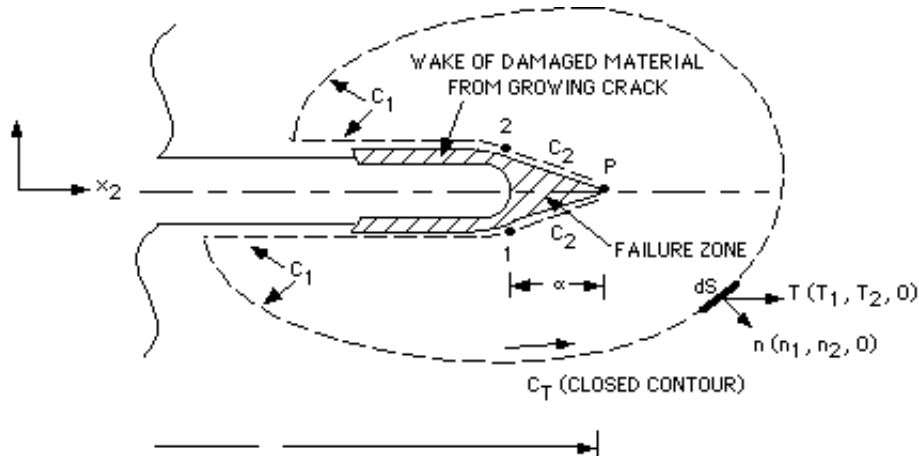


Figure 4.1: Cross section of a crack in nonlinear viscoelastic material showing contour C_1 (- - -) used in the line integral of Equation 4.7. Only the opening mode of displacement is drawn, although the basic formulation allows for shearing deformation and asymmetric damage. From (Schapery, 1986)

Implementing a correspondence principle which relates the mechanical state of nonlinear elastic and nonlinear viscoelastic media with growing damage (Schapery, 1981) provides the solution of stress, strain and displacement

in a viscoelastic body based on a reference elastic solution

$$\begin{aligned}\sigma_{ij} &= \sigma_{ij}^R \\ \epsilon_{ij} &= E_R \int_0^t D(t - \tau, t) \frac{\partial \epsilon_{ij}^R}{\partial \tau} d\tau \\ u_i &= E_R \int_0^t D(t - \tau, t) \frac{\partial u_i^R}{\partial \tau} d\tau\end{aligned}\tag{4.8}$$

where the reference solution satisfies all field equations and traction boundary conditions for an elastic body.

Schapery (1986) made some simplifying assumptions about the crack tip failure or process zone, the primary one being that it is a thin layer. Several models for crack initiation and growth in nonlinear viscoelastic media were then developed. From them, a fairly simple implicit equation for crack speed is found

$$E_R D(k\alpha/\dot{a}, t) J_v = 2\Gamma\tag{4.9}$$

where 2Γ is the fracture energy or the work required (per unit area of new crack surface) for crack growth and the left side of the equation is the work available. The quantity \dot{a} is crack speed and the coefficient k depends somewhat on the undeformed geometry of the failure zone boundary; a value of $k=1/3$ is a good approximation but in general depends on the creep compliance (Schapery, 1975b). The length of the failure zone, α , shown in Figure 4.1.

4.1.2 Unstable Crack Growth for a Power-law Material

Assuming power-law nonlinearity by representing the pseudo strain energy density as a homogeneous function of degree $N+1$,

$$\Phi(c\epsilon_{ij}^e) = |c|^{N+1} \Phi(\epsilon_{ij}^e)\tag{4.10}$$

where N and c are constants, an explicit result for the length of the failure zone can be found (Schapery, 1986),

$$\alpha = \left| \frac{\sigma_n}{\sigma_m} \right|^{1/N} \frac{J_v}{|\sigma_m| I_f}. \quad (4.11)$$

The σ_n and σ_m are measures of the continuum yield stress and strength of the failure zone material respectively. The I_f is a dimensionless function of N . As all of these are material parameters, Equation 4.11 may be written as

$$\alpha = f_1 J_v \quad (4.12)$$

where

$$f_1 = \left| \frac{\sigma_n}{\sigma_m} \right|^{1/N} \frac{1}{|\sigma_m| I_f}. \quad (4.13)$$

Combining Equation 4.9 with 4.12 and assuming a power-law creep compliance with no material aging,

$$D(t) = D_1 t^n \quad (4.14)$$

we have an implicit equation for crack speed in a power-law material

$$E_R D_1 (k f_1 / \dot{a})^n J_v^{n+1} = 2\Gamma \quad (4.15)$$

in which Γ and f_1 may depend on \dot{a} ; if they obey power laws, then Equation 4.15 implies

$$\dot{a} = k_1 J_v^m \quad (4.16)$$

where k_1 and m are constants.

4.1.3 Effect of 2-Phase Material on the J_v Integral

Ramp/hold testing of 90° samples gave evidence of microstructural relaxation during the hold portions of loading, as will be discussed in Section 7.5.

This type of relaxation is possible if there are separate phases of material, a softer high-stressed region in front of a crack tip and a stiffer region away from the crack each characterized by a creep compliance with different time-dependence. The toughening mechanism of rubber particles embedded in the matrix will encourage this type of phenomenon.

The primary toughening mechanisms of rubber particles in a heavily cross-linked epoxy matrix are particle cavitation and shear yielding of the matrix adjacent to the particles (Kinloch and Hunston, 1983) (Pearson and Yee, 1983) (Shaw, 1994). Interaction between the triaxial stress state at a crack tip with the triaxial stress in a rubber particle from the cure process lead to cavitation of the particles. Shear yielding occurs around the particles after cavitation. Due to their close proximity, this frequently happens in bands between the particles as they also act as termination sites. Consequently, this yielding stays localized in the vicinity of the crack tip and occurs to a much greater degree than in an unmodified epoxy.

The consequence of localized yielded material in front of a crack may be to have a region of material that is strongly nonlinear viscoelastic, surrounded by far-field weakly nonlinear or simply a linear viscoelastic region. Schapery (1990b) explored such a situation using J-like integrals to characterize fracture behavior. The result is a fairly complicated situation with a transition from one region to the other, and is analogous to what exists in metals exhibiting primary and secondary creep.

If both phases of material are power-law media, J_v still determines the local stress field provided α is sufficiently small. The correspondence principle 4.8 states that the stresses in the viscoelastic body are the same as in the reference elastic body. Stresses are therefore of the form of the HRR

singularity solution for power-law hardening elastic materials (Rice, 1968),

$$\sigma_{ij} \sim J_v^{\frac{1}{1+N}}. \quad (4.17)$$

For the case of mode-I fracture, Schapery shows by using a ‘quasi-elastic’ approximation of the constitutive equations that

$$J_v \sim K_I^2 \frac{D_l}{D} \quad (4.18)$$

where K_I is the mode-I stress intensity factor and the material exhibits far-field linear viscoelastic behavior. The D_l and D are the creep compliances of the linear and nonlinear viscoelastic phases respectively. Therefore,

$$\sigma_{ij} \sim \left[K_I^2 \frac{D_l}{D} \right]^{\frac{1}{1+N}}. \quad (4.19)$$

For pure shear loading,

$$J_v \sim K_{II}^2 \frac{D_l^s}{D^s} \quad (4.20)$$

where K_{II} is the mode II stress intensity factor and D_l^s and D^s are the linear and nonlinear shear creep compliances respectively. Mixed-mode loading is therefore complicated by different transverse and shear creep compliances in each phase of the material. Introducing,

$$\Omega(t) = \frac{D_l^s D}{D^s D_l} \quad (4.21)$$

the J_v for mixed mode loading is

$$J_v \sim (K_I^2 + \Omega K_{II}^2) \frac{D_l}{D} \quad (4.22)$$

which results in the single mode J_v for either of the mode I or mode II limiting cases. Therefore, J_v depends on the specific geometry and location of a given crack. For example, for a crack at or near the interface of and parallel to two

dissimilar materials, as is the case in our material for a crack at or close to a fiber interface, a two dimensional elastic analysis shows (Hutchinson and Rice, 1987)

$$(K_I^2 + K_{II}^2) \simeq \frac{w^2 \pi a}{2} [(\sigma_{22}^\infty)^2 + (\sigma_{12}^\infty)^2] \quad (4.23)$$

where σ_{22}^∞ and σ_{12}^∞ are the remotely applied transverse and shear stress. The w is a function of the dissimilar material properties and a is crack length. In light of Equations 4.22 and 4.23 and assuming the fiber is much stiffer than the matrix,

$$J_v \sim a [(\sigma_{22}^\infty)^2 + \Omega(\sigma_{12}^\infty)^2] \frac{D_l}{D}. \quad (4.24)$$

Indeed, for a constant globally applied stress, and a larger creep exponent in the nonlinear material, the viscoelastic J integral will decrease with time and arrest crack growth. With the crack at the fiber/matrix interface, an idealized geometry of the crack tip is shown Figure 4.2 where there is no displacement of the relatively stiff fiber. This analysis shows the general nature of having a two-phase material, but to make this complexity more manageable an idealized model will be adopted.

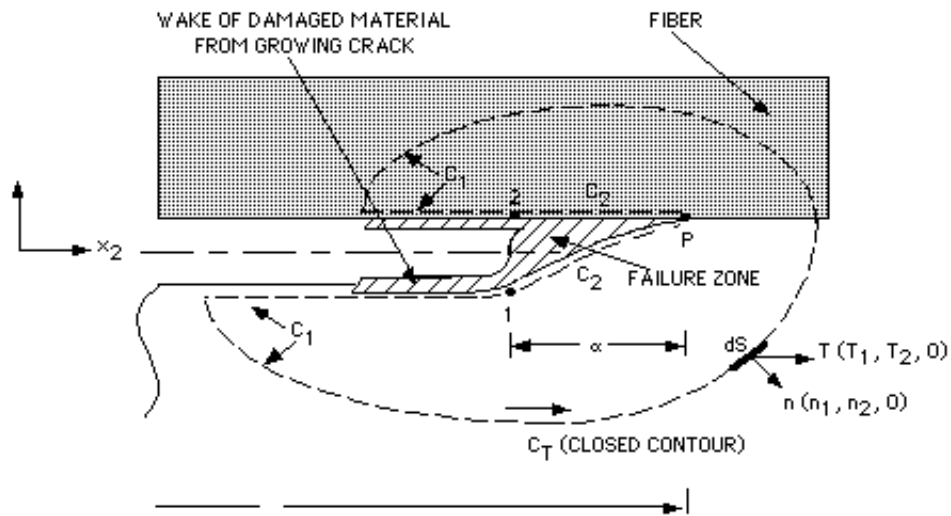


Figure 4.2: Cross section of a crack at the fiber/matrix interface in a nonlinear viscoelastic material. The opening mode of displacement is drawn with the contour C_1 (- - -) used in the line integral of Equation 4.7 shown.

4.2 Analysis of Crack Growth

4.2.1 Analysis and Simplification of the 2-Phase Material

As will be discussed in Chapter 6, matrix cracking and fiber/matrix debonding are the primary mechanisms of damage viewed in the carbon epoxy studied (Figures 6.1 through 6.3 display some photomicrographs of this damage). A majority of the cracking occurs at or near the fiber/matrix interface. High stresses near the fibers with and without existing debonds may create a phase of NLVE material in which this cracking occurs. It is difficult to idealize the three-dimensional geometry in which this takes place but a two-dimensional diagram of the cross-section is useful in conceptualizing behavior in the microstructure, as shown in Figure 4.3. Here groups of fibers with NLVE regions between them are shown adjacent to lower-stress LVE regions. If the group of tightly-packed fibers with the high-stress regions between them is treated as having some effective NLVE property, we can consider just two phases of material.

Figure 4.4 shows an idealized mechanical analog of the material containing a nonlinear viscoelastic phase in the vicinity of crack tips (driving the crack growth) adjacent to a linear viscoelastic material. Each phase has effective LVE and NLVE properties to approximate the real situation where there is a transition from a nonlinear to a linear one. A viscoplastic component has also been added for consistency with experiments and probably reflects far-field permanent rearrangement of the material. Separate dashpots on each phase were also considered for the model. However, a dashpot on the NLVE arm has no impact on the stress driving crack growth. It would only

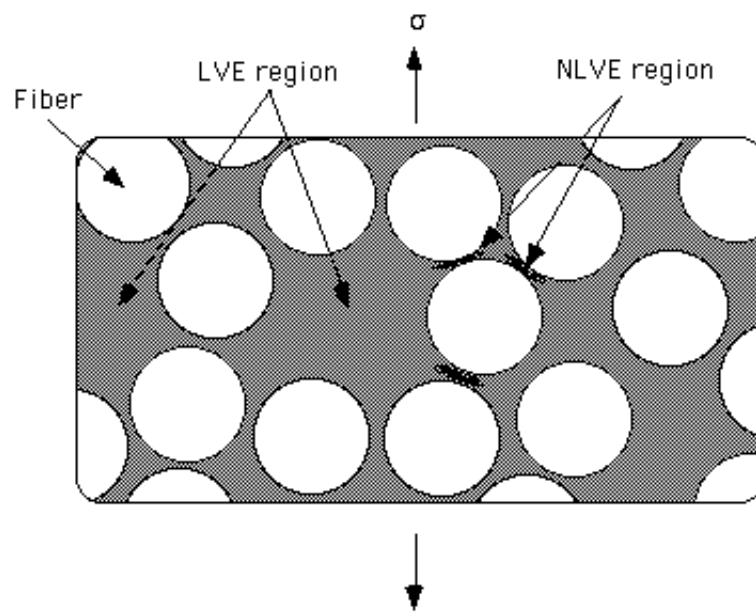


Figure 4.3: Cross-sectional diagram of a fiber composite. Groups of fibers with highly stressed NLVE regions between them are shown adjacent to lower stress LVE resin-rich regions.

add unneeded complexity to the model. A dashpot on the linear arm was not needed to collapse the data. This idealization is consistent with the observed stress-strain behavior as well as the relaxation viewed during the ramp/hold AE experiments. Assuming that the NLVE phase is much softer than the linear one, stresses will redistribute to the linear phase when the global stress is held constant, thus explaining the relaxation observed from the AE data. Also, as discussed in Chapter 8, conditioned recovery strains could not be shifted to the linear recovery behavior. One possible explanation is crack interference upon unloading. However, the separate phases of material proposed here will have the same effect, but also explain the microstructural relaxation observed while under load. Upon unloading, the nonlinear phase will be compressed and the linear phase held in tension. Over long times the stresses between phases will redistribute and complete recovery will occur.

Returning to the mechanical analog in Figure 4.4, the total strain is ϵ due to the globally applied stress σ . The component of strain which is viscoplastic is designated by ϵ^{vp} . Each phase of the material takes on a portion of the load, σ_l on the linear viscoelastic component and σ_{nl} on the nonlinear one. A common mechanical analog for each phase is a system of generalized Voigt units as shown in Figure 4.5. The strain on the viscoelastic segment is

$$\epsilon^{ve} = \epsilon - \epsilon^{vp}. \quad (4.25)$$

Here all cracking is occurring in the NLVE phase of the material, not with a LVE phase surrounding it, but adjacent to it. This situation is therefore slightly different than the case discussed in the previous section. Here the stresses just on the NLVE portion, and therefore in the nonlinear stress field, control fracture. To the authors knowledge the problem of a crack in a non-

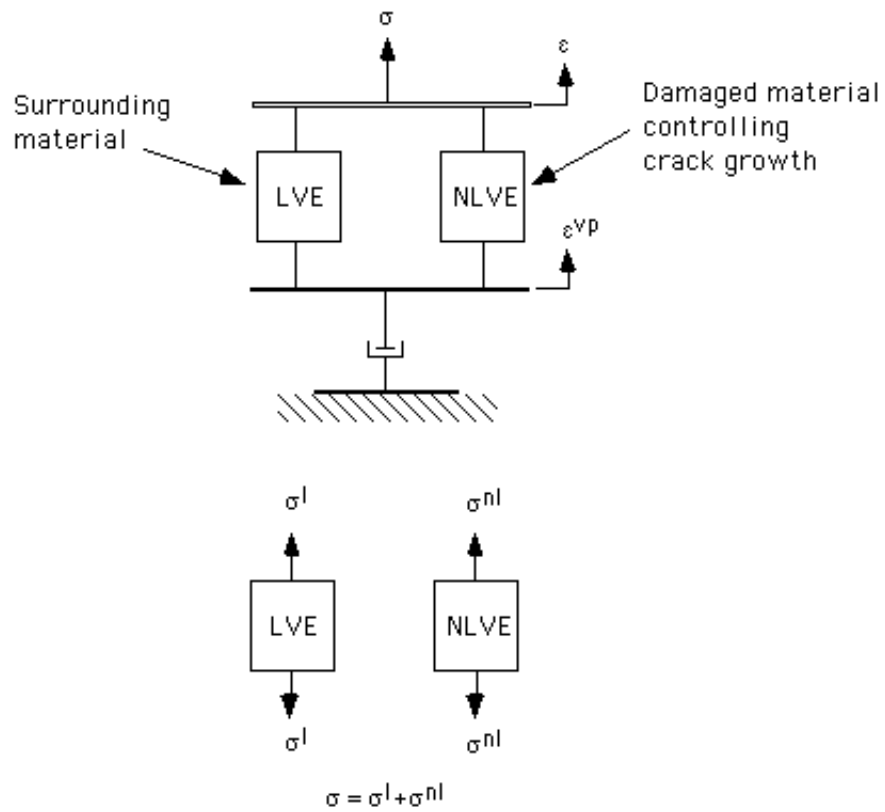


Figure 4.4: Idealized mechanical analog of the material containing a nonlinear viscoelastic phase in the vicinity of crack tips (driving the crack growth) surrounded by a linear viscoelastic material. A viscoplastic component has also been added.

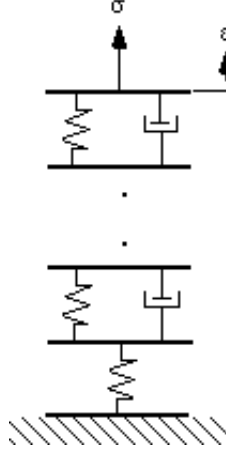


Figure 4.5: Generalized Voigt unit.

linear elastic power-law material has not been solved for the mixed-mode case except for the case of no shear loading (He and Hutchinson, 1981). Therefore we will assume the same dependence of the J_v integral on the globally applied stresses as in the previous section,

$$J_v \simeq \frac{w^2 \pi a}{2} \left[(\sigma_{22}^{nl})^2 + \Omega (\sigma_{12}^{nl})^2 \right]^s \quad (4.26)$$

except here the exponent s reflects the power-law nonlinearity of the material. The Ω is still a time-dependent function, but is not clearly defined as in the previous section. It reflects changes in the viscoelastic Poisson's ratio of the matrix. How this material property dependence may enter is seen in work by Kachanov (1999) where he shows that the change in the elastic potential of a linear elastic solid due to the addition of a penny-shaped crack depends on a quadratic function of the stresses where the Poisson's ratio weights the normal stress components. Specific functional forms for J_v will of course be needed for each crack in the material as the local geometry varies. Here we will keep the form from the 2D analysis of a crack at or near the fiber interface

for purposes of discussion. However, the functional dependence of J_v on the stresses is of primary importance here and will have the only bearing on the subsequent analysis.

With only the globally applied stress known, we may calculate σ^{nl} by first calculating the stress on the linear element,

$$\sigma^l = \int_0^t E(t - \tau) \frac{d\epsilon^{ve}}{d\tau} d\tau \quad (4.27)$$

where E is an *effective relaxation function* for the LVE material phase and

$$\sigma^{nl} = \sigma - \sigma^l. \quad (4.28)$$

A functional form for the plastic strain proposed by Zapas and Crissman (1984) was assumed based on its successful use by others in fiber composites and other polymers [(Tuttle et al., 1995); (Lai and Bakker, 1995); (Guedes and Marques, 1998); (Qin et al., 1998); (Cardon et al., 2000)]. This functional has the form,

$$\epsilon^{vp} = \left[C \int_0^t \sigma^p dt \right]^r \quad (4.29)$$

where C , p , r are constants for constant temperature.

Crack Growth Using a Simplified Model

Implementing the idealized model of the previous section, we combine Equations 4.15 and 4.26 to find the instantaneous size of a crack at time t ,

$$\frac{1}{a_0^n} - \frac{1}{a^n} = \int_0^t k f_1 \left(\frac{E_R D_1}{2\Gamma} \right)^{\frac{1}{n}} \left(\frac{w^2 \pi}{2} \right)^{q/s} \left[(\sigma_{22}^{nl})^2 + \Omega (\sigma_{12}^{nl})^2 \right]^q dt \quad (4.30)$$

where $q = s(1 + \frac{1}{n})$ and a_0 is the initial crack length. In general, Γ and σ_m , which affects f_1 , may depend on the crack speed and other parameters. They shall be assumed constant for this analysis, but don't need to be. If a power-law is assumed for each, the only differences is that q becomes independent

of n . We are specifically interested in when a given crack becomes unstable and runs dynamically or ‘fails’. Calling this time t_f , or failure time, we let $a \rightarrow \infty$ yielding,

$$\left(\frac{2\Gamma}{E_R D_1 a_0}\right)^{\frac{1}{n}} \frac{1}{k f_1} \left(\frac{2}{w^2 \pi}\right)^{q/s} = \int_0^{t_f} [(\sigma_{22}^{nl})^2 + \Omega(\sigma_{12}^{nl})^2]^q dt \quad (4.31)$$

4.2.2 Analysis of Distributed Cracking

We will assume that each initial flaw obeys Equation 4.31, where each has it’s own unique initial length a_0 , fracture energy Γ , and strength of the failure zone, σ_m . Values of σ_n and w may also vary locally. We will define

$$L_i = \left(\frac{2\Gamma}{E_R D_1 a_0}\right)^{\frac{1}{n}} \frac{1}{k f_1} \left(\frac{2}{w^2 \pi}\right)^{q/s} \quad (4.32)$$

as a combined fracture parameter of all the factors affecting fracture of the i^{th} crack. As L is a random variable, we define $p(L)$ as the *probability mass function*, or PMF, of this variable for each specimen tested. Each sample, representative of the material, will have the same mass function or distribution of initial flaws. In general, a PMF of an event is the relative frequency of that event occurring out of a discrete number of events. So the frequency of a flaw in the material of having a value of L ,

$$p(L) = \frac{n_L}{M} \quad (4.33)$$

where n_L is the number of flaws with a value of L and M is the total number flaws. As shown in Equation 4.31,

$$L = \int_0^{t_f} [(\sigma_{22}^{nl})^2 + \Omega(\sigma_{12}^{nl})^2]^q dt. \quad (4.34)$$

With knowledge of the failure time t_f and the stress, this distribution can be found. Acoustic emission testing provides this information as the time and

stress at which each flaw fails during loading is known. Therefore, for our purposes we will define n_L as the number of *detectable* flaws with a value of L , and M is the total number of detectable flaws. Provided with an adequate sampling from the AE data, $p(L)$ will be the same. Note that the functional dependence in Equation 4.32 is not of importance here. Given all information about a given flaw, a different form would undoubtedly be derived for each flaw. Of primary importance is its relation to the stresses and time of failure shown in Equation 4.34.

The *cumulative distribution function* CDF,

$$P(L) = \sum_{\text{all } L_i \leq L} p(L_i) \quad (4.35)$$

gives the probability that $L_i \leq L$. In physical terms, $P(L)$ gives the percentage of flaws that have a value of $L_i \leq L$. The reader is referred to Schapery (1974) for a similar discussion in linear viscoelastic media.

From a practical standpoint, the entire distribution of flaws will not be measurable. Each sample will fail at a different point, thus yielding only a portion of $p(L)$ for that sample, up to say L_f . Such a distribution is said to be truncated above L_f (Benjamin and Cornell, 1970). In which case,

$$p(L) = \begin{cases} \beta p(L) & L < L_f \\ 0 & L \geq L_f \end{cases} \quad (4.36)$$

where

$$\beta = \frac{1}{1 - P(L_f)}. \quad (4.37)$$

For a given test, $P(L_f)$ is not known, so β becomes a free variable from one sample to the next.

The CDF as a damage variable

A common damage variable used in calculating the stiffness reduction in a laminate due to transverse cracking is crack density [e.g. (Hashin, 1985) (Highsmith and Reifsnider, 1982), (Talreja, 1985b)]. Here, laminates are used where a transverse crack travels the entire width of the sample. Crack density is defined as the number of cracks per unit length and the loss in stiffness is readily calculated (for a linear elastic material) based on this density.

In unidirectional material, the situation is more complicated. Cracks propagate various distances depending on the local geometry. Fortunately, the constraining nature of the fibers tend to keep the crack orientation parallel to the fibers. The acoustic emissions emitted from this material indicate that the arrested crack length is not a function of stress level for most of the samples tested. Therefore, there is an *average* crack size independent of stress level. Fiber-waviness probably plays a significant role in this typical size.

An approach from the standpoint of micromechanics may be to first analyze the effect of this typical crack on the global response of a representative volume element of material. It can then be scaled with the number of cracks present. It is not implied this is a simple task in a NLVE material. Indeed, a numerical study of the effect of a debond or microcrack in a NLVE matrix would be helpful in describing the effect of such damage. However, from a practical standpoint, it is *not* possible at this time to count each and every crack and measure its size. What is possible is to monitor a portion of them, the largest ones. Monitoring this portion provides a population with which to perform the statistical analysis suggested above and to find the CDF of microcracking. The same proportionality between the number of average

cracks and the effect of these cracks on the global response will hold for the percentage of cracks that have failed relative to the amount at failure. If the typical arrested length of a crack is dependent on stress level, this is just an additional nonlinearity that needs to be considered in accounting for the *effect* of the damage on the global response.

The CDF is useful as a damage variable as it can be measured directly and does not need to be inferred from stress-strain information that may be affected by other softening mechanisms. Finally, variability in *detectable* cracks from sample to sample, which can mask differences in the time or rate effects, is easily normalized without testing a large number of specimens for each loading condition.

As an aside, a CDF of transverse cracks could also be used as the damage variable in cross-ply laminates. The CDF in this case is the total crack density, measured in the usual way, divided by the number of cracks in the Characteristic Damage State (Reifsnider, 1977), that is the maximum number of transverse cracks attainable in a laminate. This idea may prove useful in laminates where the transverse cracks do *not* traverse the full width of a sample, as is typically the case when single plies are used and probably more representative of a real structure. In this case the situation is similar to that of the unidirectional material.

Chapter 5

Experimental Setup

5.1 Material and Processing Information

The material under study is comprised of AS4C carbon fibers with a rubber-toughened epoxy resin E719LT produced by B-P Chemicals. Flat panels, 12 in. x 12 in., were constructed by a filament winding process by R-Cubed Composites, Inc., West Jordan, UT. The plates were cured in an autoclave/vacuum bag procedure at a cure temperature of 250° F. So that results from this study may be reproduced, details of the curing process have been supplied by R-Cubed Composites and provided by Bocchieri (1996). The resulting material has a low glass transition temperature, T_g , of approximately 250-275° F. A typical T_g seen for more brittle composite systems, such as AS4/3501-6, is approximately 410° F with a cure temperature of 350° F. Greater time dependence in material behavior of AS4C/E719LT at room temperature is expected as a result of this low value.

5.2 Load Frames and Strain Measurement

All constant stress rate testing was performed on a 20 kip Instron screw-driven load frame 4505 with Instron 4500 controller. Three different stress rates were used in the constant stress rate testing. Ratios of the two lower rates to the highest rate were 6:1 and 18:1 with failure occurring at roughly 10 minutes, 1 hour and 3 hours. All testing was performed at room temperature and humidity conditions (moisture absorption of the dessicated samples for these short-term tests is negligible). They were assumed to be in the dry condition, having been stored on desiccant for more than 2 years. The average testing temperature was approximately 77° F (25° C).

Creep/recovery testing was performed on three in-house built creep frames as shown in Figure 5.1. Creep frames were calibrated using a strain-gaged 0° sample with 10 lb. increments in load. Due to the long duration of testing, all samples were loaded in sealed plexiglass tanks with dessicant inside. Humidity was held to less than 10 percent RH.

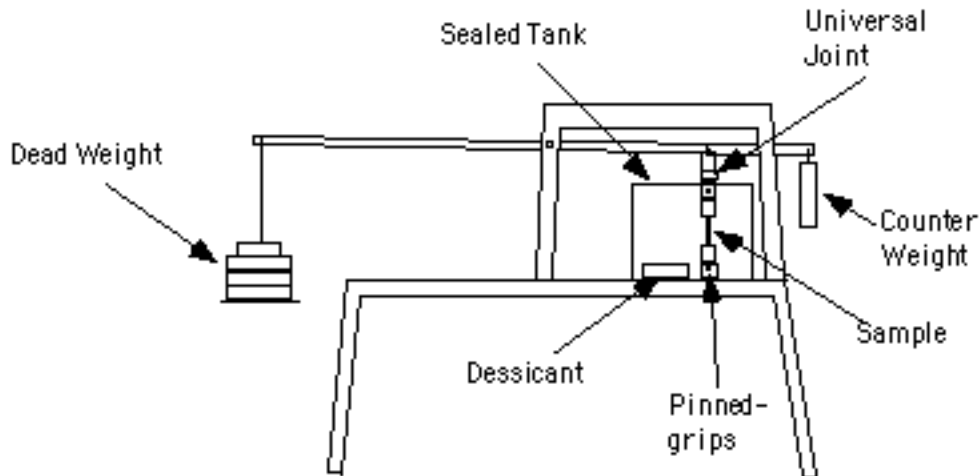


Figure 5.1: Creep testing frame with plexiglass tank.

The 45° and 30° off-axis specimens were equipped with Micromeasurements 90° tee rosettes (CEA-06-125UT-350) with the gage sections oriented in the longitudinal and transverse directions. A rosette (CEA-06-250UR-10C) was used for the 90° specimens. Gages in the rosette were oriented in the longitudinal and transverse directions. All gages on off-axis samples were transversely corrected according to the manufacturers specifications (Micromeasurements-TN-509, 1982). Gages were placed on both faces of each specimen to correct for out of plane bending. A dummy specimen of identical fiber orientation and gage configuration was used to compensate for temperature fluctuations.

An in-house program written in Labview was used for computer data acquisition. Both variable gain and constant gain strain conditioners were used. A conditioner built in-house capable of computer-controlled gain was used for four strain channels while additional channels were conditioned by a fixed-gain Vishay 2120. Because of the large strains encountered by many of the specimens, the variable gain strain conditioner proved to be beneficial in maintaining low electrical noise throughout the test.

5.3 Acoustic Emission Equipment and Setup

All hardware and software used for acoustic emission data acquisition and analysis were provided by Digital Wave Corporation, and are shown in Figure 5.2. Hardware and software settings are shown in Table 5.1. These settings afforded maximum sensitivity from the available equipment just above the background noise level.

Broadband sensors were attached to a sample with electrical tape, as shown in Figure 5.3, after applying high vacuum grease to the sensor faces.

Table 5.1: Typical hardware and software settings for the two acoustic emission sensors used.

B225 Sensors	B1025 Sensors
<p>** Conditioner Settings ** Signal HPF Cutoff (kHz): 20 Trigger HPF Cutoff (kHz): 20 Signal LPF Cutoff (kHz): 1500 Trigger LPF Cutoff (kHz): 1500 Signal Gain (dB): 9 Trigger Gain (dB): 9 Signal Gain Switch (dB): 21 Trigger Gain Switch (dB): 21 Preamplifier Gain (dB): 40 Threshold (V): 0.1 Echo Delay Time (microsec): 0.0</p>	<p>** Conditioner Settings ** Signal HPF Cutoff (kHz): 20 Trigger HPF Cutoff (kHz): 20 Signal LPF Cutoff (kHz): 1500 Trigger LPF Cutoff (kHz): 1500 Signal Gain (dB): 6 Trigger Gain (dB): 6 Signal Gain Switch (dB): 21 Trigger Gain Switch (dB): 21 Preamplifier Gain (dB): 40 Threshold (V): 0.1 Echo Delay Time (microsec): 0.0</p>
<p>** Software Settings ** Digitization Rate (MHz): 12.5 Memory Length (Points): 1024 Pre-Trigger (Number of AE Channels: 2 Number of Parametric Channels: 2 Parametric Reading Information: Display (sec): 60.0 Digitization Rate (sec): 1.00 Gate (V): 0.00</p>	<p>** Software Settings ** Digitization Rate (MHz): 25 Memory Length (Points): 1024 Number of AE Channels: 2 Number of Parametric Channels: 2 Parametric Reading Information: Display (sec): 60.0 Digitization Rate (sec): 1.00 Gate (V): 0.00</p>

A free length of approximately 5 cm was chosen by trial and error. A longer length covers more material so there will be more events to detect. There will also be a greater difference in arrival time for events outside the ‘free length’, thereby affording greater accuracy in filtering those events. However, damping of events must be considered. It was found that when longer free lengths were used smaller events closer to one sensor were barely detectable by the time the acoustic wave reached the far sensor. A 5 cm free length offered a compromise between these factors. Strain gages were placed outside the free length as the strain gage bond system gave off acoustic events at many stress levels. Aluminum/rubber dampers were lightly clamped onto the sample to reduce noise coming from the gripped/tabbed regions. A simple experiment using lead-breaks indicates that these dampers reduce the maximum amplitude of the lead-break by approximately 40%.

Two types of broadband sensors were used during testing. A B1025 sensor, with a face-to-face calibration, as measured by Digital Wave Corporation, shown in Figure 5.4. This sensor offers a wide range of sensitivity up to 1.5 MHz. Most testing of the 90° samples was performed with this sensor. A second sensor, B225 with face-to-face calibration shown in Figure 5.5 was needed to detect cracking in the off-axis samples, as will be discussed in Section 7.2. The B225 has approximately four times the sensitivity of the B1025 up to 500 kHz.

5.3.1 AE Testing of Off-Axis Specimens

Unidirectional off-axis samples have a mix of transverse and shear stress in the primary material directions. Cracking behavior is now more complicated than in the 90° samples as it is now mixed mode. The AE testing also gets

more involved.

First, angled tabs [(Sun and Berreth, 1988), (Bocchieri and Schapery, 2000)] were used to ensure a uniform stress region from which to detect AE events, which we will call 'good events', and to take strain readings as shown in Figure 5.6. Second, the criteria for accepting an AE event as being from the uniformly stressed material needs to be critically examined due to changing wave speed with material direction. As shown in Figure 5.7, if cracking occurs off the centerline of the sample, there is a significant difference in wave propagation direction relative to the fibers. This has a large effect on relative arrival time as shown in Figure 5.8 where the relative arrival time for an event occurring along the top edge, centerline, and bottom edge have been calculated from equation 6.1 for a sensor spacing of 4.7 cm. Lead breaks were performed at the locations indicated in Figure 5.9 prior to running each test to validate sensor spacing.

This complexity can be managed by adopting an acceptance criterion, as shown for a 30° off-axis sample in Figure 5.10, where a relative arrival time of 12 μs is illustrated. A volume represented by the hash-marks indicates the volume from which events are then accepted. A skewed volume has no consequence as long as it is under uniform stress. A final complexity that needs to be considered is the effect on wavespeed from material softening; it will be discussed in Section 7.7.

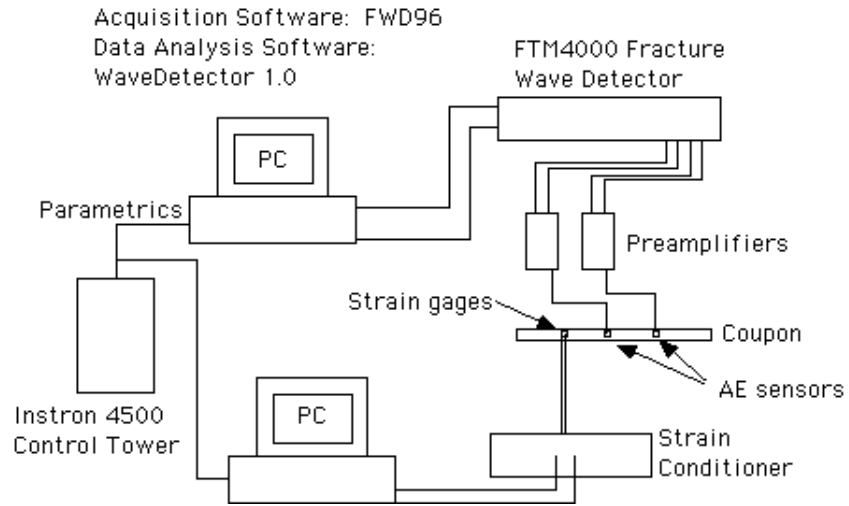


Figure 5.2: Hardware and software used for acoustic emission and stress-strain data acquisition.

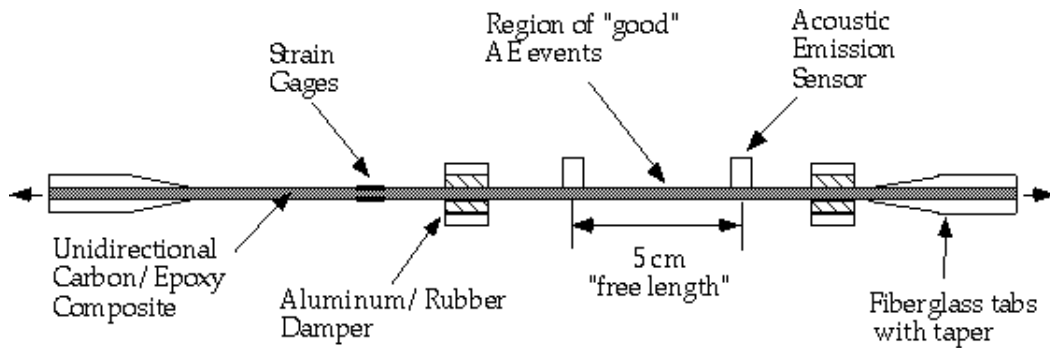


Figure 5.3: Unidirectional coupon with placement of strain gages, acoustic emission sensors and dampers shown.

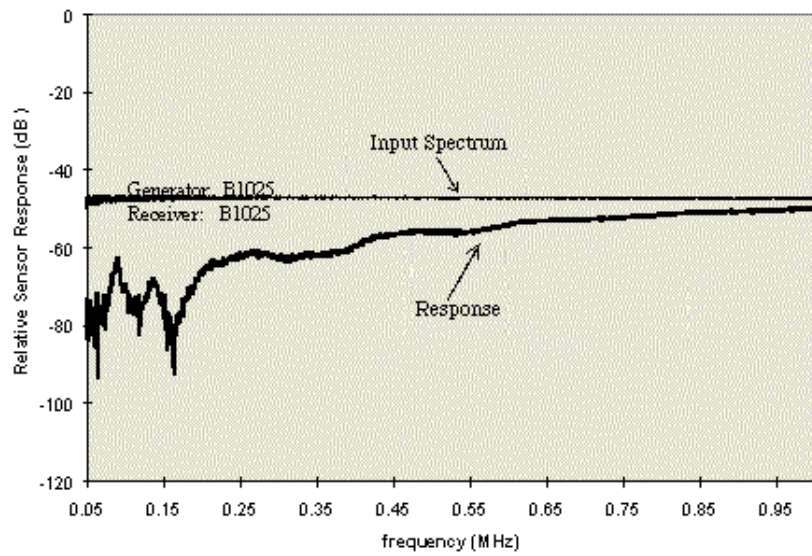


Figure 5.4: Face to face calibration of a Digital Wave Corp. B1025 broadband sensor.

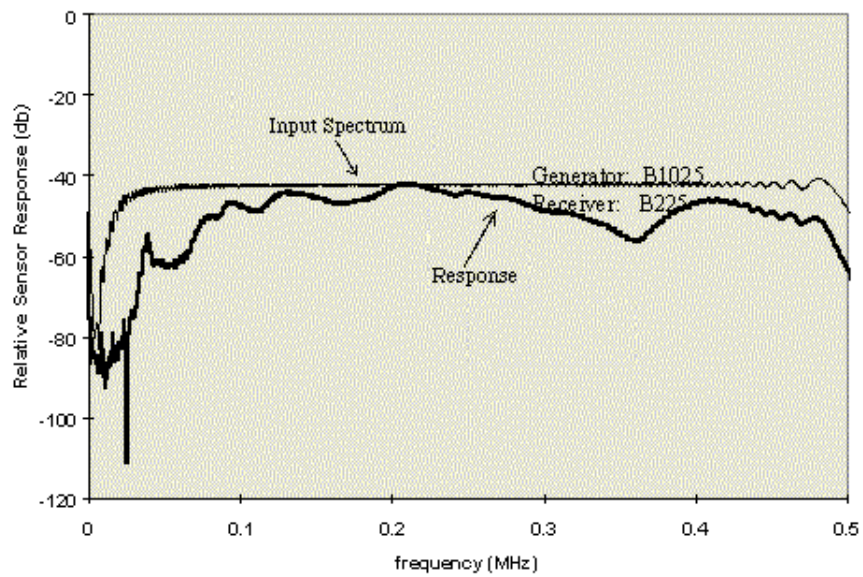


Figure 5.5: Face to face calibration of a Digital Wave Corp. B225 broadband sensor.



Figure 5.6: Stress distribution in a 30° off-axis sample with elastic shear and transverse moduli uniformly degraded to 20% of their original value. Each contour represents a 1% difference from that predicted by stress transformation assuming uniform stress.

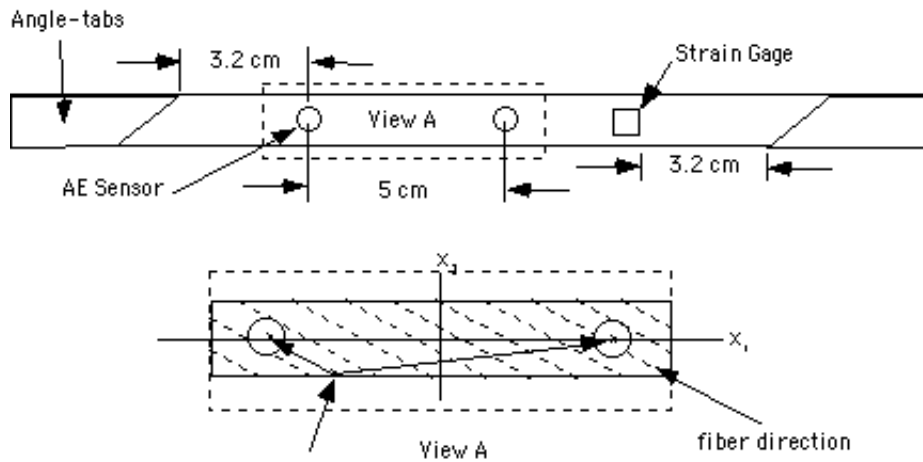


Figure 5.7: Wave Direction.

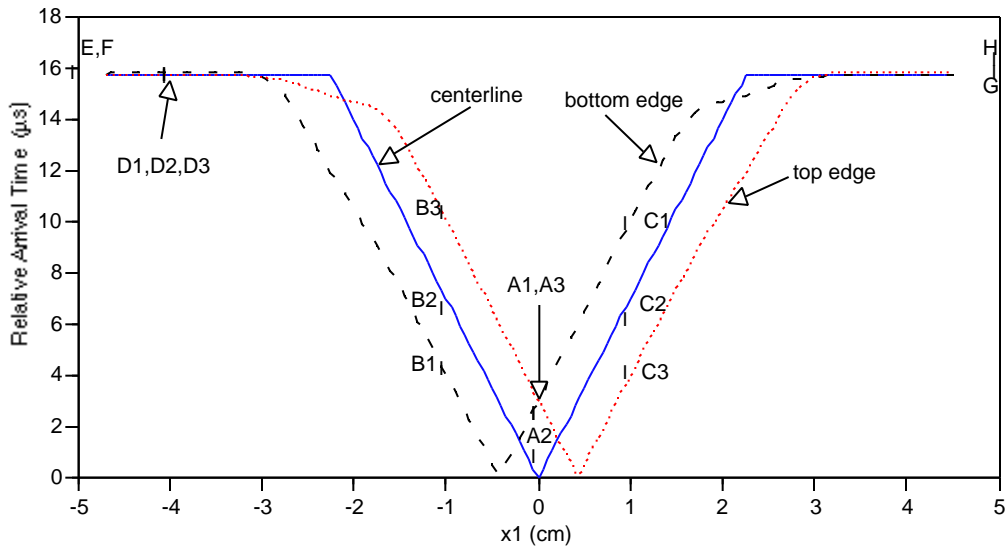


Figure 5.8: Relative arrival times in a 45° off-axis sample. Lead break positions are indicated in Figure 5.9.

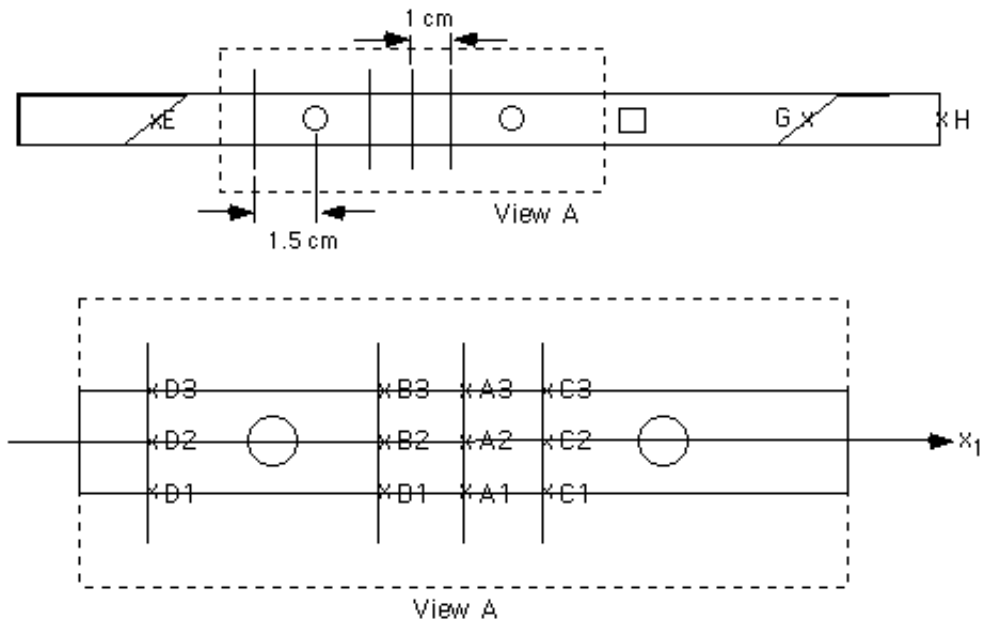


Figure 5.9: Lead break positions on an off-axis sample.

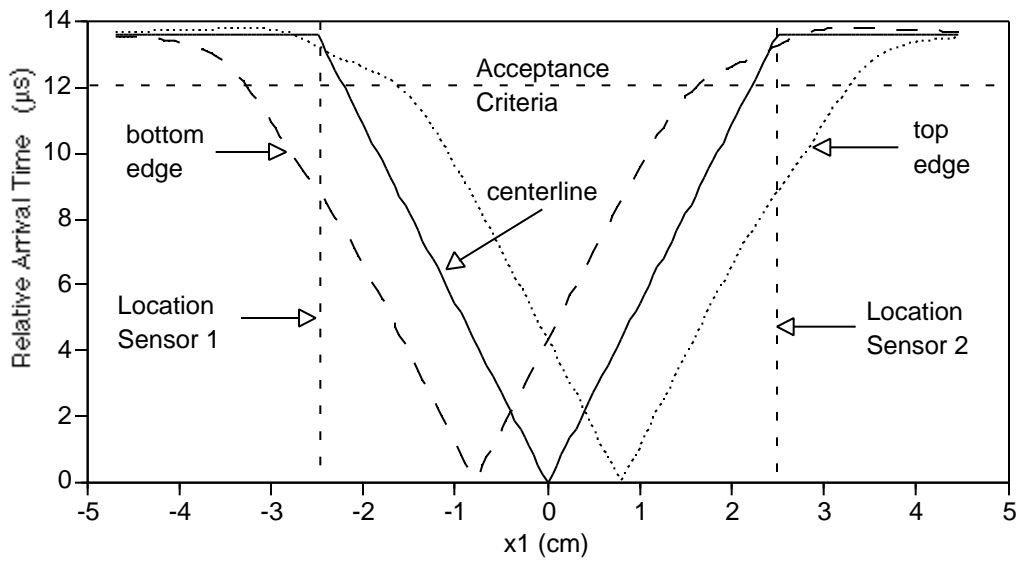


Figure 5.10: Relative arrival times for events occurring at the bottom edge, center, and top edge of a 30° off-axis sample.

Chapter 6

Acoustic Emission Testing

6.1 Microstructural Damage and AE Detection

Microstructural Damage

In all AE testing it is desirable to have a one-to-one correspondence between a visually observed event and its detected acoustic wave. In this way, there is no question about the emission source. This has been done with good accuracy for large scale cracking, such as transverse cracking in cross-ply laminates, where the entire ply fails (Gorman and Ziola, 1991) (Prosser et al., 1995). Here the acoustic signals were used to locate the position of a given crack by modal analysis of the waveform and subsequent wavespeed calculation. These locations correlated well with cracks observed by polar backscatter scans. Our goal is to detect much smaller events that are below the scale where they can be observed by polar backscatter scans, x-radiography or edge-replicate techniques. Monitoring their acoustic emissions is the only

practical way at this time to track distributed cracking real-time.

In an independent study by Wood (1996) on the same carbon/epoxy in this study, it was found that matrix cracking and fiber/matrix debonding were indeed the mechanisms of damage viewed in this material. They developed a special sample geometry for viewing the material under load in an environmental SEM. They found a variety of initial flaws in the material prior to loading, including voids, cracks around voids and fiber/matrix debonds. Figure 6.1 shows glowing debonds in a sample prior to loading. These occur primarily in resin rich regions. During loading, the damage events include formation of new debonds, opening of debonds, cracks in the bottom of voids connecting to debonds and the coalescing of debonds. Some examples are shown in Figures 6.2 and 6.3. Damage first initiates at the boundaries of resin rich regions but also initiates in other regions at higher stress.

Figure 6.1: Glowing debonds in a sample prior to loading. Image borrowed with permission from Wood (1996)

Other possible dynamic damage not observable by this method is the cavitation of rubber particles and the subsequent shear yielding around these

Figure 6.2: Crack in the bottom of a void which has grown to neighboring debonds while under load. Image borrowed with permission from Wood (1996)

Figure 6.3: Coalesced debonds while under load. Image borrowed with permission from Wood (1996)

particles. Imaging of rubber particles in polymer matrices has only been accomplished in pure resins or composites with very low fiber volume fractions by use of a TEM (Tunneling Electron Microscope) [e.g. (Laura et al., 2000)]. Successful sample preparation for use in the TEM has not yet been accomplished for composites with high volume fractions.

Detection of Microcracking and Debond with AE Sensors

Several steps were taken to ensure that only the damage mechanisms seen by Wood (1996) were detected by the AE sensors. First, events were only accepted from the free-length of the material by locating the event source using two sensors. Second, by using simple unidirectional samples, we have limited the number of types of damage to those mentioned. By testing in the 90° and off-axis directions the possibility of significant fiber breakage is eliminated. Frictional sliding may also produce acoustic emissions (Awerbuch et al., 1985) and will occur repeatedly whenever the material is loaded and unloaded.

Loading/unloading cycles were performed on 90° and 30° off-axis samples to see if the detected events are indicative of friction. As shown in Figures 6.4 and 6.5, the detected events do not display this pattern. Few events are detected during unloading and the ones that are detected occur predominantly close to the highest stress attained. Upon reloading, few are detected until the previous stress is approached.

There is further supporting evidence that the acoustic waves detected originate from microcracking. First, as shown in Figure 7.36 the onset of nonlinearity in the 90° samples coincides very well with significant AE events in these samples. In addition, on average the waveforms detected all have

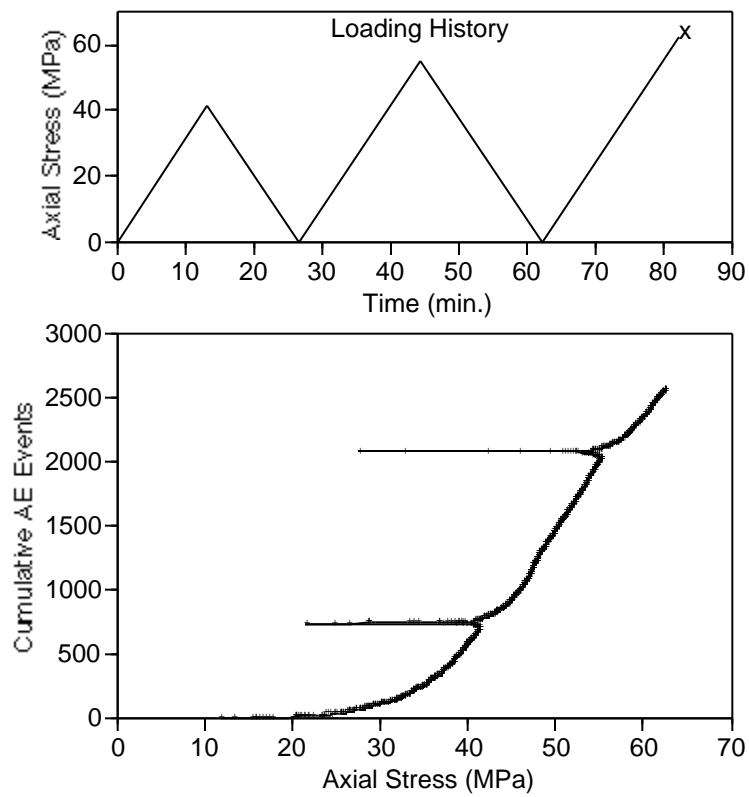


Figure 6.4: Cumulative events detected in a 90° unidirectional sample during loading/unloading and reloading cycles. The loading history is shown in the top figure.

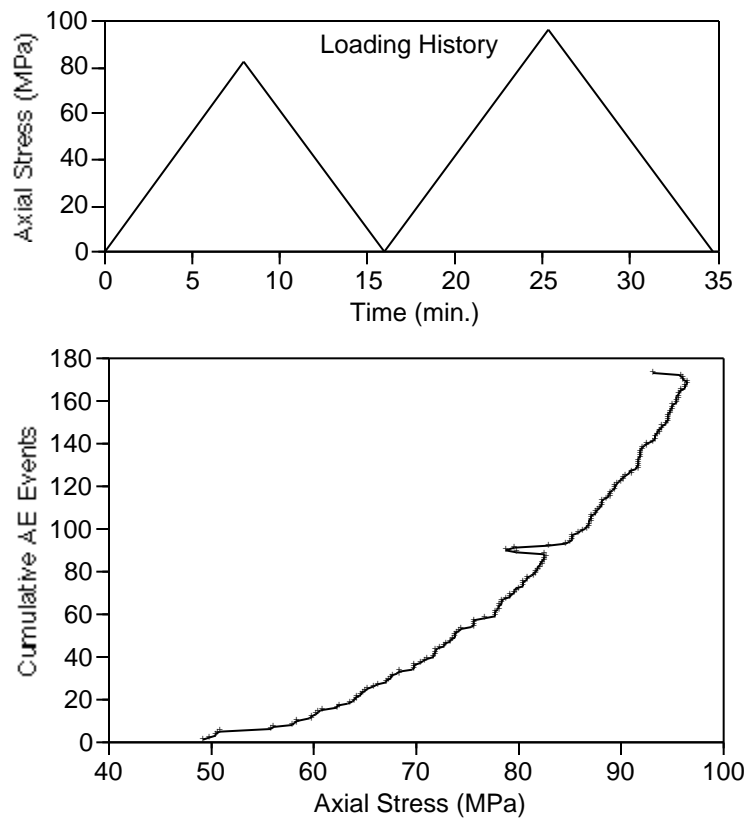


Figure 6.5: Cumulative events detected in a 30° off-axis sample during loading/unloading and reloading cycles. The loading history is shown in the top figure.

similar frequency and energy content indicating that the same type of phenomenon is detected throughout the test.

6.2 Anticipated Waveforms

In designing a modal acoustic emission (MAE) experiment, one should first determine which waveforms will be detectable in the structure tested. Then the test-setup and analysis can be tailored accordingly. As already mentioned, the two types of detectable damage expected in unidirectional material are microcracking and fiber-matrix debond. Acoustic emissions from rubber particle cavitation are not expected to be of sufficient strength to be detectable. If a sufficiently thin sample is used, it is anticipated that both damage forms will create a waveform which is a combination of extensional and flexural plate waves. Gorman and Ziola (1991) found this to be the case for transverse matrix cracking in cross-ply laminates.

Samples were chosen to ensure that plate waves were detected from the anticipated damage modes. For this to hold true, the thickness of the sample must be of the order or less than the wavelength of the emitted waves (CARP, 1993). This can be checked by first calculating the speed of the extensional mode, which is independent of frequency, and is given by (Gorman and Ziola, 1991)

$$C_e = \left(\frac{A_{xx}}{\rho h} \right)^{\frac{1}{2}} \quad (6.1)$$

where A_{xx} is the first component of the laminate force-strain stiffness matrix, as given by lamination theory [e.g. (Daniel and Ishai, 1994)]. The ρ is density and h is laminate thickness. Speed of the flexural mode is given by

$$C_f = \left(\frac{D_{xx}}{\rho h} \right)^{\frac{1}{4}} \omega^{\frac{1}{2}} \quad (6.2)$$

where D_{xx} is the first component of the moment-strain stiffness matrix and ω is the frequency. These velocities have been plotted versus fiber direction for the material under study in Figure 6.6.

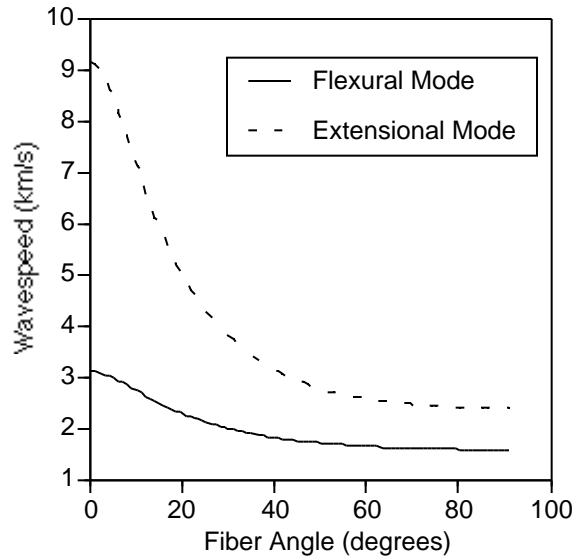


Figure 6.6: Wavespeed as a function of angle relative to the fiber direction for AS4C/E719LT.

Wavelength is $\lambda = c/f$ where c is the wavespeed and f is the frequency. As wavespeed is lowest in the 90° samples, it imposes the most stringent condition on testing (as waves will be traveling at all angles relative to the fibers). It is expected that microcracking and debonding will create a predominantly extensional wave which always travels faster than the flexural mode and has minimal dispersion below 1MHz. This mode will therefore be used for location finding and also used for the calculation of wavelength. As will be shown in the results, a predominant amount of wave energy detected in this material has frequencies from approximately 100 to 400 kHz. Wavespeed was calculated to be approximately 2450 m/s corresponding to a wavelength of

6.1 mm (for 400kHz). Thin 6-ply coupons, 1.65 mm thick, were used for all MAE testing so predominantly plate waves were detected.

6.3 Waveform Filtering

6.3.1 Digital Filtering

Digital filtering of the captured waveforms was based on background noise, response of a given sensor, and frequency range of the detected events. Figure 6.7 shows the FFT (Fast Fourier Transform) of noise from the B1025 and B225 sensors in the testing environment. Notice that a predominant amount of the energy in these signals is below 200 kHz. The B1025 and B225 sensors have good response above approximately 150 kHz and 30 kHz respectively. These frequencies were therefore used for the digital high pass filtering of events.

6.3.2 Filtering by location

Two sensors were used so that events coming from the ‘free length’ of a sample were discernible from those coming from other sources. Thousands of events were typically detected during a test so it was not feasible to use more accurate location techniques such as manual phase matching. An initial threshold crossing criterion just outside of the noise amplitude was used to calculate arrival time. In this way, the non-dispersive extensional wave is used for location finding. As we are only concerned with whether an event came from the free length, but not finding its exact location, this technique should be sufficient and expedient. To be conservative about only accepting events from the free length, any locations found within 5 mm of a sensor

were not accepted. If an event was only detected on one sensor it was also discarded. After all events were filtered by the aforementioned techniques and reduced to a more manageable number, they were visually inspected for events that may have slipped through due to spikes in noise, etc.. A typical histogram of locations in the free length of a 90° sample are shown in Figure 6.8, indicating that cracking is evenly distributed along the length and not isolated to specific regions of the material, as expected.

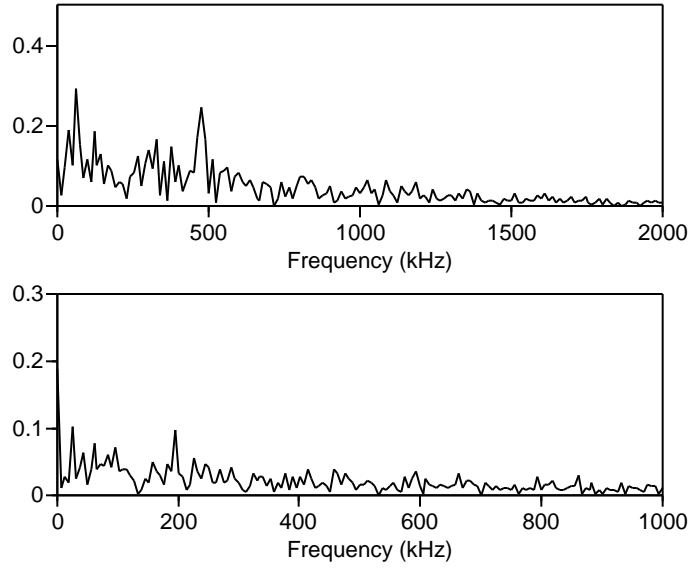


Figure 6.7: Background noise detected by the B1025 and B225 sensors in the laboratory working environment.

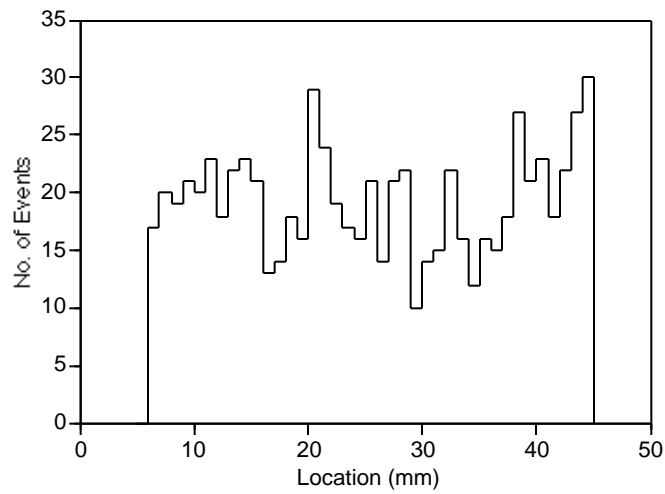


Figure 6.8: Histogram of cracking in the free length of a 90° sample.

Chapter 7

Acoustic Emission Results and Analysis

7.1 Waveform Analysis

Significant cracking, evenly distributed along the length of 90° and off-axis samples, was detected with the AE sensors. It is interesting to note that such cracking was not detected with the same testing apparatus in two untoughened, more brittle material systems T1000/8852 (carbon/epoxy) and S2/8852 (glass/epoxy) when tested in both the 90° and off-axis directions. The only events acquired came from the region of failure just prior to specimen failure.

Following is a review of the waveforms detected at the locating sensors from the primary material under study, AS4C/E719LT. Careful examination of the waveforms emitted from the microcracking was necessary to validate that the anticipated modes were indeed detected, to explore their frequency content, confirm calculations of wavespeed, and to tailor the experiment on the effects of material softening on material acoustical properties.

7.1.1 Waveforms detected at location sensors

Waveforms detected in 90° Samples - B1025 Sensors

Unidirectional 90° coupons were first tested with broadband B1025 sensors. These sensors offered sensitivity to the widest range of frequencies. A wide range of amplitudes and frequency content was observed in the waveforms emitted by cracking in the composite. This is due to variations in arrested crack size and where a given crack fails relative to the sensors. Distance to the sensors has a strong effect due to strong attenuation in this polymeric material. Figures 7.1 through 7.3 show some typical waveforms detected in 90° samples.

The frequency distribution in the detected waveforms were viewed by taking the FFT (Fast Fourier Transform). To eliminate background noise and wave reflections, the TCOT feature of the Wavedetector software was used. This feature windows on a particular time interval as shown in Figures 7.4 through 7.6. Here a $15\mu\text{s}$ window was used on the same events shown in Figures 7.1 through 7.3. Their frequency distributions are shown in Figures 7.7 through 7.9.

The large event shown in Figure 7.1, which occurred close to sensor 1, demonstrates the extent to which higher frequencies are attenuated relative to lower frequencies in this material. The frequency content in channel 1, shown in Figure 7.7 contains components up to 1500 kHz. After traveling a larger distance to sensor 2, only frequencies below 500kHz are detected. Neither channel shows these higher frequencies when the event is from the center of the free length, as is the case for events shown in Figures 7.2 and 7.3. These events show very similar frequency content despite being of very different magnitude. Although frequency content may not be a clear criterion

for differentiating damage types at this time, the lack of a difference provides no reason to assume there is any difference in cracking.

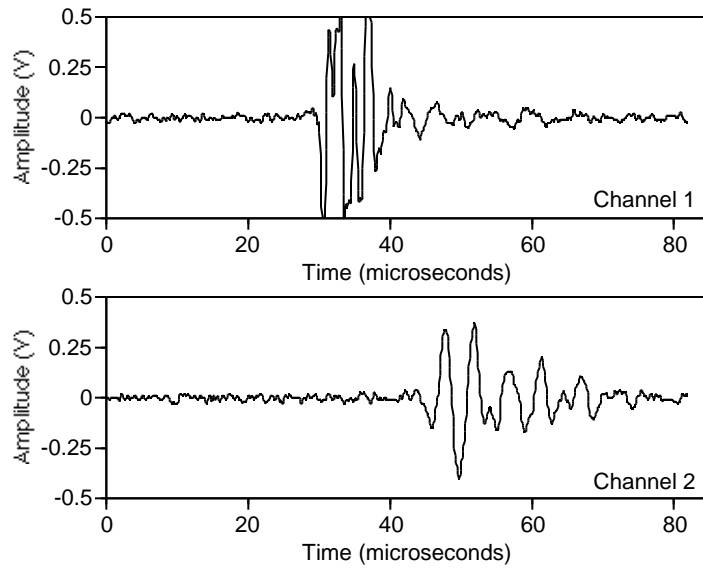


Figure 7.1: Typical large event detected from a 90° sample where cracking occurred close to sensor 1. B1025 sensors were used (1V=47db).

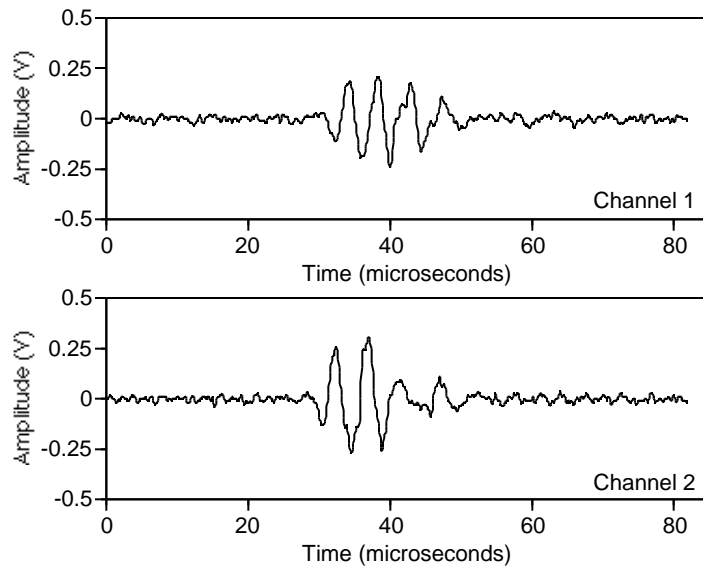


Figure 7.2: Typical large event detected from a 90° sample where cracking occurred close to the center of the free length. B1025 sensors were used (1V=47db).

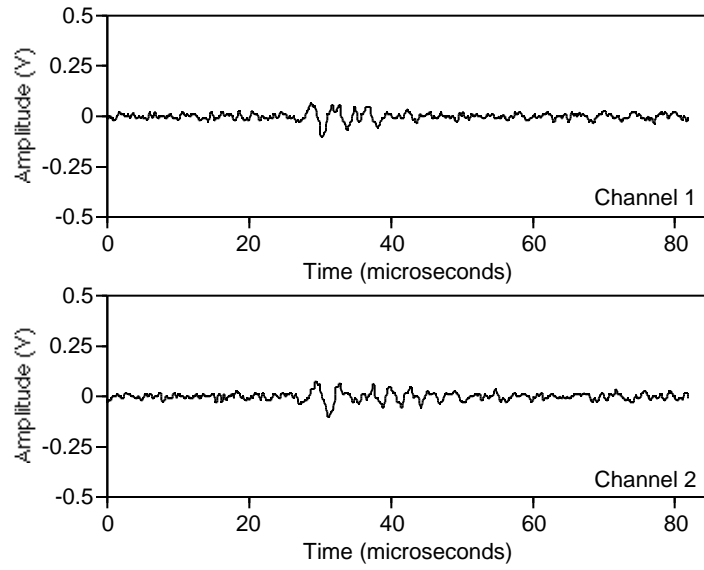


Figure 7.3: Typical small event detected from a 90° sample where cracking occurred close to the center of the free length between sensors. B1025 sensors were used (1V=47db).

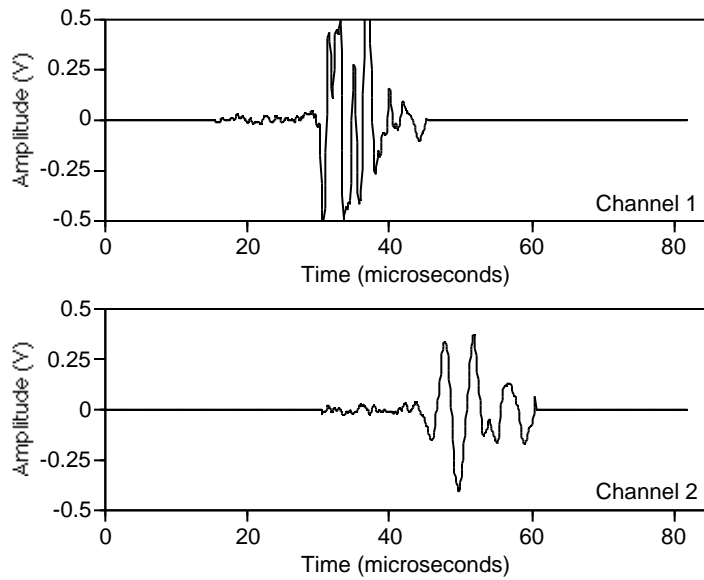


Figure 7.4: Windowed waveform (TCOT=15 μ s) of the event shown in Figure 7.1

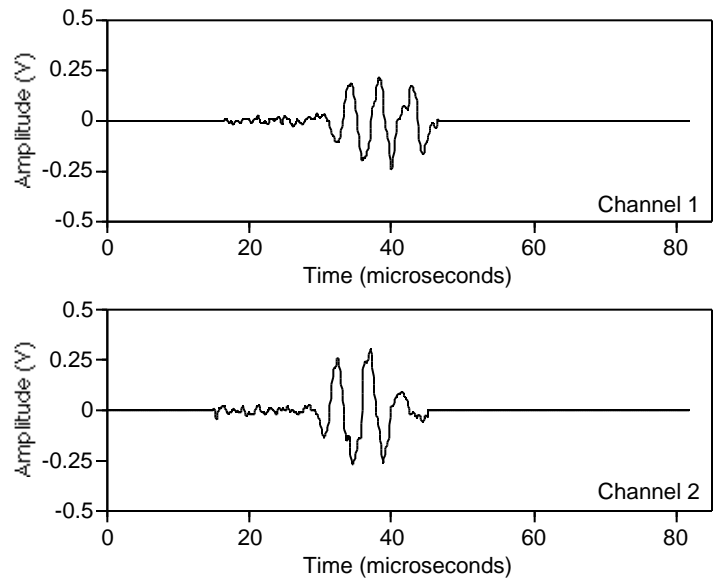


Figure 7.5: Windowed waveform (TCOT= $15\mu s$) of the event shown in Figure 7.2

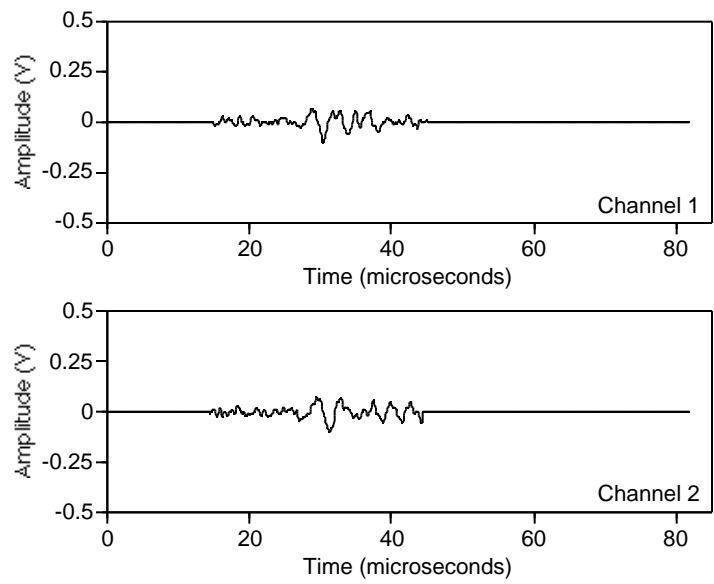


Figure 7.6: Windowed waveform (TCOT= $15\mu s$) of the event shown in Figure 7.3

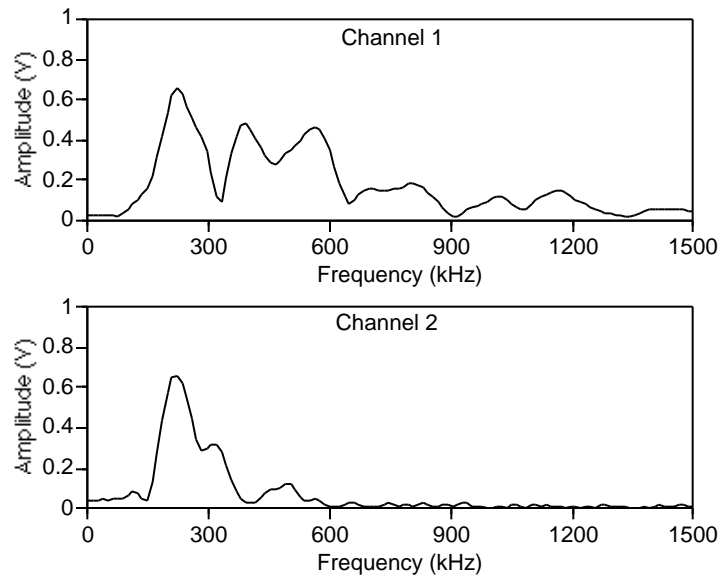


Figure 7.7: Frequency distribution of the event shown in Figure 7.4

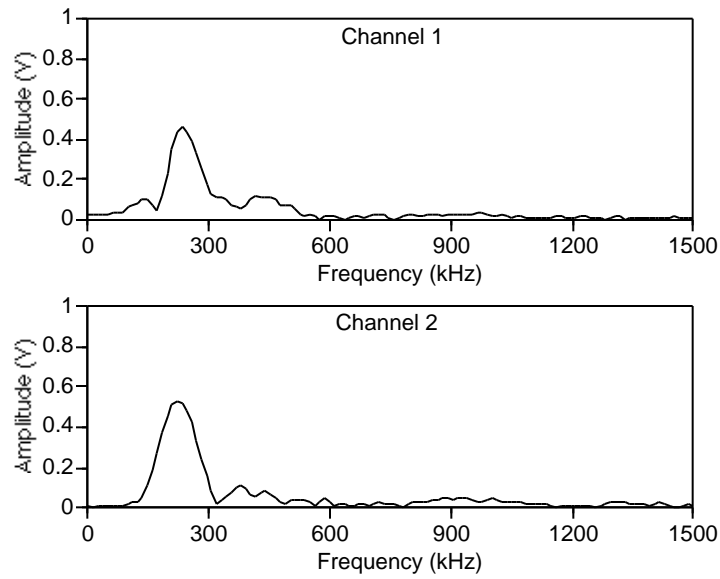


Figure 7.8: Frequency distribution of the event shown in Figure 7.5

Waveforms detected in 90° Samples - B225 Sensors

The B225 sensors were also used in testing of 90° samples. Due to their greater sensitivity and difference in frequency response, waveforms detected with these sensors were also evaluated and compared to those from the B1025 sensors. Some examples of the variety of events detected are shown in Figures 7.10 to 7.18. Once again, the waveforms display frequency content primarily between 100 and 400 kHz. No significant differences were observed from those detected with the B225 sensors.

Waveforms detected in 30° Samples - B225 Sensors

Following are some examples of waveforms detected from 30° off-axis samples with B225 sensors. It is not appropriate to compare these events with those detected from the 90° samples due to differences in attenuation with fiber direction. However, in comparing them amongst themselves, all the same conclusions drawn for the 90° samples apply here. Notice, however, that a window of 25 μs has been used to perform the frequency analysis. Also, the energy content goes to slightly lower frequencies than in those detected in the 90° samples.

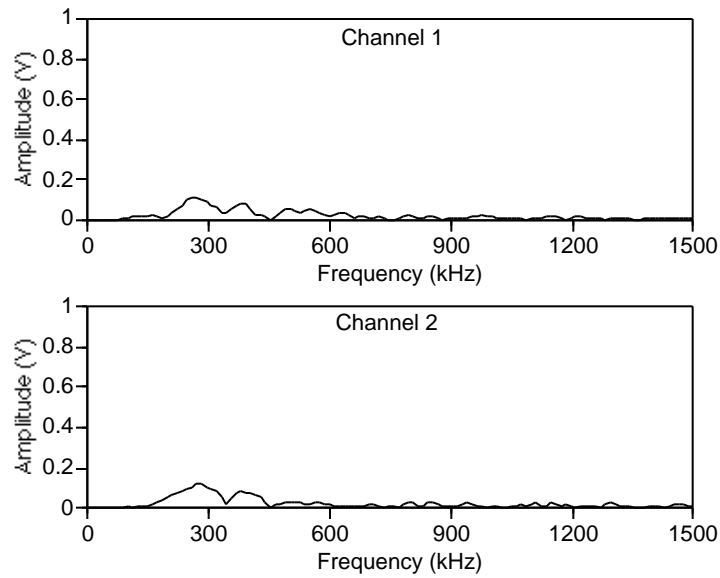


Figure 7.9: Frequency distribution of the event shown in Figure 7.6

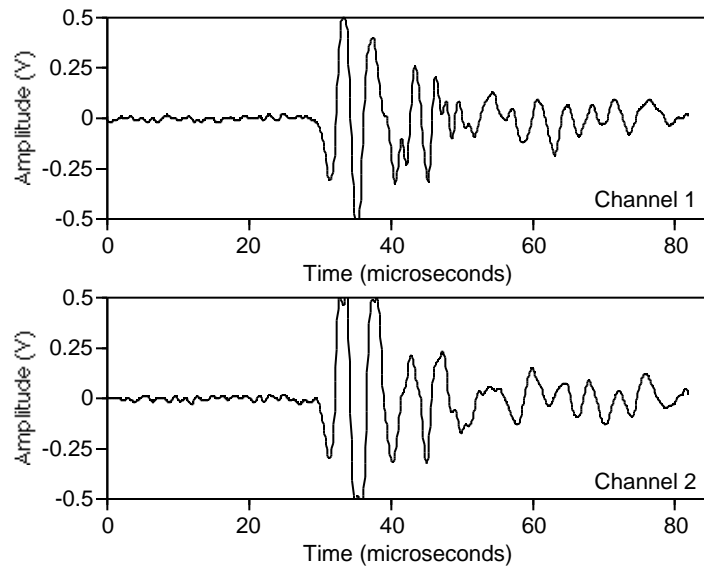


Figure 7.10: Typical large event detected from a 90° sample where cracking occurred close to the center of the free length. B225 sensors were used ($1V=50\text{db}$).

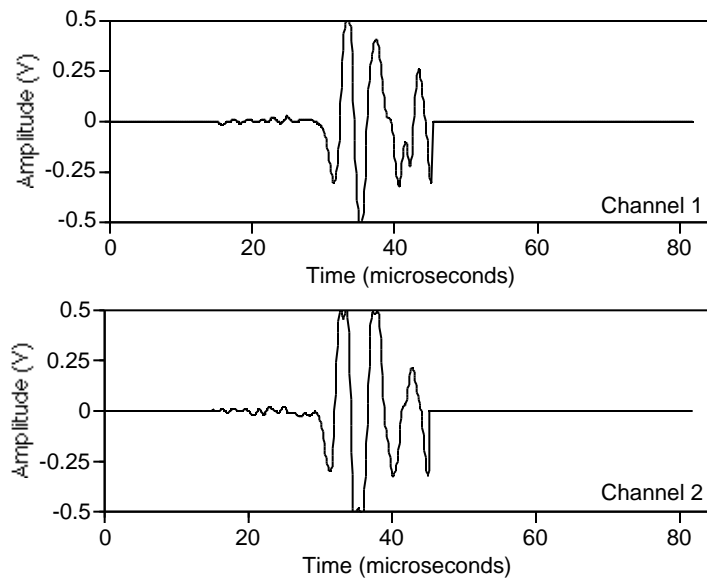


Figure 7.11: Windowed waveform ($TCOT=15\mu s$) of the event shown in Figure 7.10

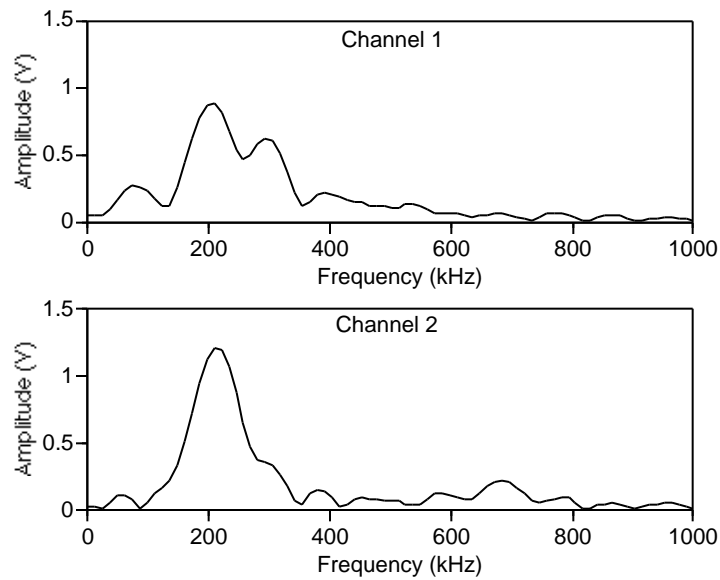


Figure 7.12: Frequency distribution of the event shown in Figure 7.11

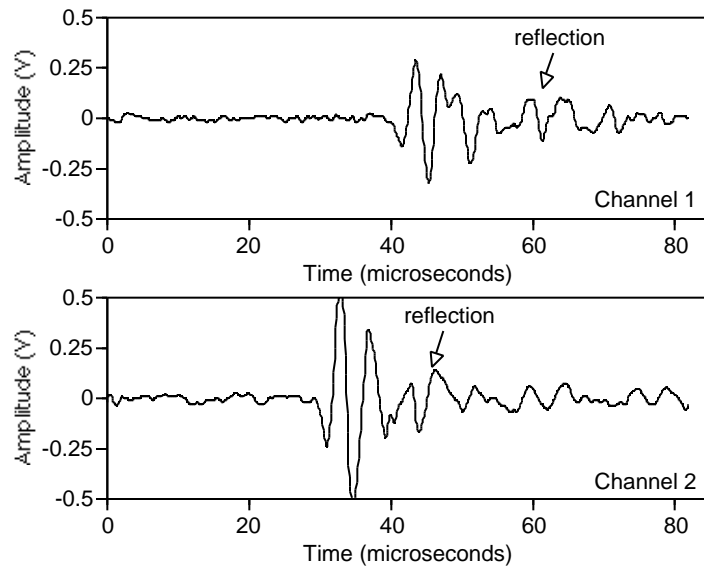


Figure 7.13: Typical large event detected from a 90° sample where cracking occurred close to sensor 2. B225 sensors were used ($1V=50db$).

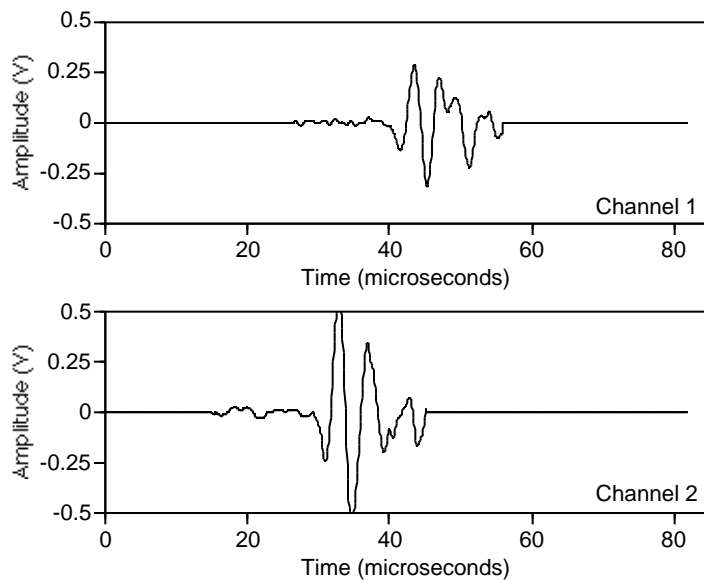


Figure 7.14: Windowed waveform ($TCOT=15\mu s$) of the event shown in Figure 7.13

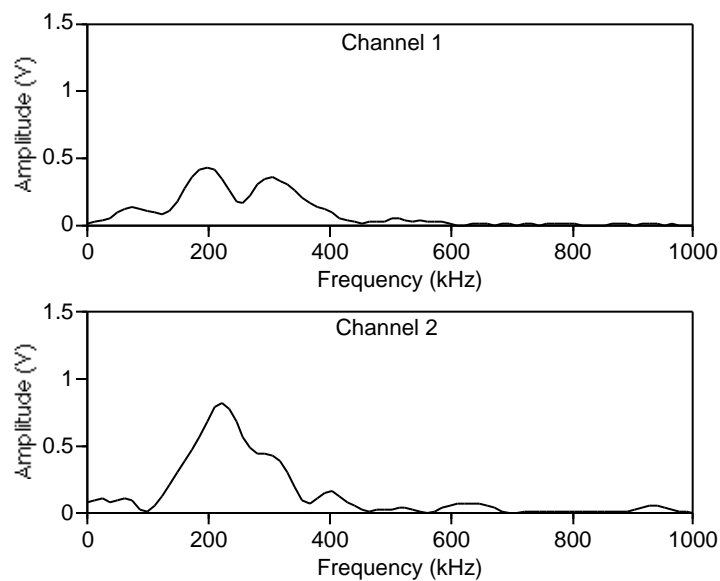


Figure 7.15: Frequency distribution of the event shown in Figure 7.14

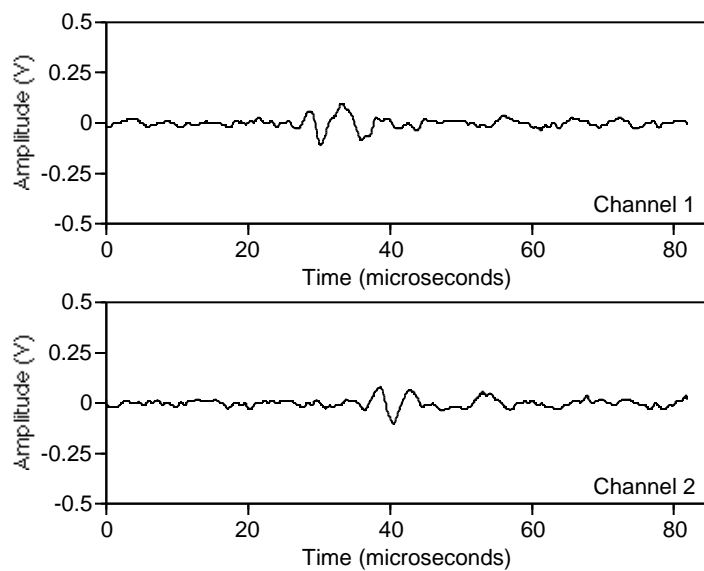


Figure 7.16: Typical small event detected from a 90° sample. B225 sensors were used (1V=50db).

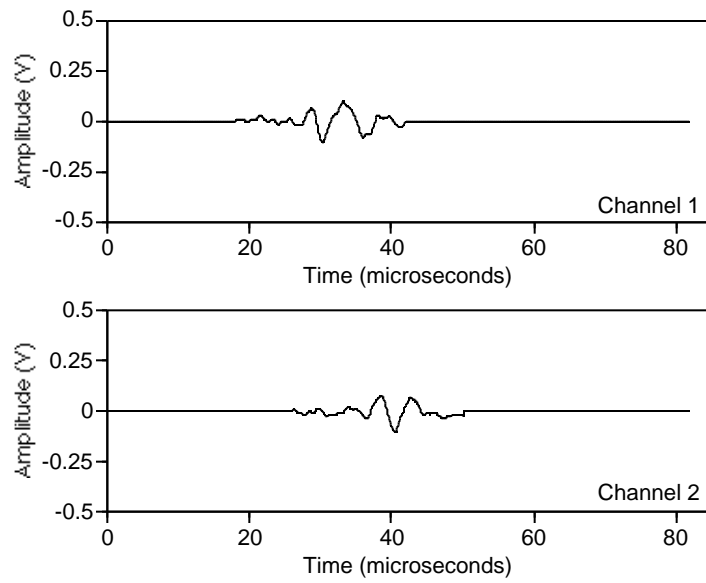


Figure 7.17: Windowed waveform ($TCOT=15\mu s$) of the event shown in Figure 7.16

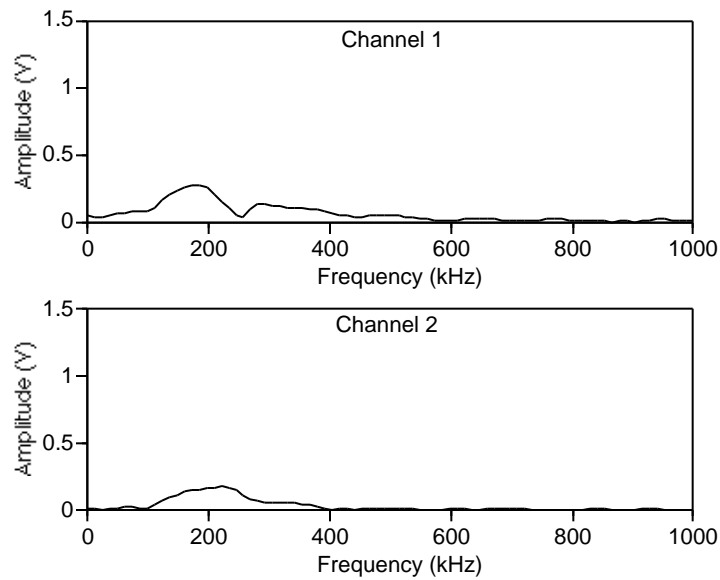


Figure 7.18: Frequency distribution of the event shown in Figure 7.17

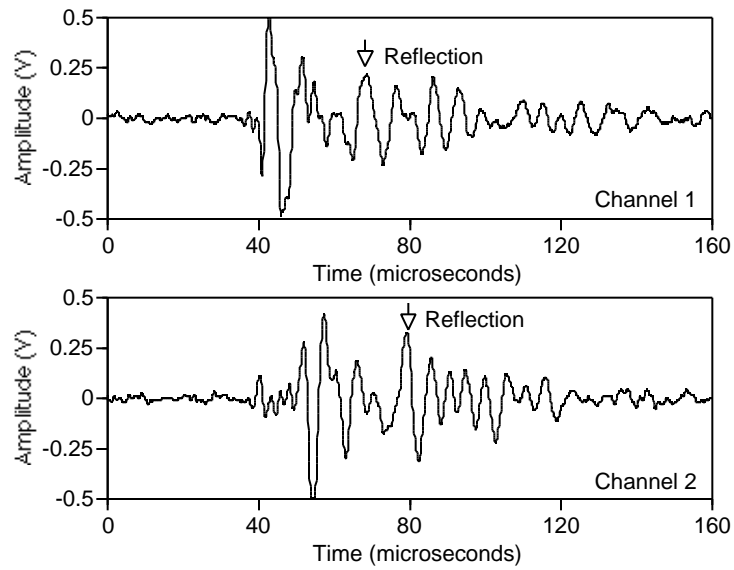


Figure 7.19: Typical large event detected from a 30° sample. B225 sensors were used (1V=50db).

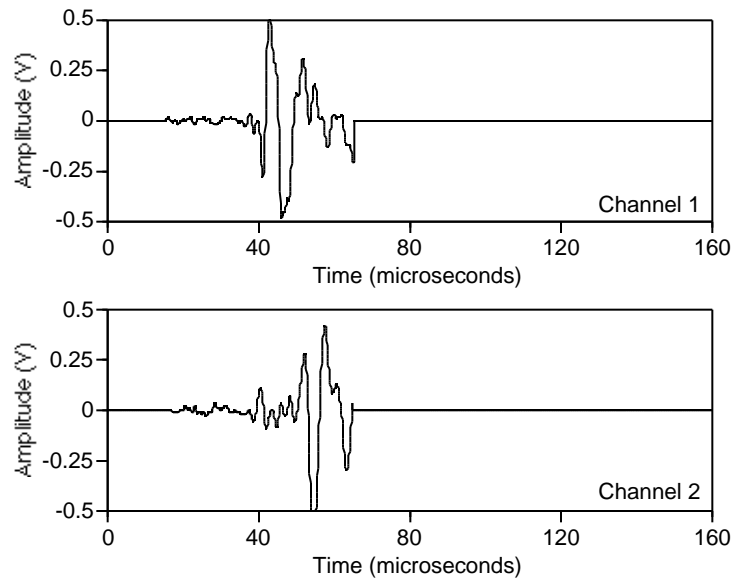


Figure 7.20: Windowed waveform (TCOT=25 μ s) of the event shown in Figure 7.19.

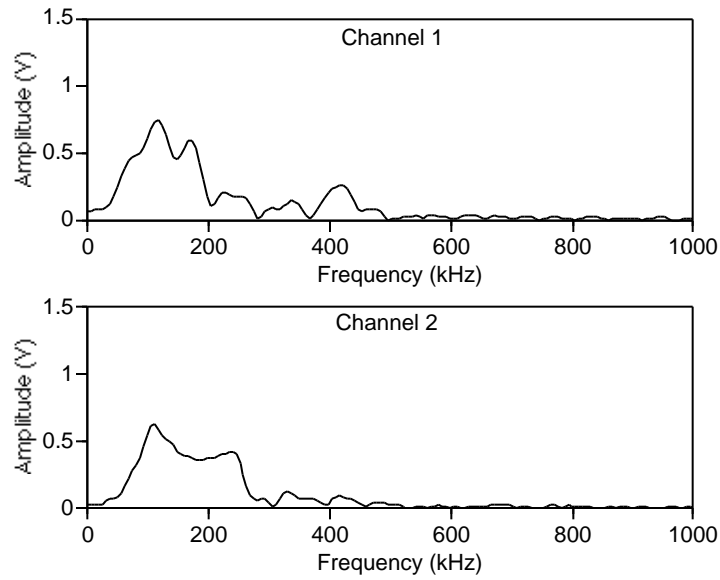


Figure 7.21: Frequency distribution of the event shown in Figure 7.20

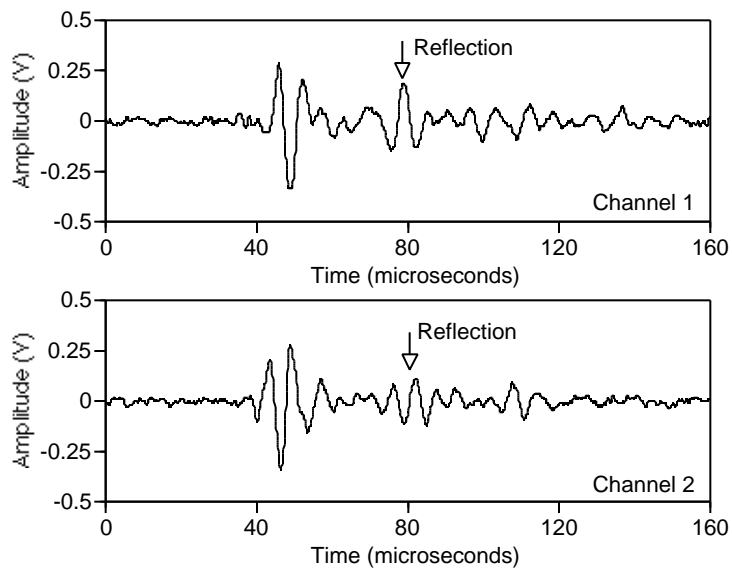


Figure 7.22: Typical moderate event detected from a 30° sample. B225 sensors were used (1V=50db).

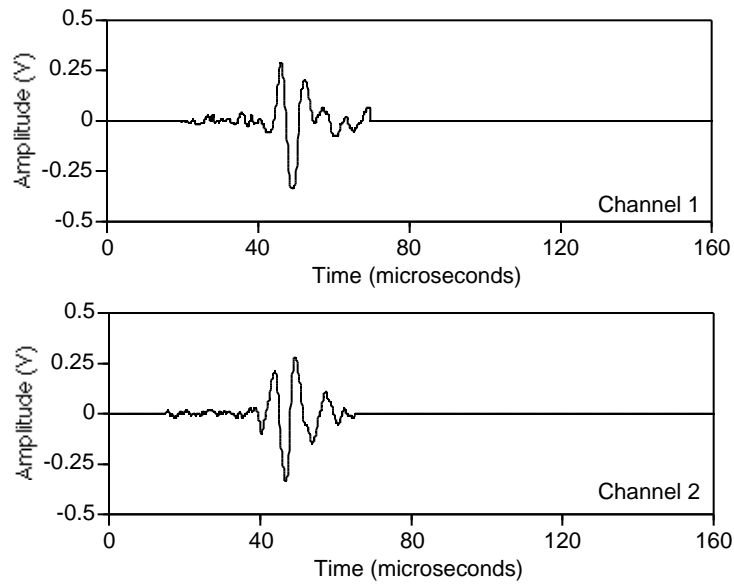


Figure 7.23: Windowed waveform ($TCOT=25\mu s$) of the event shown in Figure 7.22.

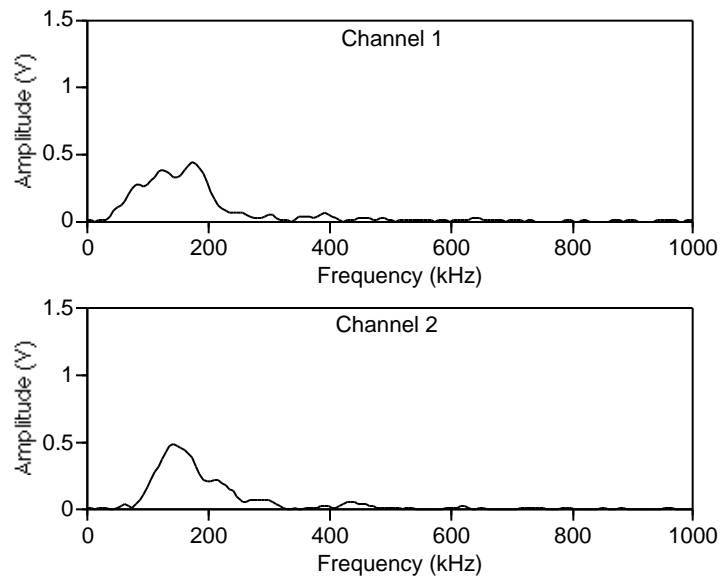


Figure 7.24: Frequency distribution of the event shown in Figure 7.23

Waveforms detected in 45° Samples - B225 Sensors

Following are some examples of waveforms detected from 45° off-axis samples with B225 sensors. Once again, comparing these events amongst themselves, all the same conclusions drawn for the 90° and 45° samples apply here. Notice, just as in the 30° samples, a window of 25 μs has been used to perform the frequency analysis. Also, the energy content goes to slightly lower frequencies than in those detected in the 90° samples.

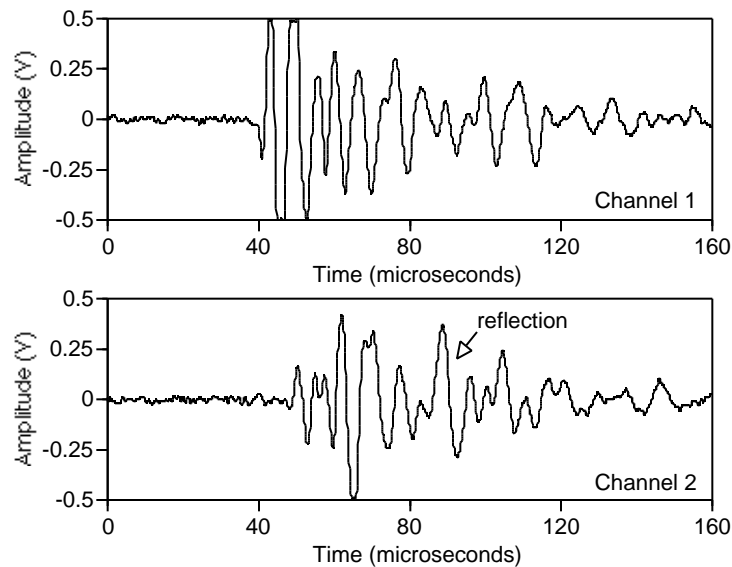


Figure 7.25: Typical large event detected from a 45° sample. B225 sensors were used (1V=50db).

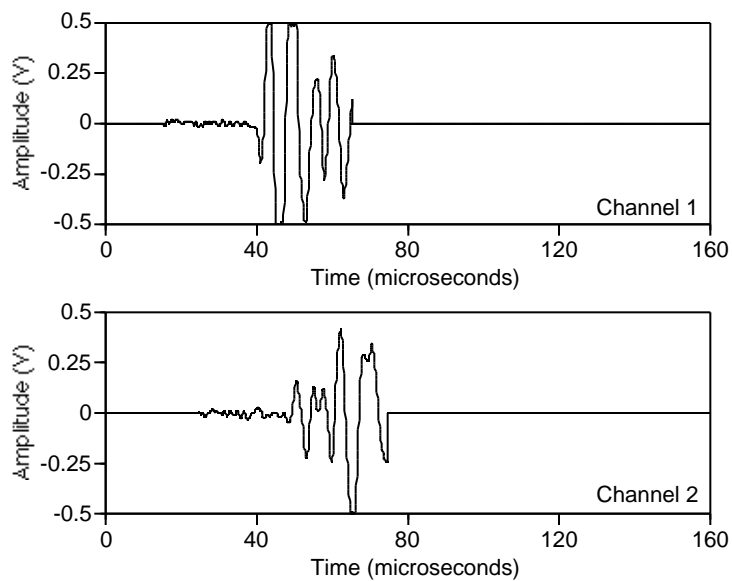


Figure 7.26: Windowed waveform ($TCOT=25\mu s$) of the event shown in Figure 7.25.

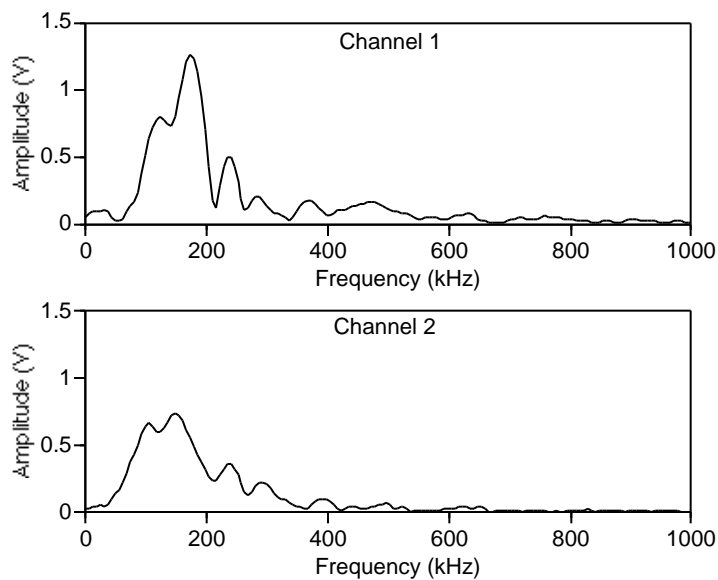


Figure 7.27: Frequency distribution of the event shown in Figure 7.26

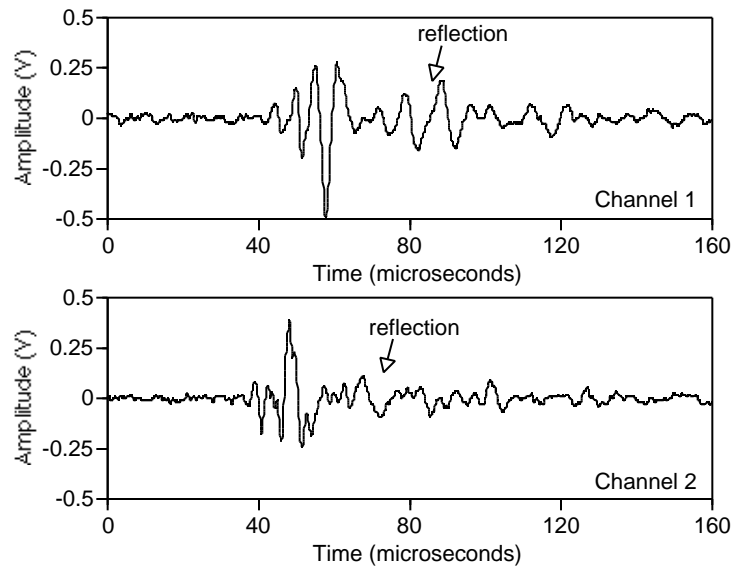


Figure 7.28: Typical moderate event detected from a 45° sample. B225 sensors were used ($1V=50\text{db}$).

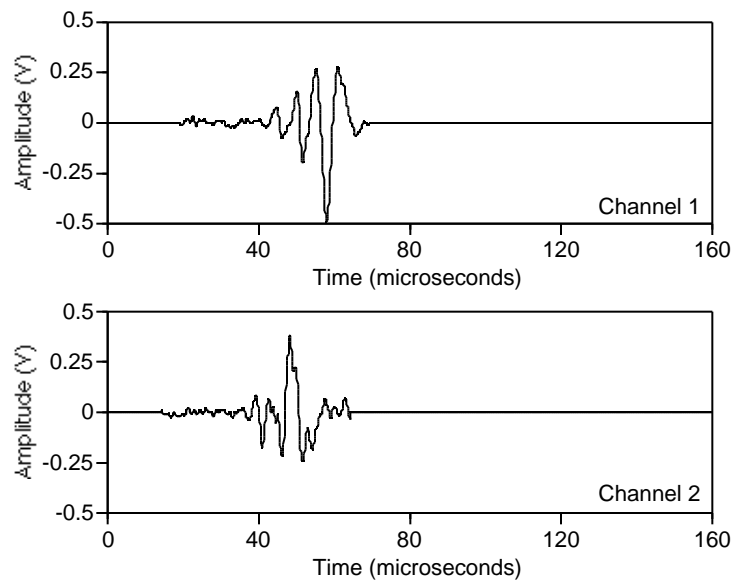


Figure 7.29: Windowed waveform ($\text{TCOT}=25\mu\text{s}$) of the event shown in Figure 7.28.

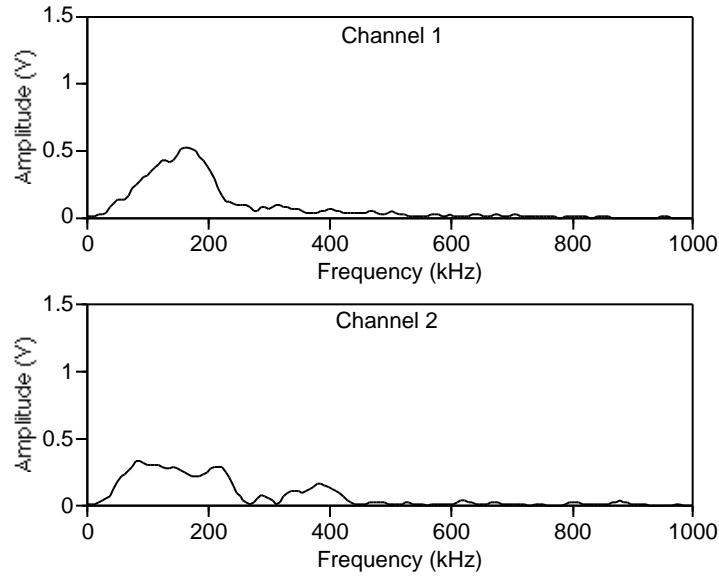


Figure 7.30: Frequency distribution of the event shown in Figure 7.29

7.1.2 Extensional and Flexural Waveforms

Comparison of microcracking waveforms from different sample types can be made for events occurring directly beneath a sensor. In this way, differences in attenuation with direction and distance are eliminated. The sensor setup shown in Figure 7.31 was used for this purpose. Two B225 sensors supply the location of a given event as done in previous testing. The adjacent B1025 sensors were used to evaluate waveforms occurring directly beneath them. By suggestion of Dr. Michael Gorman of Digital Wave Corporation, they were placed on opposite sides of the sample so that the extensional and flexural components of the waveform could be discriminated. An extensional waveform is symmetric, with equal displacement on the top and bottom of the sample. A flexural waveform is asymmetric. By adding and subtracting the signals from both sensors, the extensional and flexural components may be

extracted. Testing of this nature was performed on both 90° and 30° off-axis samples.

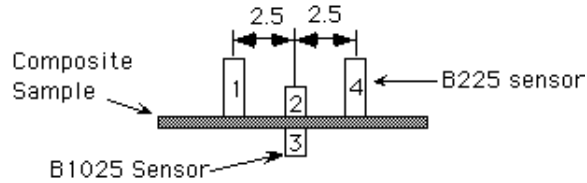


Figure 7.31: Four sensor setup. Two B225 sensors (1 & 4) are used for location. The B1025 sensors (2 & 3) are used to evaluate waveforms. Units in cm.

Figures 7.32 and 7.33 are two examples of waveforms detected in a 90° sample. Figures 7.34 and 7.35 are from a 30° off-axis sample. Variation from event to event makes a comparison of waveforms in both samples difficult. However, there are some similarities. Signal duration of the extensional mode is approximately $5 \mu\epsilon$. The extensional mode is also of greater magnitude than the flexural mode and has similar shape in both samples. Both modes display frequencies covering the entire range of the broadband sensors used. Based on these observations, there is no evidence of a difference between the microcracking in 90° and 30° off-axis samples. It may be that any differences do not display different acoustic signatures, or that a large number of events need to be observed for those differences to become evident. Based on the evidence at hand, events from both samples will be treated in a similar fashion as outlined in Section 7.6.

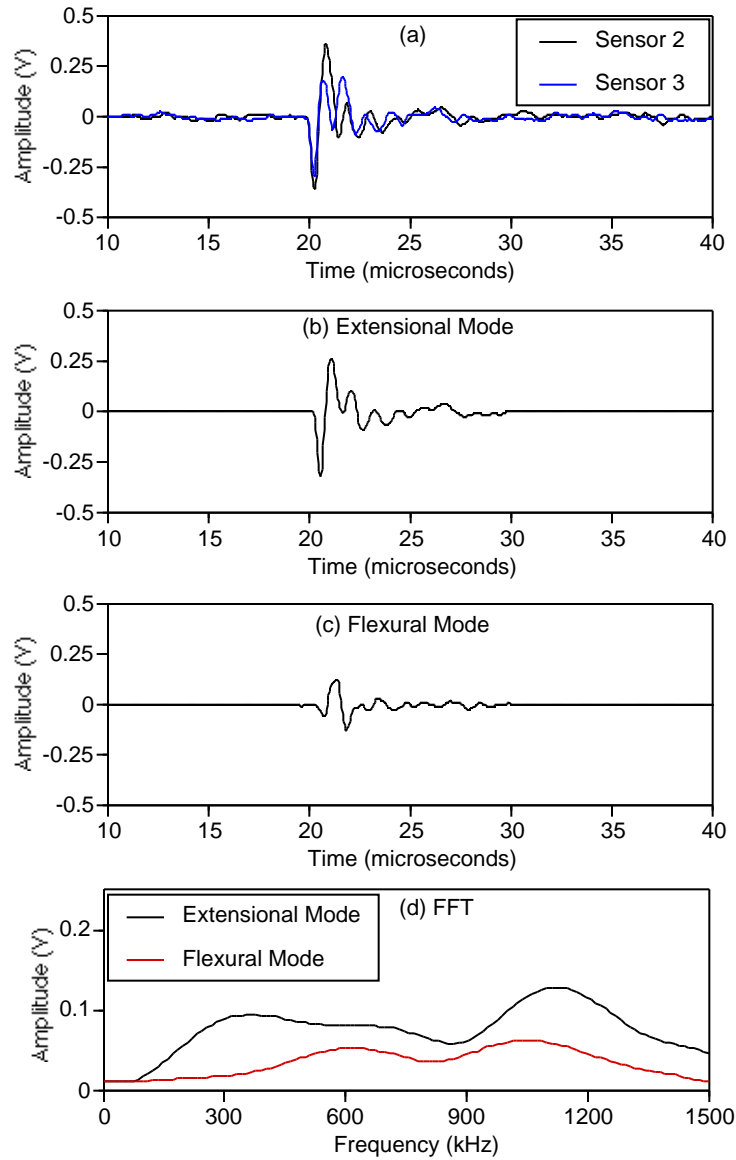


Figure 7.32: (a) Waveforms detected directly beneath sensors 2 and 3 in a 90° sample. (b) Extensional and (c) flexural components of the waveform in (a). (c) FFT of the extensional and flexural components. (1V=47 dB)

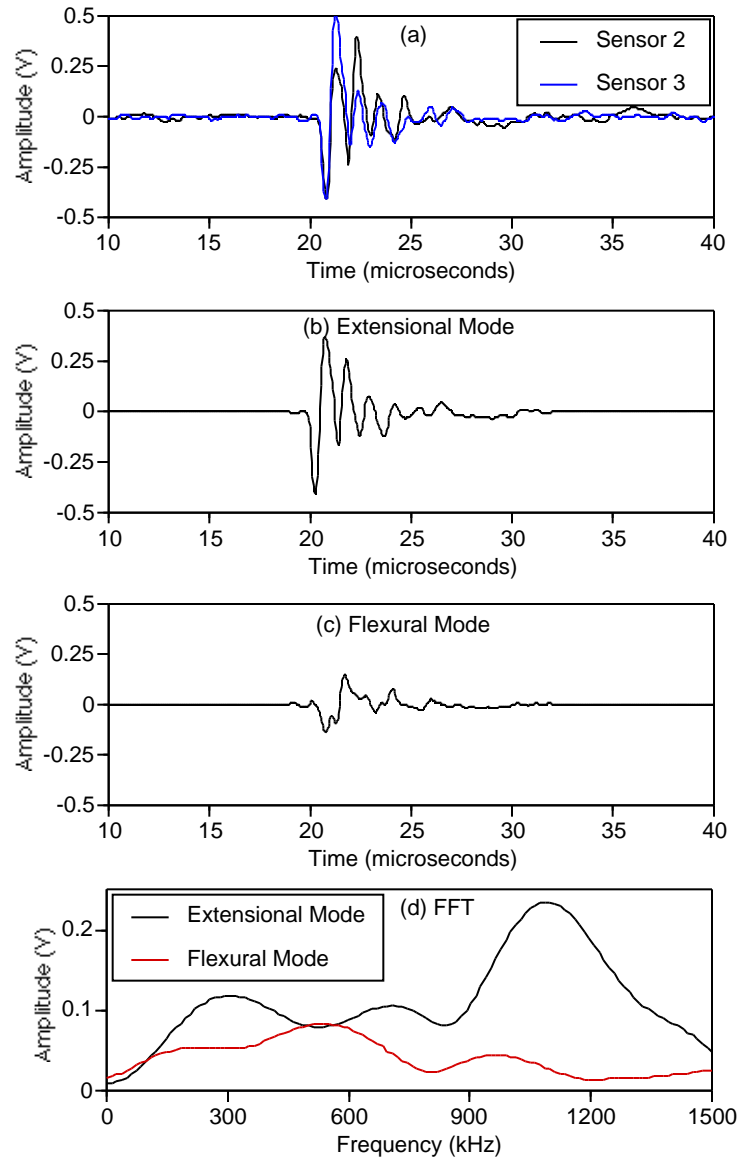


Figure 7.33: (a) Waveforms detected directly beneath sensors 2 and 3 in a 90° sample. (b) Extensional and (c) flexural components of the waveform in (a). (c) FFT of the extensional and flexural components. ($1V=47$ dB)

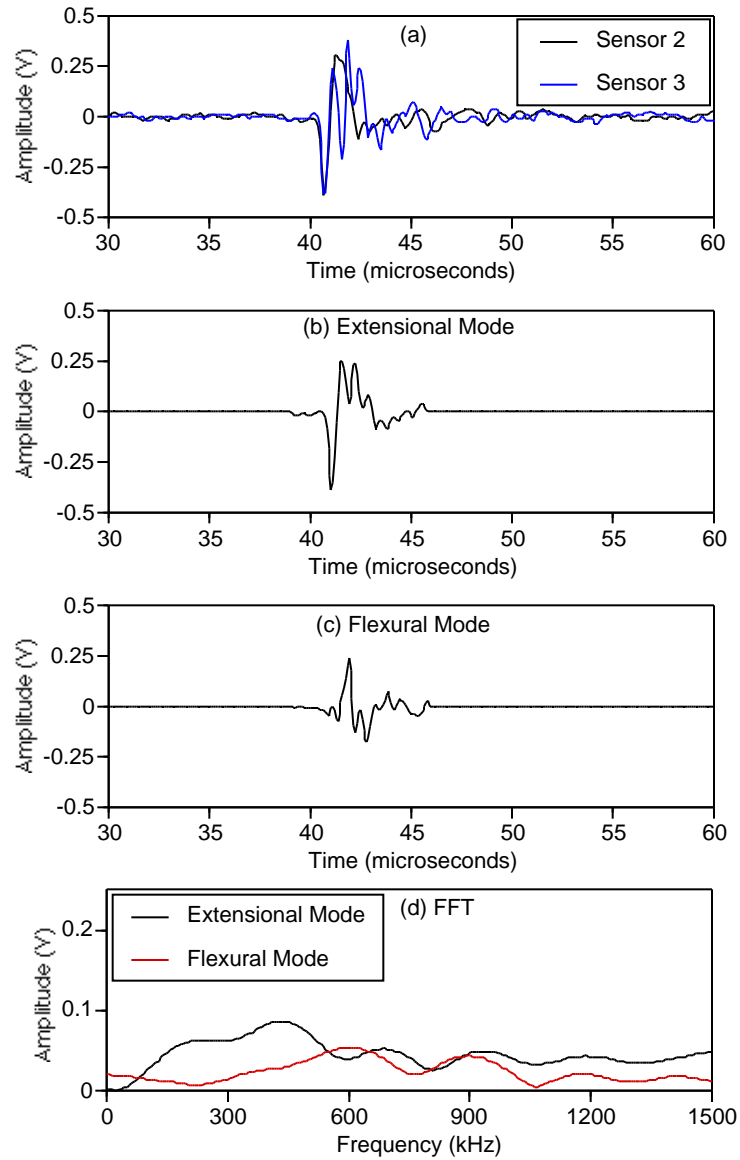


Figure 7.34: (a) Waveforms detected directly beneath sensors 2 and 3 in a 30° off-axis sample. (b) Extensional and (c) flexural components of the waveform in (a). (d) FFT of the extensional and flexural components. ($1V=47$ dB)

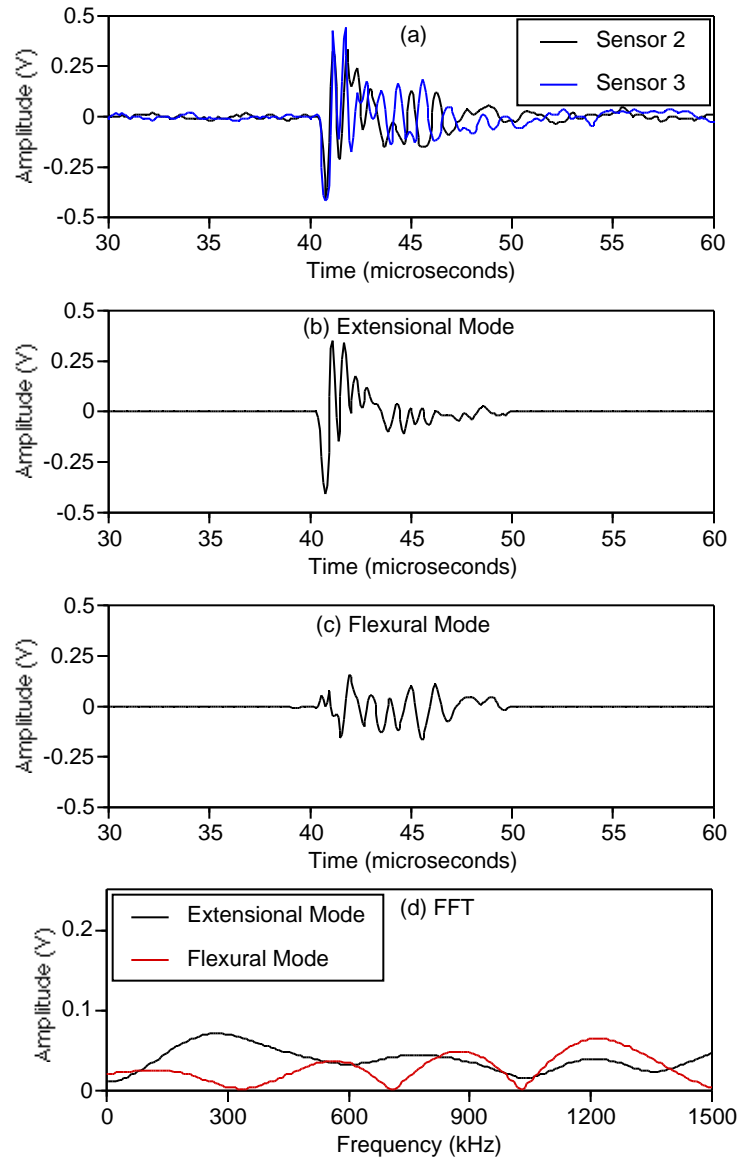


Figure 7.35: (a) Waveforms detected directly beneath sensors 2 and 3 in a 30° off-axis sample. (b) Extensional and (c) flexural components of the waveform in (a). (d) FFT of the extensional and flexural components. ($1V=47$ dB)

7.2 Cumulative Events versus Load Level

Cumulative AE events detected in 90° samples are plotted versus axial stress in Figure 7.36. There is no pattern with loading rate. Apparently, there is significant scatter between samples in terms of the number of detectable events. Up to twice the number of events were detected in separate samples tested at equal rates.

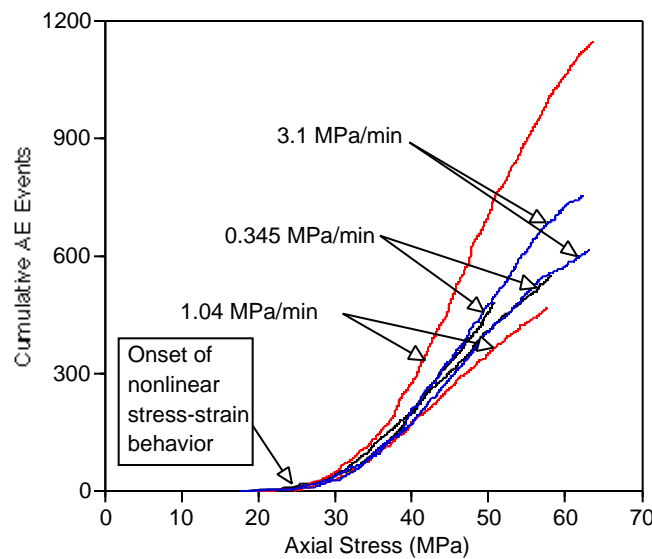


Figure 7.36: Cumulative AE events detected in 90° samples versus axial stress for three loading rates. All testing was performed with B1025 sensors.

Emissions detected from 45° and 30° off-axis samples are shown in Figures 7.37 and 7.38. Note that the more sensitive B225 sensors were used for this testing. When the B1025 sensors were used, far fewer events were detected as shown in Figure 7.39. There is a large swing in event count at high stress when using these sensors. Since this was not seen when using the more sensitive sensors, we may conclude that these events are of greater magnitude and a study of event magnitude is needed.

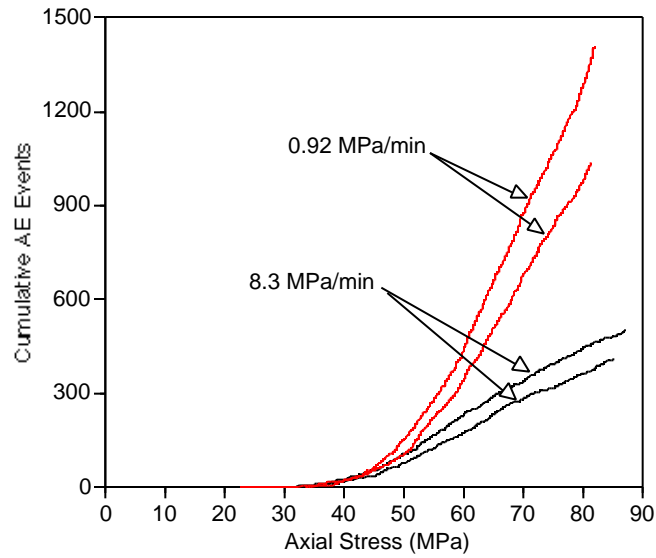


Figure 7.37: Cumulative AE events detected in 45° off-axis samples versus axial stress for two loading rates. All testing was performed with B225 sensors.

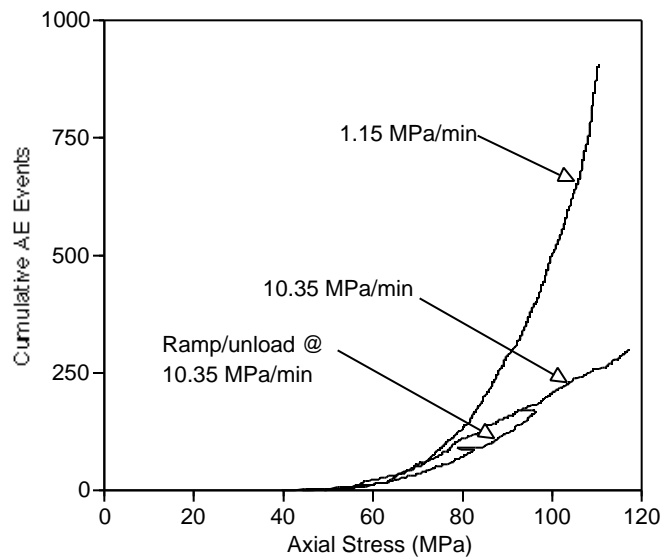


Figure 7.38: Cumulative AE events detected in 30° off-axis samples versus axial stress for two loading rates. All testing was performed with B225 sensors.

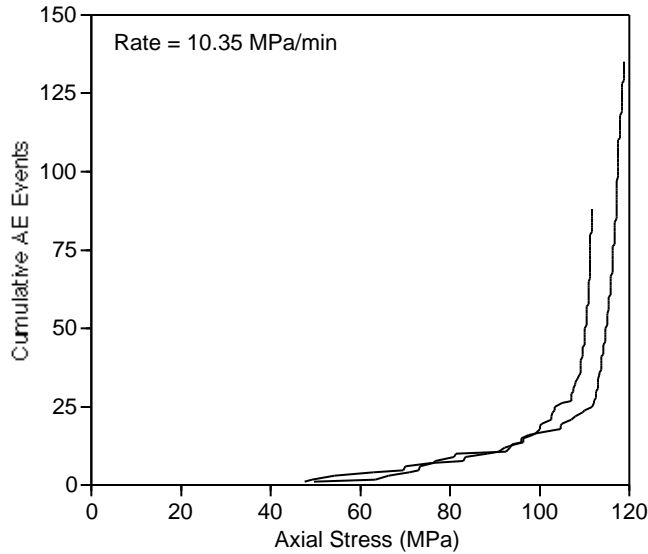


Figure 7.39: Cumulative AE events detected in 30° off-axis samples with B1025 sensors.

7.3 Waveform Energy

Distributed cracking in the material emits a variety of acoustic waves depending on the size of the crack that formed and the fracture energy of the material that fails. The *detected* waveform is also affected by the distance of the sensor and direction of travel to the sensor. As discussed in previous sections, a range of signals was detected; going from those which barely registered, with the most sensitive sensors available, to those which registered full scale. The energy of a waveform (i.e., the time-integrated squared amplitude) provides a measure of the fracture energy and how much material failed; larger faster cracks create larger acoustic waves. We are concerned, however, with the ‘average’ cracking which is being distributed throughout the material. The average energy of the distributed events can therefore pro-

vide some insight into how the nature of the cracking changes as the load and time under load increases. In this way, all variables that affect signal energy (crack size, fracture energy, distance and direction to sensors) is averaged.

The average energy of an event was calculated from both of the signals received by the AE sensors using the ‘Energy’ feature of the WaveDetector software. Waveforms were windowed as shown in the previous section so that background noise and reflections were omitted from the energy calculation. These energies were then averaged over all the events detected for every 2 MPa of loading, as shown in Figure 7.40 for 90° samples tested with various rates.

The average energy emitted during loading is constant from first cracking to failure. This observation has some interesting ramifications. First, because the energy of an event is a measure of how large a crack gets before stopping, the average distance a crack runs is therefore not a function of stress level. Cracks which initiate at low stress propagate the same average distance as those that initiate at high stress. Second, if cracking is occurring both in the matrix and at the fiber/matrix interface and their fracture energies are different, the same portion of cracks initiate in each up until failure. An increase in average energy would be observed if, for example, a greater portion of matrix cracking was occurring and its fracture energy were higher. Finally, and of importance in Section 7.6, the ‘detectability’ of individual cracks does not change throughout the test. If cracks ran a greater distance at higher stress-levels, they would be more detectable; a greater portion of the cracks which initiate would trigger the AE equipment. As this does *not* appear to be the case, we may conclude that the same portion of cracks are detected throughout the test. To maintain the same sampling of events in a material where arrested crack size *is* a function of stress level, the increase in average

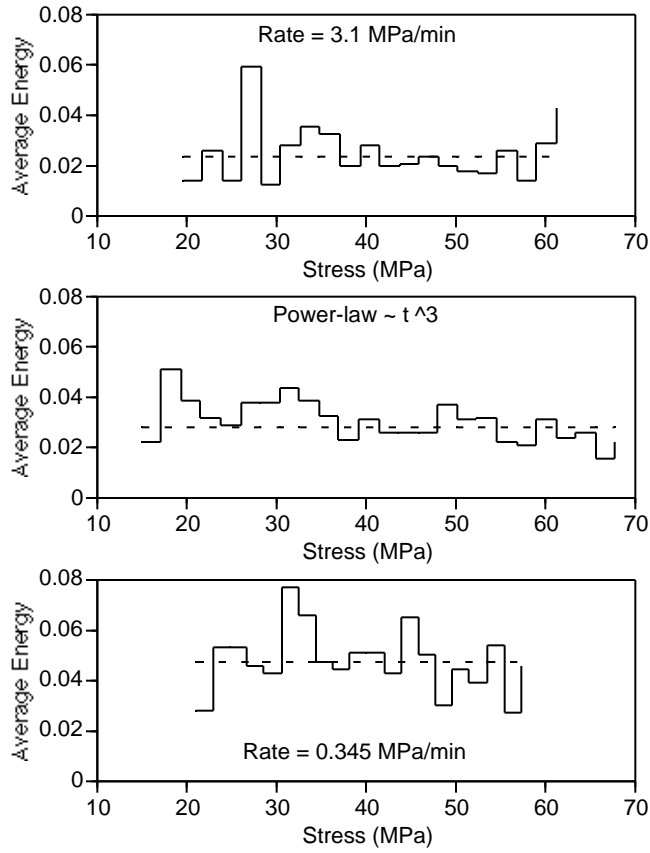


Figure 7.40: Average event energy detected in 90° unidirectional samples for three loading histories. The mean energy of all events is shown by the dotted line.

event amplitude may be used to account for this effect. By scaling the voltage threshold for which an event is accepted with the increase in average event amplitude, the same portion of cracks will be counted throughout the test.

The existence of shear stress in the matrix of the 30° and 45° off-axis samples does have an impact, however, as shown in Figures 7.41 and 7.42. Results from both off-axis samples show an upswing in average event energy at high stress. Since a few large-energy events can quickly bias these results for the 2 MPa interval used, finer detail is needed to see when this upswing occurs. With the shear and transverse stresses equal, as in the 45° off-axis specimen, the upswing in event-energy occurs just prior to failure as shown in Figure 7.43. These large-energy events account for only 15% of those detected and have little effect on subsequent analysis. When the proportion of shear stress is increased to 1.7:1, as in the 30° samples, a larger effect is seen. In the high rate test shown in Figure 7.44, larger events are detected only in the last six seconds of loading (about 1 MPa) and again only accounts for a small portion of events detected. In the low rate test, however, the average event energy begins to steadily increase about six minutes prior to failure (at approx. 103 MPa). These events account for approximately 40% of those detected. It may be that cracks are now running dynamically farther than they did at lower stress. This has several ramifications as will be discussed in Section 7.6.

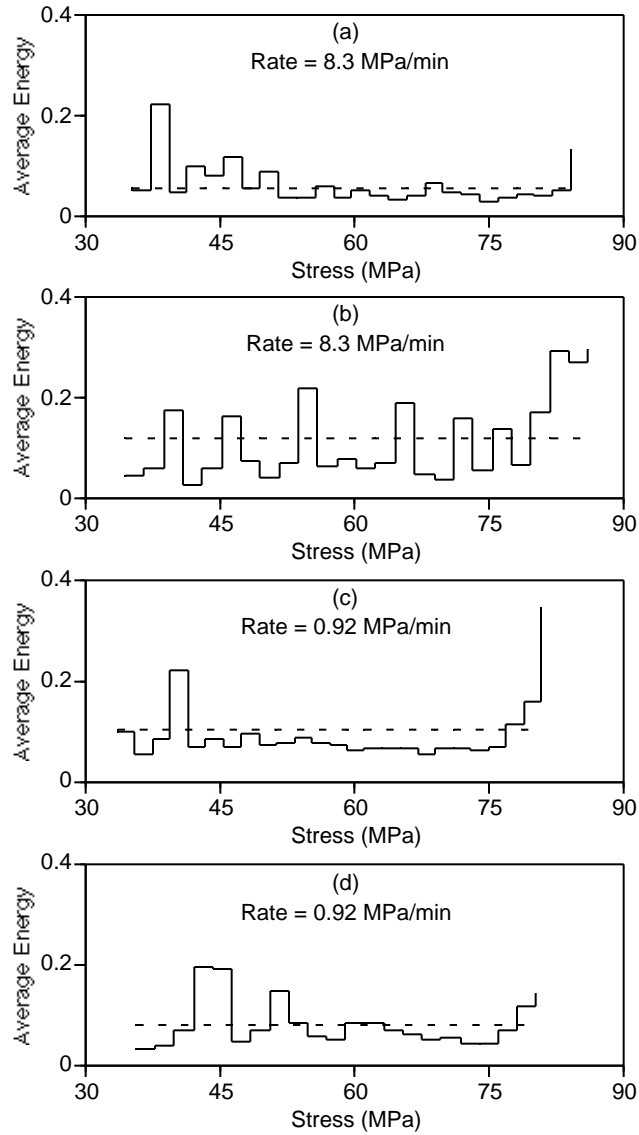


Figure 7.41: Average event energy detected in 45° off-axis samples at 0.92 MPa/min. The mean energy of all events is shown by the dotted line.

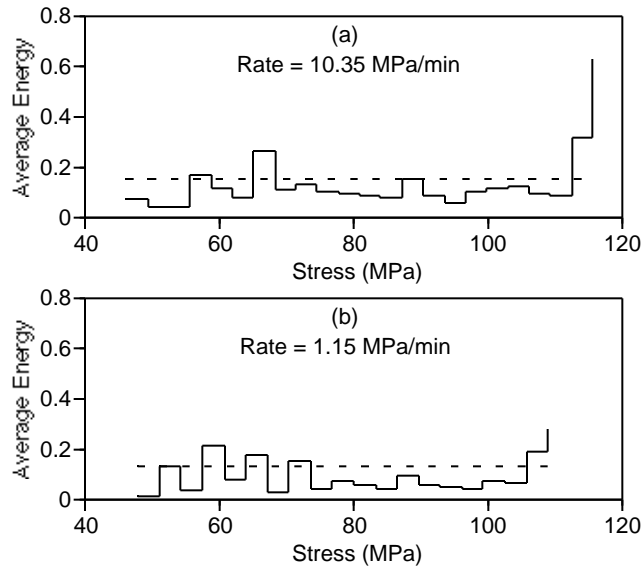


Figure 7.42: Average event energy detected in 30° off-axis samples for two loading rates. The mean energy of all events is shown by the dotted line.

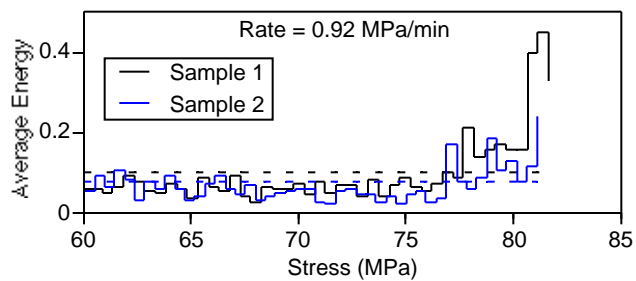


Figure 7.43: Average event energy detected in two 45° off-axis samples from 30 MPa to failure for two loading rates. The mean energy of all events is shown by the dotted line.

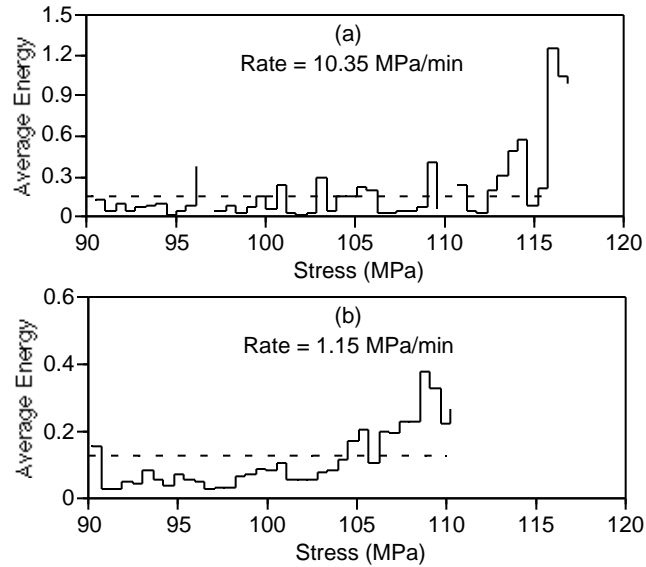


Figure 7.44: Average event energy detected in 30° off-axis samples from 90 MPa to failure . The mean energy of all events is shown by the dotted line.

7.4 Location of Large Events

The increase in average waveform energy discussed in the previous section may indicate a general increase in arrested crack length for the distributed microcracking. However, this is only true if these larger microcracks are uniformly distributed in the free length. To study the location of these larger cracks, waveforms detected before and after the increase in waveform energy were first separated. A histogram of the events prior to the increase are shown in Figures 7.45 and 7.46. Microcracking is uniformly distributed between the sensors as previously discussed (note: these distributions assume all cracking occurred along the centerline of the sample).

Next, the location of a subset of the events detected after the increase

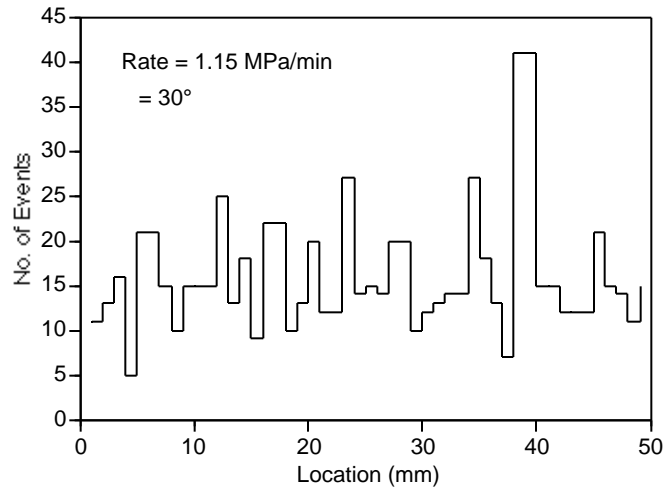


Figure 7.45: Location histogram of microcracking in the free length of a 30° off-axis sample. All events after the increase in average waveform energy have been removed.

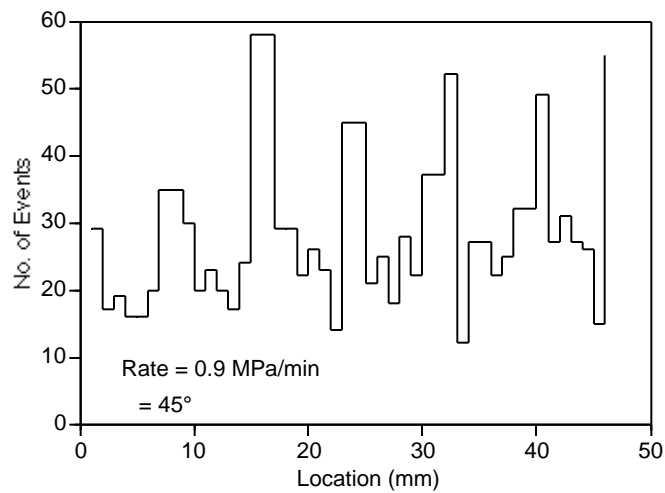


Figure 7.46: Location histogram of microcracking in the free length of a 45° off-axis sample. All events after the increase in average waveform energy have been removed.

in waveform energy (those with maximum amplitude greater than 200 mV) were found as shown in Figures 7.47 and 7.48. Here there is a concentration of microcracking in both the 30° and 45° off-axis samples in a specific region of each sample. This concentration may indicate the beginning of crack interaction where a larger crack is created than would be otherwise. It may also simply indicate a region of material that is relatively ‘weaker’ or less able to arrest crack growth under certain loading conditions. Regardless, this microcracking is not indicative of the distributed cracking and only occurs in the final stages of loading.

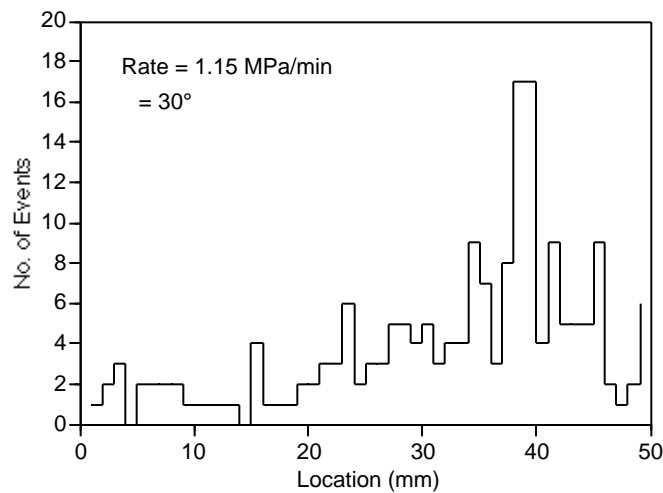


Figure 7.47: Location histogram of microcracking in the free length of a 30° off-axis sample. All events before the increase in average waveform energy have been removed and only events greater than 200mV have been included.

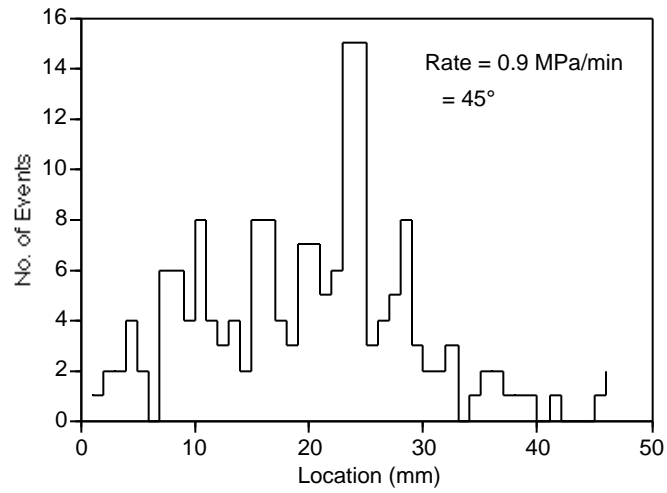


Figure 7.48: Location histogram of microcracking in the free length of a 45° off-axis sample. All events before the increase in average waveform energy have been removed and only events greater than 200mV have been included.

7.5 Ramp/Hold Testing

In order to exaggerate time-dependent cracking in the 90° samples, a ramp hold test was performed with hold periods of 20 hours. By using modest rates, no events were lost during the load-up period. The loading history and strain response are shown in Figure 7.49. Figures 7.50 and 7.51 show cumulative events versus time under load and stress respectively. Significant time-dependent damage is evident from the large accumulation of events during the hold periods. Of even greater interest is the behavior seen during the second and third ramp periods shown in Figure 7.51. During the second load-ramp, damage does not begin to accumulate until the stress was increased by about 6 MPa. During the third ramp, an increase of about 3 MPa is needed. Thus, no additional cracking occurs until the load has increased significantly above the holding stress. This may indicate that microstructural stress relaxation has occurred.

Rubber particles in the matrix produce zones of yielded material between particles, as discussed in Section 6.1. This will happen especially in the high stress zones in front of crack tips. The separate phases of material will result in a redistribution of microstructural stresses resulting in relaxation of the yielded regions which drive the crack growth. If stress relaxation did not occur, the theory in Section 4.1 implies that cracking would occur *immediately* upon increased loading. However, with relaxation, the global stress needs to first overcome the stress relaxation before significant damage growth can again begin.

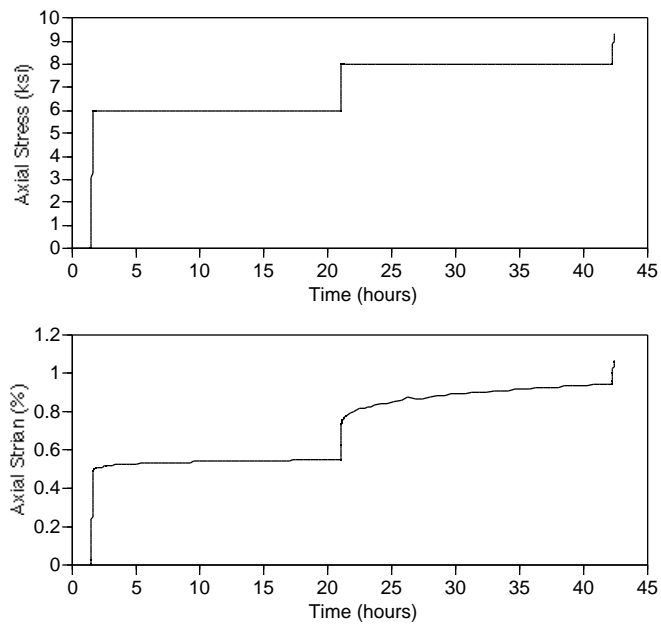


Figure 7.49: Loading history and strain response from ramp/hold testing.

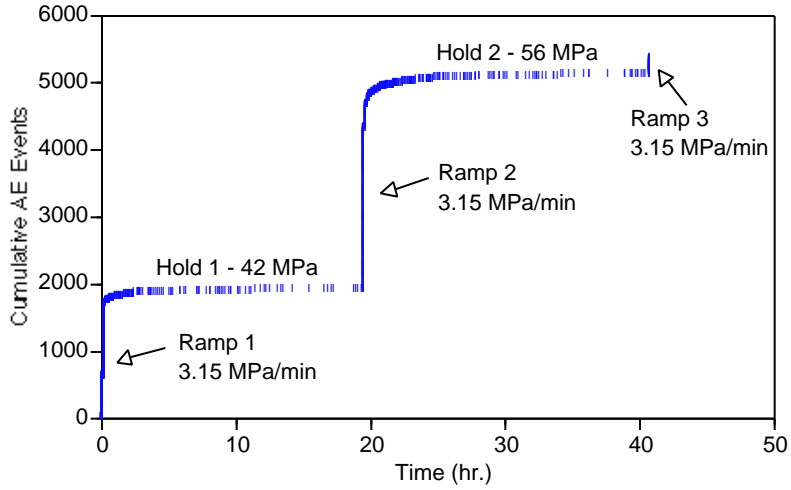


Figure 7.50: Cumulative AE events versus time detected during ramp/hold testing of a 90° sample. Testing was performed with B225 sensors.

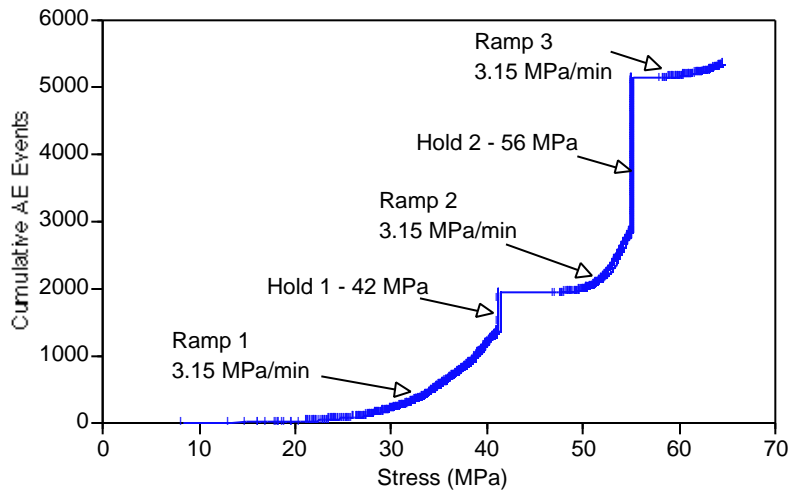


Figure 7.51: Cumulative AE events versus stress detected during ramp/hold testing of a 90° sample. Testing was performed with B225 sensors.

The previous study of average event energy measured in 90° samples indicated that the ‘detectability’ of individual cracks does not change throughout the test. Although not seen during load-ramp testing, it *is* possible that during the hold periods cracks do not travel as far as they did during the periods of continuous loading, consequently not being as detectable. If this were the case, a decrease in average event energy would be observed. As shown in Figure 7.52, with the exception, perhaps, of the second ramp, this was not seen to be the case. Average event energy did not increase or decrease during each period of loading. Therefore, the same portion of damage is detected during the entire test, just as in single ramp to failure testing.

7.6 Interpretation of AE Results

Unidirectional material in its as-manufactured state contains some statistical distribution of small flaws or cracks that serve as initiation sites for crack growth. These are the voids, cracks around voids and fiber/matrix debonds that were viewed by Wood (1996) prior to loading the material. As the composite is loaded, some of these flaws will become unstable at given levels of stress, propagate at high speed, and stop upon reaching a crack inhibitor (fiber, reduced stress zone, etc.). For example, Wood (1996) observed that the cracks around voids coalesced with debonded fibers around it. Each flaw has its own distinct initial crack geometry, local stress field (which depends on the microstructure in the vicinity of the crack tip) and fracture energy or process zone. Fiber-matrix debond is the same except here we have adhesive-type failure. As the material fails, energy is transferred from the continuum and dissipated in a non-conservative fashion to heat and among other things, an acoustic wave which we detect with the AE sensors.

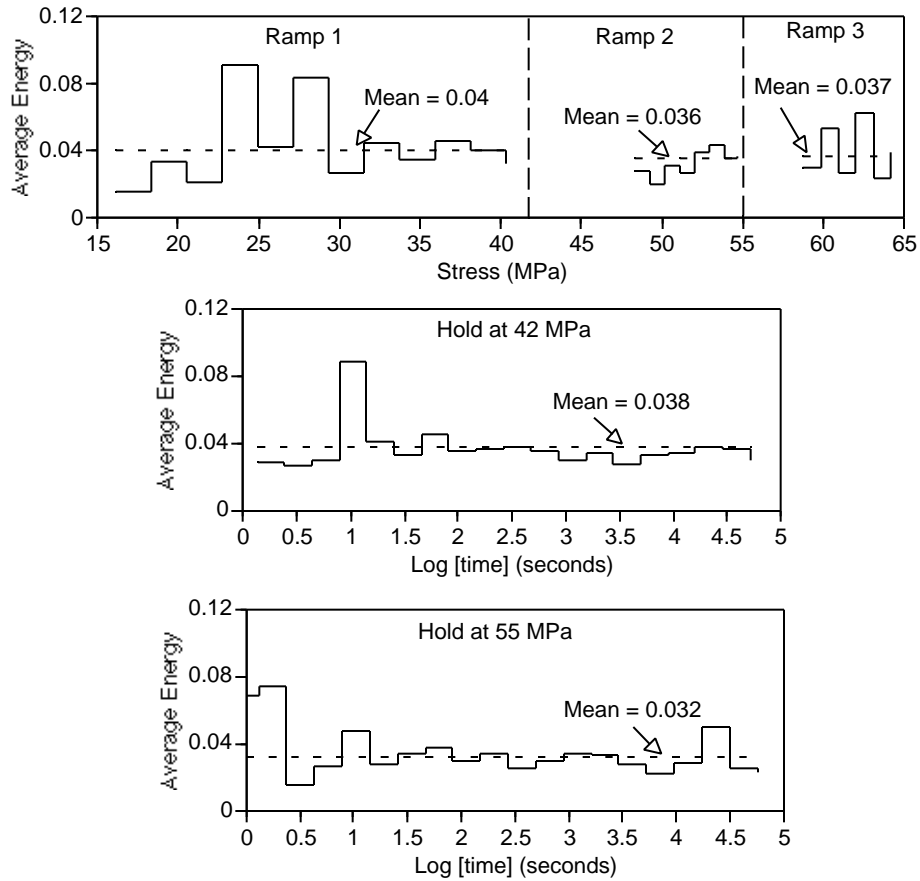


Figure 7.52: Average event energy during the ramp and hold periods of testing. Note that the ramp periods are versus stress and the hold periods are versus $\log(\text{time})$. The mean energy of events for each period is shown by the dotted line.

If the material were elastic, each flaw would fail at a given level of globally applied stress. For a given volume of material, if we could count the number of cracks which fail at each level of global stress, a histogram of the number of cracks which initiate at each stress level could be found. This histogram would reflect the distribution of initial crack lengths and orientations, local stress concentrations (due to local geometry) and fracture energies of the initial flaws. This distribution will be common to all samples tested. As the material is actually viscoelastic, crack initiation is a function of both stress and time. The same flaw will initiate at a lower load given sufficient time.

The *effect* of distributed microdamage is a separate issue from how it varies with loading history. *When* a given flaw grows is a function of the properties mentioned. How far it travels depends upon the geometric material feature that stops its growth, which is again statistical in nature and varies from flaw to flaw. Indeed, as discussed in Section 7.3, the average energy of an event, and therefore the average size of crack growth, does not vary with stress level. The *effect* of the growth of a given flaw will be proportional to how large a given crack gets; a larger crack yields more softening. The AE data tells us *when* and at what *load* a crack has grown rapidly. The magnitude of that event is not relevant to finding how the distribution of flaws varies with different loadings. These factors lead to the question of whether all cracking in the composite is detectable.

Not all matrix-cracks are detected with the acoustic emission sensors. Some are too small as they start and don't travel far before stopping, thus not giving off a strong acoustic wave. Others, depending on the loading, may not grow dynamically but exhibit slow sub-dynamic growth. This is acceptable as *only a statistically significant number needs to be detected to get*

the correct distribution. For example, say you want the strength distribution for a material. You have 100 samples but have information on only 50. As long as that 50 is representative of the initial population of flaws, you still get the same distribution of strengths regardless of whether one hundred or one thousand are tested. Testing one coupon gives the same information as cutting small samples around each flaw and testing these individually to find its fracture stress and time.

Recognizing that not all matrix-cracks are detected with the acoustic emission sensors and that variations in the ‘detectability’ of events can change during a test, three items must be held constant to ensure that the correct distribution of cracks is found:

- 1- The *volume* of material over which cracking is detected.
- 2- The *minimum size* of cracks being detected.
- 3- The *portion* of cracks detected.

Changes in the wavespeed will affect the volume over which events are accepted and damping affects the minimum detectable size. Cracking that increases in magnitude with stress level, which affects the portion of cracks detected, has already been addressed. Loading the material may have an effect on both wavespeed and damping as the stiffness of the material changes and damage is introduced throughout the volume. If wavespeed drops, and we assume it to be constant throughout the test, the volume of material from which events are accepted will decrease. Fewer events will be registered than should have been. If damping increases, fewer events will be detectable and the proportion of cracking detected will change throughout the test. Whether significant changes do occur needs to be checked; if there are any, analysis of the AE data needs to be calibrated accordingly.

7.7 Change in Material Acoustical Properties

In order to measure changes in the wavespeed and damping of acoustic waves in the material during loading, waveforms similar to those emitted by matrix cracking need to be introduced. We saw in Section 7.1.1 that the predominant amount of energy in the waveforms detected at the location sensors lay between 100 to 400 kHz. From the study in Section 7.1.2, we know that these waves are predominantly extensional. The same experimental setup as shown in Figure 7.31 was used for this study except one of the B225 sensors (previously used for location) is now used as a pulsing sensor. This sensor was pulsed at 150kHz and 300kHz using the AE-CAL equipment built by Physical Acoustics Corporation. Table 7.1 shows the settings used. A 90° and 30° off-axis sample was ramped and held at various stress levels where the sensor was pulsed at both frequencies.

Once again, sensors 2 and 3 were used to differentiate extensional and flexural waveforms. As shown in Figures 7.53 through 7.56, the waves produced in both 90° and 30° off-axis samples are predominantly extensional as desired. Wavespeed of the extensional mode was measured from the arrival times at sensors 2&3 and 4. This speed was found to vary less than 5% in 90° and 30° off-axis samples from zero load to the highest stress tested. However, there was an effect on damping.

The maximum amplitudes of the extensional and flexural modes measured at sensors 2&3 at various load levels are shown in Figures 7.57 and 7.58. From the stress level at which events are first detected, the maximum decrease in amplitude is at most 12% (300 kHz extensional mode in the 90° sample). One could correct for this effect by weighting the number of events detected by these ratios, but the changes are small enough that the derived distribution

is not significantly affected, and no corrections were made.

Table 7.1: Hardware settings on AE-CAL to produce waveforms for the wavespeed/damping study.

Amplitude	99dB
Burst	$10\mu s$
Delay	$70\mu s$
Rise Time	$10\mu s$
Delay Time	$10\mu s$
Frequency	150 or 300 kHz

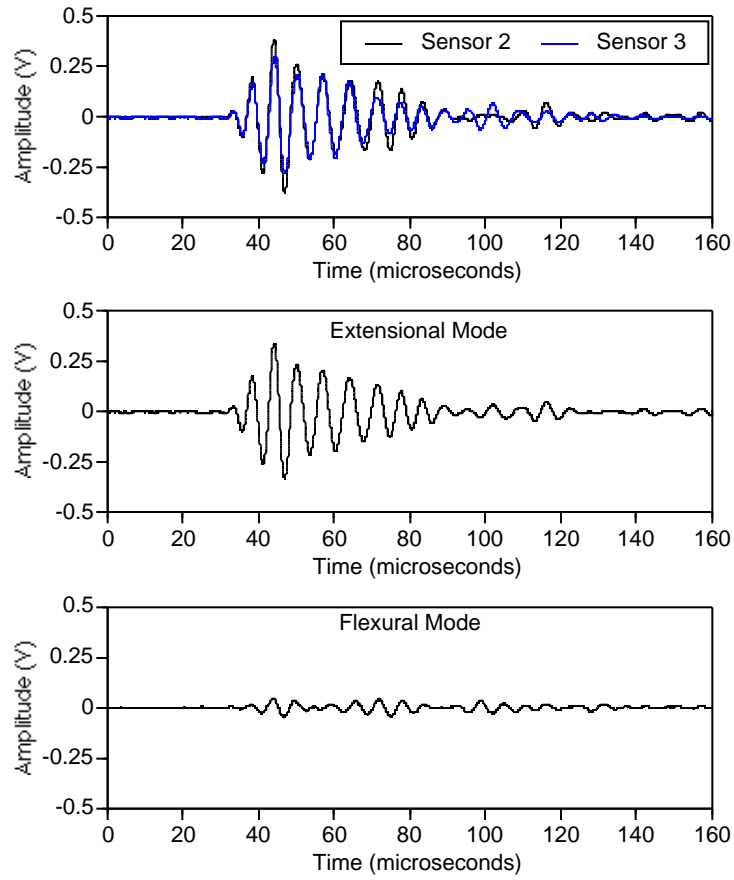


Figure 7.53: Extensional and flexural waveforms at 150kHz detected by sensors 2&3 and produced by sensor 4 in a 90° sample.

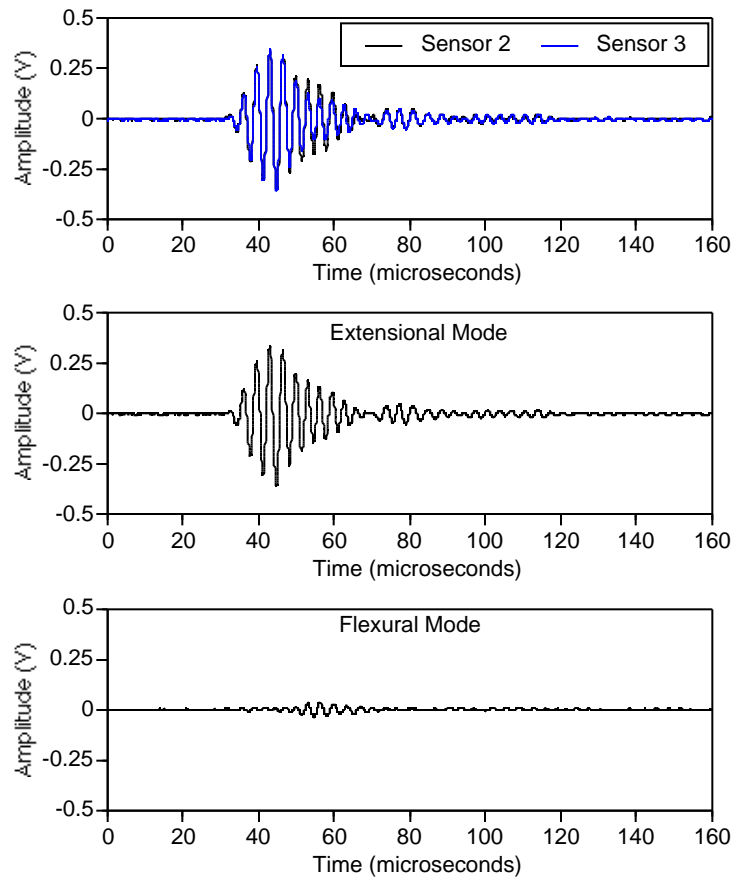


Figure 7.54: Extensional and flexural waveforms at 300kHz detected by sensors 2&3 and produced by sensor 4 in a 90° sample.

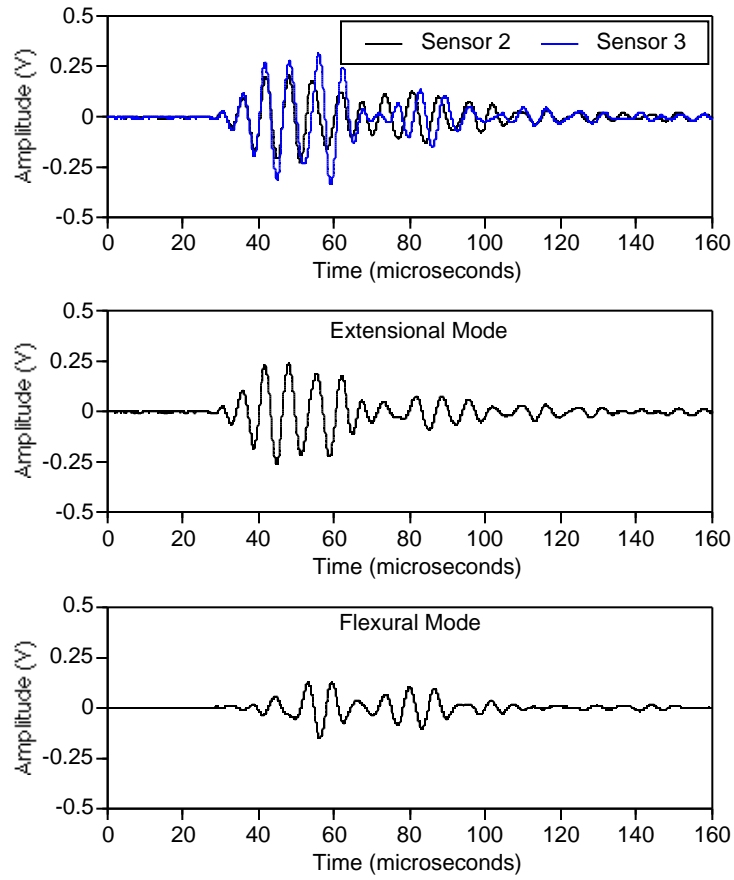


Figure 7.55: Extensional and flexural waveforms at 150kHz detected by sensors 2&3 and produced by sensor 4 in a 30° sample.

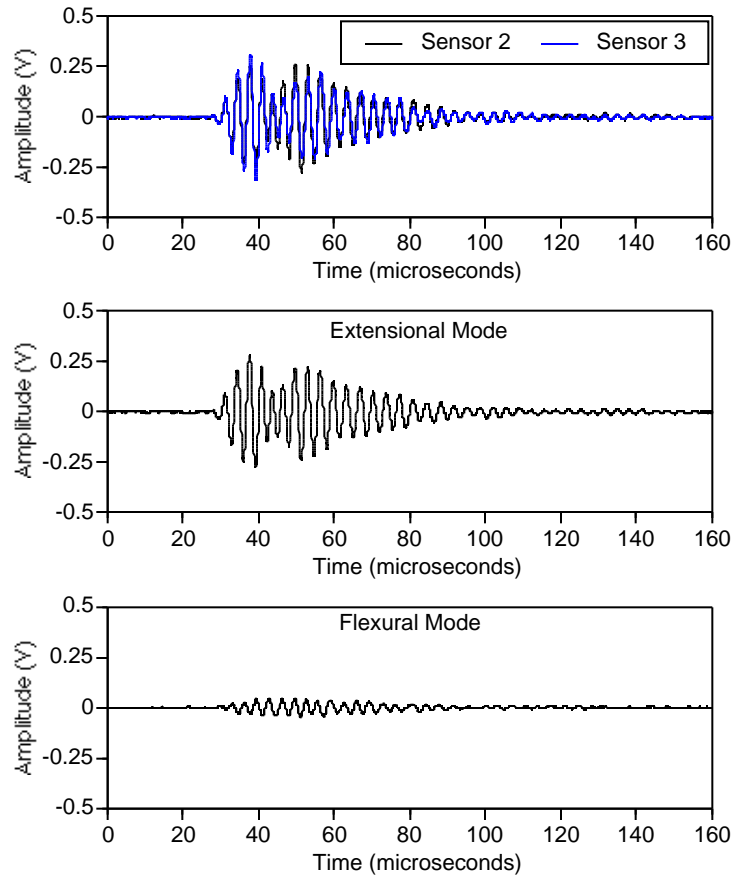


Figure 7.56: Extensional and flexural waveforms at 300kHz detected by sensors 2&3 and produced by sensor 4 in a 30° sample.

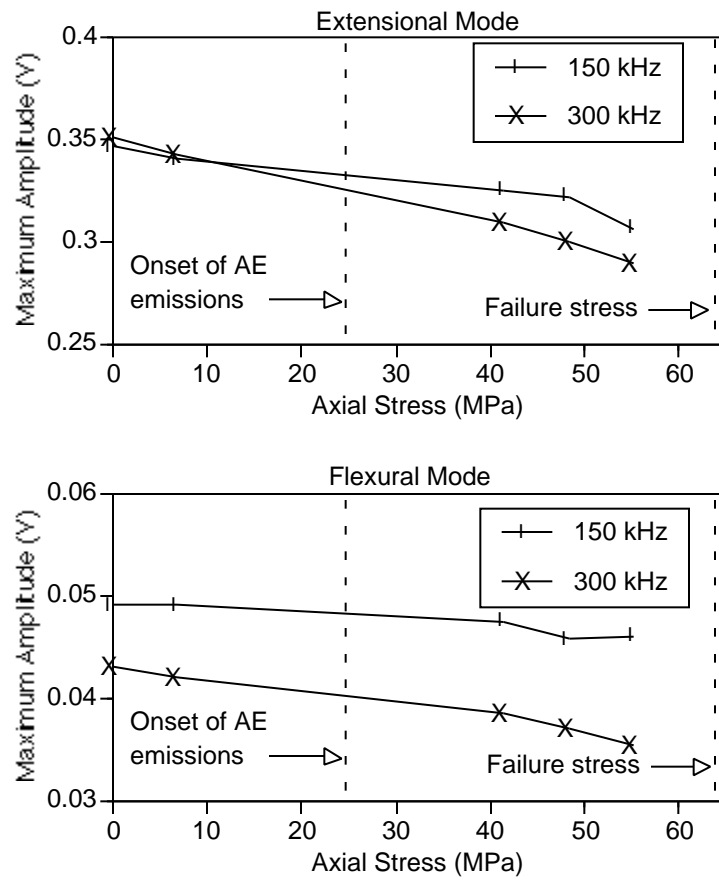


Figure 7.57: Maximum amplitude of the pulsed waves in a 90° sample at 150 and 300kHz versus axial stress.

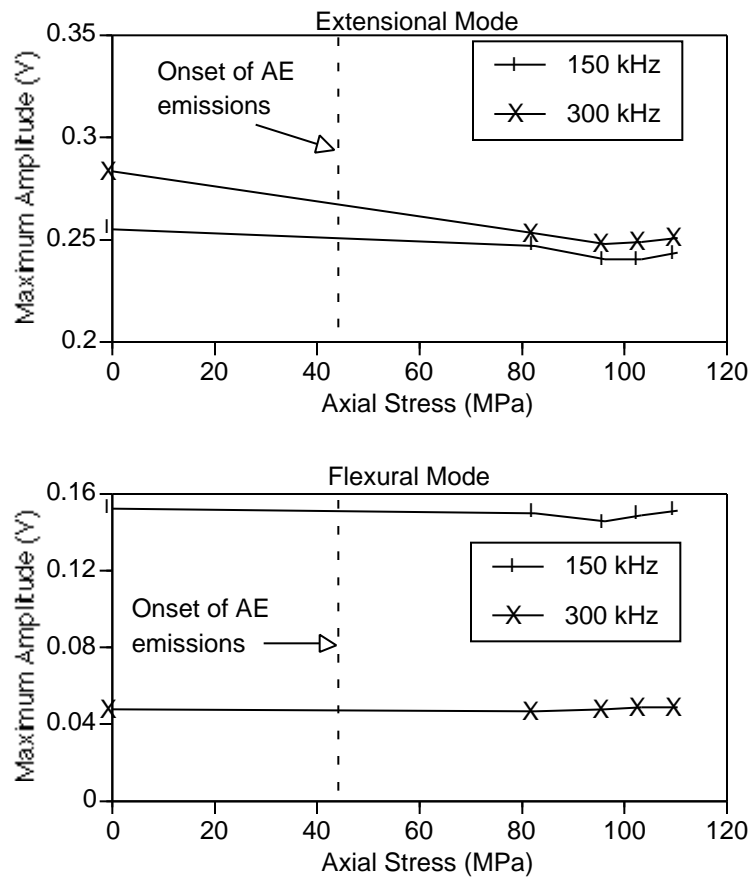


Figure 7.58: Maximum amplitude of the pulsed waves in a 30° sample at 150 and 300kHz versus axial stress.

7.8 Calculation of the CDF of Microcracking

Having confirmed that the same portion of cracking relative to the total number of cracks is detected throughout a given experiment, we may find the CDF of microcracking, $P(L)$, as discussed in Chapter 4. The loading parameter, L , of Equation 4.34 was calculated for every event detected based on its failure time and calculated stress on the NLVE phase of the material. This stress was found by subtracting a viscoplastic strain, Equation 4.29, from the global strain and using this strain to find the stress on the LVE material through Equation 4.27. Stress on the NLVE phase is found by subtracting this stress from the global stress at the time of the event, Equation 4.28. Finally, a histogram of events versus L was used to calculate the PMF and CDF, Equations 4.33 and 4.35.

Material constants to perform the above analysis, shown in Table 7.2, were found by comparing distribution functions found from samples loaded with different loading histories. In the 90° samples, of primary importance were data from the ramp/hold test as these data emphasized the time-dependence of the microcracking. In addition to the ramp/hold testing from Section 7.5 and the load/unload test from Section 6.1, other loading histories used on 90° samples are shown in Figure 7.59. Due to shortages in unidirectional material, only constant ramp testing was performed on off-axis 45° and 30° samples.

Time or rate-dependence of the microcracking in 90° samples was very weak. In fact, the range of rates used in Figure 7.59 had very little impact. Shown in Figure 7.60 is the PMF of cracking using axial stress as a distribution parameter, the parameter used if the material were simply elastic. Similar distributions were found for all monotone increasing loadings. Each

curve represents the average of multiple samples. The CDF is shown in Figure 7.61. The rate effect is only evident from ramp/hold and load/unload testing as shown in Figure 7.62. With the addition of shear stress, as in the

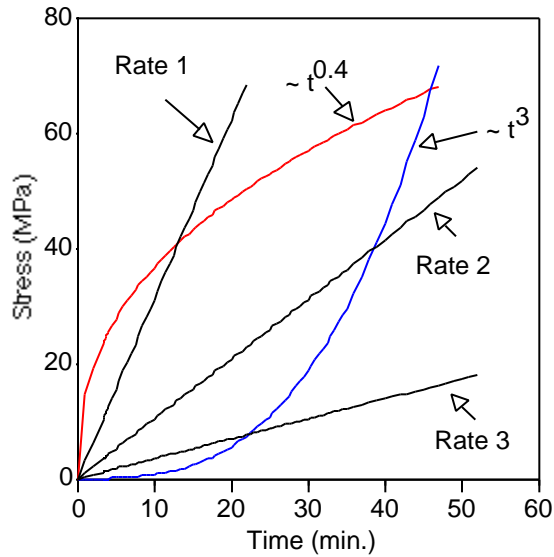


Figure 7.59: Loading histories used in AE testing of 90° samples.

off-axis samples, the rate effect on cracking becomes much stronger. Shown in Figure 7.63, the distribution of cracking with axial stress is affected by loading rate. Each curve for the 45° off-axis data represents the average of multiple tests.

Using material properties shown in Table 7.2 and a value of $q=12.5$, data from all 90° testing was collapsed to a single distribution of the loading parameter L , as shown in Figure 7.64. Data bounds collected from rate testing shown in Figure 7.59 are indicated by the dotted lines. Again, no difference is seen between these loading histories. Data from ramp/hold testing has been broken into separate pieces so cracking from each segment is easily viewed. Data from the load/unload experiment is also shown.

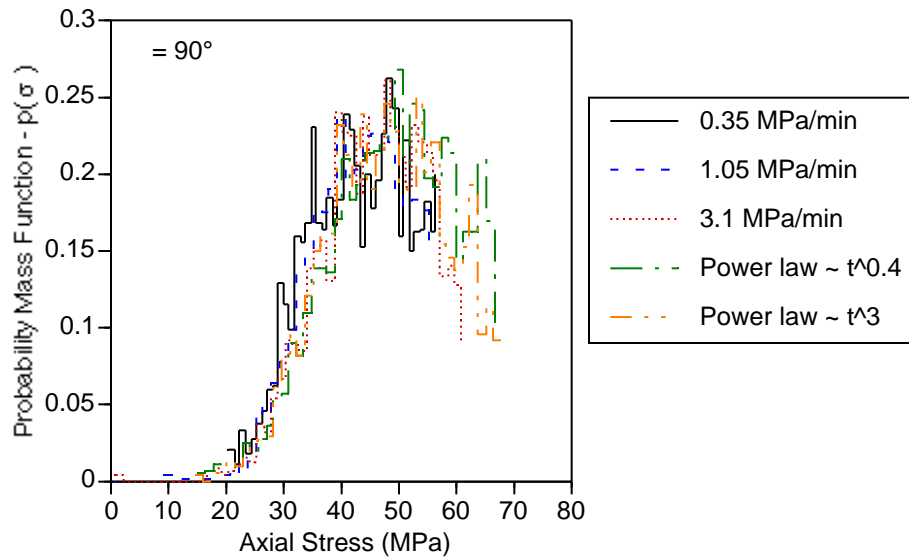


Figure 7.60: PMF of AE events detected from 90° samples loaded with different histories when using axial stress as the distribution parameter.

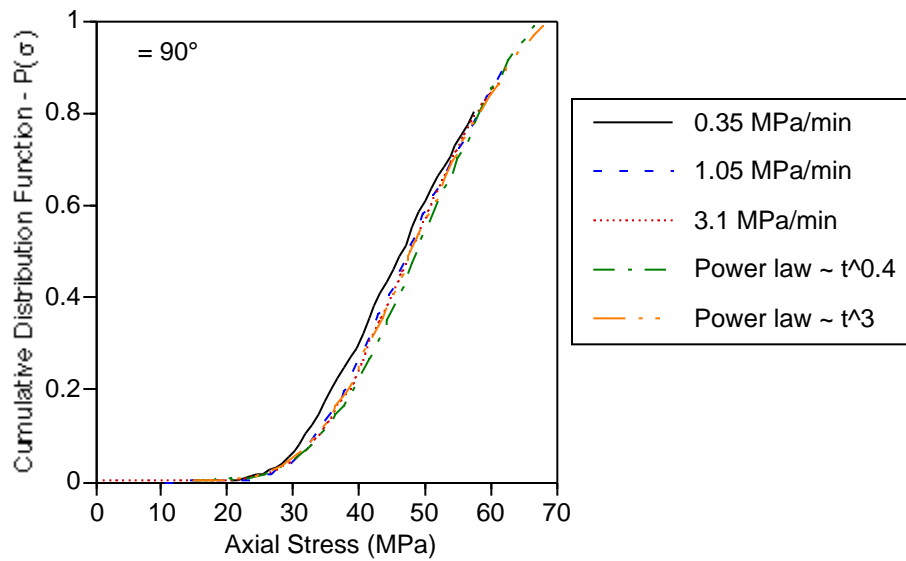


Figure 7.61: CDF of AE events detected from 90° samples loaded with different histories when using axial stress as the distribution parameter.

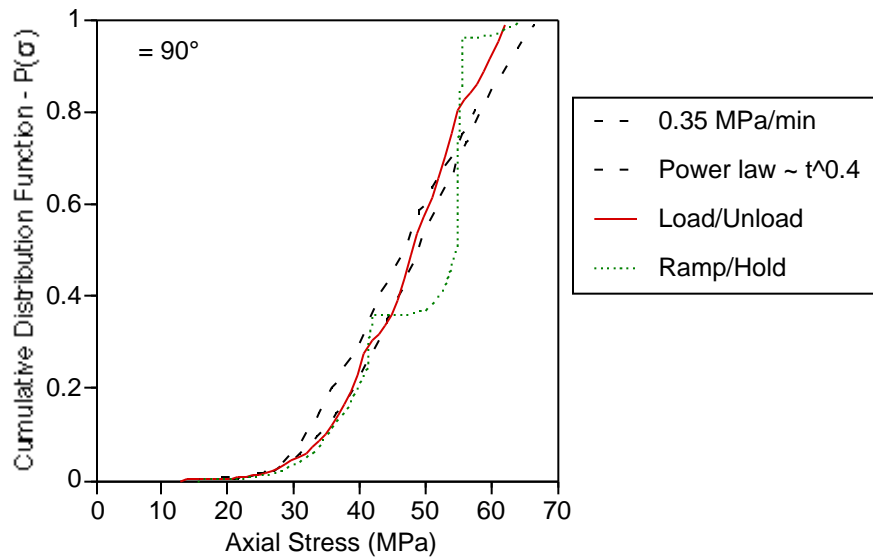


Figure 7.62: CDF of AE events detected from 90° samples using axial stress as the distribution parameter . Results from the Load/Unload testing and Ramp/Hold testing are compared with the other loadings.

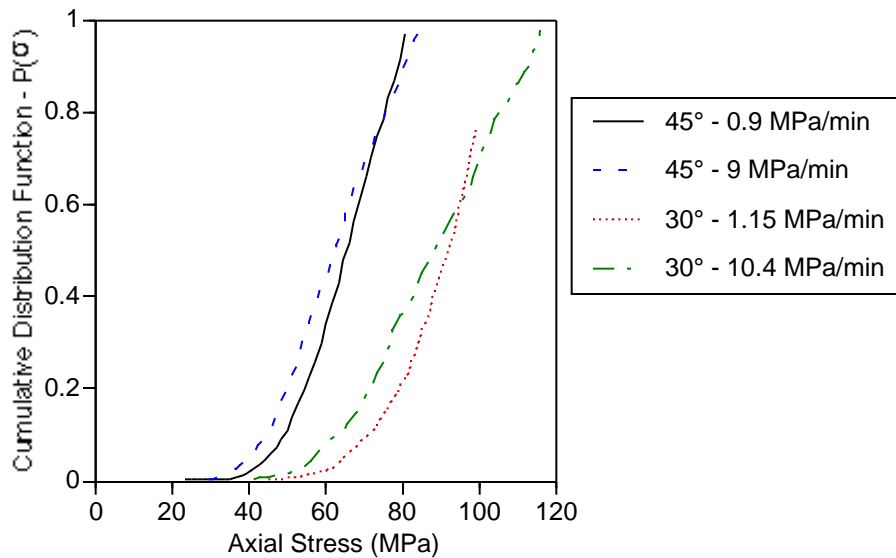


Figure 7.63: CDF of AE events detected from off-axis samples loaded with different rates when axial stress is used as the distribution parameter.

Table 7.2: Effective transverse properties of the LVE phase used to calculate the loading parameter L for 90° samples.

LVE Properties	
E_0	5.52 GPa
E_1	1.04 GPa min ⁿ
n	0.08
V/P Properties	
C	1.69E-11 GPa ^{-p} min ⁻¹
p	8.5
r	0.8

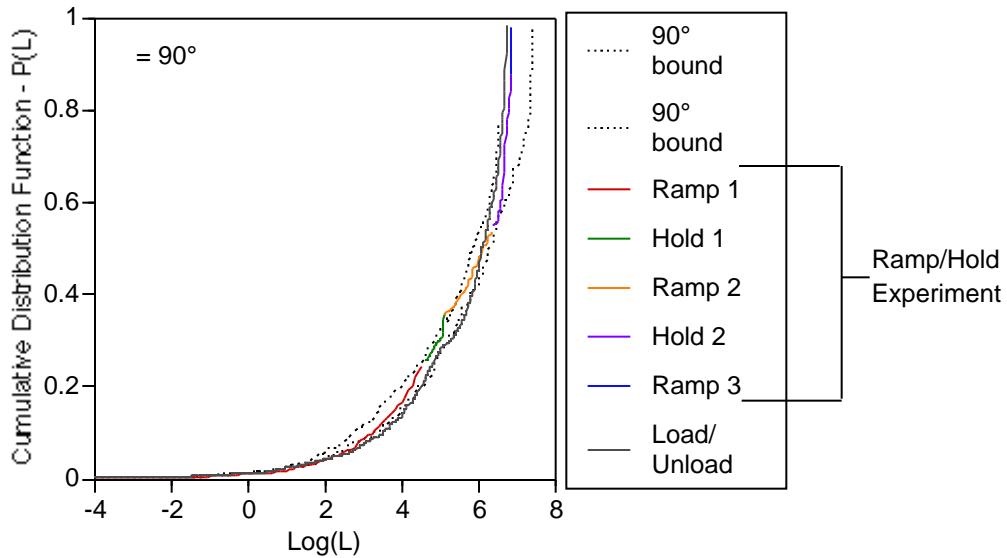


Figure 7.64: CDF of AE events detected from all 90° samples with L as the distribution parameter. Data bounds collected from the rate testing are shown by the dotted lines. Data from ramp/hold testing has been broken into separate pieces so cracking from each segment is easily viewed.

Limited data from off-axis samples restricted full analysis of the mixed-mode distributed cracking. Either ramp/hold testing or testing with much larger differences in rate are needed to exaggerate the time effects. However, based on this data a simplified analysis was performed where much of the microstructural relaxation was neglected for the short duration of testing. Figure 7.65 includes cracking detected in the off-axis samples with 90° data for reference, where only $E_0 = 0.55GPa$ (transverse stiffness) has been used in calculating L . All other material parameters were not included. Using this one adjustment, all *high rate* testing collapses to a single distribution regardless of loading direction (also note that $\Omega=1$ so that transverse and shear stresses contribute equally to the loading parameter). There is a distinct shift at the lower rates, however. Recall that β , of Equation 4.37, is a free parameter as it is unknown how much of the distribution $P(L)$ is detected prior to specimen failure. Estimated values of β for the lower rate tests are also shown. Notice, for example, that $\beta = 0.58$ for the low-rate test on 45° off-axis samples. This indicates that approximately 60% of the distribution of flaws grew dynamically prior to failure of the sample. However, as shown in Figures 7.37 and 7.38, there are clearly more events detected from samples loaded at lower rates. One might conclude that a higher event count indicates just the opposite, that β be smaller for the higher rate test. However, changes in the *detectability* of cracking with rate will have the same effect.

Two mechanisms may alter the detectability of a crack with loading rate. First, as already discussed, the average arrested crack length may be affected. Second, higher loading rates may result in a greater percentage of the flaws growing sub-dynamically, consequently they do not emit a strong acoustic signal. In that the average energy of a waveform is not affected by loading rate, indicating that the average arrested crack length does not

depend on rate, the latter physical explanation appears more likely. Therefore, we conclude that the quantity of cracks which fail dynamically depends on loading rate. The initial distribution of flaws is still the same. Only the quantity that are detectable changes, thereby reducing the sampling of the population of flaws.

A consequence of having both dynamic and sub-dynamic cracking is a change in the effect of each with loading rate. If less cracks fail dynamically at higher rates, less softening is attributable to this type of damage which can be monitored. Sub-dynamic cracking is consequently a damage effect which can not be tracked and must currently be inferred through the stress-strain behavior.

To complete the analysis of the detectable cracks, we return to Equation 4.34. At longer times the quantity Ω now becomes significant. Although it is principally a function of time, constant values (less than the value at the high rate) for both the 30° and 45° samples were sufficient to match the rest of the data, as shown in Figure 7.66.

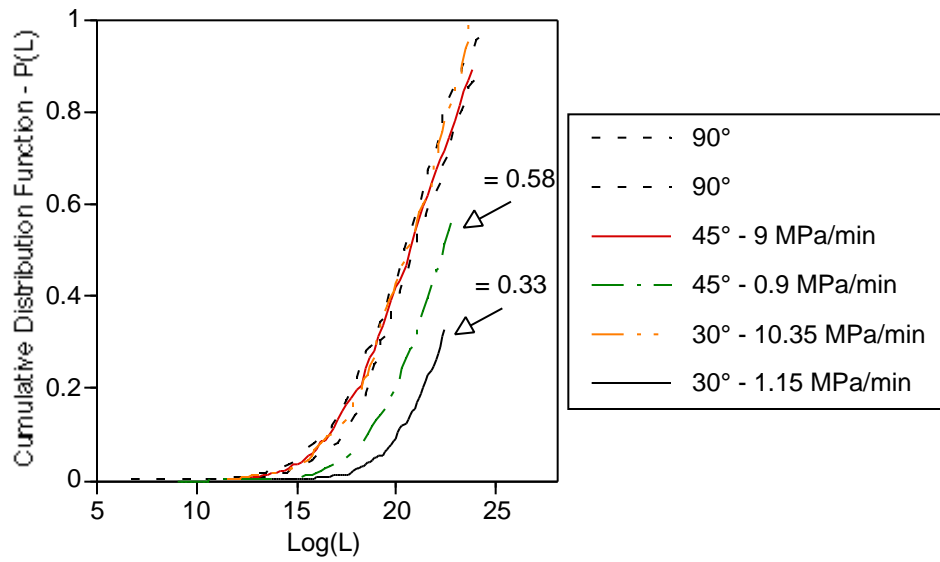


Figure 7.65: CDF of AE events detected from off-axis and 90° samples loaded with different rates with L as the distribution parameter.

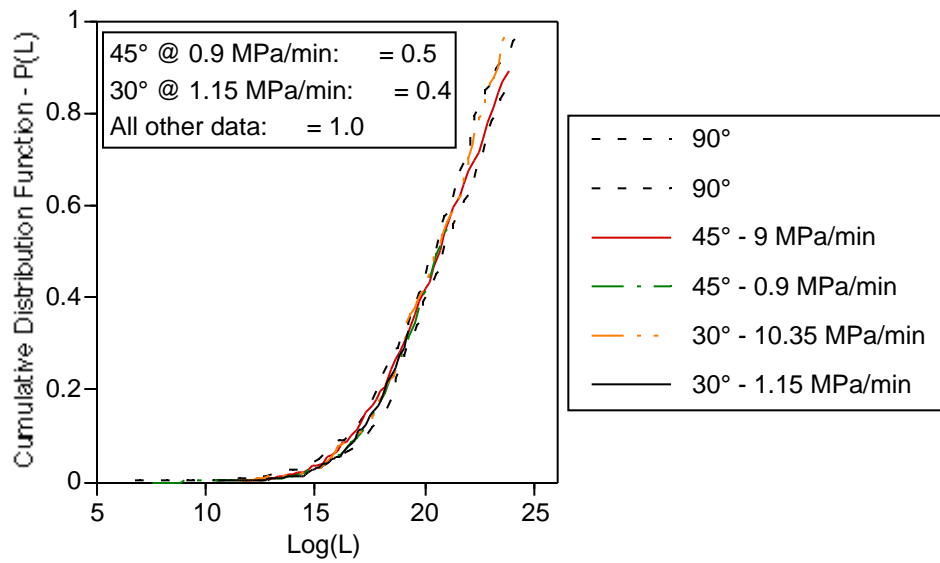


Figure 7.66: CDF of AE events detected from off-axis and 90° samples loaded with different rates with L as the distribution parameter.

7.9 Final Comments on AE Experiments and Analysis

Ramp/Hold testing was the most beneficial in isolating the time or rate effects of microcracking in 90° samples. Although creep testing is frequently used to find time-dependence of stress-strain behavior, as analysis is greatly simplified, here the limitation is with data acquisition. A step loading (in reality a very high rate ramp) causes a large quantity of cracking in a very short interval. Current data acquisition computers are not fast enough to capture all of this data. In addition, continued loading subsequent to a hold period is also important. Material parameters which successfully account for a first ramp and hold portion of loading do not account for cracking detected in the subsequent loading. Data from a subsequent loading gives the best indication of the amount of microstructural relaxation which has occurred from the observed delay in cracking.

Using the CDF of microcracking as a damage variable greatly simplifies the analysis of rate-dependent cracking. A wide variation in cumulative event count was observed for identical loadings and can completely mask any rate effects. This is probably due to variations in test to test on the ‘detectability’ of events. Sensor placement, coupling, choice of the region of material to be tested, thickness, variation in sensor sensitivity and many other factors can affect the total number of events detected. However, very little variation was observed in the CDF of this cracking from sample to sample and from two sensor types. Indeed, this may be effective for viewing differences in cracking of different material systems where the ‘detectability’ of events varies with material system due to differences in material acoustical properties.

Chapter 8

Characterization of Viscoelastic Functions

8.1 Linear Viscoelastic Properties

The linear viscoelastic compliance of the composite under study was fit with a power-law

$$D(t) = D_0 + D_1 t^n. \quad (8.1)$$

Typically, one extracts the creep compliance by performing creep testing and plotting the data against t^n while iterating on n until the best linear fit is found. The D_1 is the slope and D_0 the intercept. However, from a practical standpoint, one must test at very low stresses to see linear behavior. Consequently, the change in strain is quite small. Experimental scatter can significantly affect the results. Indeed, small errors in n can lead to large error for long-term predictions (Tuttle and Brinson, 1986).

The material under study displayed considerable scatter at low stress during creep loading, as shown for a 90° sample in Figure 8.1. However, the

recovery portion showed very little scatter. Linear viscoelastic recovery strain can be written as

$$\epsilon_r = D_1\sigma[(1 - \lambda)^n - \lambda^n]t_1^n \quad (8.2)$$

where t_1 is the unloading time and λ is the normalized time

$$\lambda = \frac{t - t_1}{t_1}. \quad (8.3)$$

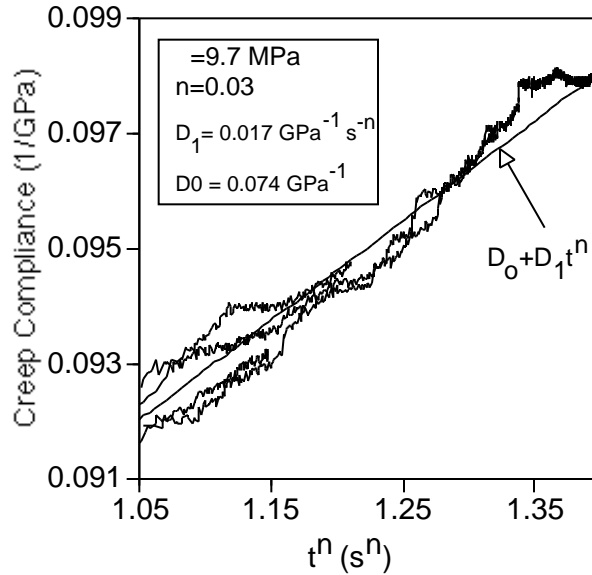


Figure 8.1: Linear viscoelastic creep of a 90° unidirectional sample. Multiple length creep cycles are shown.

Recovery data can easily be fit by iterating on n until a best linear fit is found to $\frac{\epsilon_r}{\sigma}$ plotted against $[(1 - \lambda)^n - \lambda^n]$ where D_1 is the slope. Alternatively, one could also perform creep tests for several lengths of time, t_1 . Upon choosing the correct value for n , the recovery curves will collapse into a single curve (Lou and Schapery, 1971). This method was used in this study for additional reasons.

Forseeing that the LVE creep compliance will be used as a basic function in conducting the NLVE analysis, and that stress tends to accelerate the time scale, we need to validate that the material behaves as a power law for all times of interest, that is for very small and very large λ . Long creep cycles provide accurate data for small values and short creep cycles for large values. Large values of λ are affected by strain wandering in long creep tests and small values of λ are affected by the fact that loading is not instantaneous for short tests; one typically only analyzes data starting at 10x's the loading time. Therefore, accurate data can be acquired for all λ constructing an entire recovery curve from multiple length creep tests while only using recovery data from those tests over a time for which strain wandering was negligible.

In this study multiple length creep tests at $1E2, 1E3, 1E4$ and $1E5$ seconds were used to generate a recovery curve as shown in Figure 8.2 for a 90° sample. A power law is found to fit this data extremely well for all λ . Figures 8.3 and 8.4 show the transverse and shear compliance recovery curves generated from a 30° off-axis sample by the same methodology. Notice that the exponent, n , needed to collapse the shear compliance data is different than for the transverse data. This implies that the matrix is not isotropic. The fiber/matrix interphase region probably plays a significant role in the causing the observed behavior. If this region is rubbery (incompressible) in nature, transverse loading will appear stiffer as the interphase region draws in surrounding material. With shear loading, this does not occur and the region allows larger relative motion of the fiber and matrix. Consequently, a larger compliance, and higher effective exponent, is observed in shear. Figures 8.5 and 8.6 show the recovery curves from 45° off-axis samples where once again the difference in exponents is observed.

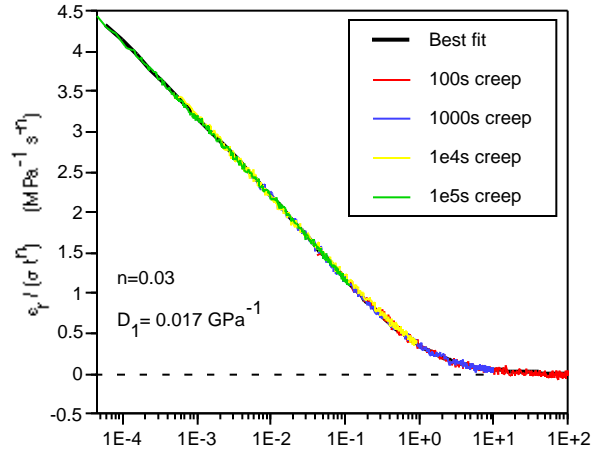


Figure 8.2: Low stress recovery of a 90° unidirectional sample. Multiple length creep cycles have been used to construct the entire recovery curve.

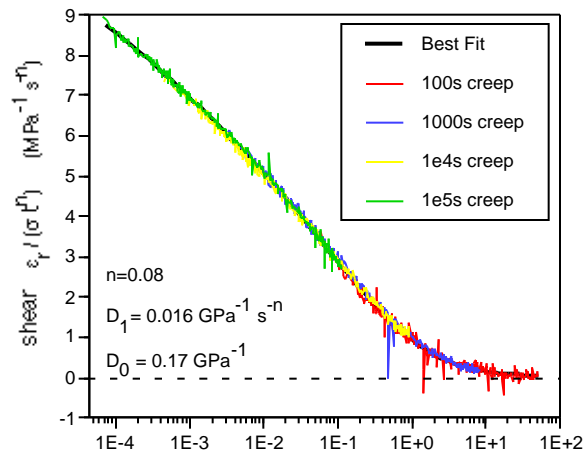


Figure 8.3: Linear viscoelastic recovery of the shear compliance in a 30° off-axis sample. Multiple length creep cycles have been used to construct the entire recovery curve.

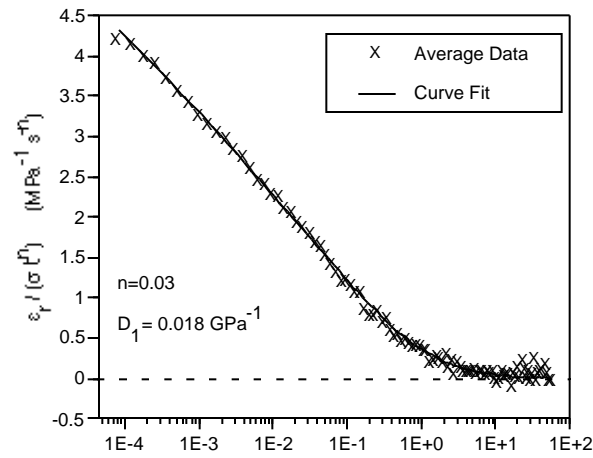


Figure 8.4: Linear viscoelastic recovery of the transverse compliance in a 30° off-axis sample. Multiple length creep cycles have been used to construct the entire recovery curve.

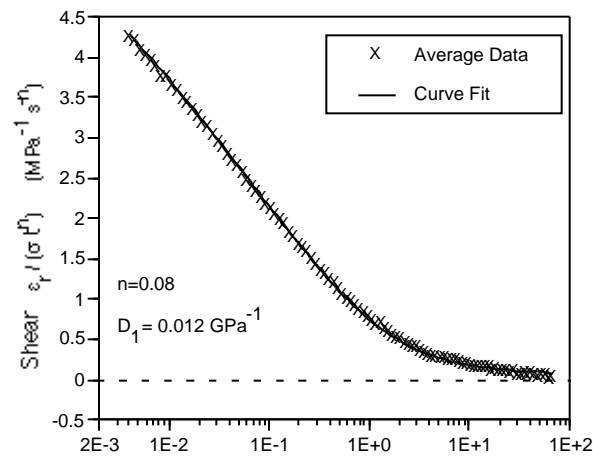


Figure 8.5: Linear viscoelastic recovery of the shear compliance in a 45° off-axis sample. Multiple length creep cycles have been used to construct the entire recovery curve.

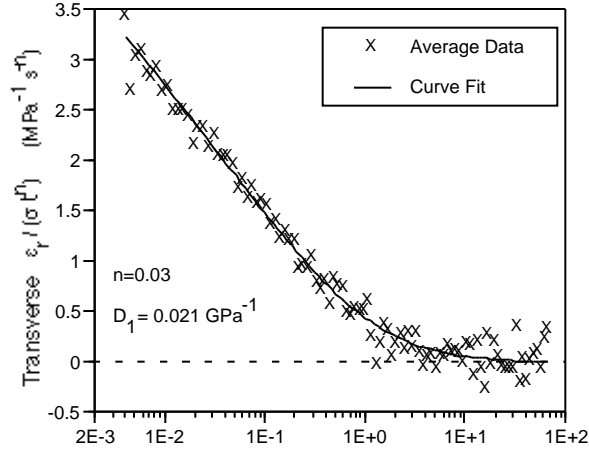


Figure 8.6: Linear viscoelastic recovery of the transverse compliance in a 45° off-axis sample. Multiple length creep cycles have been used to construct the entire recovery curve.

8.1.1 Effect of Damage on Linear Viscoelastic Response

The effect of damage on the linear viscoelastic response can be evaluated in the same way as the nonlinear response. Recovery at low stress is given by Equation 2.42,

$$\frac{(\epsilon_r - \epsilon_{vp}^c)}{\sigma t_i^n} = g_1^{lc} D_1 [(1 - \lambda)^n - \lambda^n]. \quad (8.4)$$

where all effects of damage are in g_1^{lc} ; $g_1^{lc} = 1$ in the as-manufactured state.

Low-stress creep/recovery tests were performed on several 90° and 30° samples before and after high stress loadings. Tables 8.1 and 8.2 show the loading used to damage the material and the effect on g_1^{lc} . A small, but identical, increase was seen in 90° samples at all stress levels tested. No effect was seen on either the shear or transverse recovery in 30° off-axis samples.

Table 8.1: Creep cycling and the effect on g_1^{lc} in 90° samples.

Creep Stress (MPa)	Cycles	g_1^{lc}
35	9 @ 100s	1.08
41	9 @ 100s	1.09
55	9 @ 1000s	1.08

Table 8.2: Creep cycling and the effect on g_1^{lc} in 30° off-axis samples.

Creep Stress (MPa)	Cycles	g_1^{lc} Shear	g_1^{lc} Transverse
61	2 @ 1000s	1.0	1.0
83	1 @ 1000s	1.0	1.0

8.2 Cyclic Effect on Creep and Recovery

When the material is loaded quickly to a high stress it is damaged upon load-up and the damage continues to grow while the load is held. Plastic strain may also increase during this period. Upon unloading, the damage growth ceases as does the increase in plastic strain. Upon repeated loadings, the increment of damage and plastic strain with each cycle may become negligible. A measurement of interest is the additional strain due to each cycle. When the change in creep/recovery strain due to each additional cycle is negligible, the material is called ‘mechanically conditioned’. All data displayed in this section has been conditioned with 9 creep/recovery cycles.

Following are some examples of the cyclic creep/recovery response from 90° and off-axis laminates. In each case, strains from each cycle have been zeroed at the beginning of that cycle so that only strain due to the current loading is displayed. For all stresses tested, some portion of the strain in the initial cycles was permanent. Sufficient time was left between cycles so that hereditary effects from the previous cycles do not affect the data shown.

8.2.1 Cyclic Response of 90° Samples

Cyclic behavior at 60% of failure strength

Figures 8.7 and 8.8 show the cyclic creep and recovery of a 90° sample loaded at 41 MPa. The conditioned curve represents an average of repeated cycles. First looking at creep, little effect, aside from that at initial load-up, is seen from cycle to cycle. One might conclude that little damage has been done to the material. However, as will be shown in Section 8.3, loading to this stress produces considerable damage and has a distinct effect on strain. We may therefore conclude that the majority of damage is done upon load-up and there is little effect from damage growth during the 100s creep period. This is confirmed by looking at the recovery portion. A small amount of plastic strain has been removed from cycles 1 and 2 (9 and 2 microstrain respectively). If strain during creep was significantly affected by the growth of damage, the shape of the recovery curve in Figure 8.8 would not match that of the conditioned response due to the hereditary effect of the damage history integral, I_2 of Equation 2.25. Yet, cycles 1 and 2 match the conditioned response.

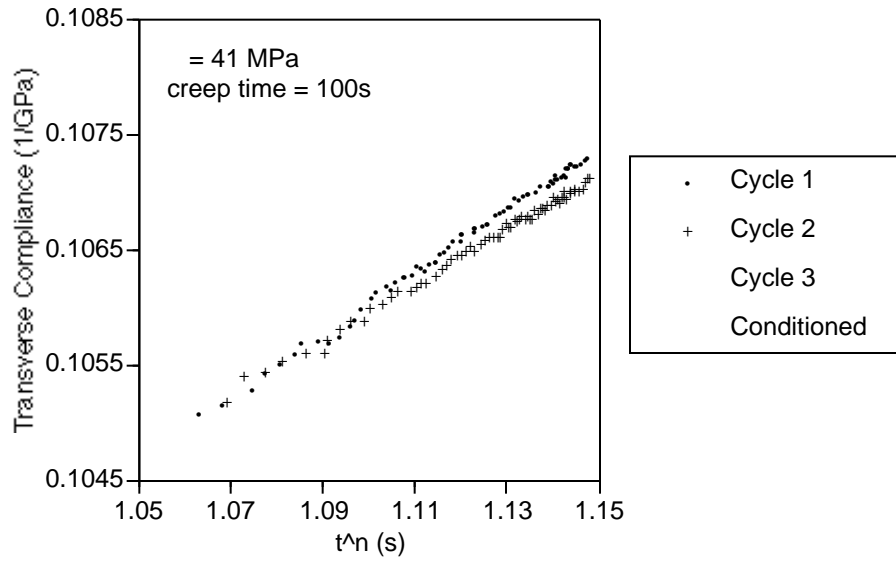


Figure 8.7: Cyclic transverse creep compliance at 41 MPa in a 90° sample. Strain has been zeroed at the beginning of each cycle.

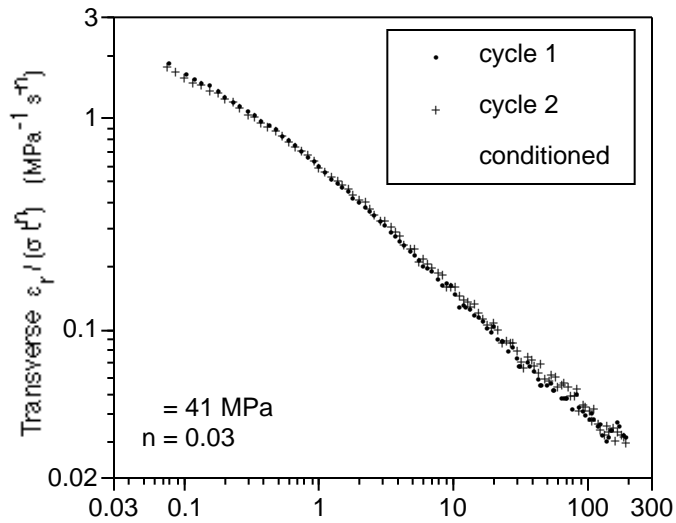


Figure 8.8: Cyclic transverse recovery compliance at 41 MPa in a 90° sample. Strain has been zeroed at the beginning of each cycle. A small amount of plastic strain has been removed from cycles 1 and 2.

Cyclic behavior at 80% of failure strength

Figures 8.9 and 8.10 show the cyclic creep and recovery of a 90° off-axis sample loaded at 55 MPa. The conditioned curve represents an average of repeated cycles. Here the effect of damage and growth of plastic strain is more evident as the first creep cycle clearly shows more time dependence than the other cycles. A large difference in the recovery curves is due to the viscoplastic strain accumulated during creep and masks the damage effects on the v/e strain. It is not possible to find the exact value of the v/p strain without curve fitting Equation 2.26, unless the effect of damage growth during creep has little hereditary effect, as was the case at 41 MPa. That is, whether or not the g_2 parameter changes appreciably during creep. Without going through this rigor, it is possible to quickly check if the effect is significant.

If g_2 does not change appreciably during creep, then $g_2(0) \approx g_2(t_i)$ and $I_2 \approx 0$ as shown in Equation 2.26. This leads to a recovery equation similar to that for the conditioned material, Equation 2.29, except the conditioned parameters are the values at the end of the creep cycle, time t_i . If this is the case, then the removal of a constant v/p strain and vertical shifting, as outlined in Section 2.3.2, will collapse the recovery data from each cycle. Here, after vertical shifting and the removal of plastic strain, the shape of the conditioned recovery curve is still different than seen in the first two cycles, as shown in Figure 8.11. The hereditary damage effect appears to be significant.

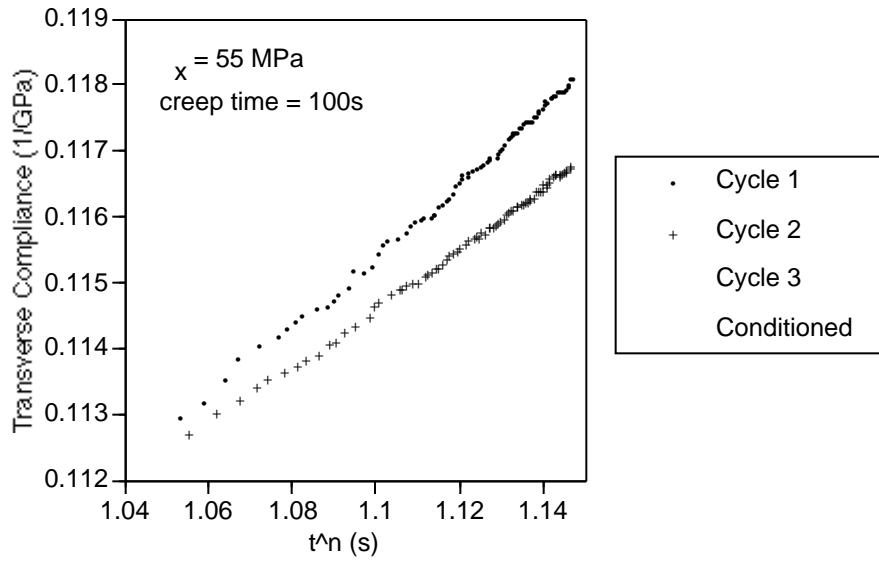


Figure 8.9: Cyclic transverse creep compliance at 55 MPa in a 90° sample. Strain has been zeroed at the beginning of each cycle.

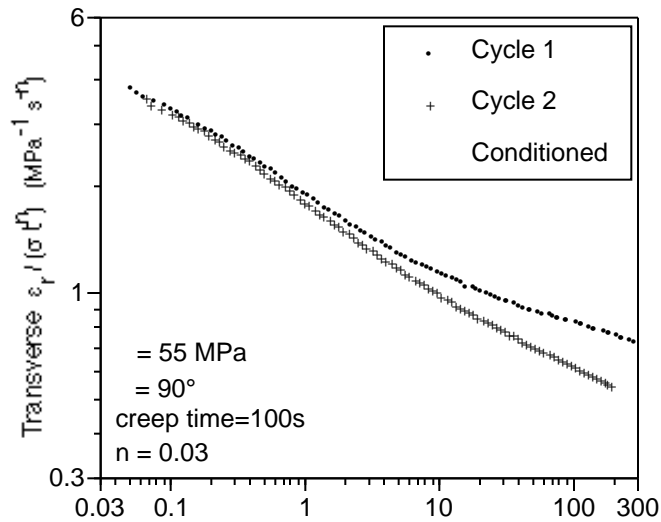


Figure 8.10: Cyclic transverse recovery compliance at 55 MPa in a 90° sample.

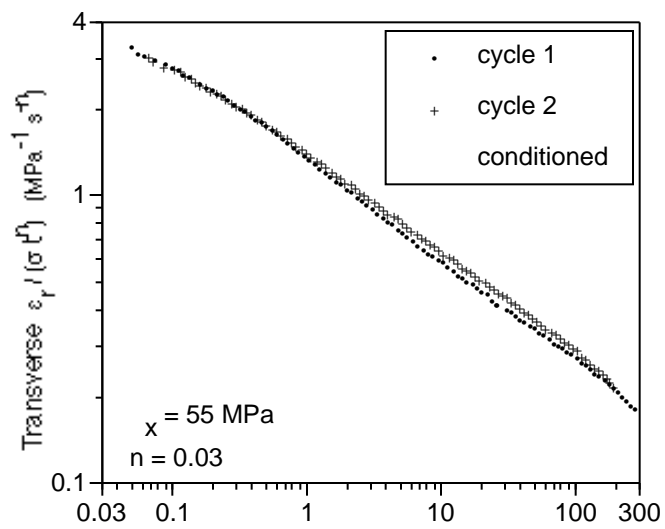


Figure 8.11: Cyclic transverse recovery compliance at 55 MPa in a 90° sample. Strain has been zeroed at the beginning of each cycle. Cycles 1 and 2 have been vertically shifted and plastic strain removed.

8.2.2 Cyclic Response of 30° Off-axis Samples

Figures 8.12 and 8.13 show the cyclic creep and recovery of a 30° off-axis sample loaded at 69 MPa. The conditioned curve represents an average of repeated cycles. Despite the softening effect of damage, the amount of shear creep strain decreases with each cycle as the addition of plastic strain drops off. Aside from the initial compliance, little effect of damage is seen on the transverse strains.

That transverse strains are not affected by cycling at this load is also evident in the recovery where no difference from cycle to cycle is seen. Since the Damage Effect Study clearly shows an effect of loading even to 10 MPa below this stress, we again conclude that all damage affecting the transverse strains was done upon load-up in the first cycle.

Recovery of the shear strain sees a strong cycle-to-cycle variation. A large effect is due to plastic strain accumulated during creep and masks the damage effects on the v/e strain. As done for the 90° data at 55 MPa, this strain is removed to see if vertical shifting will collapse the data, as shown in Figure 8.14. Here, the shape of the conditioned recovery curve is still different than seen in the first two cycles. Once again the hereditary damage effect is significant and/or the effect of damage is more complicated in this material than assumed.

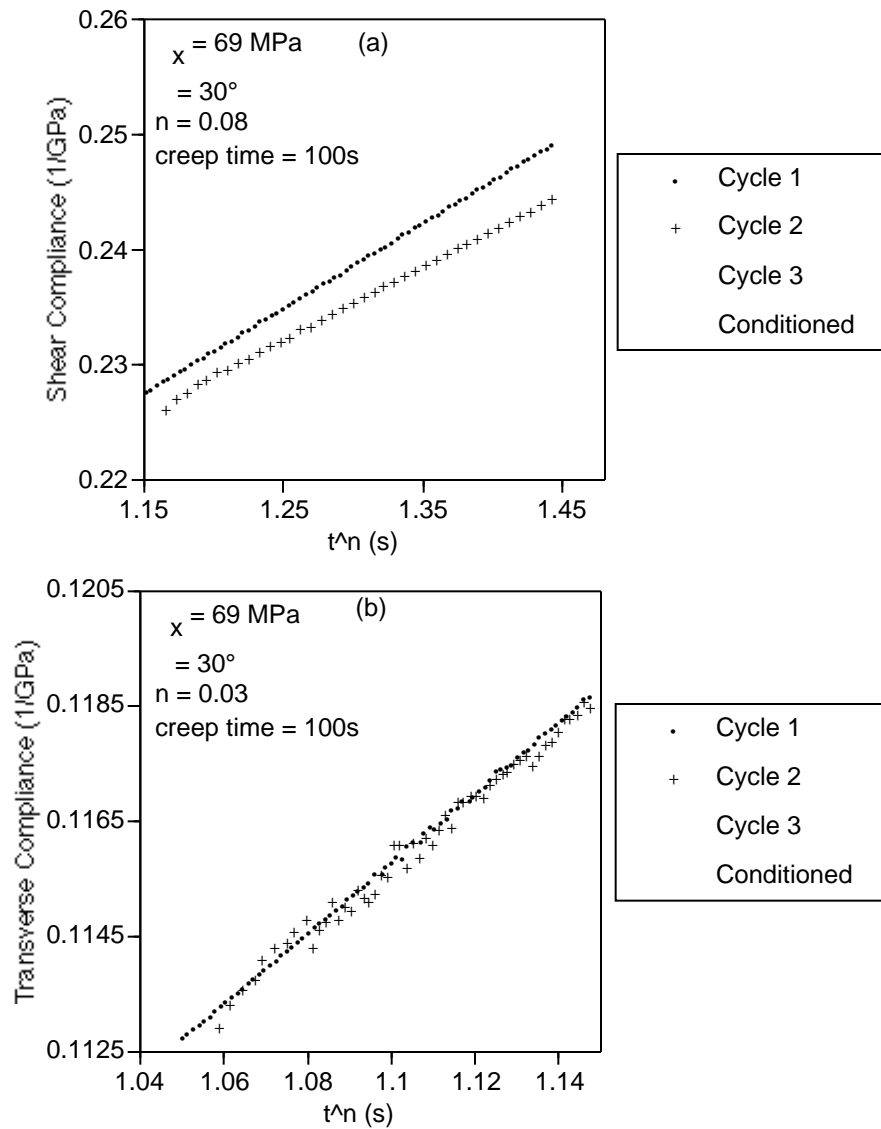


Figure 8.12: Cyclic (a) shear and (b) transverse creep compliance at 69 MPa in a 30° off-axis sample. Strain has been zeroed at the beginning of each cycle.

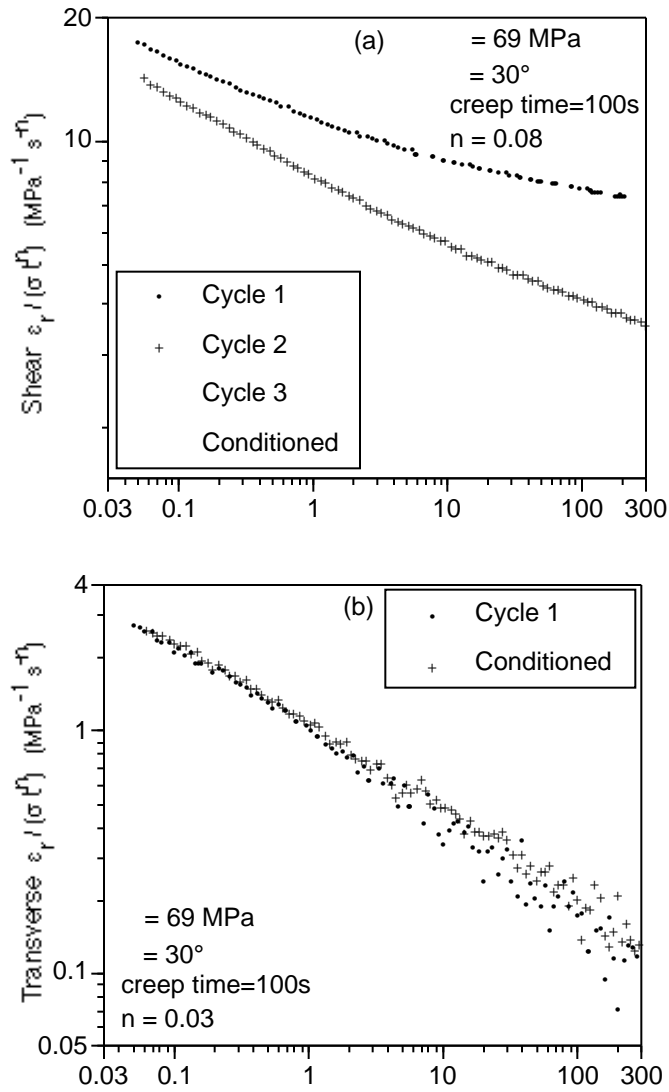


Figure 8.13: Cyclic (a) shear and (b) transverse recovery compliance at 69 MPa in a 30° off-axis sample. Strain has been zeroed at the beginning of each cycle.

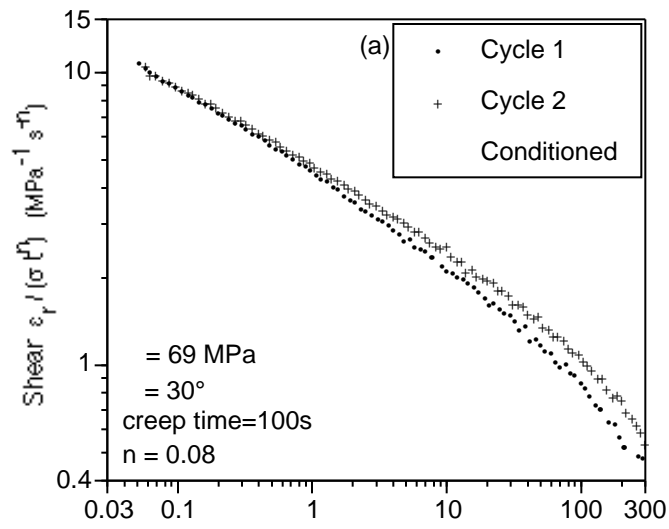


Figure 8.14: Cyclic shear recovery compliance at 69 MPa in a 30° off-axis sample. Strain has been zeroed at the beginning of each cycle. Cycles 1 and 2 have been vertically shifted and plastic strain removed.

8.3 Results from the Damage Effect Study

8.3.1 Damage Effect in 90° Samples

Figure 2.2 shows the general loading history used in this study. Table 8.3 designates each damage state by the stress level used and number of cycles. These stress levels are shown on a stress-strain curve for reference in Figure 8.15. Conditioned cycles were for 100s and 1000s.

Table 8.3: Damage states used in the damage effect study on 90° samples.

Damage State	Stress (MPa)	Cycles
S_1	31	9 @ 1000s
S_2	41	9 @ 1000s
S_3	55	9 @ 1000s

Figures 8.16 and 8.17 show the effect of damage on the transverse creep compliance at 31 and 41 MPa. Figures 8.18 and 8.19 show the effect on recovery from these cycles. Each curve represents the average of multiple cycles. As discussed in Section 2.3.2, if when plotted on a log-log scale the recovery strain at different damage states can be vertically shifted to coincide for a given stress level, damage only enters the recovery equation through $g_1^c g_2^c$ and does not affect a_σ . As shown in Figure 8.20, vertical shifting does indeed collapse the recovery curves at both stress levels. However, it should be noted that a small amount of constant strain needed to be removed from the more highly damaged cycles prior to vertical shifting.

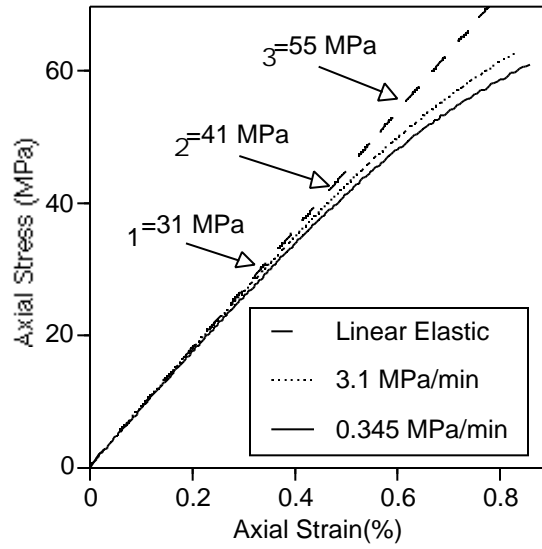


Figure 8.15: Stress strain response of 90° samples with the stresses used in the damage effect study.

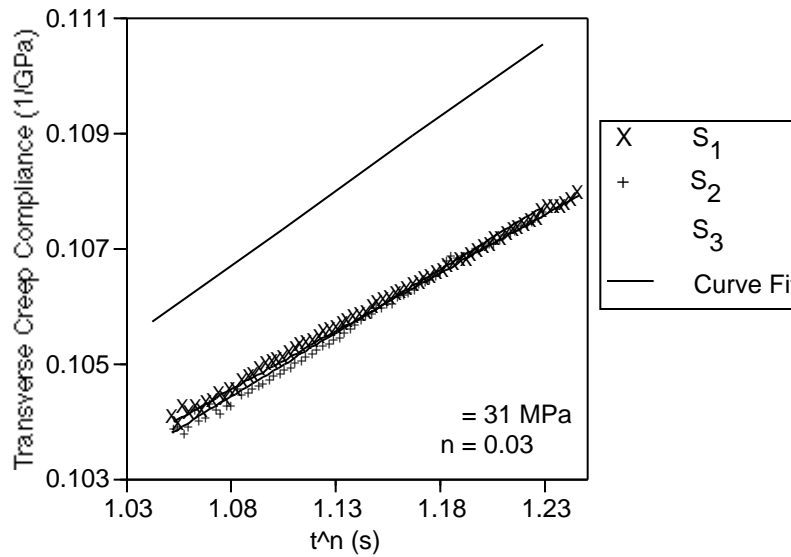


Figure 8.16: Transverse creep compliance of a 90° sample at 31 MPa for three damage states. Damage states are shown in Table 8.3.

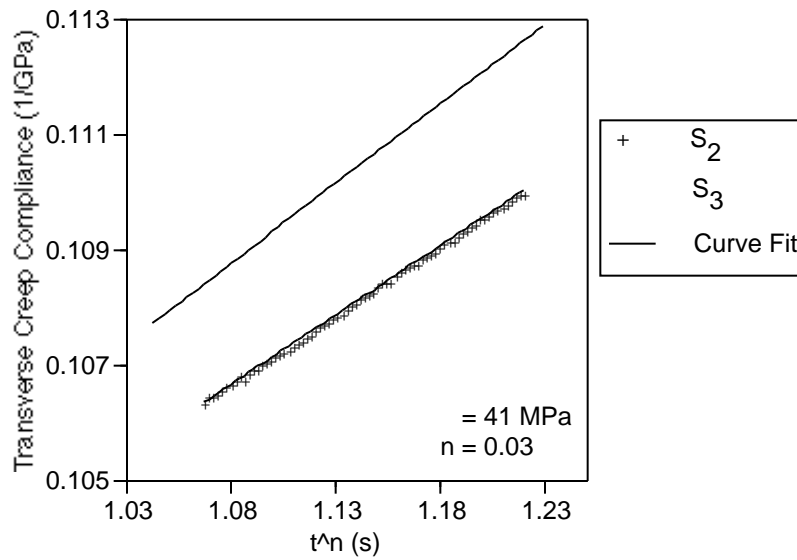


Figure 8.17: Transverse creep compliance of a 90° sample at 41 MPa for three damage states. Damage states are shown in Table 8.3.

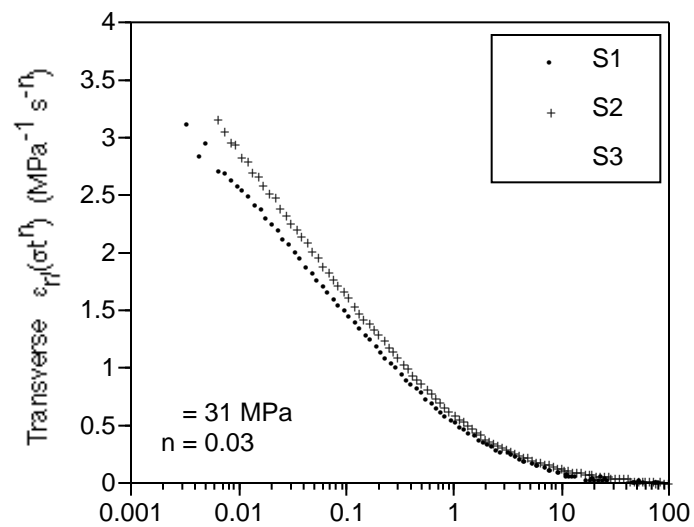


Figure 8.18: Transverse recovery compliance of a 90° sample at 31 MPa for three damage states. Damage states are shown in Table 8.3.

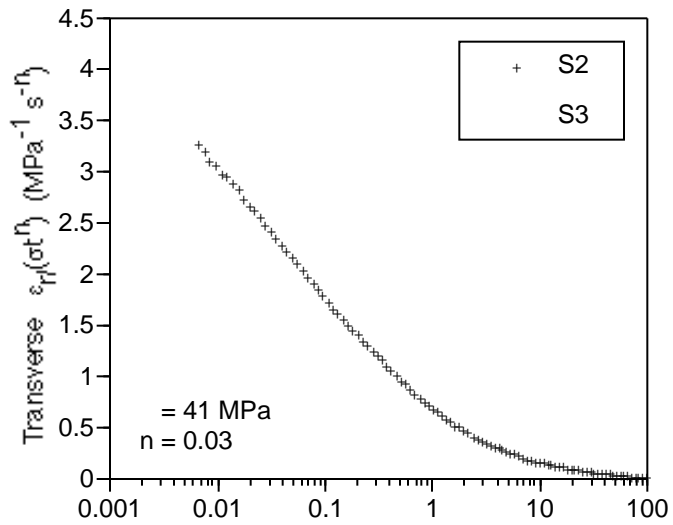


Figure 8.19: Transverse recovery compliance of a 90° sample at 41 MPa for three damage states. Damage states are shown in Table 8.3.

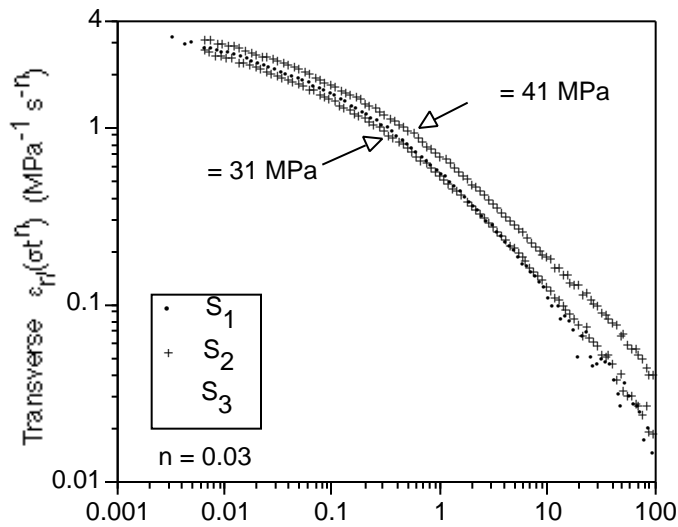


Figure 8.20: Transverse recovery compliance of a 90° sample at 31 and 41 MPa. Higher damage states have been vertically shifted to the lowest state tested. Damage states are shown in Table 8.3.

Analyses of this data as described in Section 2.3.2 yields the damage ratios shown in Figure 8.21. Here we have defined the damage state, S , as the value of the Cumulative Distribution Function of microcracking. Estimates of these values were made based on the CDF derived from the ramp testing presented in Section 7.8 for the three damage states shown. At both stress levels, the creep and recovery ratios, R_c and R_r , are the same. This indicates that damage only affects g_2^c and does not affect g_1^c . The elastic compliance actually stiffens with increased damage as R_e decreases with S .

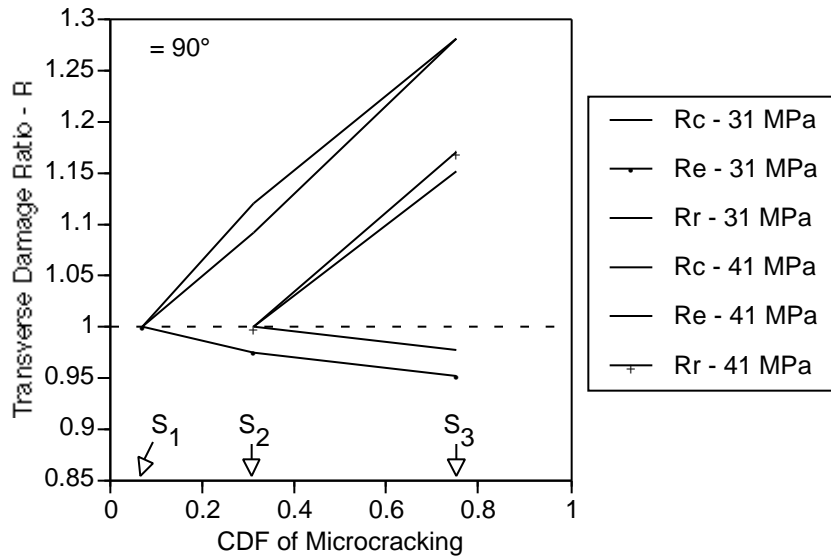


Figure 8.21: Transverse compliance damage effect ratios from a 90° sample. A damage state has been characterized by the Cumulative Distribution Function of microcracking at that state. Estimates for the value of the CDF were made from the ramp testing of Section 7.8.

8.3.2 Damage Effect in 45° Samples

Table 8.4 designates each damage state in this study by the stress level and number of cycles at that stress. A stress-strain curve with these stresses

labeled is shown for reference in Figure 8.22. Conditioned cycles were for 100s and 1000s.

Table 8.4: Damage states used in the damage effect study on 45° samples.

Damage State	Stress (MPa)	Cycles
S_1	38	9 @ 1000s
S_2	62	9 @ 1000s
S_3	76	1 @ 10s

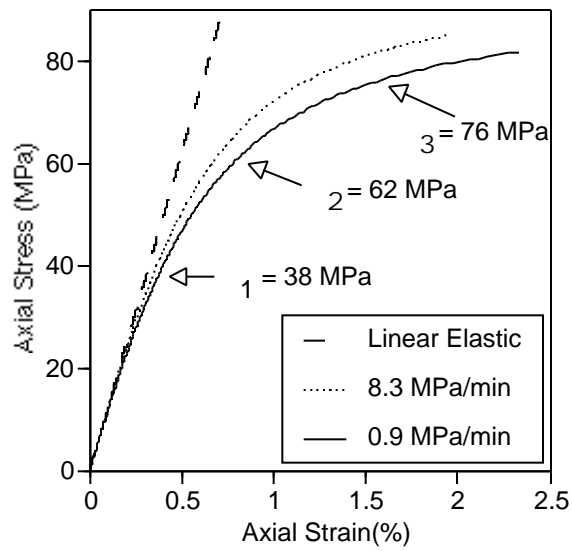


Figure 8.22: Stress strain response of 45° samples with the stresses used in the damage effect study.

45° Off-axis: Shear Compliance

Figures 8.23 and 8.24 show the effect of damage on the shear creep and recovery compliances at 38 and 62 MPa. Each curve represents the average of multiple cycles. Note that the recovery curves have been vertical shifted to the lowest damage state at each stress and a constant amount of strain was removed prior to vertical shifting, as was done for the 90° samples. This strain was larger for the 1000s cycles than for the 100s cycles. Also, the vertical shifting did not completely account for the effect of damage at 38 MPa. Notice the curves from different damage state did not collapse well. After removing the additional strain, the data was analyzed as described in Section 2.3.2. Damage ratios are shown in Figure 8.25. Unlike the transverse strain measured for 90° samples, the creep and recovery ratios, R_c and R_r , are *not* the same. Damage therefore enters through both g_1^c and g_2^c .

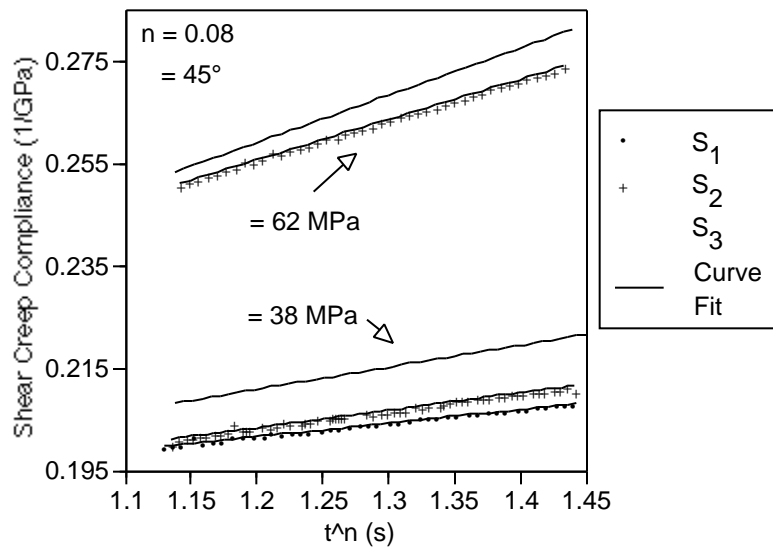


Figure 8.23: Shear creep compliance of a 45° off-axis sample at 38 MPa and 62 MPa for three damage states. Damage states are shown in Table 8.4.

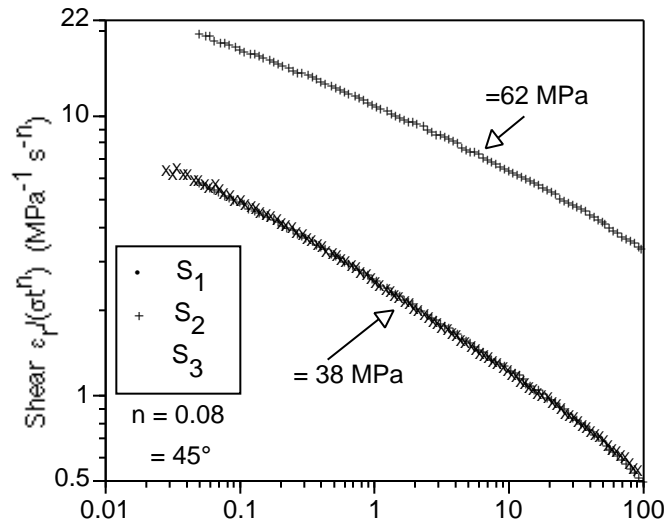


Figure 8.24: Shear recovery compliance at 38 and 62 MPa of a 45° off-axis sample. Higher damage states have been vertically shifted to the lowest state tested. Damage states are shown in Table 8.4.

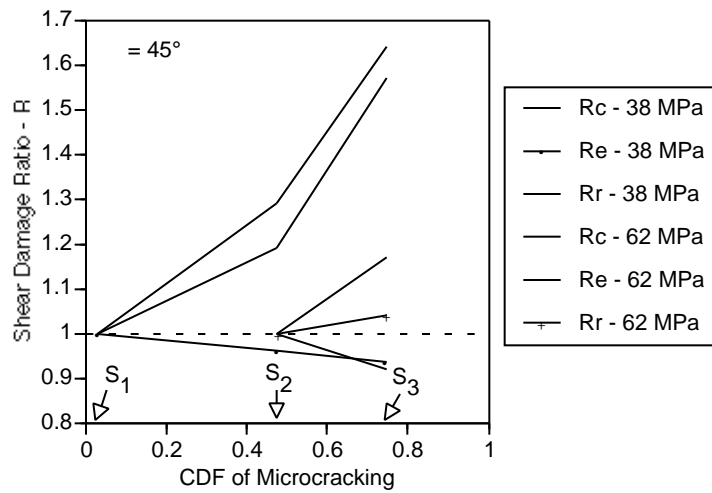


Figure 8.25: Shear compliance damage effect ratios from a 45° sample. A damage state has been characterized by the Cumulative Distribution Function of microcracking at that state. Estimates for the value of the CDF were made from the ramp testing of Section 7.8.

45° Off-axis: Transverse Compliance

Figures 8.26 and 8.27 show the effect of damage on the transverse creep and recovery compliances at 38 and 62 MPa. As was done for the shear recovery data, the transverse recovery curves have been vertically shifted to the lowest damage state at each stress after a constant amount of strain was removed. This shifting worked better for the transverse data than for the shear. This strain was larger for the 1000s cycles than for the 100s cycles. Damage ratios are shown in Figure 8.28. As in the 90° sample, the creep and recovery ratios, R_c and R_r , are the same, indicating that damage does not affect g_1^c .

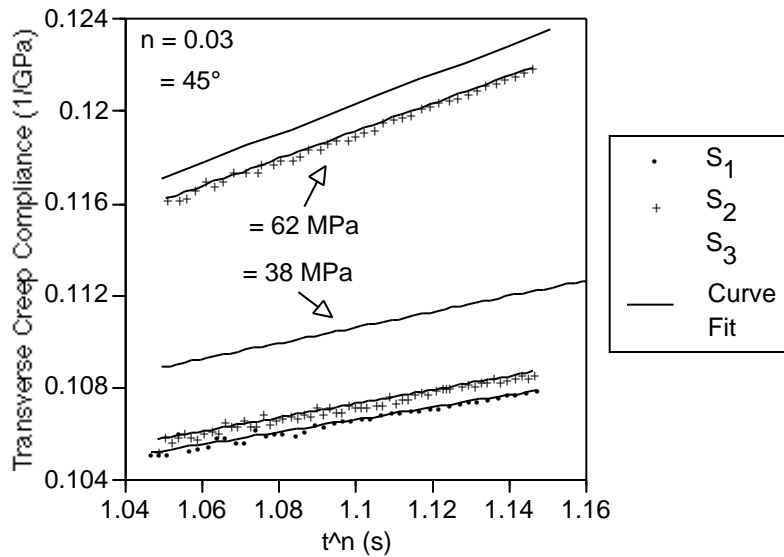


Figure 8.26: Transverse creep compliance of a 45° off-axis sample at 38 MPa and 62 MPa for three damage states. Damage states are shown in Table 8.4.

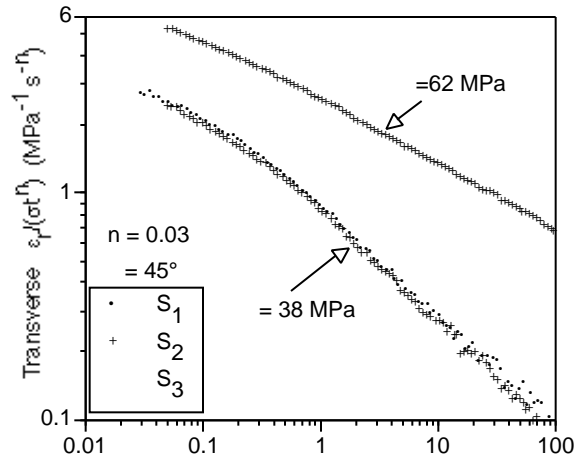


Figure 8.27: Transverse recovery compliance at 38 and 62 MPa of at 45° off-axis sample. Higher damage states have been vertically shifted to the lowest state tested. Damage states are shown in Table 8.4.

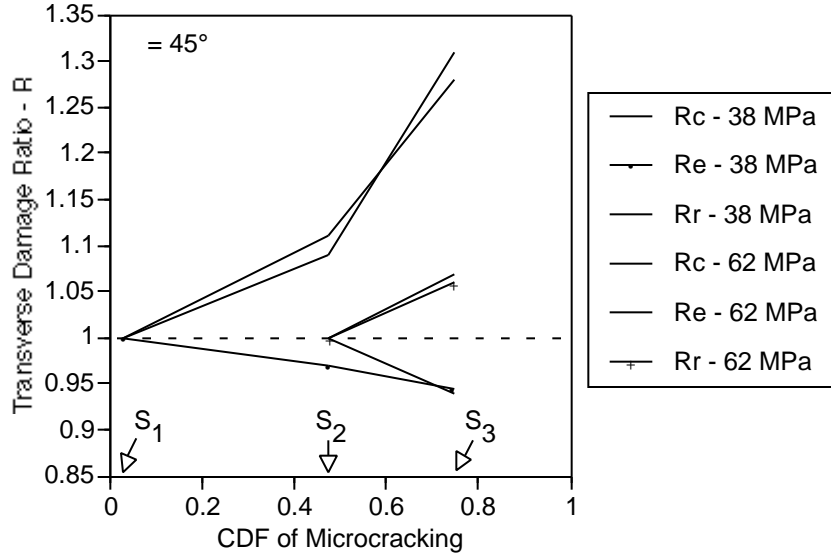


Figure 8.28: Transverse compliance damage effect ratios from a 45° sample. A damage state has been characterized by the Cumulative Distribution Function of microcracking at that state. Estimates for the value of the CDF were made from the ramp testing of Section 7.8.

8.3.3 Damage Effect in 30° Samples

Table 8.5 designates each damage state in this study by the stress level and number of cycles at that stress. A stress-strain curve with these stresses labeled is shown for reference in Figure 8.29. Conditioned cycles were for 100s.

Table 8.5: Damage states used in the damage effect study on 30° samples.

Damage State	Stress (MPa)	Cycles
S_1	38	9 @ 100s
S_2	59	9 @ 100s
S_3	97	1 @ 15s

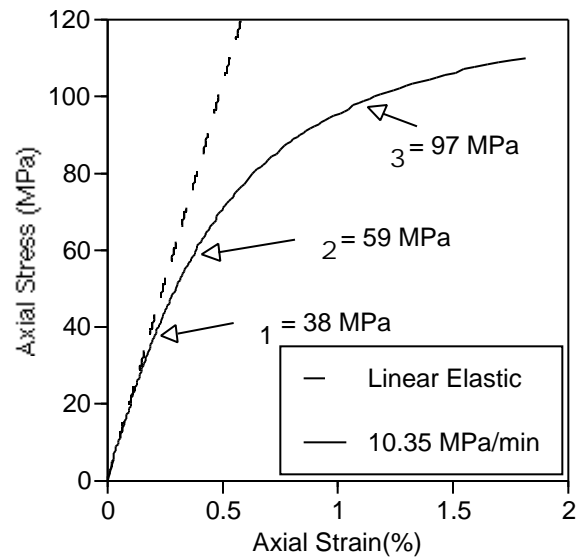


Figure 8.29: Stress strain response of 30° samples with the stresses used in the damage effect study.

30° Off-axis: Shear Compliance

Figures 8.30 and 8.31 show the effect of damage on the shear creep and recovery compliances at 38 and 59 MPa. Each curve represents the average of multiple cycles. Once again, the recovery curves have been vertical shifted to the lowest damage state at each stress and a constant amount of strain was removed prior to vertical shifting. Vertical shifting worked better in the 30° samples than in the 45° at 38 MPa, but there are slight differences at long times. After removing the additional strain, the data was analyzed as described in Section 2.3.2. Damage ratios are shown in Figure 8.32. Once again, as seen for the 45° samples, the creep and recovery ratios, R_c and R_r , are *not* the same. Damage therefore enters through both g_1^c and g_2^c .

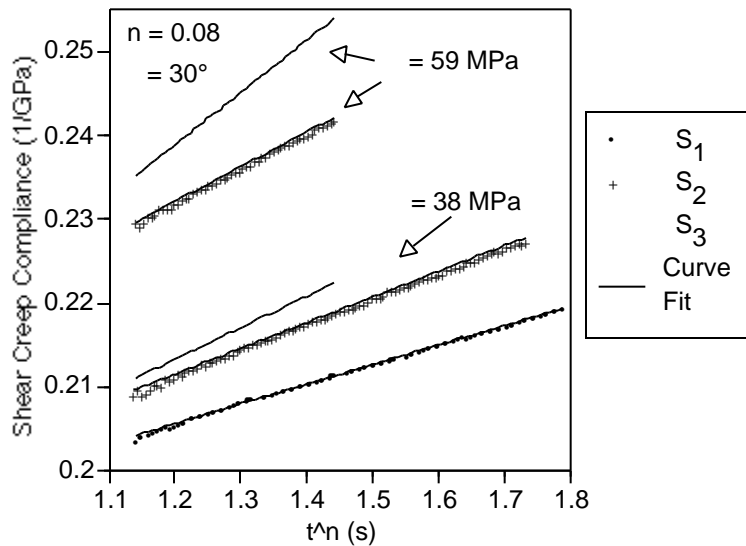


Figure 8.30: Shear creep compliance of a 30° off-axis sample at 38 MPa and 59 MPa for three damage states. Damage states are shown in Table 8.5.

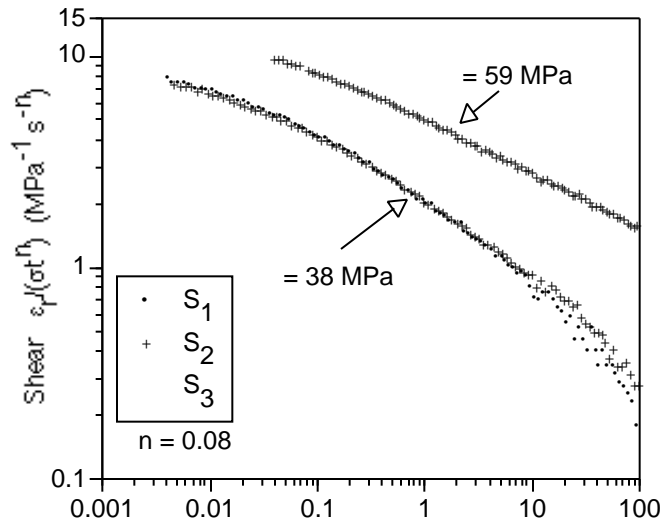


Figure 8.31: Shear recovery compliance at 38 and 59 MPa of a 30° off-axis sample. Higher damage states have been vertically shifted to the lowest state tested. Damage states are shown in Table 8.5.

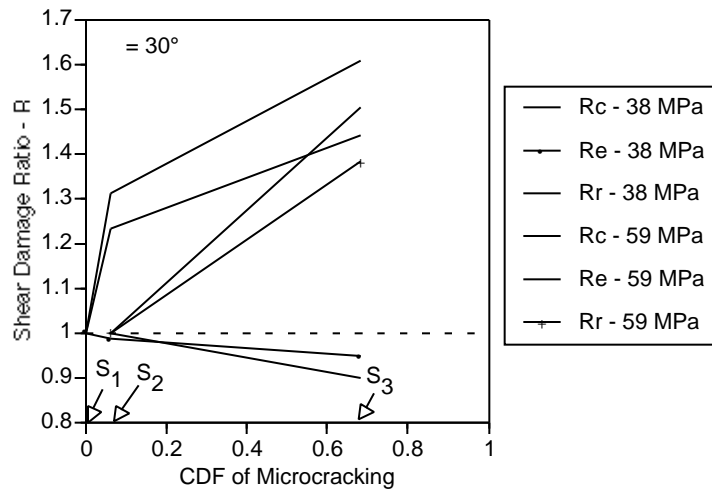


Figure 8.32: Shear compliance damage effect ratios from a 30° sample. A damage state has been characterized by the Cumulative Distribution Function of microcracking at that state. Estimates for the value of the CDF were made from the ramp testing of Section 7.8.

30° Off-axis: Transverse Compliance

Figures 8.33 and 8.34 show the effect of damage on the transverse creep and recovery compliances at 38 and 59 MPa. As was done for the shear recovery data, the transverse recovery curves have been vertically shifted to the lowest damage state at each stress after a constant amount of strain was removed. Damage ratios are shown in Figure 8.35. Once again, the creep and recovery ratios, R_c and R_r , are the same, indicating that damage does not affect g_1^c .

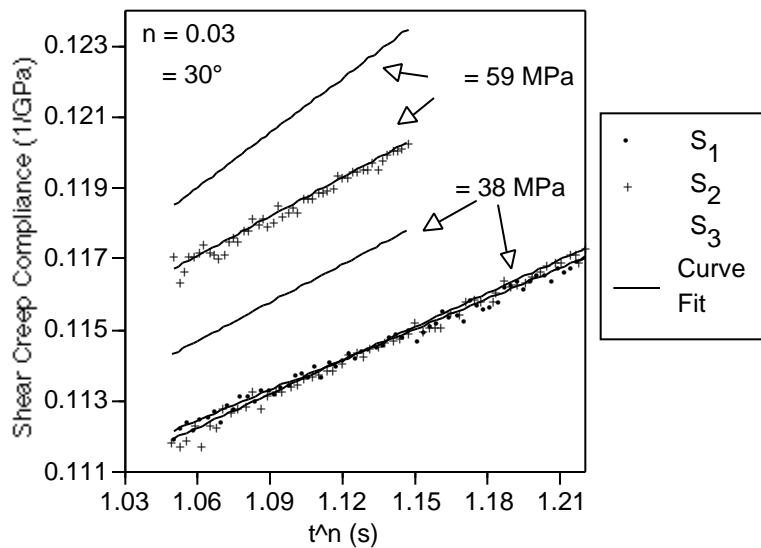


Figure 8.33: Transverse creep compliance of a 30° off-axis sample at 38 MPa and 59 MPa for three damage states. Damage states are shown in Table 8.5.

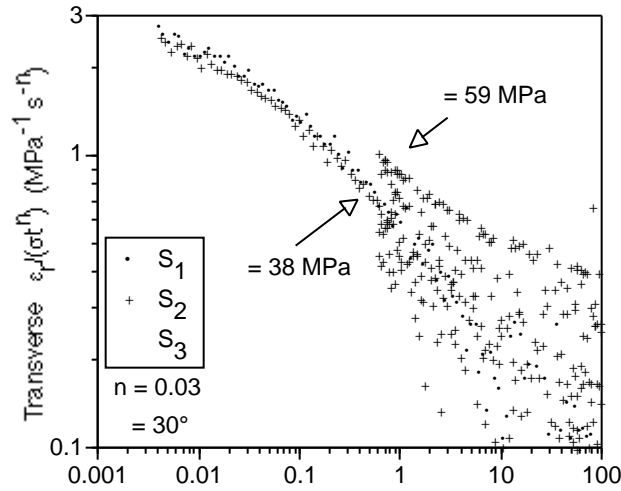


Figure 8.34: Transverse recovery compliance at 38 and 59 MPa of a 30° off-axis sample. Higher damage states have been vertically shifted to the lowest state tested. Damage states are shown in Table 8.5.

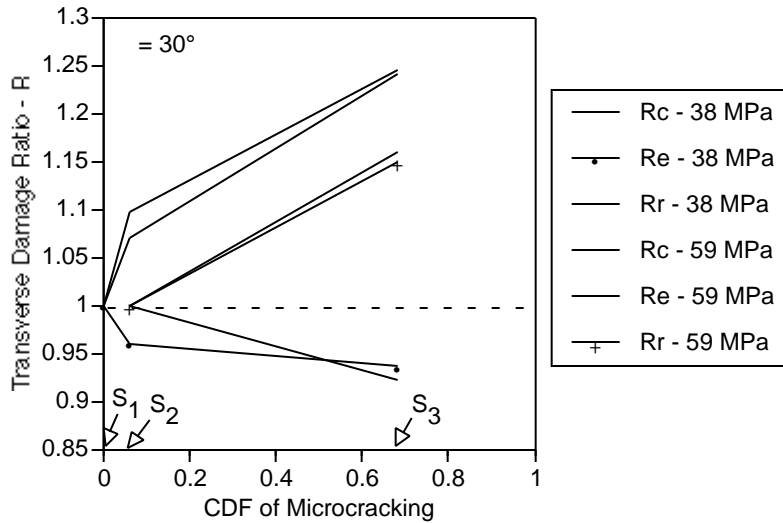


Figure 8.35: Transverse compliance damage effect ratios from a 30° sample. A damage state has been characterized by the Cumulative Distribution Function of microcracking at that state. Estimates for the value of the CDF were made from the ramp testing of Section 7.8.

8.4 Conditioned Material Behavior

The following section displays that the material with fixed amount of damage is clearly nonlinear elastic and viscoelastic. However, standard data analysis methods for deriving the stress dependence of nonlinear viscoelastic materials without growing damage, as described by the constitutive theory by Schapery (1969), do not work on the material under study. We find that horizontal and vertical shifting of the recovery data for the effect of stress does not work in this case, despite being a successful method for many materials in the past. A similar method of data analysis will be briefly reviewed and compared with the data for this material.

For fixed amounts of damage, the stress dependence of the material is found through creep/recovery testing at multiple stress levels. All stresses are at or below the stress at which the material was conditioned and for cycle durations equal or less than the conditioning cycles. In this way, little or no additional damage is done to the material and we effectively have a snapshot of the material behavior at a fixed damage state.

Data analysis was performed in a similar fashion to that outlined by Schapery (1969) for materials without damage where the creep and recovery curves at elevated stresses are shifted to the linear response. Here in the conditioned state we have Equations 2.36 and 2.37 for the creep and recovery behavior. The slope of the creep response when plotted versus t^n is $\frac{g_1^c g_2^c D_1}{a_\sigma^n}$ and the intercept $g_0^c D_0$. Knowing D_0 and D_1 from low stress testing, creep data yields $\frac{g_1^c g_2^c}{a_\sigma^n}$ and g_0^c for each stress level. As discussed previously, g_1^{lc} has a negligible effect on the recovery response. Removing it and rearranging,

$$\frac{(\epsilon_r - \epsilon_{vp}^c)}{\sigma \left(\frac{t_r}{a_\sigma}\right)^n} = g_2^c D_1 [(1 - a_\sigma \lambda)^n - (a_\sigma \lambda)^n]. \quad (8.5)$$

Using the linear behavior as a reference the high stress data was shifted to

$$\frac{\epsilon_r}{\sigma} = D_1[(1 - \lambda)^n - (\lambda)^n]. \quad (8.6)$$

where the a_σ divides the time scale and g_2^c is a vertical shift when plotted on a log-log plot. Thus, a_σ and g_2^c are found directly and can be compared to the ratio $\frac{g_1^c g_2^c}{a_\sigma^n}$ found from creep testing to find g_1^c .

8.4.1 90° testing

A 90° sample was conditioned at 55 MPa (80% of failure strength) with creep/recovery durations of 100s. Figure 8.36 shows the creep response of this conditioned behavior for stress levels at or below 55 MPa. Each curve represents the average response from multiple cycles at a given stress. Clearly this the material is nonlinear as both the slope and intercept of the creep curves increase with stress level. Figure 8.37 shows the recovery of the same 90° sample after creep at various stress levels. The higher stress curves represent the average of multiple cycles and have been shifted to the linear response by various amounts. At no stress level does the data shift well to the linear behavior even with removal of some constant strain.

8.4.2 30° off-axis testing

A 30° off-axis sample was conditioned at 69 MPa (60% of failure strength) with creep/recovery durations of 100s. Figures 8.38 and 8.39 show the creep response of this conditioned behavior for stress levels at or below 69 MPa. Each curve represents the average response from multiple cycles at a given stress. The shear compliance is also clearly nonlinear elastic and viscoelastic as both the slope and intercept of the creep data increases with stress level.

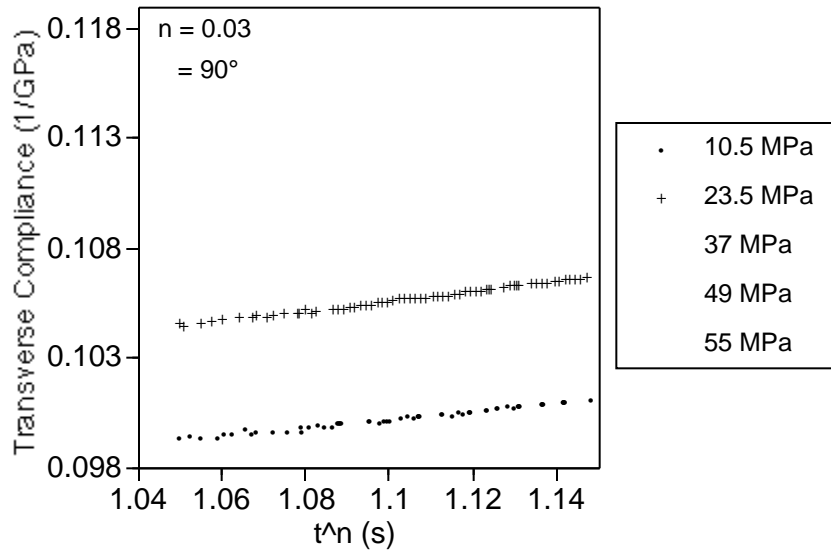


Figure 8.36: Transverse creep compliance of a 90° sample at various stress levels. The sample has been mechanically conditioned at 55 MPa.

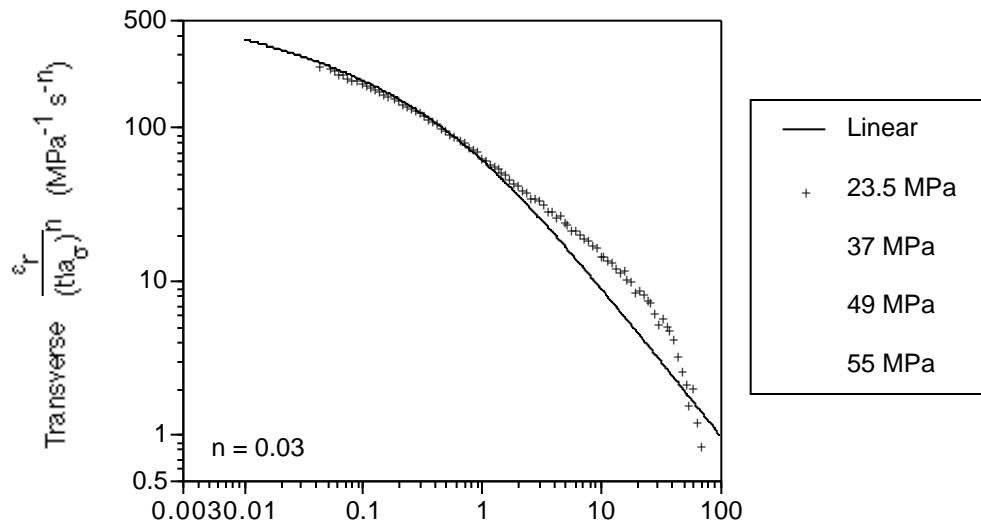


Figure 8.37: Transverse recovery compliance of a 90° sample from creep at various stress levels. Higher stress data has been shifted to the linear curve after subtracting small amounts of constant strain.

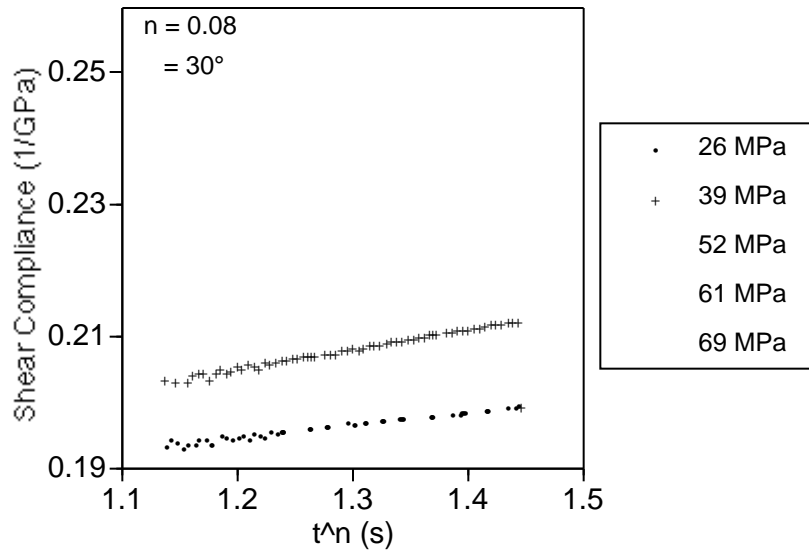


Figure 8.38: Shear creep compliance of a 30° sample from creep at various stress levels. The sample has been mechanically conditioned at 69 MPa.

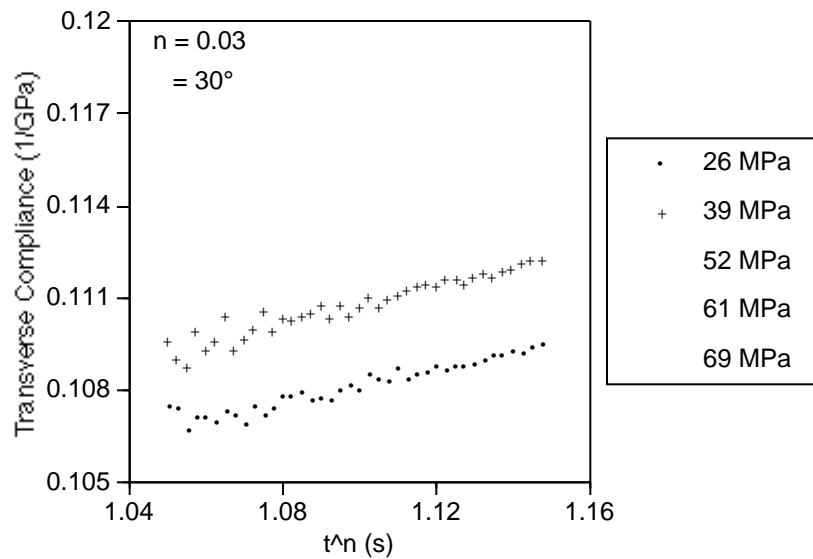


Figure 8.39: Transverse creep compliance of a 30° sample from creep at various stress levels. The sample has been mechanically conditioned at 69 MPa.

Figures 8.40 and 8.41 show the shear and transverse recovery of a 30° off-axis sample after creep at various stress levels. The higher stress curves represent the average of multiple cycles and have been shifted to the linear response. The shear data clearly does not shift well to the linear behavior. The effect of stress is more complicated than Equation 8.5 would imply. The transverse data, matches fairly well over the time-frame shown, but a small constant strain needed to be subtracted from each cycle.

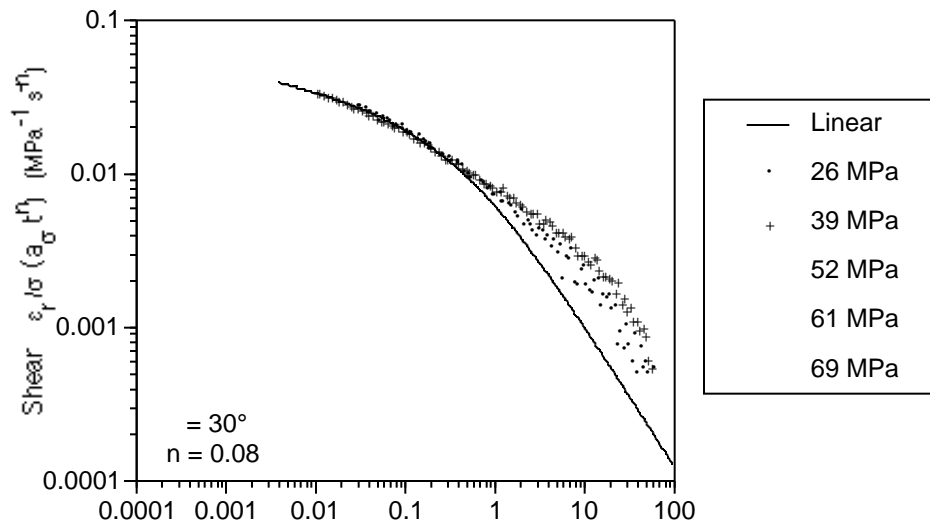


Figure 8.40: Shear recovery compliance from creep at various stress levels. Higher stress data has been shifted to the linear curve.

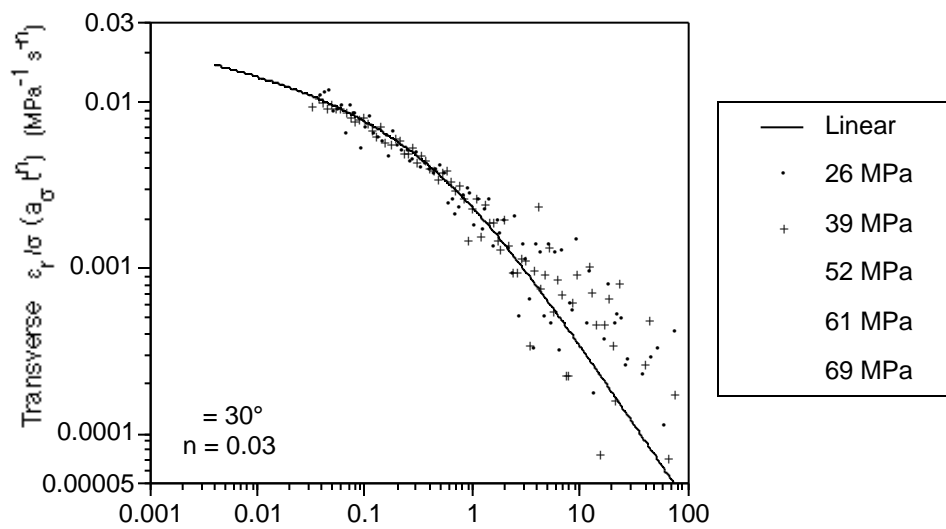


Figure 8.41: Transverse compliance from creep at various stress levels. Higher stress data has been shifted to the linear curve.

8.5 Discussion on Viscoelastic Behavior

Conditioned Behavior

The inability to shift recovery data at higher stress levels to the linear response makes a full characterization of this material impossible at this time. Such shifting is essential to all the experimental and data analysis methods developed to accommodate growing damage. It was implicitly assumed based on the wealth of materials that have displayed such behavior. Presumably, they will work on this wide class of materials.

Several analysis methods to characterize the conditioned recovery were attempted. First, returning to the theory presented in Chapter 2, it was assumed that a single hereditary integral would describe the viscoelastic behavior, again based on past experimental studies. However, damage may necessitate the use of two or more hereditary integrals due to the damage effect coefficient, P_{ij} . A two-integral representation was assumed, each with separate power-law v/e behavior. Using a Levenberg-Marguart numerical scheme [e.g. (Press and Flannery, 1986)], material parameters were fit based on the average recovery from a 100s loading at a given stress level. A very good fit could be made. However, predictions of recovery from 1000s creep were wildly inaccurate. The material clearly does not behave in the way a double hereditary integral representation would predict.

Noting from the Damage Effect Study that a constant strain needed to be removed from higher damage state data before vertical shifting would collapse this data, the interference of closing cracks was considered as a possible physical source of the irregularities observed in the recovery data (recall that no further accumulation of plastic strain was observed for this conditioned data). Presumably, with more cracking, there would be a greater number

of cracks to cause interference and the effect of crack interference greater at higher damage states. However, no studies of NLVE materials found in the literature report or analyze such a phenomenon, even when damage is considered. In light of the microstructural relaxation seen in the AE testing, it seems more likely that the regions of shear yielded, highly stressed material play a significant role on the global response and not just on crack growth. A constitutive model similar to that used in interpreting the AE data may be needed. Having separate phases of material causes the same effect as crack interference, where the NLVE phase is in compression upon unloading and the LVE phase in tension, but also accounts for the relaxation noted while under load. Indeed, the recover data has the same general shape of a 2-step creep loading where the second loading is compressive.

Having two phases of material greatly complicates behavior as the state of stress on each phase is always changing, even when the global stress is held constant or removed (except at very long times). The use of creep/recovery data greatly simplifies analysis for more standard NLVE materials as all stress-dependent material parameters are constant during both the creep and recovery portions. Here, nonlinear parameters of the NLVE phase will always change. Analysis of such behavior requires the development of rather robust numerical methods to fit all the material parameters even when assuming the simplified model of Figure 4.4.

Cyclic Creep/Recovery

Cyclic behavior varied depending on stress level. In some instances (at sufficiently low stress), the creep of the transverse strains showed little variation with cycle aside from initial load-up, apparently indicating that the effect of

growing damage is small for the length cycles used.

Recovery strains show that the removal of a constant viscoplastic strain and vertical shifting of recovery data only roughly accounts for the cyclic effect in this material. For modest loads and short creep duration on 90° samples, little effect from damage growth is seen and such a method works well. At higher loads, the shape of the conditioned recovery curve is still different than seen in the first two cycles, indicating that either the hereditary damage effect is significant and/or the effect of damage is more complicated in this material than assumed. Since the conditioned recovery for this material can not be fully characterized by the constitutive equations used, it is difficult to quantify the hereditary damage effect and, for that matter, exact values for the viscoplastic strain without waiting very long times for full recovery. The same behavior was seen for the shear strain in 30° off-axis samples, but the transverse strain showed no change from cycle to cycle. Apparently the stress was not high enough for the hereditary effect to be significant.

Damage Effect

Although one would expect distributed cracking to only soften the material, the elastic compliance actually stiffens with increased damage as R_e decreases slightly with S . Recall that a net plastic strain is present at each damage state. With the two phases of material in mind, a highly damaged NLVE phase and an intact LVE one, and possible interference from crack faces the regions of soft material are put into compression while the intact material remains in tension upon unloading. If the intact material stiffens with increased stress, it will be stiffer at higher damaged states; it has a net tensile stress at zero load which increases with damage. The softer, damaged material, probably

contributes little to the overall elastic stiffness. Consequently, stiffening of the intact regions dominate the global elastic response.

The Damage Effect Study was successful in isolating the effect of stress from that of damage, thereby indicating which NLVE material parameters are affected by damage. It was found that both the shear and transverse viscoelastic strains were affected by damage regardless of fiber orientation. Vertical shifting of the recovery data at different damage states worked well for all sample types once a small constant strain was removed. This constant strain is not a plastic strain, as the sample does eventually recover to the starting strain for a given cycle. This was checked on a few cycles where very long recovery was allowed between cycles and consequently is not shown in the data presented. This constant strain is most likely an effect of the two phases of material mentioned in the discussion on conditioned behavior. In that the same stress is used in comparing damage states, the effect seems to be small enough that it can be approximated by a constant strain that is a function of the time under load. It is likely also responsible for the slightly imperfect vertical shifting seen in the shear recovery of the 30° off-axis data. Vertical shifting for the effect of damage worked well for all other data, however. The material parameter affecting the time scale, a_σ , is therefore independent of damage.

Another major simplification found for this material is that damage only affects the transverse behavior through the g_2^c parameter regardless of fiber direction. No effect is seen on g_1^c for any of the samples tested. However, no such simplification can be made for the shear behavior. Both the 30° and 45° samples displayed unequal creep and recovery shear damage ratios.

Chapter 9

Conclusion

The rubber-toughened fiber composite under study displayed significant softening effects due to many mechanisms. It is nonlinearly elastic and viscoelastic and displays large viscoplastic strains at high stress. Small-scale damage also had a significant effect on the viscoelastic behavior. A complete analysis, including the isolated effects of each mechanism and for loading and unloading behavior, was complicated by the inability to characterize the stress-dependence of conditioned material (that without growing damage) using existing theory. A constitutive model containing two phases of material, a highly nonlinear viscoelastic phase and a linear viscoelastic one, appears to be needed. Microstructural relaxation apparent only in the acoustic emission data played a key role in developing this model. For monotone increasing loadings, a relatively simple constitutive theory which lumps the damage with other stress and time effects is adequate [e.g. Bocchieri and Schapery (2000)].

It is believed the principal contribution of this dissertation is the development of theoretical, experimental and data analysis methods for identifica-

tion, isolation and characterization of the primary deformation mechanisms in a rubber-toughened fiber composite. There are four parts to this contribution.

First, the constitutive theory proposed by Schapery (1999) was tailored for a continuous fiber composite and evaluated for a creep/recovery loading where nonlinear viscoelasticity, viscoplasticity and damage growth have a significant effect on strain. A *numerical method* using a Genetic Algorithm in conjunction with the Levenberg-Marguart method was then developed to fit material parameters in these equations. This method successfully fits simulated recovery data with hereditary damage effects. Performance was improved when fitting the difference between ‘conditioned’ recovery and that from first loading. This method was not implemented on real data due to the more complicated constitutive model apparently needed for unloading this particular material. It should be useful in analyzing data from the wide class of materials whose conditioned behavior has been characterized by the constitutive theory without growing damage as proposed by Schapery (1969) and others.

Second, a *Damage Effect Study* was successful in isolating the effect of stress from that of damage, thereby indicating which material parameters are affected by damage. Vertical shifting of recovery data at different damage states, much like vertical shifting for the effect of stress, worked well for all sample types once a small constant strain was removed. The material parameter affecting the time scale, a_σ , is therefore independent of damage. An additional simplification found for this material is that damage only affects the transverse behavior through g_2^c regardless of fiber direction. No effect was seen on g_1^c for any of the samples tested. However, no such simplification can be made for the shear behavior. Both the 30° and 45° samples displayed

unequal creep and recovery damage ratios. Finally, both the transverse and shear elastic compliances are found to stiffen with increased damage.

Third, a method of *Acoustic Emission monitoring* and waveform analysis was developed as a means for tracking two of the primary dynamic damage mechanisms in these materials, matrix-cracking and fiber/matrix debond. With direct monitoring, the extent of this type of damage in the material does not need to be inferred from its effect on the stress-strain response. After developing an experimental and waveform filtering method for off-axis coupons, unidirectional 30° , 45° and 90° samples of a rubber-toughened carbon/epoxy were monitored in this way for various loading histories. Significant cracking, evenly distributed along the length of all sample types was detected with the AE sensors during loading. A method of comparing waveforms from samples with different fiber angles was also suggested. Little difference was observed in these waveforms; consequently, events from each sample type were treated in a similar fashion. An interpretation of the AE data was proposed based on an initial population of existing flaws. Then a cumulative distribution function of microcracking was defined and used to study effects of stress history. Key elements of the proposed interpretation of the AE data require that

- 1- The *volume* of material over which cracking is detected
- 2- The *minimum size* of cracks being detected
- 3- The *portion* of cracks detected

remain constant throughout a test. Studies of changes in wavespeed, damping and waveform energy during loading were performed to ensure the constancy of these items. Independence of the detected waveform energy with stress level indicates that the average arrested crack length was not a function of stress level for most samples and loading histories tested.

Finally, after developing an *idealized model of the material* consisting

of two viscoelastic phases, a single loading parameter, which is theoretically independent of loading history and derived from viscoelastic fracture mechanics, was proposed. It was found that time or rate-dependence of the microcracking in 90° samples was very weak and only evident from ramp/hold and load/unload testing. With the addition of shear stress, as in the off-axis samples, the rate effect of cracking became stronger. Material parameters for the proposed idealized model of the 2-phase material were found and a single damage distribution parameter was found independent of loading history for the 90° samples, thus supporting the theory. A simplified analysis of data from off-axis testing collapses data from all samples and loading histories, thus supporting the model proposed.

Recommendations for Further Work

Due to the apparent effect of having two or more phases of viscoelastic material in the microstructure, both theoretical models and data analysis methods need to be further developed to explain the conditioned response of this material before further analysis of the effects of damage can be made. A first step may be to use the idealized 2-phase model implemented in the AE analysis to model global deformation. If the constitutive model described in Chapter 2 is used for the NLVE phase, it may be possible to adequately fit the recovery data. With stresses redistributing from one phase to the other, the nonlinear parameters in the model will change over time, even with complete unloading. A powerful numerical method, possibly implementing a Genetic Algorithm, may prove useful in fitting data with such a model.

For non-toughened material systems, the numerical method developed here to fit data with hereditary damage effects may prove useful. It is encouraged that it be tried on one or many of the material systems that have displayed more simplified conditioned behavior. Also, the Damage Effect Study, although effective on this material, may be more easily implemented on non-toughened systems as the effect of two material phases is not present.

A numerical micromechanical study that includes effects of multiple phases of material, both linear and nonlinear viscoelastic and viscoplastic, with debonding and cracking may also be helpful in deducing functional forms for the global material parameters affected by these mechanisms. Effects of extensive shear yielding, caused by the rubber particles, can then be studied independent of cracking as well as their interrelated effect. Such studies may aid in developing better models for each form of damage evolution.

Further acoustic emission studies on 90° samples should include addi-

tional loading histories and expansion of this study to various temperatures. First, ramp/hold tests to various stress levels should be performed to confirm the amount of microstructural relaxation observed with different stress levels. This may also be coupled with unloading sequences. Also needed is a way to extrapolate back to very high loading rates where data acquisition is not possible and to very long times where the time-frame of testing is not reasonable from a practical standpoint. Elevated and cold temperature testing may prove useful for both. Whether temperature dependence of the damage growth rate and intrinsic viscoelastic behavior are the same needs to be investigated. Such an understanding will aid in performing accelerated studies of long-term behavior.

There is some evidence that the off-axis samples may contain both dynamic and steady cracking depending on the loading rate, where only the dynamic cracking is detectable by the AE method. Before running ramp/hold testing in the off-axis samples, which obviously has drastic differences in rate within the same test, additional rates should be run. It may be that after a certain rate is reached only dynamic cracking occurs, or vice versa. Studies in an environmental SEM similar to that of Wood (1996), but with variations in loading rate, may also be helpful in studying this phenomenon on isolated regions of material.

Development of more sensitive sensors in the frequency range of 100 to 500 kHz would be helpful in monitoring distributed microcracking and debonding in the material studied. Many events from smaller-scale cracks were discarded as they could not be accurately located. These waveforms were comparable in amplitude to background noise. In conjunction with this, an acquisition system that adapts gains to the incoming signal would also be helpful. Due to the variation in event size, more sensitive sensors will

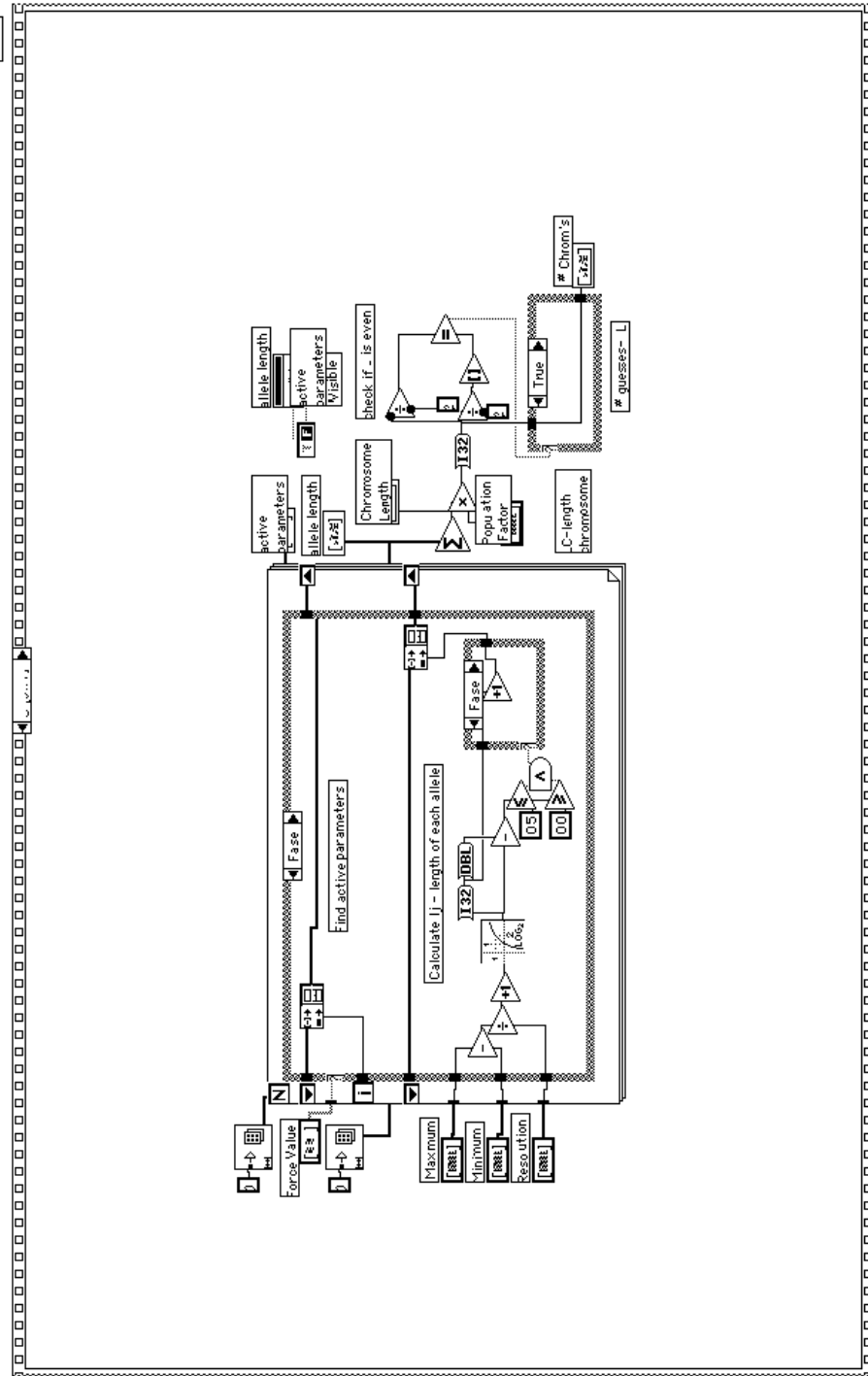
cause the large signals to go off-scale with a fixed gain system. In this way, sensitivity is not lost and all information about a waveform is still captured.

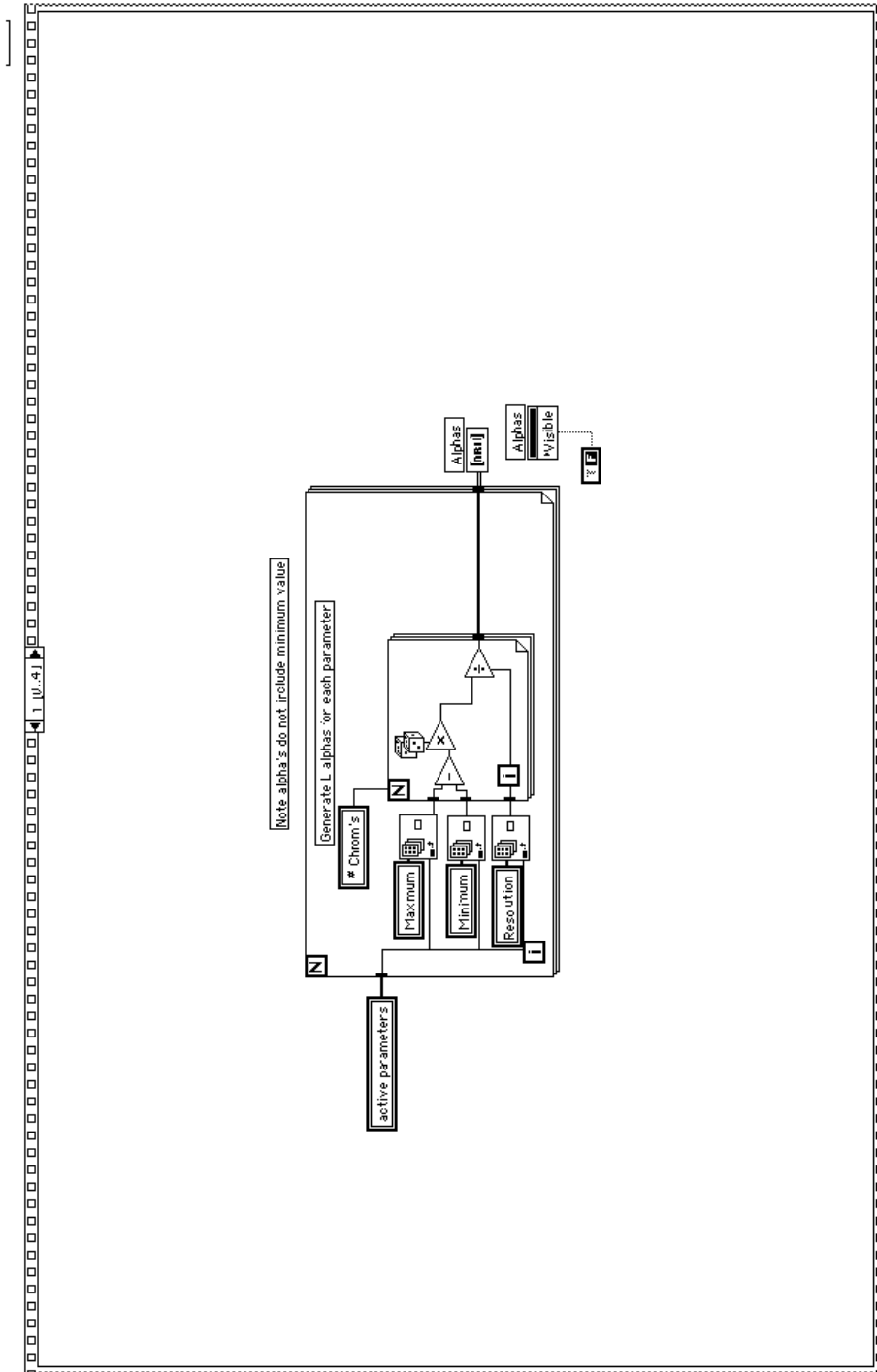
Appendix A

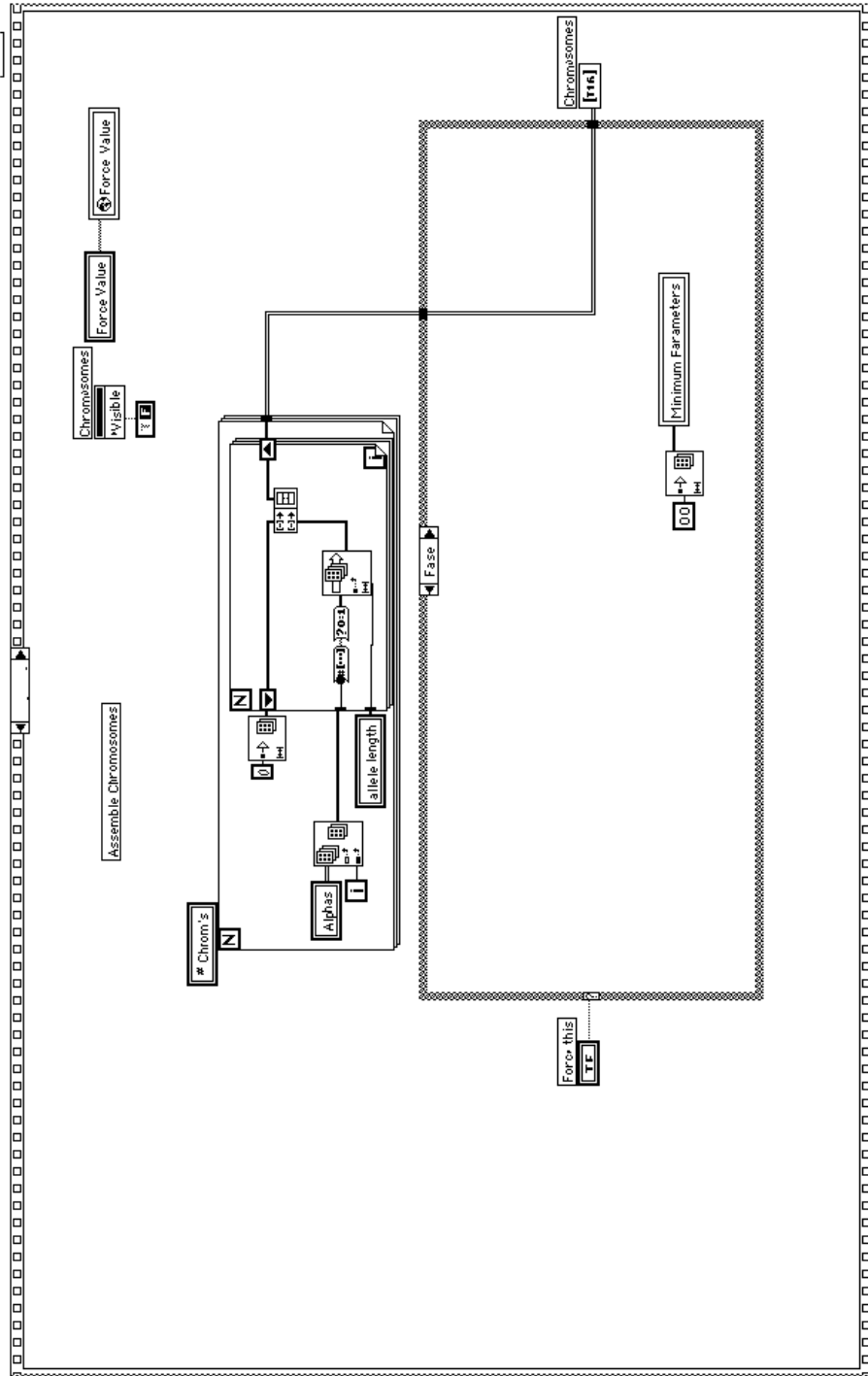
Genetic Algorithm Code

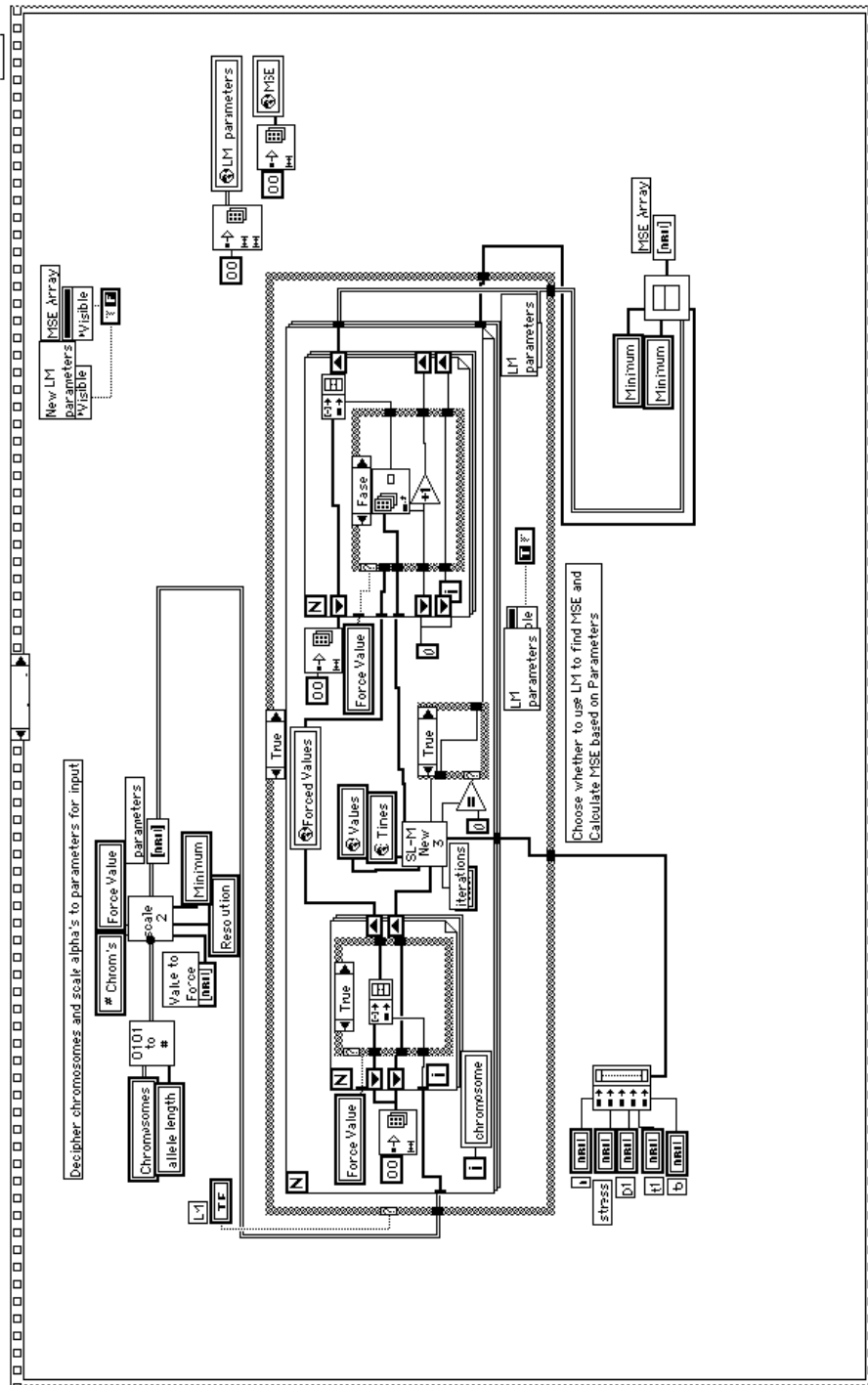
The Genetic Algorithm code was written in Labview (software produced by National Instruments Corporation) to be easily used with data collected with the same software. Subroutines that come packaged with this software are not shown in the following appendix unless they have been altered.

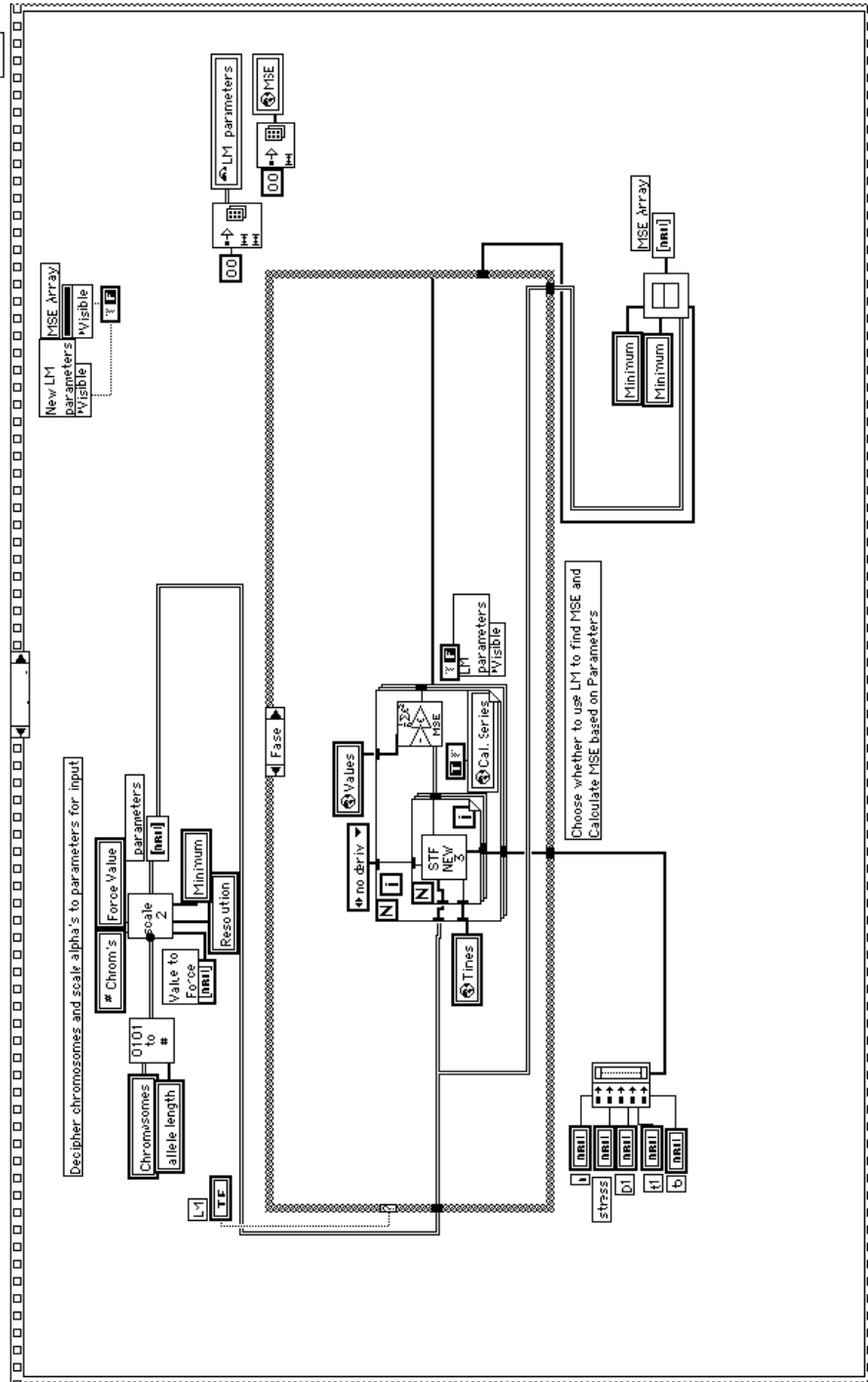
Main Program

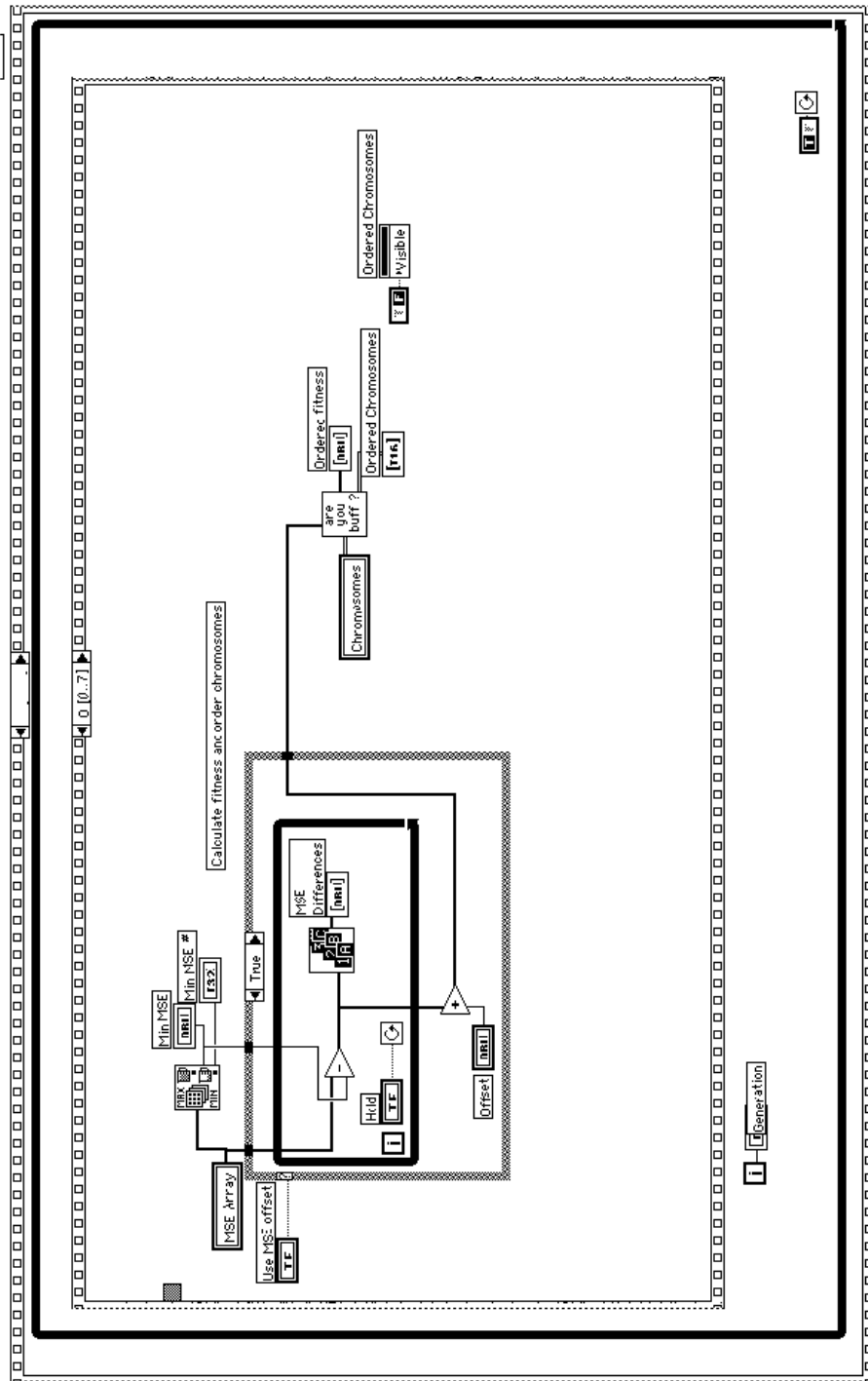


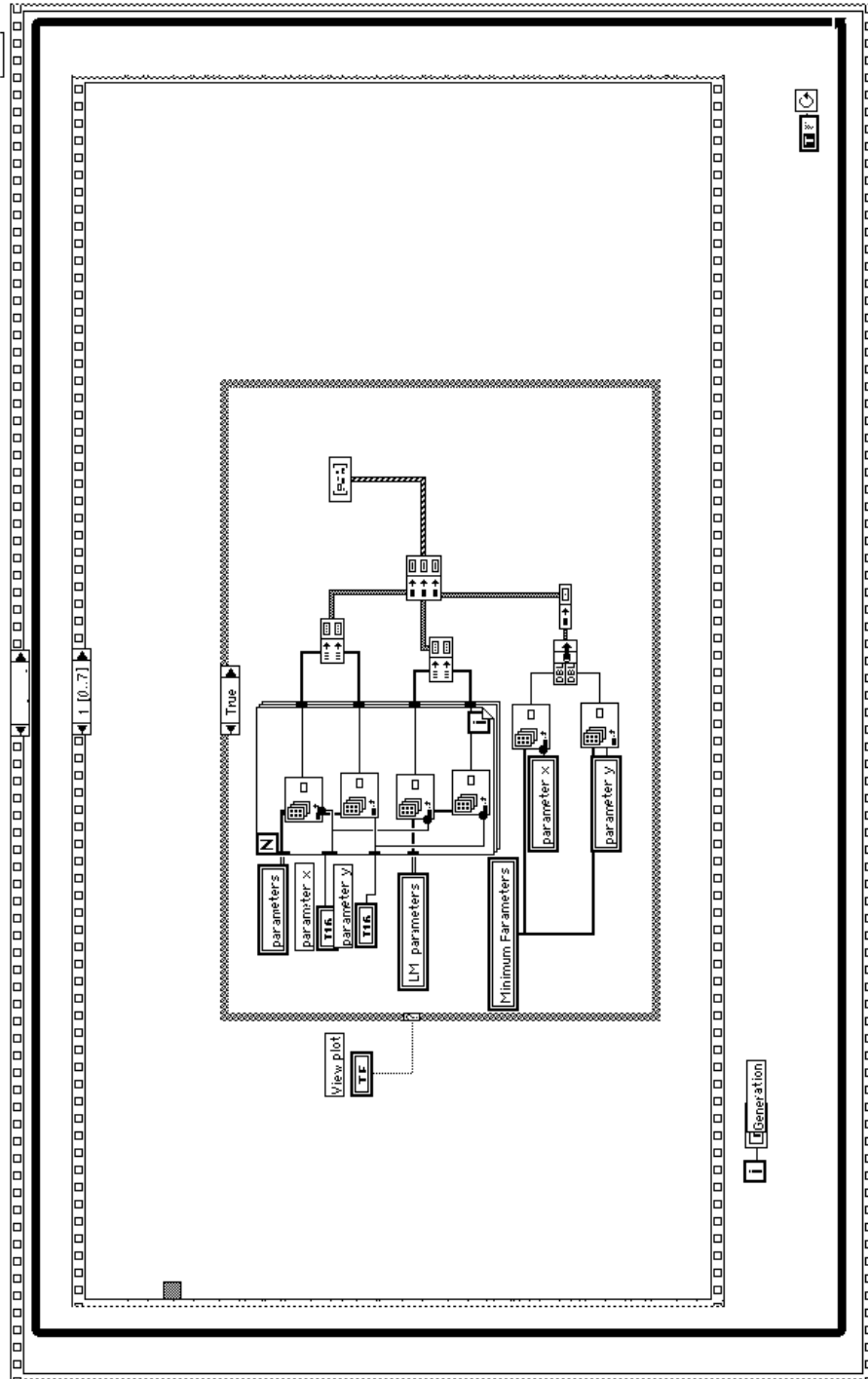


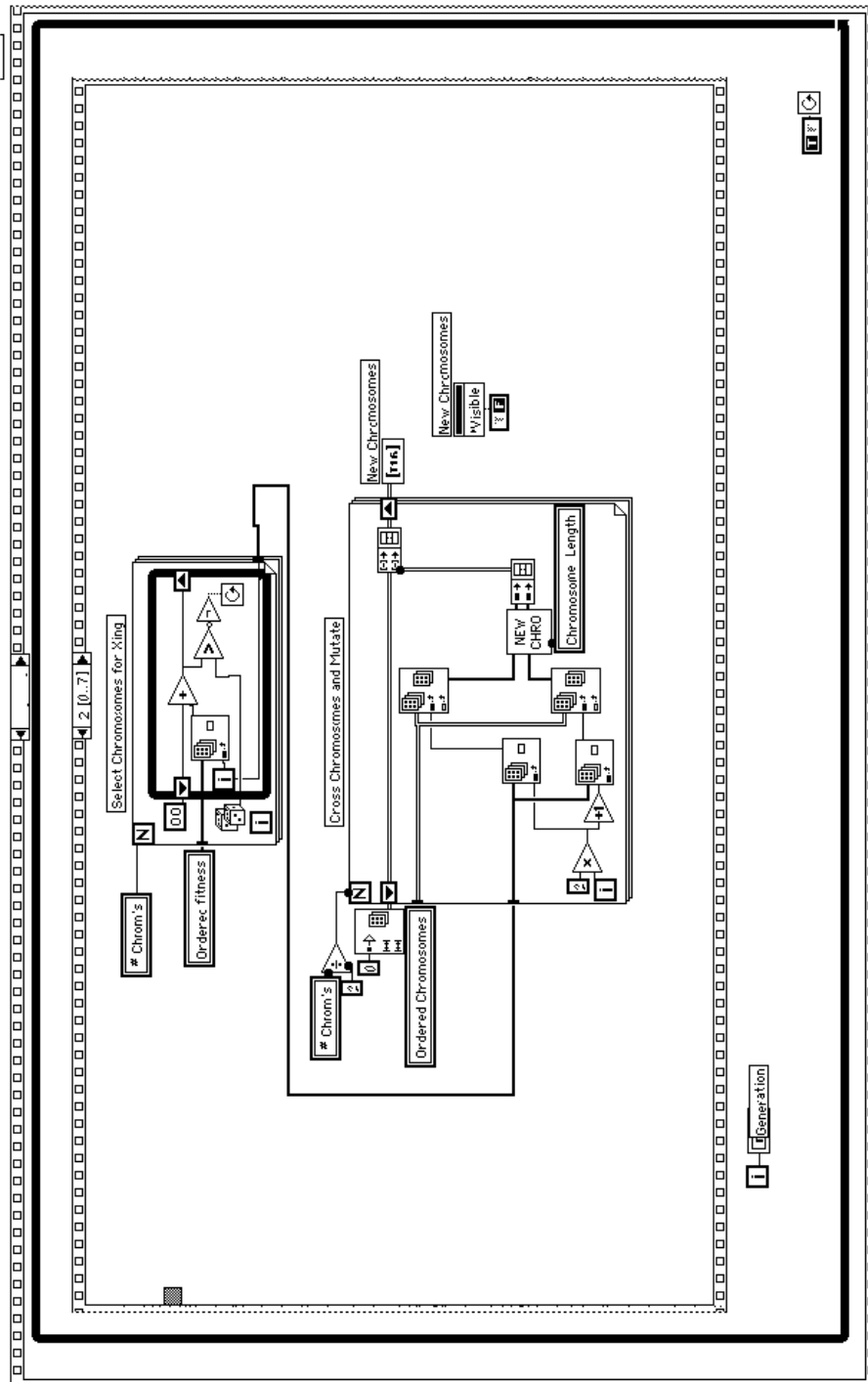


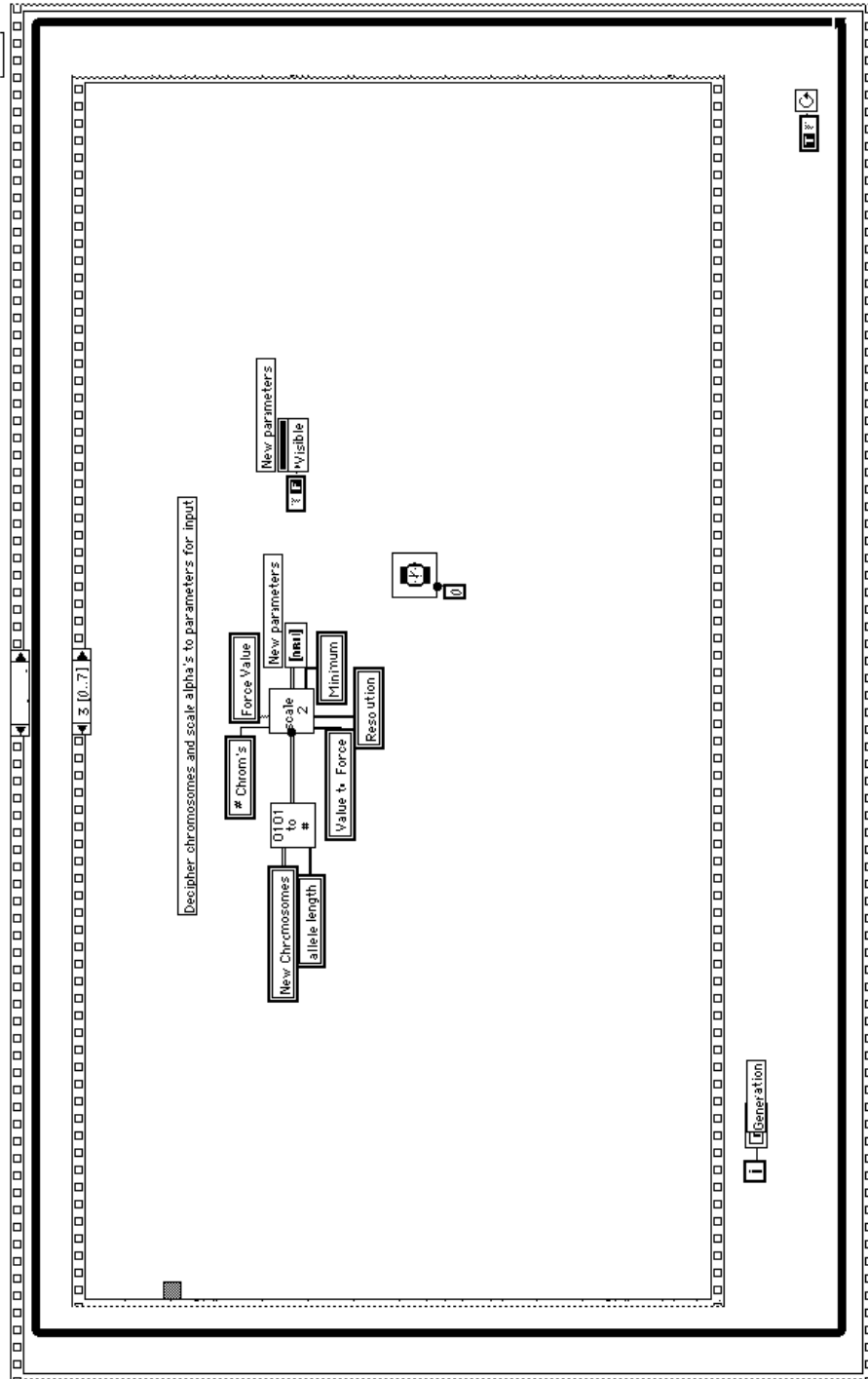


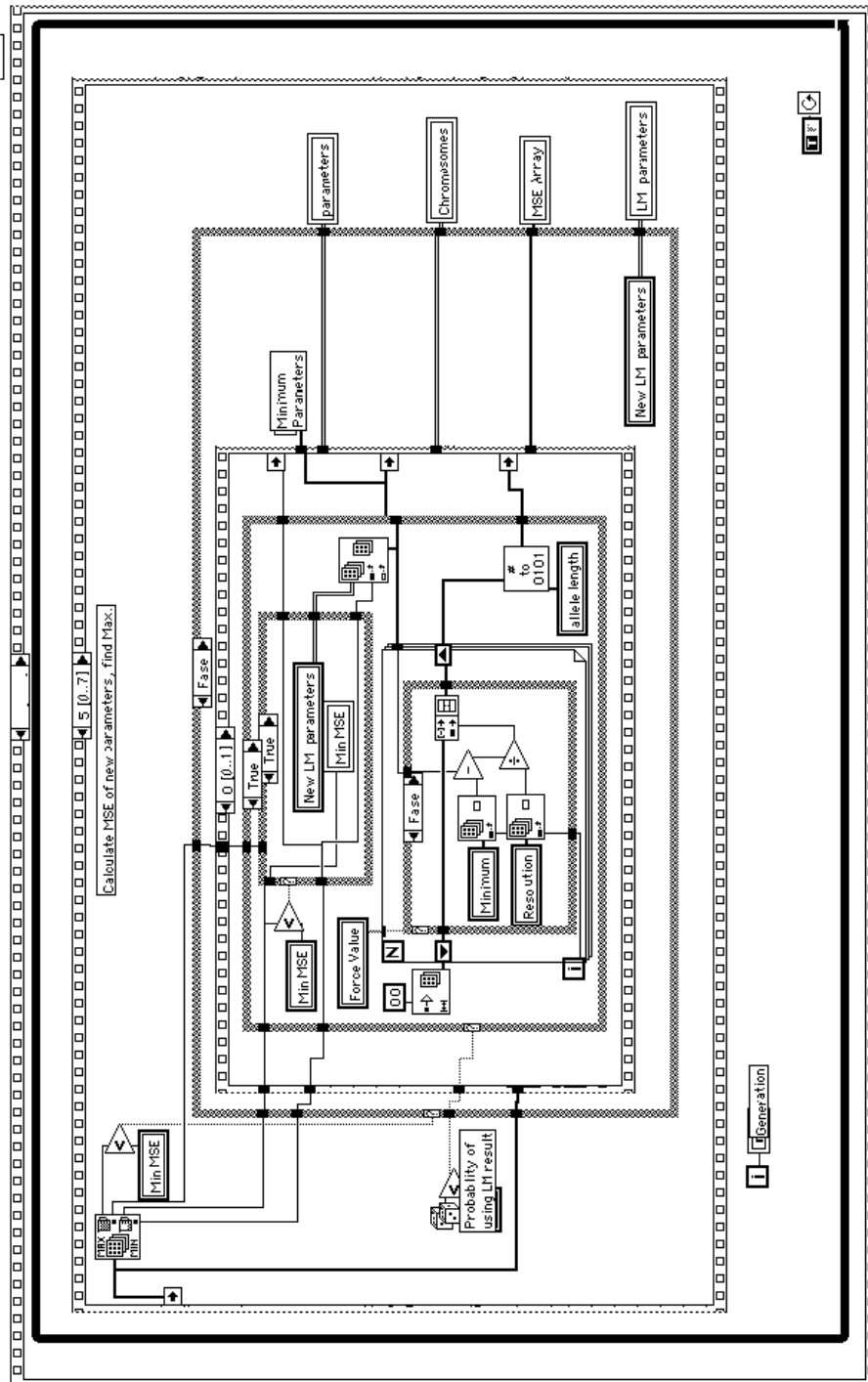


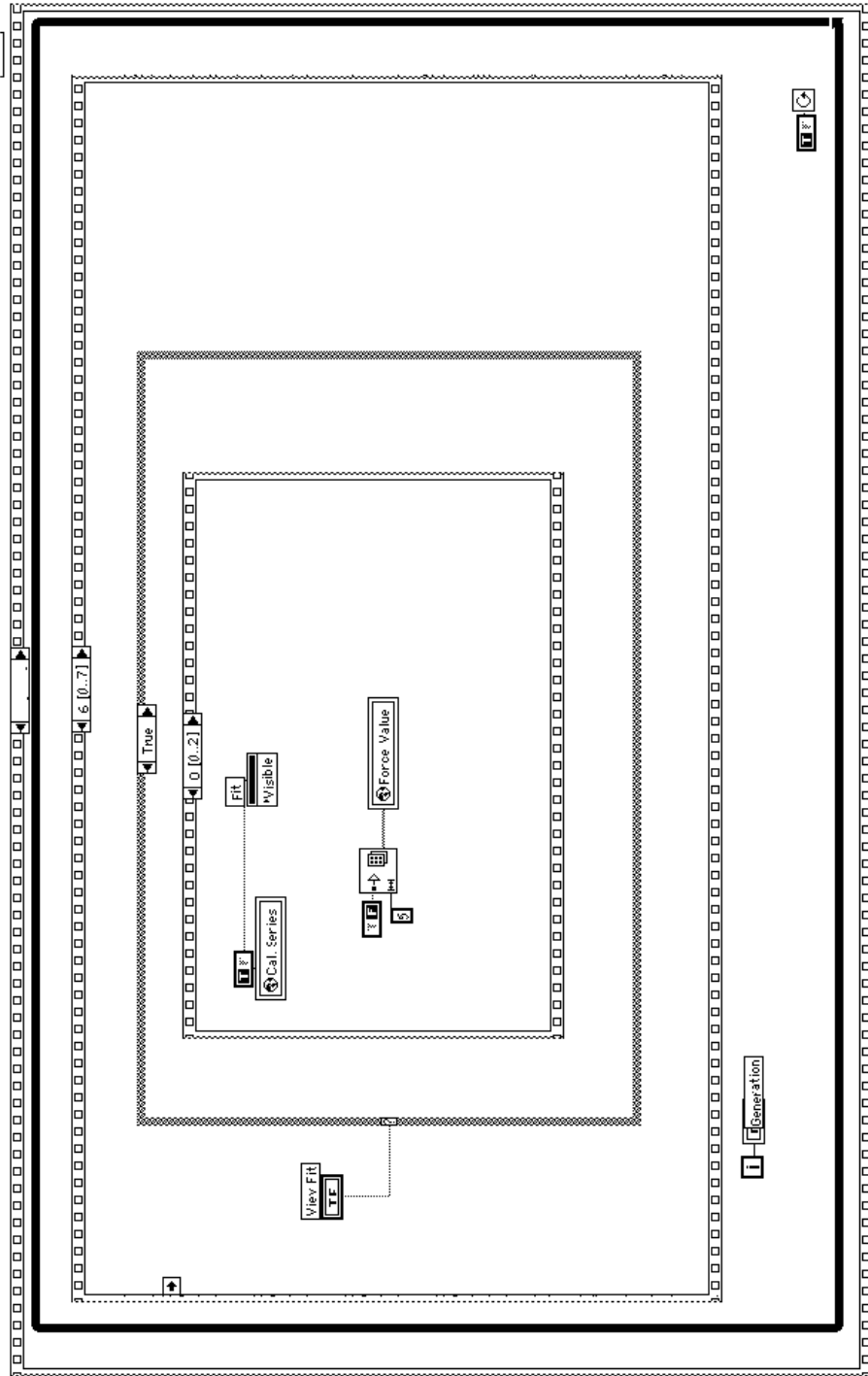


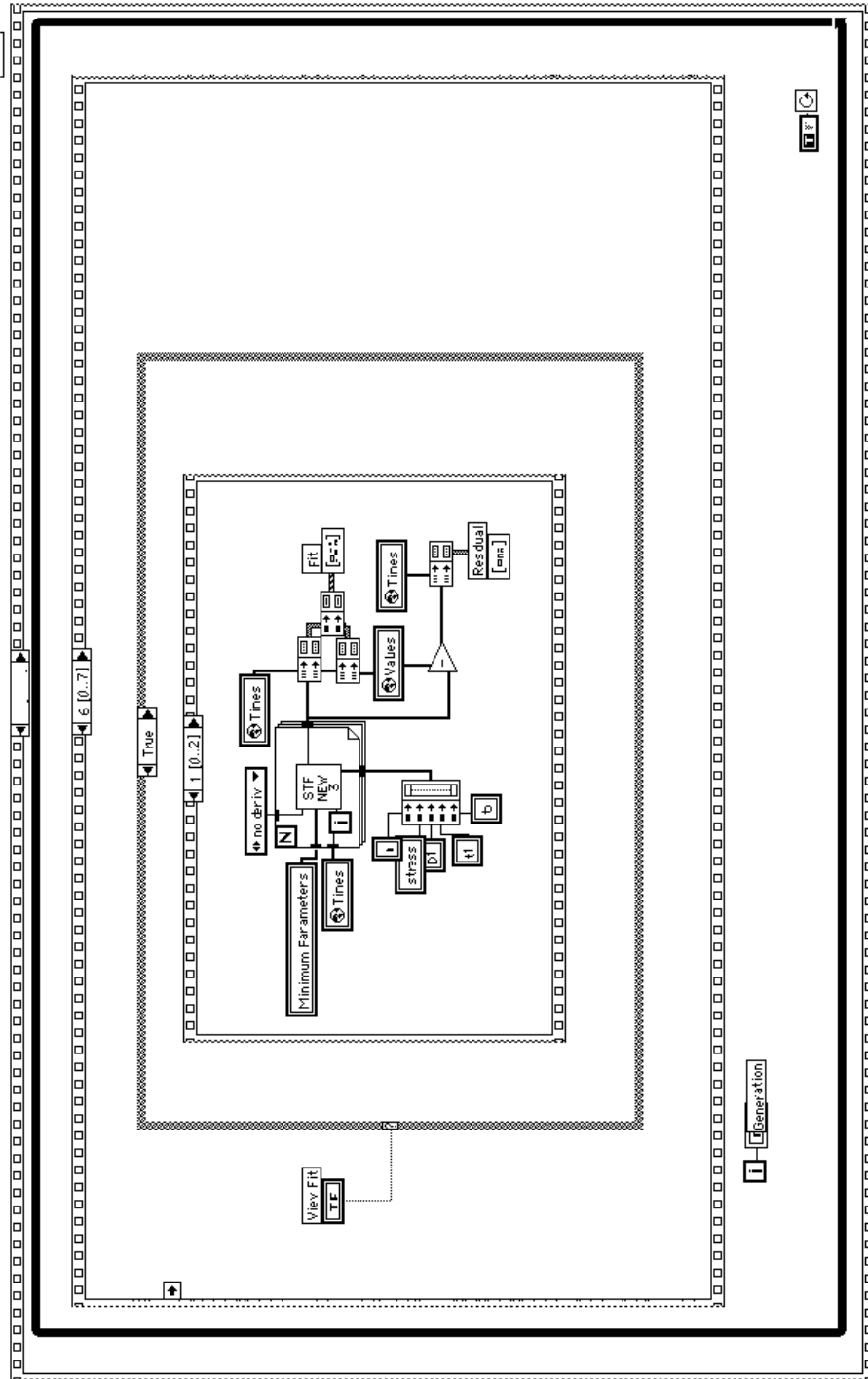


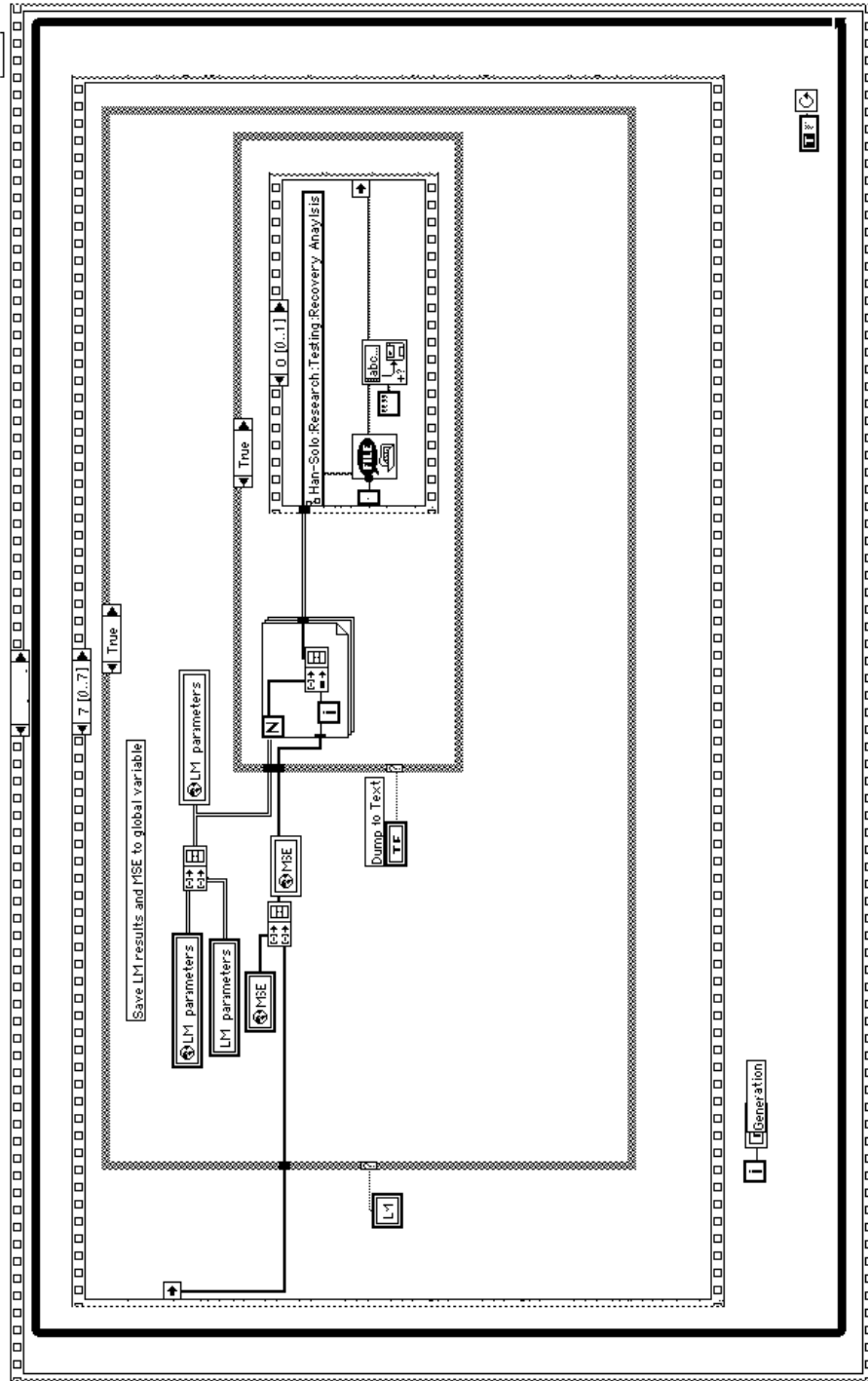




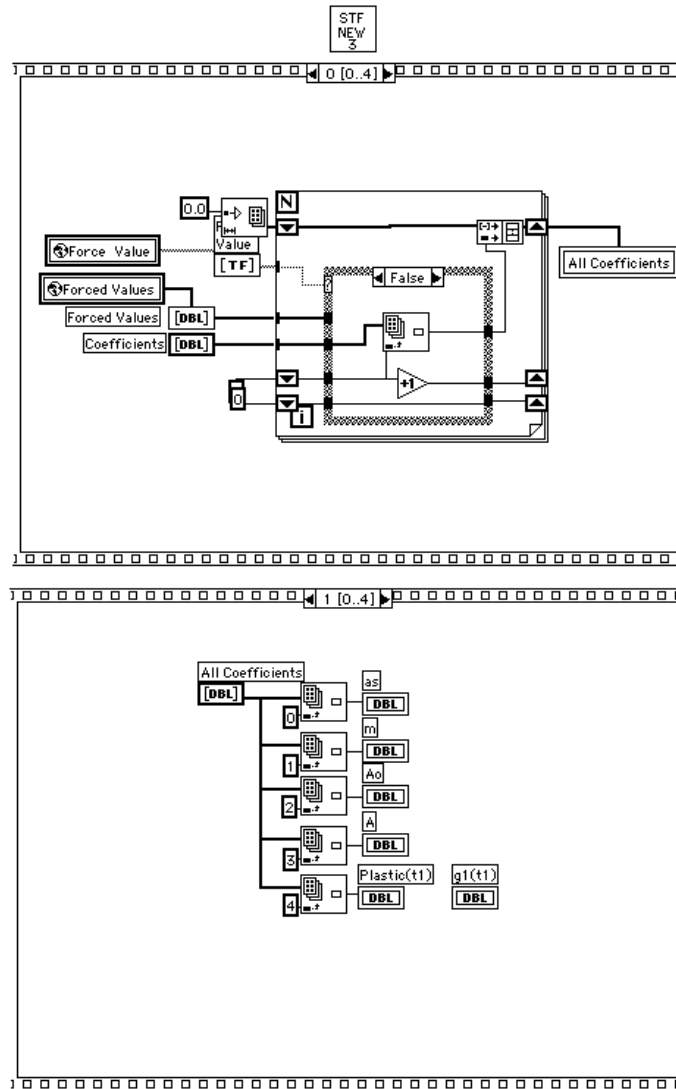




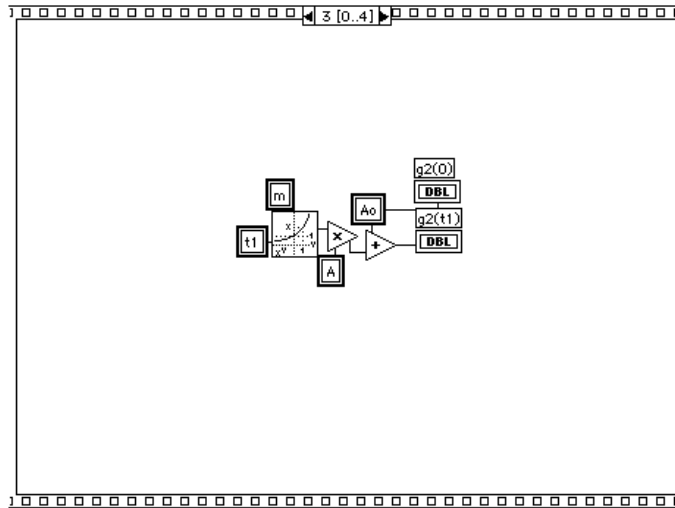
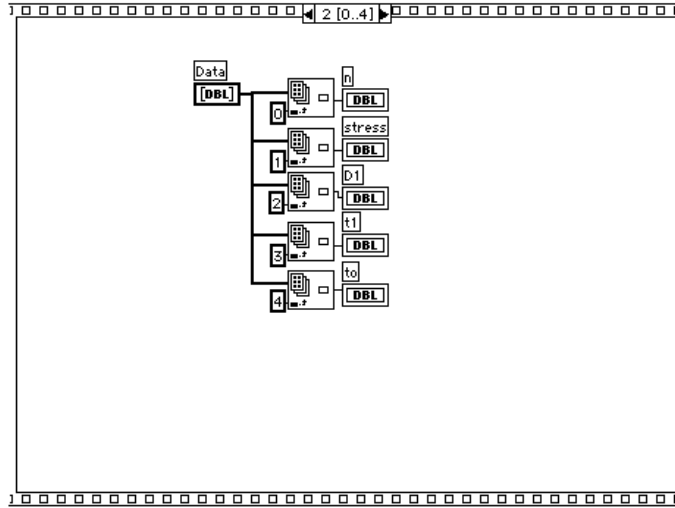




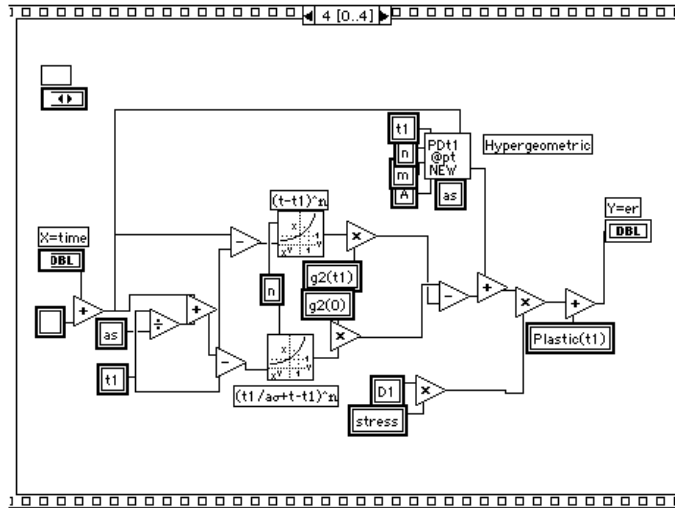
Target Function Subroutine



STF
NEW
S

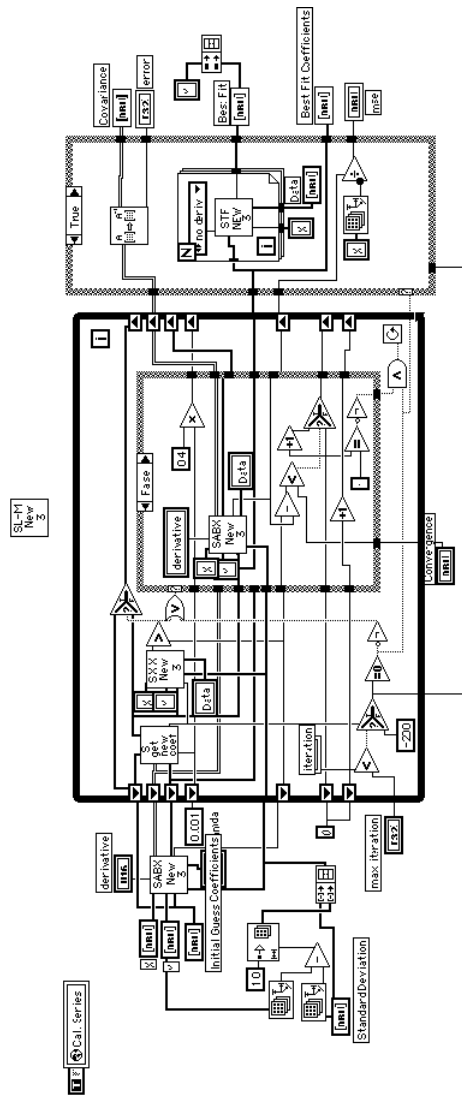


STF
NEW
S

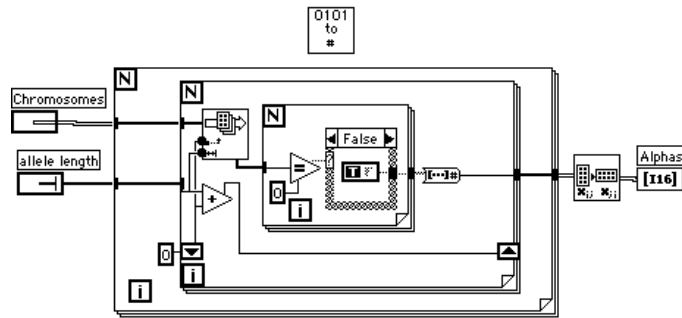


Levenberg-Marguart Subroutine

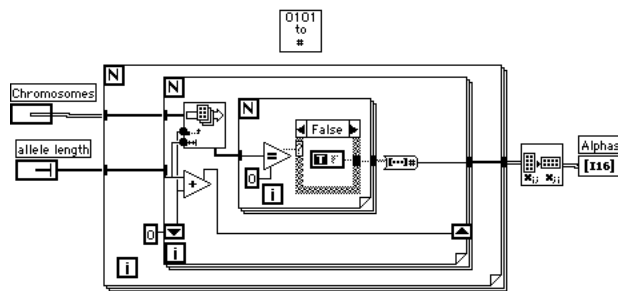
This subroutine comes packaged with Labview. It has been modified by incorporating the Target Function of the previous section and a few alterations for convergence.



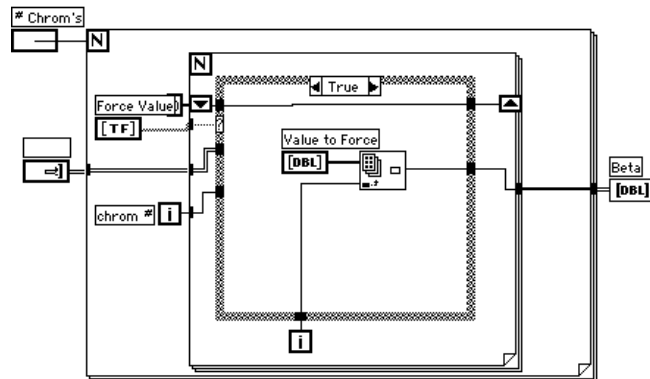
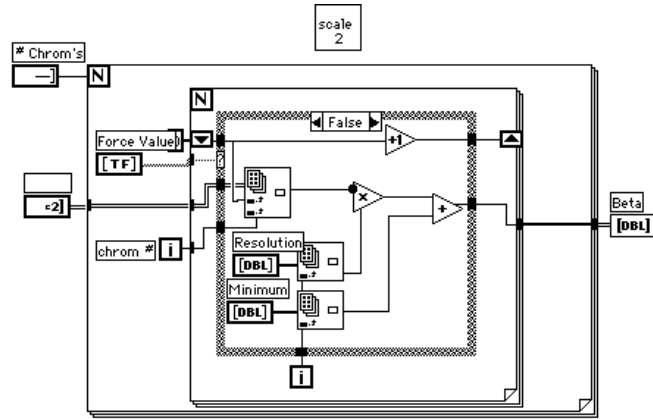
Decipher Parameter Subroutine



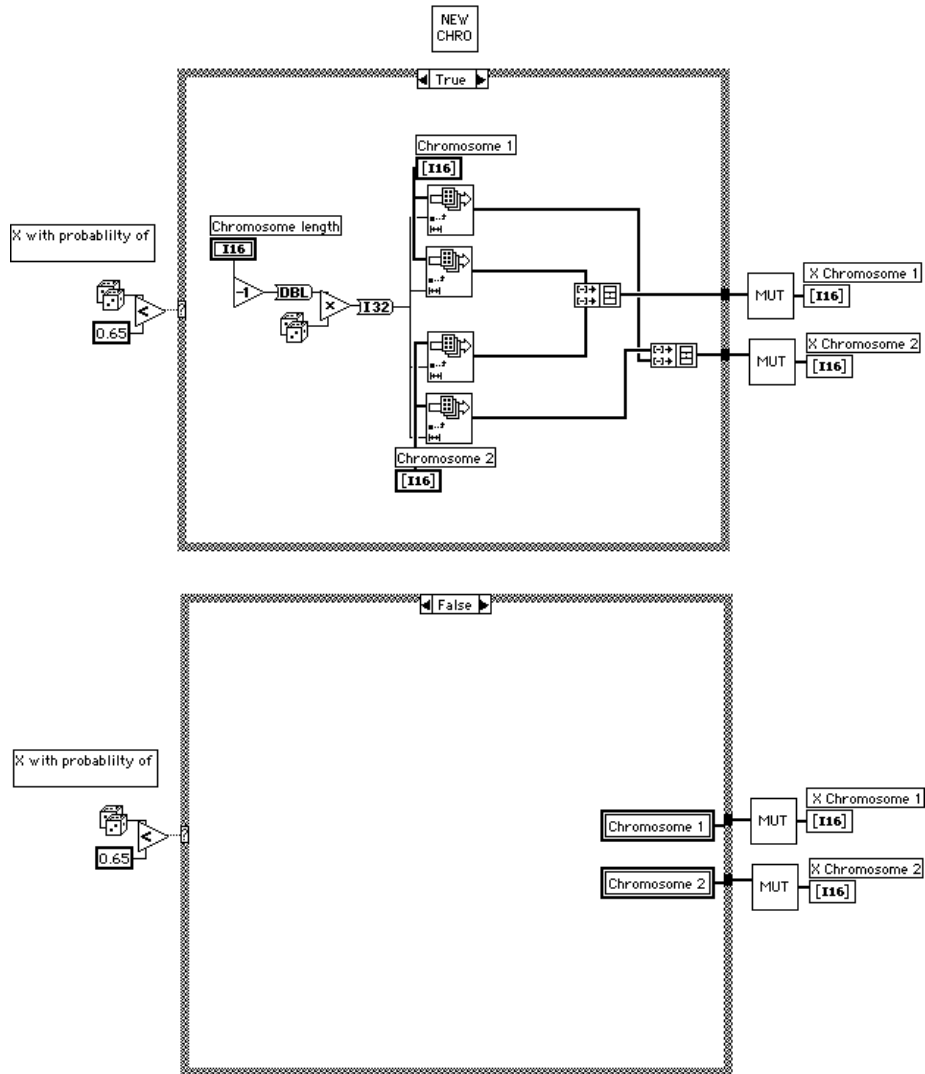
Decipher Chromosome Subroutine



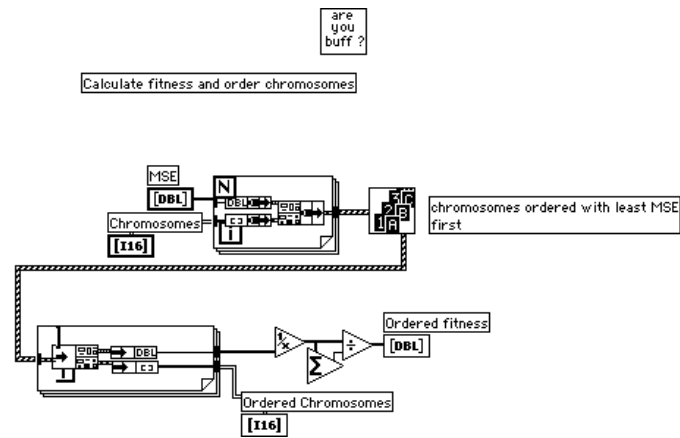
Scale Parameters Subroutine



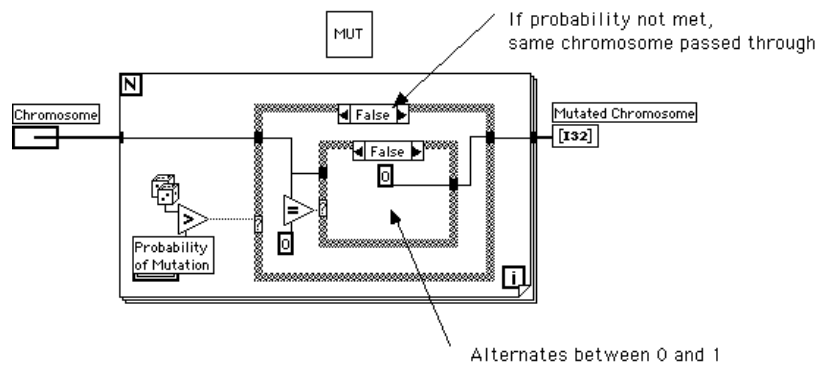
Cross Chromosomes and Mutate Subroutine



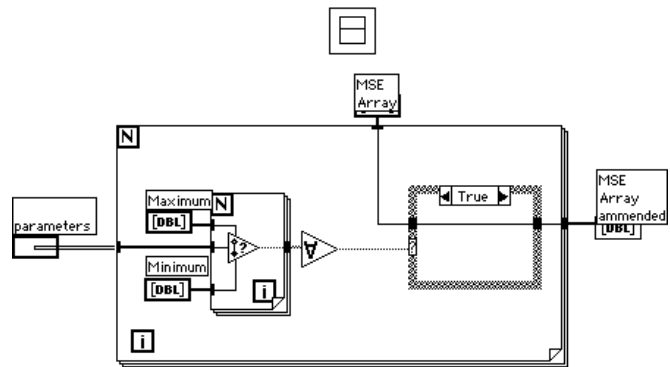
Fitness Subroutine



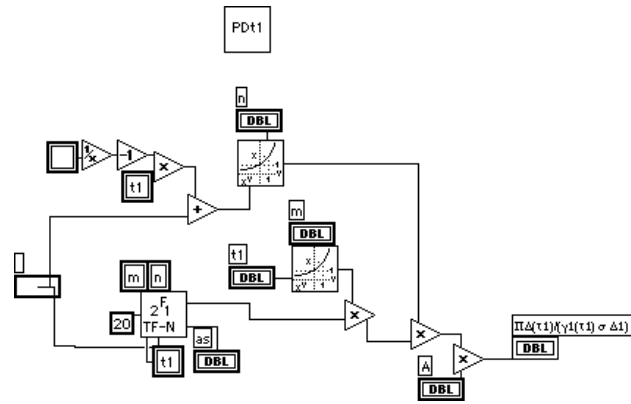
Mutation Subroutine



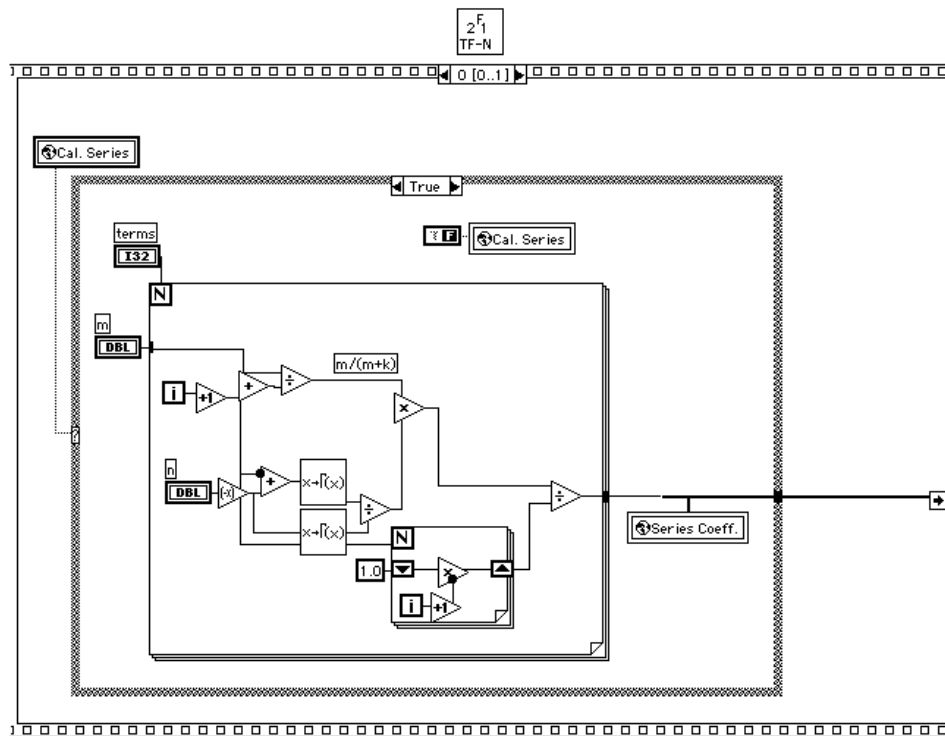
Windowing Parameters Subroutine

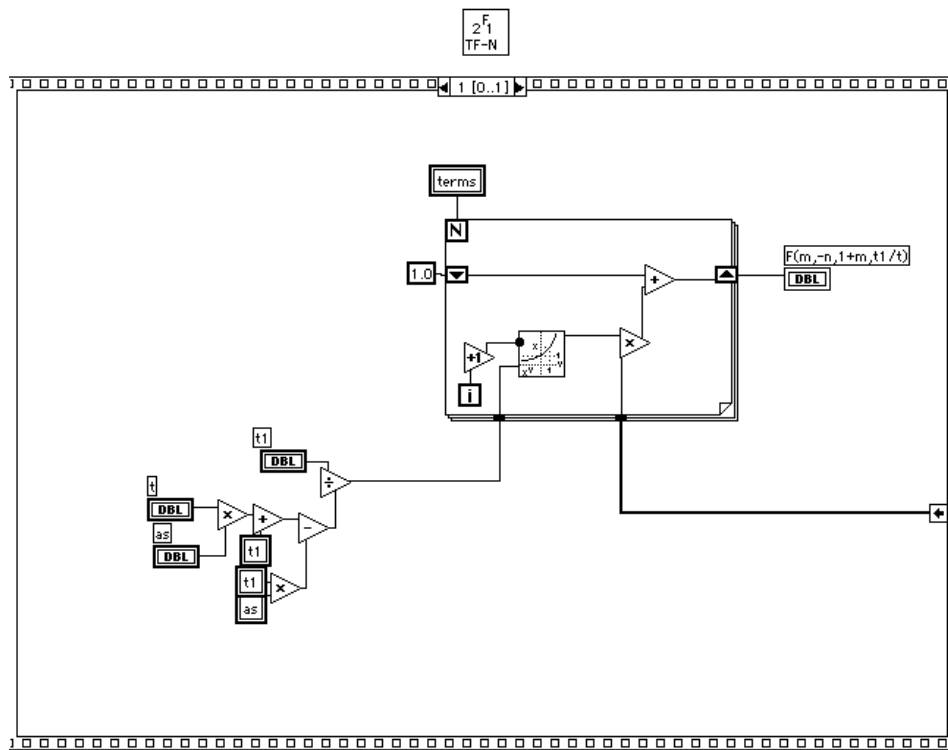


Hereditary Damage Subroutine



Hypergeometric Function Subroutine





References

- Abdel-Tawab, K., and Weitsman, Y., 1998, “A Coupled Viscoelasticity/Damage Model with Application to Swirl-Mat Composites,” *Int. Journal of Damage Mechanics*, Vol. 7, pp. 351–380.
- Awerbuch, J., Gorman, M., and Madhukar, M., 1985, “Monitoring Acoustic Emission during quasi-static loading-unloading cycles of filament-wound graphite-epoxy laminate coupons,” *Materials Evaluation*, Vol. 43, pp. 754–764.
- Bader, M.G., Bailey, J.E., Curtis, P., and Parvizi, A., 1979, “The Mechanisms of Initiation and Development of Damage in Multi-axial Fibre-reinforced Plastics Laminates,” In *Proc. 3rd Int. Conf. on Mechanical Behavior of Materials*, pp. 227–239.
- Beckwith, S., 1974, *Viscoelastic Characterization of a Nonlinear, Glass/Epoxy Composite Including the Effects of Damage* Ph.D. dissertation, Texas A&M University.
- Beckwith, S., 1980, “Creep Evaluation of a Glass/Epoxy Composite,” *SAMPE Quarterly*, Vol. January, pp. 8–15.
- Benjamin, J., and Cornell, C., 1970, *Probability, Statistics, and Decision for Civil Engineers* McGraw-Hill Book Company.
- Bocchieri, R., 1996, *A Baseline Nonlinear Material Characterization for Predicting the Long-Term Durability of Composite Structures*, Master’s Thesis, The University of Texas at Austin.
- Bocchieri, R., and Schapery, R., 2000, “Nonlinear Viscoelastic Behavior of Rubber-toughened Carbon and Glass/Epoxy Composites,” In Schapery, R., and Sun, C. eds., *Time Dependent and Nonlinear Effects in Polymers and Composites, ASTM STP 1357*, pp. 238–265. American Society for Testing and Materials.
- Budiansky, B., and Fleck, N., 1993, “Compressive failure of fiber composites,” *J. Mech. Phys. Solids*, Vol. 41, pp. 183–211.

- Cardon, A., Qin, Y., Vossolo, C. V., and Bouquet, P., 2000, "Prediction of the Residual Structural Integrity of a polymer Matrix Composite Construction Element," *Mechanics of Time-Dependent Materials*, Vol. 4, pp. 155–167.
- CARP, 1993, "Guidance for Development of AE Applications on Composites," *J. of Acoustic Emission*, Vol. 11, pp. 1–C24.
- Chen, F., , and A. Hiltner and E. Baer , 1992, "Damage and Failure Mechanisms of Continuous Glass Fiber Reinforce Polyphenylene Sulfide," *J. Composite Materials*, Vol. 26, pp. 2289–2307.
- Crain, T., 1999, *Application of a Hybrid Optimizer to a Mission Design for Mars Transhab Verification*, Master's Thesis, The University of Texas at Austin.
- Daniel, I., and Ishai, O., 1994, *Engineering Mechanics of Composite Materials* Oxford University Press, New York.
- De Groot, P., Wijen, P., and Janssen, R., 1995, "Real-time Frequency Determination of Acoustic Emission for Different Fracture Mechanisms in Carbon/Epoxy Composites," *Composites Science and Technology*, Vol. 55, pp. 405–412.
- Goldberg, D., 1989, *Genetic Algorithms in Search, Optimization, and Machine Learning* Addison-Wesley.
- Gorman, M., and Ziola, S., 1991, "Plate waves produced by transverse matrix cracking," *Ultrasonics*, Vol. 29, pp. 245–251.
- Guedes, R., and Marques, A., 1998, "Time-dependent behavior of T300/5208 under creep, relaxation and ramp loading," In Reifsnider, K., and Cardon, A. eds., *Progress in Durability Analysis of Composite Systems*, pp. 279–283. Balkema.
- Gustafson, C., and Selden, R., 1985, "Monitoring Fatigue Damage in CFRP Using Acoustic Emission and Radiographic Techniques," In Johnson, W. ed., *Delamination and Debonding of Materials, ASTM STP 876*, pp. 448–464. American Society for Testing and Materials.
- Ha, K., and Schapery, R., 1997, "A Three-Dimensional Viscoelastic Constitutive Model for Particulate Composites with Growing Damage and its Experimental Validation," *Int. J. Solids Structures*, Vol. 35, pp. 3497–3517.
- Hashin, Z., Bagchi, D., and Rosen, B., 1974, "Nonlinear behavior of fiber composite laminates," Tech. Rpt., NASA CR-2313.
- Hashin, Z., 1985, "Analysis of Cracked Laminates: A Variational Approach," *Mechanics of Materials*, Vol. 4, pp. 121–136.

- He, M., and Hutchinson, J., 1981, "The Penny-Shaped Crack and the Plane Strain Crack in an Infinite Body of Power-Law Material," *Journal of Applied Mechanics*, Vol. 48, pp. 830–840.
- Highsmith, A., and Reifsnider, K., 1982, "Stiffness Reduction Mechanisms in Composite Laminates," In Reifsnider, K. ed., *Damage in Composite Materials*, ASTM STP 775, pp. 103–117. American Soc. for Testing Materials.
- Hutchinson, J.W., Mear, M., and Rice, J., 1987, "Crack Paralleling an Interface Between Dissimilar Materials," *J. Applied Mechanics*, Vol. 54, pp. 828–832.
- Kachanov, M., 1999, "Solids with cracks and non-spherical pores: proper parameters of defect density and effective elastic properties," *International Journal of Fracture*, Vol. 97, pp. 1–31.
- Kamimura, K., 1985, "Continuum Damage Approach to Mechanical Behaviour of Damaged Laminate and a Modelling of Damage Parameter," In A.H. Cardon, e. a. ed., *Mechanical characterisation of load bearing fibre composite laminates*, pp. 115–126. Elsevier.
- Kinloch, A.J., Shaw, S., and Hunston, D., 1983, "Deformation and Fracture Behavior of a Rubber-Toughened Epoxy: 2. Failure Criteria," *Polymer*, Vol. 24, pp. 1355.
- Knauss, W., 1973, "The Mechanics of Polymer Fracture," *Applied Mechanics Reviews*, Vol. 26, pp. 1–17.
- Komai, K., Minoshima, K., and Shibutani, T., 1991, "Investigations of the Fracture Mechanism of Carbon/Epoxy Composites by AE Signal Analyses," *JSME International Journal*, Vol. 34, pp. 381–388.
- Lai, J., and Bakker, A., 1995, "An Integral Constitutive Equation for Non-linear Plasto-Viscoelastic Behavior of High-Density Polyethylene," *Polymer Engineering and Science*, Vol. 35, pp. 1339–1347.
- Laroche, D., and Bunsell, A., 1998, "Stress and Time Dependent Damage in Carbon Fibre Reinforced Plastics," In Reifsnider, K., and Cardon, A. eds., *International Conf. on Composite Materials (3rd)*, pp. 119–127. Balkema.
- Laura, D., Keskkula, H., Barlow, J., and Paul, D., 2000, "Effect of glass fiber and maleated ethylene-propylene rubber content on tensile and impact properties of Nylon 6," *Polymer*, Vol. 41, pp. 7165–7174.
- Lou, Y., and Schapery, R., 1971, "Viscoelastic Characterization of Nonlinear Fiber-Reinforced Plastic," *J. Composite Materials*, Vol. 5, pp. 208–234.
- Micromeritics-TN-509, 1982, "Errors Due to Transverse Sensitivity in Strain Gages," Micromeritics Group, Inc.

- Mignery, L., and Schapery, R., 1991, "Viscoelastic and Nonlinear Adherend Effects in Bonded Composite Joints," *J. Adhesion*, Vol. 34, pp. 17–40.
- Moore, R., and Dillard, D., 1990, "Time-dependent Matrix Cracking in Cross-ply Laminates," *Composites Science and Technology*, Vol. 39, pp. 1–12.
- Nairn, J., and Hu, S., 1994, "Matrix Microcracking," In Talreja, R. ed., *Damage Mechanics of Composite Materials*, pp. 187–243. Elsevier Science B.V.
- Okoroafor, E.U., Huddleston, P.R., and Hill, R., 1996, "Alternative means for evaluating fibre-matrix adhesion in composites," *J. Materials Science*, Vol. 31, pp. 3057–3064.
- Park, S., Kim, Y., and Schapery, R., 1996, "A viscoelastic continuum damage model and its application to uniaxial behavior of asphalt concrete," *Mechanics of Materials*, Vol. 24, pp. 241–255.
- Park, S., and Schapery, R., 1997, "A Viscoelastic Constitutive Model for Particulate Composites with Growing Damage," *Int. J. Solids and Structures*, Vol. 34, pp. 931–947.
- Pearson, R., and Yee, A., 1983, "Effect on Crosslink Density on the Toughening Mechanism of Elastomer Modified Epoxies," *Polym. Mater. Sci. Eng.*, Vol. 49, pp. 316–.
- Press, W., and Flannery, E., 1986, *Numerical Recipes: The Art of Scientific Computing* Cambridge University Press.
- Prosser, W., Jackson, K., Kellas, S., Smith, B., McKeon, J., and Freidmant, A., 1995, "Advanced Waveform-based acoustic emission detection of Matrix Cracking in Composites," *Materials Evaluation*, Vol. September, pp. 1052–1058.
- Pyrz, R., 1990, "A Hybrid Model for Nonlinear Characterization of Composite Materials," In Dvorak, G. ed., *Inelastic Deformation of Composite Materials- IUTAM Symposium*, pp. 695–706. Springer-Verlag.
- Qin, Y., Cardon, A., and Guedes, R., 1998, "Characterization and prediction of nonlinear VE-VP behavior of CRP under cyclic loading using a neuro-fuzzy model," In Reifsnider, K., and Cardon, A. eds., *Progress in Durability Analysis of Composite Systems*, pp. 249–253. Balkema.
- Reifsnider, K., 1977, "Some fundamental aspects of the fatigue and fracture response of composite materials," In *Proc. 14th Annual Meeting of Society of Engineering Science*, p. 343.
- Rice, J., 1968, "A Path Independent Integral and the Approximate Analysis of Strain Concentration by Notches and Cracks," *J. Applied Mechanics*, Vol. 35, pp. 379–386.

- Rotem, A., and Baruch, J., 1974, "Determining the load-time history of fibre composite materials by acoustic emission," *J. Materials Science*, Vol. 9, pp. 1789–1798.
- Roy, C., Maslouhi, A., and Gaucher, D., 1988, "Classification of Acoustic Emission Sources in CFRP Assisted by Pattern Recognition Analysis," *Canadian Aeronautics and Space Journal*, Vol. 34, pp. 224–232.
- Schapery, R. A., and Sicking, D., 1995, "On Nonlinear Constitutive Equations for Elastic and Viscoelastic Composites with Growing Damage," In Bakker, A. ed., *Mechanical Behaviour of Materials*, pp. 45–76. Delft University Press, Delft, The Netherlands.
- Schapery, R., 1969, "On the Characterization of Nonlinear Viscoelastic Materials," *Polymer Engineering and Science*, Vol. 9, pp. 295–310.
- Schapery, R., 1974, "A Nonlinear Constitutive Theory for Particulate Composites Based on Viscoelastic Fracture Mechanics," In *JANNAF Structures and Mechanical Behavior Working Group*.
- Schapery, R., 1975a, "A theory of crack initiation and growth in viscoelastic media, I. Theoretical Development," *International Journal of Fracture*, Vol. 11, pp. 141–159.
- Schapery, R., 1975b, "A theory of crack initiation and growth in viscoelastic media, II. Approximate methods of analysis," *International Journal of Fracture*, Vol. 11, pp. 369–388.
- Schapery, R., 1981, "On Viscoelastic Deformation and Failure Behavior of Composite Materials with Distributed Flaws," In Wang, S., and Renton, W. eds., *1981 Advances in Aerospace Structures and Materials*, pp. 5–20. The American Society of Mechanical Engineers.
- Schapery, R., 1984, "Correspondence principles and a generalized J integral for large deformation and fracture analysis of viscoelastic media," *International Journal of Fracture*, Vol. 25, pp. 195–223.
- Schapery, R., 1986, "Time-Dependent Fracture: Continuum Aspects of Crack Growth," In Bever, M. ed., *Encyclopedia of Materials Science and Engineering*, pp. 5043–5053. Pergamon Press.
- Schapery, R., 1987, "Deformation and fracture characterization of inelastic composite materials using potentials," *Polymer Engineering and Science*, Vol. 27, pp. 63–76.
- Schapery, R., 1989, "Mechanical Characterization and Analysis of Inelastic Composite Laminates with Growing Damage," *Mech. Comp. Mat. and Structures*, Vol. 100, pp. 1–9.

- Schapery, R., 1990a, "On some path independent integrals and their use in fracture of nonlinear viscoelastic media," *Int. J. Fracture*, Vol. 42, pp. 189–207.
- Schapery, R., 1990b, "A theory of mechanical behavior of elastic media with growing damage and other changes in structure," *J. Mech. Phys. Solids*, Vol. 38, pp. 215–253.
- Schapery, R., 1999, "Nonlinear viscoelastic and viscoplastic constitutive equations with growing damage," *International Journal of Fracture*, Vol. 97, pp. 33–66.
- Shaw, S., 1994, "Rubber modified epoxy resins," In Collyer, A. ed., *Rubber Toughened Engineering Plastics*, pp. 165–209. Chapman & Hall.
- Sun, C., and Berreth, S., 1988, "A new end tab design for off-axis tension test of composite materials," *J. Composite Materials*, Vol. 22, pp. 766–779.
- Sun, C., and Chung, I., 1993, "An oblique end-tab design for testing off-axis composite specimens," *Composites*, Vol. 24, pp. 619–623.
- Talreja, R., 1985a, "A Continuum Mechanics Characterisation of Damage in Composite Materials," *Proc. Roy. Soc. London*, Vol. 399, pp. 195–216.
- Talreja, R., 1985b, "Transverse Cracking and Stiffness Reduction in Composite Laminates," *J. Composite Materials*, Vol. 19, pp. 355–375.
- Talreja, R., 1994, In Talreja, R. ed., *Damage Mechanics of Composite Materials*. Elsevier Science B.V.
- Tamuzs, V., Andersons, J., and Aniskevich, K., 1998, "Creep-damage interaction in composites," In Reifsneider, K., and Cardon, A. eds., *Progress in Durability Analysis of Composite Systems*, pp. 143–149. Balkema.
- Tuttle, M., and Brinson, H., 1986, *Proceedings of the 1986 SEM Conference on Experimental Mechanics* Pergamon Press.
- Tuttle, M., Pasricha, A., and Emery, A., 1995, "The Nonlinear Viscoelastic-Viscoplastic Behavior of IM7/5260 Composites Subjected to Cyclic Loading," *J. of Composite Materials*, Vol. 29, pp. 2025–2046.
- Valentin, D., 1985, "Critical analysis of amplitude histograms obtained during acoustic emission tests on unidirectional composites with an epoxy and a PSP matrix," *Composites*, Vol. 16, pp. 225–230.
- Wevers, M., Verpoest, I., Aernoudt, E., and Meester, P. D., 1985, "Analysis of Fatigue Damage in DFR Epoxy Composites by Means of Acoustic Emission: Preparing a Calibration Exercise," In *Mechanical Characterisation of Load Bearing Fibre Composite Laminates. Proceedings of the European Mechanics Colloquium 182*, pp. 161–168.

Wevers, M., Verpoest, I., Meester, P. D., and Aernoudt, E., 1991, "Identification of Fatigue Failure Modes in Carbon Fibre Reinforced Composites with the Energy Discriminating Acoustic Emission Method," In W. Sachse, J. R., and Yamaguchi, K. eds., *Acoustic Emission: Current Practice and Future Directions*, ASTM STP 1077, pp. 416–423. American Society for Testing and Materials.

Wood, C., 1996, *Determinating the effect of seawater on the interfacial strength of an interlayer e-glass/graphite/epoxy composite using observations of transverse cracking made in-situ in an environmental SEM*, Master's Thesis, Texas A&M University.

Zapas, L., and Crissman, J., 1984, "Creep and Recovery Behavior of Ultra-High Molecular Weight Polyethylene in the Region of Small Deformations," *Polymer*, Vol. 25, pp. 57–62.

Zhang, L., 1995, *Time-Dependent Behavior of Polymers and Unidirectional Polymeric Composites* Ph.D. dissertation, Shanghai Jiao Tong University.

Zhu, C., and Sun, C., 2000, "A Viscoplasticity Model for Characterizing Loading and Unloading Behavior of Polymeric Materials," In Schapery, R., and Sun, C. eds., *Time Dependent and Nonlinear Effects in Polymers and Composites*, ASTM STP 1357, pp. 266–284. American Society for Testing and Materials.

Zimcik, D., Proulx, D., and Roy, C., 1988, "Real-Time Monitoring of Carbon-Epoxy Composites Using Acoustic Emission NDE," *SAMPE Quarterly*, Vol. 19, pp. 5–11.

Vita

Robert T. Bocchieri was born in Albany, New York on August 18, 1971, the son of Dr. Samuel F. Bocchieri and Dr. Maureen H. Bocchieri. He attended Syracuse University in Syracuse, New York starting in 1989. After spending his Junior year at the City University of London, London, England, he graduated in May, 1993 with a Bachelor of Science in Aerospace Engineering from Syracuse University. For the following year, he worked for Martin Marietta Astro Space as an entry level engineer and graduated from their Technical Development and Advanced Courses programs. In September, 1994, he entered The Graduate School at The University of Texas at Austin where he completed a Master's degree in Aerospace Engineering by December of 1996. He hopes to complete a Ph.D. in Aerospace Engineering at the same university by May of 2001.

Permanent Address: 1018 Ellingson Lane
Austin, Texas, 78751

This dissertation was typeset with $\text{\LaTeX} 2_{\epsilon}$ by the author.